Coupling methods of phase-resolving coastal wave models

José Galaz

To cite this version:

José Galaz. Coupling methods of phase-resolving coastal wave models. Modeling and Simulation. Université de montpellier, 2024. English. NNT : . tel-04689721

HAL Id: tel-04689721
https://inria.hal.science/tel-04689721v1

Submitted on 5 Sep 2024

THÈSE POUR OBTENIR LE GRADE DE DOCTEUR DE L'UNIVERSITÉ DE MONTPELLIER

En Mathématiques et Modélisation

École doctorale : Information, Structures, Systèmes

Unité de recherche : Inria – Équipes CARDAMOM & LEMON / IMAG

Coupling methods of phase-resolving coastal wave models

Présentée par José Daniel GALAZ MORA
Le 26 juin 2024

Sous la direction de Antoine ROUSSEAU
et Maria KAZOLEA

Devant le jury composé de

Patricio Andrés CATALÁN, Full professor, Universidad Técnica Federico Santa María	Rapporteur
Laurent DEBREU, Directeur de recherche, INRIA	Rapporteur
Maria KAZOLEA, Chargée de recherche, INRIA	Co-directrice de thèse
Véronique MARTIN, Maitre de conférences, LAMFA	Examinatrice
Hélène MATHIS, Professeure, Université de Montpellier	Examinatrice
Antoine ROUSSEAU, Directeur de Recherche, INRIA	Directeur de thèse
Elwin VAN'T WOUT, Associate Professor, Pontificia Universidad Católica de Chile	Examinateur

UNIVERSITÉ
DE MONTPELLIER

A Claudia y Nina ...

Acknowledgements

Working on my doctorate has been an amazing experience, filled with challenges—including a global pandemic—and opportunities. I am deeply grateful for the people I have encountered who have helped me reach this point and take pride in this period of my life.

I want to first thank Antoine Rousseau, my thesis director, for encouraging me from the very beginning to "be the boss", for supporting me with attentive listening and advice as well as kind and insightful criticism. I also thank his dedication and commitment, which helped me move forward while adapting to the new life abroad.

I also want to thank Maria Kazolea, who co-directed this thesis. Despite being in Bordeaux—about four hours away from Montpellier, where I was based—I am grateful for her engagement and commitment to my work and ideas. Whether in our numerous video calls or during my visits to Bordeaux, the stimulating discussions and exchanges we had allowed me to learn and grow.

Many thanks to Patricio Catalan and Laurent Debreu for reviewing this thesis. Their comments have been insightful and have helped me improve my understanding of this work and ideas for the next steps.

Thanks to Véronique Martin, Hélène Mathis and Elwin Van't Wout for joining the presentation's jury. Their questions and comments were also super interesting, helped me think outside the box and at the same time enjoy the whole experience.

I am grateful of the Sea Uncertainty Representation and Forecast (SURF) Inria Challenge (former Project-Lab), that funded most of the activities developed during this PhD, including this book and more.

I am thankful also of the collaboration on médiation scientifique that we had with Luc Hogie, Dorian Mazauric from Terra Numerica and Antoine Rousseau. Together we got TsunamiLab[1] *to be permanently deployed in Terra Numerica, Sohia-Antipolis, which is something I feel very proud of. I certainly look forward to how this project will continue to grow!*

I thank the members of the Inria Lemon team in Montpellier for having received me during this period of time. Thanks to Pascal, Vincent, Carole, Gwladys and Nico for the lunch conversations, the good energy and disposition to help. Also, many thanks to Annie Aliaga and Cathy Desseaux for their kind help, especially at the beginning and at the end of the PhD.

I thank also the friends who I shared with the most during this period. Thanks to Joao Caldas, Seba Nash, Marc Hétier and Katia Ait Ameur. Thanks for the conversations and fun we had together and also for the many things you have

---

[1] See `https://tsunamilab.cl/`

helped me with. Knowing you has certainly helped me be better and reach the place where I am now.

From the Inria Cardamom team in Bordeaux I thank Mario Ricchiuto for the energy and good disposition. Thanks also to Martin Parisot for the enthusiasm, interest and feedback on my work.

Thanks also to Mathieu Rigal and David Lannes from the Institute des Mathématiques de Bordeaux for reaching out and showing interest. Our discussions and exchanges to untangle ”what was going on” were very inspiring and energizing.

Gracias a mi familia que me apoyó desde la distancia. Gracias a mis padres por escucharme y aconsejarme, y también por haberme llevado de niño por el camino que me permitió llegar hasta aquí. Gracias a mi hermana Vale por estar y por ser mi amiga. Y gracias a mis cuñados Pelu y Pablo por escucharme, por el apoyo y el ánimo cuando más lo necesitaba...como al acompañarme al aeropuerto (por ej.).

A Claudia y Nina, a quienes dedico este trabajo, les agradezco por atreverse a que vivamos juntos esta aventura, por animarme, darme la felicidad de estar y crecer juntos ...

Abstract

This thesis investigates the coupling of coastal phase-resolving water wave models, commonly employed in the study of nearshore wave propagation. Despite numerous models and the existing coupling examples, there has been a significant lack of consensus concerning the artifacts and issues induced by these strategies, as well as a vague understanding of how to analyze and compare them. To tackle this problem, this research adopts a domain decomposition approach, anchored in the principle that 3D water wave models (e.g., Euler or Navier-Stokes) serve as the ideal reference solution.

Structured in two parts, the thesis first proposes new models and evaluates them through numerical experiments, identifying specific hypotheses about their accuracy and limitations. Subsequently, a theoretical framework is developed to prove these hypotheses mathematically, utilizing the one-way coupled model as an intermediate reference to distinguish between expected and unexpected effects and categorize errors relative to the 3D solution.

The total error is split in three parts—coupling error, Cauchy-model error, and half-line-model error—and these concepts are applied to the linear coupling of Saint-Venant and Boussinesq models using the so called 'hybrid' model. The analysis confirms that the coupling error accounts for wave reflections at the interfaces, and varies with the direction of propagation. Moreover, thanks to the choice of the one-way model as the intermediate reference solution, this analysis proves several important properties such as the well-posedness and the asymptotic size of the reflections. Additionally, the thesis also addresses the weak-wellposedness of the Cauchy problem for the B model and its implications for mesh-dependent solutions that have been reported. As a byproduct, a new result for the half-line problem of the linear B model is obtained for a more general class of boundary data, including a description of the dispersive boundary layer, which had not been addressed in the literature yet.

The proposed pragmatic definition of coupling error aligns with and extends existing notions from the literature. It can be readily applied to other BT models, discrete equations, linear and nonlinear cases (at least numerically), as well as other coupling techniques, all of which are discussed in the perspective work.

Résumé

Cette thèse s'intéresse au couplage de modèles hydrauliques en zone côtière, à phase résolue, couramment utilisés pour l'étude de la propagation des vagues près du rivage. Malgré de nombreux modèles et des exemples de couplage existants, il y a eu un manque significatif de consensus concernant les artefacts et les problèmes induits par ces stratégies, ainsi qu'une compréhension vague de la façon de les analyser et de les comparer. Pour aborder ce problème, cette recherche adopte une approche de décomposition de domaine, ancrée dans le principe que les modèles de vagues 3D (par exemple, Euler ou Navier-Stokes) servent de solution de référence.

Structurée en deux parties, la thèse propose d'abord de nouveaux modèles et les évalue à travers des expériences numériques, identifiant des hypothèses spécifiques sur leur précision et leurs limites. Par la suite, un cadre théorique est développé pour élucider ces découvertes, en utilisant le modèle couplé unidirectionnel comme une référence intermédiaire pour distinguer les effets attendus et inattendus et catégoriser les erreurs par rapport à la solution 3D.

L'erreur totale est divisée en trois parties : l'erreur de couplage, l'erreur du modèle de Cauchy, et l'erreur du modèle de demi-droite, et ces concepts sont appliqués au couplage linéaire des modèles de Saint-Venant et de Boussinesq en utilisant le modèle dit 'hybride'. L'analyse confirme que l'erreur de couplage prend en compte les réflexions aux interfaces et varie selon la direction de la propagation. De plus, grâce au choix du modèle unidirectionnel comme référence intermédiaire, cette analyse prouve plusieurs propriétés importantes telles que le caractère bien posé et la taille asymptotique des réflexions. En outre, la thèse aborde également le caractère faiblement bien posé du problème de Cauchy pour le modèle B et ses implications pour les solutions dépendantes du maillage qui ont été signalées. Comme produit dérivé, un nouveau résultat pour le problème de demi-droite du modèle linéaire B est obtenu, pour une classe plus générale de données aux limites, incluant une description de la couche limite dispersive, qui n'avait pas encore été abordée dans la littérature.

La définition pragmatique proposée de l'erreur de couplage s'aligne avec et étend les notions existantes de la littérature. Elle peut être facilement appliquée à d'autres modèles BT, équations discrètes, cas linéaires et non linéaires (au moins numériquement), ainsi qu'à d'autres techniques de couplage, tous discutés dans le travail en perspective.

Contents

I Towards new coupling methods 25

List of Figures

Résumé détaillé en français

Dans cette thèse, nous étudions comment coupler différents modèles de vagues à phases résolues qui ont été développés depuis le milieu du XIXe siècle, à savoir les équations de type Boussinesq (BT) et Saint-Venant (SV). Malgré l'existence d'une grand variété de modèles aux performances diverses, ainsi que de multiples façons de les coupler en fonction des applications, il y a jusqu'à présent une abscence de consensus sur les artefacts à attendre de cette stratégie, ainsi qu'une compréhension vague de comment les analyser et les comparer. En particulier, pour l'une des méthodes de couplage les plus populaires utilisée pour la modélisation de le déferlement des vagues, le modèle hybride, la littérature recense différentes catégories de difficultés, telles que: (I) Oscillations, (II) Instabilités, et (III) Solutions dépendantes du maillage.

Dans ce contexte, les objectifs de cette thèse de doctorat sont :

Objectif 1. Développer de nouveaux modèles couplés à phases résolues

Objectif 2. Étudier et expliquer l'origine de tous les artefacts observés

Objectif 3. Contribuer à leur compréhension mathématique

Munis de ces objectifs, nous utilisons comme principe directeur le modèle 3D est la solution de référence idéale à utiliser dans l'évaluation et la comparaison des modèles. Ce modèle peut être, par exemple, les équations d'Euler en surface libre ou les équations de Navier-Stokes. En effet, si ce n'était pour le coût et la complexité du modèle 3D, dans de nombreuses situations, le modèle 3D serait le modèle privilégié. C'est également cette notion qui a permis de justifier la plupart des modèles BT connus à ce jour.

La thèse est organisée en deux parties. La partie I (chapitres 2 à 4) est principalement dédiée à l'étude théorique et/ou numérique de nouvelles méthodes de couplage. La partie II (chapitres 5 à 8), quant à elle, est consacrée au développement d'un cadre théorique pour analyser les modèles linéaires couplés. Ce cadre est utilisé avec le modèle hybride mais peut également être appliqué à d'autres modèles couplés.

Une conclusion à caractère transversal de la partie II est que le **modèle unidirectionnel est le modèle couplé optimal** dans de nombreux cas. Ceci est indépendant du régime de non-linéarité et est conforme à l'observation de Dubach [31], selon laquelle les conditions absorbantes sont également le choix optimal. En plus du résultat de Dubach, ce modèle ajoute une notion de ce qui se passe *de l'autre côté de l'interface* également dans cette solution de référence. Bien sûr, ce modèle présente de nombreuses limitations pour les calculs pratiques, mais il est très utile pour quantifier l'**erreur de couplage** (que nous introduisons également dans la partie II) et mesurer la performance d'un modèle couplé donné.

Le chapitre 2 traite de la dérivation des conditions de couplage moyennées en profondeur. Habituellement, les conditions de transmission sont obtenues pour chaque paire de modèles couplés. Ici, nous commençons par l'autre coté et voyons s'il est possible de les dériver à partir du modèle de référence 3D lui-même. Ceci est réalisé en appliquant les mêmes étapes que celles de la dérivation des modèles BT. Cette méthode est appliquée sur des équations discrètes linéaires. Les résultats montrent que, avec les conditions de couplage dérivées, lors du couplage des mêmes modèles BT des deux côtés de l'interface, il est possible de retrouver une solution de référence, mais le couplage des modèles BT linéaires et SV entraîne cependant des instabilités de nature différente de celles du modèle hybride.

Le chapitre 3 étudie un modèle simple issu de la littérature sur la décomposition de domaine hétérogène. Dans ce cas, l'hétérogénéité réside dans la dimensionnalité du problème, qui couple un problème elliptique 1D avec un 2D. La nouveauté de ce travail réside dans la dérivation d'un modèle 1D amélioré qui possède la même structure mathématique que celle trouvée dans la littérature, permettant ainsi, par une simple transformation des données, d'obtenir une meilleure erreur de consistance. L'objectif dans cet exemple concret est de montrer comment ce modèle coûteux peut être utilisé pour mesurer la précision du modèle couplé, et plus spécifiquement, d'apprendre comment ce modèle amélioré peut affecter les propriétés du modèle couplé. Par une méthode énergétique, une estimation d'erreur H^1 est dérivée. Cette estimation révèle que des paramètres tels que la localisation de l'interface ont toujours une influence sur la solution et également que l'erreur est asymptotiquement plus petite que celle rapportée dans la littérature. Des expériences numériques confirment que le modèle amélioré est plus précis, cependant, le modèle original a montré une super convergence et une précision similaire au modèle nouvellement amélioré dans certains cas. Cela requiert une estimation d'erreur plus précise avec le premier modèle et une caractérisation d'autres régimes asymptotiques impliqués.

Puisque dans le chapitre 2, le modèle présenté montrait encore plus d'artefacts que le modèle hybride, et que dans le chapitre 3, les conclusions sont plus spécifiquement liées au couplage de modèles de dimensions différentes, nous revenons dans le chapitre 4 aux modèles couplés SV-BT. L'objectif est de fournir une meilleure compréhension et des hypothèses plus spécifiques basées sur les données de simulations numériques, concernant les trois principaux problèmes observés dans la littérature, à savoir:

(I) Oscillations

(II) Instabilités

(III) Solutions dépendantes du maillage

qui peuvent apparaître dans le modèle hybride et dans certains nouvelles méthodes qui seront introduites. À certains égards, ce chapitre 4 peut être considéré comme une suite à l'étude de convergence de maillage réalisée par Kazolea & Ricchiuto [70]. La discussion porte sur la propagation d'une vague solitaire sur deux profils de bathymétrie différents en 1D : la plage simple de [109] et une bathymétrie de profondeur constante. Deux modèles BT sont testés : Nwogu

[95], et le eGN [15, 38] mentionnés dans Section 1.2. Leur discrétisation est réalisée de manière similaire à celle de [67, 38, 70], mais mise en œuvre avec une approximation du premier ordre pour minimiser les chances d'observer des oscillations. On observe que, avec une interface statique, le modèle hybride eGN-SV est stable avec la condition CFL habituelle, tandis que le hybride Nwogu-SV est instable à moins qu'une condition plus stricte que $\Delta t = O(\Delta x^2)$ soit imposée. Pour Nwogu-SV, trois nouvelles techniques de couplage sont proposées qui, dans une certaine mesure, améliorent sa stabilité : la viscosité artificielle, une méthode de relaxation d'onde de Schwarz avec recouvrement (Schwarz Waveform Relaxation Method, SWRM) et un solveur direct avec recouvrement; leur performance et leur calibration sont également discutées. Le modèle hybride SV-eGN avec une interface statique était stable pour les tailles de maillage et les cas étudiés, donc nous sommes passés à l'interface dynamique pour le déferlement. Dans ce cas, le modèle présente de grandes oscillations qui ne sont pas nécessairement instables. Grâce à une inspection détaillée, nous avons déterminé que les oscillations observées ne sont pas dues à l'interface mobile ni au fait qu'elle est calculée aux côtés de la simulation. En fait, le problème était que certains artefacts introduits par la discrétisation sont inoffensifs lors de la propagation sur le sous-domaine SV, mais, lorsqu'ils sont transmis au domaine BT, deviennent plus importants que la vague elle-même. Cela a été corrigé en utilisant une méthode numérique d'ordre supérieur, et une explication plus détaillée figure dans la partie II.

La partie II vise à fournir un cadre théorique pour caractériser les artefacts trouvés dans les chapitres précédents, tout en contribuant à leur justification mathématique, c'est-à-dire, à prouver la bonne formulation et l'erreur d'approximation par rapport au modèle 3D. Ce chapitre est le résultat de la combinaison de quatre principales techniques différentes : l'optimisation des conditions de couplage qui mènent à des conditions aux limites absorbantes, proposée initialement par Dubach [31] ; la reformulation des conditions de couplage en conditions de transmission équivalentes, comme proposé initialement par Pierre-Louis Lions [84], est couramment utilisée dans les méthodes de Schwarz optimisées [42] ; le calcul du coefficient de réflexion utilisé pour étudier les conditions aux limites absorbantes, comme étudié par Halpern [58] et Engquyst [33], et également dans l'étude des problèmes d'onde sur le demi-droite [35] ; et les techniques analytiques utilisées dans les méthodes de relaxation d'onde de Schwarz par Martin [90], avec les outils mathématiques de Lions & Magenes [83] et Kreiss [76].

La partie II commence avec le chapitre 5 qui présente son objectif principal : fournir une explication précise des artefacts caractérisés dans la partie I, et contribuer à la justification mathématique des modèles couplés. Le chapitre 5 introduit également une discussion sur les types d'interfaces entre les sous-domaines BT et SV du modèle hybride, qui sont classés en fonction de l'apparence des sous-domaines dans le plan $x - t$. Ces types sont divisés en trois simplifications principales : interfaces mobiles, verticales et horizontales. Les effets physiques attendus que les interfaces verticales et horizontales ont sur la propagation des ondes dans le cas linéaire sont également discutés. Le chapitre se clôt en proposant une définition de l'*erreur de couplage*, donnée par la différence entre un modèle couplé et le modèle unidirectionnel. Une discussion est menée sur la manière dont cette erreur de couplage peut être utilisée pour l'évaluation des modèles, comment elle peut caractériser les artefacts inattendus (par opposition aux effets physiques attendus) dans la solution, et comment elle contribue à quantifier l'erreur par rapport au modèle *idéal*, le modèle 3D.

Le chapitre 6 rappelle certaines propriétés des problèmes de Cauchy homogènes pour les équations SV et B. Ces résultats sont connus, mais sont reformulés d'une manière qui sera utile pour les chapitres suivants, en utilisant les espaces de Sobolev anisotropes de l'annexe D. En utilisant la définition de *faiblement bien posée* présentée dans [76], à partir de ces propriétés reformulées, une explication de la sensibilité du modèle eGN observée dans le chapitre 4 de la première partie est obtenue. En termes simples, le problème est que les perturbations dépendantes du maillage qui ont peu d'énergie dans le modèle SV peuvent avoir d'énormes quantités d'énergie dans le modèle BT, ce qui peut conduire à une solution complètement différente pour chaque taille de maillage. Ceci est prouvé par une solution analytique asymptotique et illustré avec des exemples numériques.

Le chapitre 7 traite des problèmes sur la demi-droite pour les équations linéaires SV et B. Les résultats connus pour le modèle SV sont reformulés pour une utilisation ultérieure comme dans le chapitre 6, tandis que la bonne formulation du modèle B est démontrée. Auparavant, Johnston et al. [64] avaient prouvé l'existence et l'unicité des équations B pour les solutions classiques qui conduisent à une condition de compatibilité comme exigence pour l'existence, et aucune caractérisation de la régularité et de la continuité n'était donnée. Ici, ces résultats sont étendus à des solutions non lisses avec une régularité donnée définie en utilisant les espaces de Sobolev anisotropes de l'annexe D, et la continuité est également prouvée. De plus, les preuves montrent qu'aucune condition de compatibilité n'est requise entre les données initiales et les données aux limites. En outre, le comportement lissant de la couche limite dispersive, d'abord observé par Bresch, Lannes et Métivier [18], est également décrit pour le cas linéaire. Comparé au problème de Cauchy, le problème de la demi-droite des équations B est plus robuste dans le sens où, grossièrement parlant, la norme L^2 de la solution est contrôlée par la norme L^2 des données aux limites, sans impliquer ses dérivées. Ceci est une preuve que ce sont les propriétés du problème de Cauchy des équations B étudiées dans le chapitre 6, et non la transmission à travers la frontière, qui sont responsables des problèmes de convergence de maillage du modèle eGN dans le chapitre 4.

Le chapitre 8 utilise les résultats des chapitres 5 à 7 pour analyser le modèle hybride linéaire B-SV dans le cas d'une interface verticale (dans le plan $x - t$). Suivant une approche de décomposition de domaine, le chapitre commence par définir une classe unique de conditions de transmission qui permettent de reformuler le modèle hybride comme un problème de transmission entre deux problèmes de la demi-droite d'équations différentes. Tout d'abord, l'existence, l'unicité et la régularité du problème sont prouvées en utilisant une méthode de relaxation d'onde avec une version optimisée des conditions de transmission précédentes (transport-Dirichlet). Ceci est fait dans l'esprit de la preuve originale par Schwarz [105], bien que son application au calcul parallèle soit également plausible, car les deux opérateurs sont locaux et la convergence est obtenue en juste 3 itérations. Ensuite, nous procédons à l'étude de l'erreur de couplage, telle que définie au chapitre 5. Il est démontré que l'erreur de couplage peut effectivement être comprise comme des réflexions d'ondes qui sont générées à l'interface; cette notion est expliquée en détail. Un coefficient de réflexion est obtenu et l'effet de la directionnalité de la propagation est étudié. Cette analyse nous permet de prouver la continuité pour des données initiales arbitraires dans une topologie spécifique. En raison de la faible formulation du problème de Cauchy de l'équation B, la continuité du modèle hybride assure seulement le contrôle sur la dérivée n-ième de la solution par rapport à la dérivée $n + 1$-ième des données initiales. Enfin, nous prouvons que l'erreur de couplage, c'est-à-dire la taille des réflexions, est de l'ordre de $O(\mu^2)$ mais un contrôle sur la dérivée $n + 2$-ième des données initiales est nécessaire, ce qui est dû au comportement asymptotique quadratique du coefficient de réflexion.

Le chapitre 9 contient les conclusions et des idées pour des travaux futurs tels que les extensions aux modèles horizontaux 2D, d'autres équations BT et des interfaces mobiles, entre autres.

Outre les chapitres du corps principal de ce document, ce document contient plusieurs annexes. Les annexes A à D récapitulent certaines propriétés et théorèmes qui ont été utiles dans les preuves présentées dans la partie II. Ces annexes couvrent des sujets liés aux transformations de Fourier et de Laplace, à l'analyse complexe, à la théorie de l'approximation, ainsi qu'aux espaces de Sobolev anisotropes et aux théorèmes de trace introduits par Lions & Magenes [83]. L'annexe E contient également une analyse de l'équation différentielle impliquée dans les termes implicites de l'équation B, également utilisée dans les preuves de la partie II.

L'annexe F présente une contribution plus marginale qui peut néanmoins intéresser certains lecteurs. Il s'agit d'une preuve de la continuité du modèle hybride qui a été tentée en utilisant la méthode WRM (Waveform Relaxation Method), mais pour laquelle nous avons rencontré des difficultés avec les outils utilisés ici. Cette preuve consiste à exploiter le fait que la WRM converge en 3 itérations, pour revenir à l'initialisation de l'algorithme, estimer les traces avec la solution d'une itération donnée, puis estimer la solution avec la trace de l'itération précédente, de manière récursive jusqu'à l'initialisation de l'algorithme. Le problème avec cette preuve est que les hypothèses des théorèmes de Lions & Magenes étaient trop strictes pour correspondre aux topologies requises obtenues dans les chapitres 6 et 7 lors des 3 étapes de l'algorithme. Pour traiter ce problème, une hypothèse de régularité a été appliquée à la solution du problème de la demi-droite des équations B, ce qui est de toute façon trop fort pour être valide sous sa forme actuelle. Cela appelle soit à une meilleure caractérisation des propriétés de lissage de la couche limite dispersive, soit à l'utilisation d'une estimation plus flexible pour la continuité des traces.

Chapter 1

Introduction

The mathematical study of free-surface water waves has been a prominent research topic since at least the mid-19th century [107]. Its impact on society is undeniable [20]. Given the growing consequences of climate change and the evolving ways in which our civilization interacts with coastal regions and the rest of our environment, the relevance of this field remains as significant, if not more so, than it was originally. These challenges require advanced modeling tools to accurately predict and mitigate the impacts of increased coastal interactions and environmental effects. Fortunately, a rich variety of models have been proposed to date, each offering different trade-offs between accuracy and efficiency, tailored to the specific phenomena being studied. Faced with such a wide array of options, researchers and practitioners of different disciplines are confronted with a critical decision: Should they adhere to a monolithic approach, using only the most accurate model? Is it feasible to adopt a modular strategy, selecting models based on the best balance of accuracy and performance across various regions in space and time? Especially in complex scenarios, the latter option seems more sensible, and there are examples in the literature demonstrating that such coupling can be convenient. However, despite these examples, there is no consensus on the potential artifacts that might arise from these methods, nor any progress towards a mathematical justification of these approaches in the field of coastal studies. How can we know which coupling strategy should be preferred? And what does it really mean to have a 'better' coupling? These questions are central to this PhD thesis.

In this introductory chapter, we present key concepts and a discussion around the state of the art that will help the reader understand the contributions contained in the main body of this document.

1.1 Coastal water wave models

In coastal oceanography and engineering, 3D models based on the full Navier-Stokes or Euler equations give the most accurate description of wave dynamics but their complexity and computational cost makes them prohibitively difficult in most situations. Instead, two main types of approximation are made which can be described using the adimensional parameters for the nonlinearity and shallowness of the flow

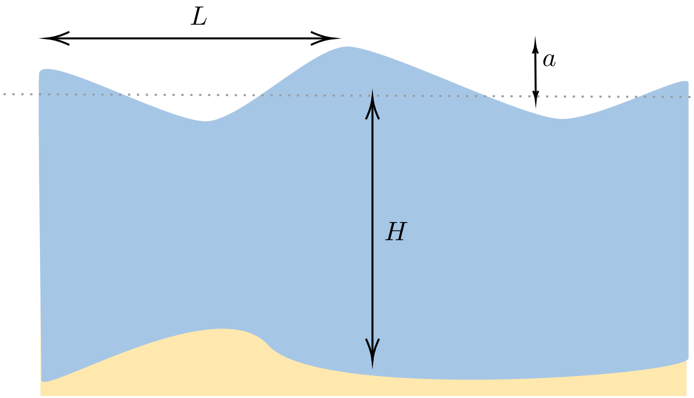

Figure 1.1: Sketch of scales H (depth), a (wave amplitude), and L (wavelength) commonly found in coastal water wave models.

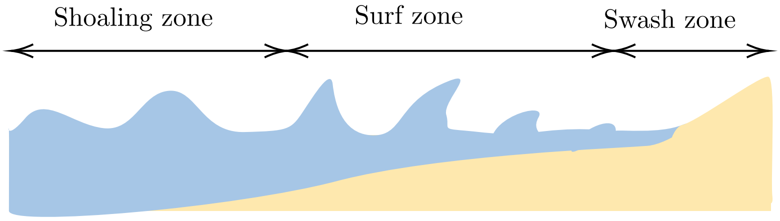

Figure 1.2: Typical zones used to describe coastal wave propagation

$$\varepsilon = \frac{a}{H}, \quad \mu = \frac{H}{L} \tag{1.1}$$

where a, H and L are scales for the amplitude, depth and wavelength, as depicted in Figure 1.1. Making the small amplitude assumption $\varepsilon \ll 1$ Airy [3] proposed the theory for linear waves of arbitrary length propagating on a bathymetry of constant depth. In this theory, the equations admit sinusoidal solutions of the form

$$\eta(x,t) = \cos(\kappa x - \omega_{Airy}(\kappa)t), \quad \omega_{Airy}(\kappa) = \sqrt{gH}\sqrt{\frac{\tanh(\kappa H)}{\kappa H}} \tag{1.2}$$

with x and t the space and time variables; $\eta(x,t)$ the free-surface elevation at (x,t), as shown in Figure 1.4 of page 11; $\kappa = 2\pi/L$ the wavenumber; and ω the frequency in radians. The constraint between ω and κ (1.2) is the dispersion relation of linear waves, from where one deduces that the phase-speed $c_p(\kappa) = \frac{\omega(\kappa)}{\kappa}$ is different for each κ. This property is the frequency dispersion of waves and explains why sometimes waves split into a train of shorter waves over time. Examples of dispersive waves found in nature can be found in Figure 1.3. A broader presentation of dispersive wave models can be found in reference [125].

The small amplitude assumption $\varepsilon \ll 1$ is valid as long as the depth does not vanish (no shoreline). This turns out to be very convenient for modelling wind-generated waves. However, as waves propagate towards the coast they experience a complex transformation process that defies this assumption. Some

(a) Tidal river bore on the River Ribble Lancashire, Northern England [51].

(b) The Sumatra 2004 tsunami reaching the island Koh Jum off the coast of Thailand [86].

Figure 1.3: Two examples of natural phenomena in which frequency-dispersion (or just dispersion) has a central role.

stages usually named to describe these processes include wave shoaling during propagation, wave breaking in the surf-zone, and run-up and run-down in the swash zone, as in Figure 1.2. To move beyond this limitation the long-wave assumption $\mu \ll 1$ was introduced, leading to a new generation of nonlinear models, starting from the Nonlinear Shallow Water Equations (NSWE) proposed by Saint-Venant (SV) in [103] for channel flows, and then Boussinesq (B) equations, proposed by Boussinesq [16], for nearshore waves. By going beyond the small-amplitude assumptions a better understanding of natural phenomena was obtained, including the propagation of bores, solitary waves, and others, as for example those displayed in Figure 1.3.

With the advent of computational methods, new mathematical models started to be proposed. Nowadays they are commonly classified as phase-averaged or phase-resolving models [7, 57, 93]. Phase-averaged equations describe the variations of wave statistics, using the expected values of the variance of the wave's (Fourier) spectrum, in balance with advection and other external forces. These models are derived from the Airy linear theory for bathymetries with mild variations, by assuming that the model is a stationary statistical system [75, 60]. This assumption enables one to understand the expected values as ensemble averages of sufficiently long samples, which is where the phase-averaged term comes from. Since the frequency and the space variables are discretized independently, these models are very efficient for computing wind-induced wave forecasts, especially at the regional and global scales. Moreover, being derived directly from Airy theory, they have no constraints regarding the length of the waves, and there exists methods to include nonlinear effects as source terms to improve results closer to the shore [56, 57, 116].

Despite their superior efficiency for predicting the effects of statistically-stationary forcing processes like the wind, many other phenomena that are either intrinsically transient or highly nonlinear are left out. A few examples are the transport of suspended sediments, as pointed out in [114]; estimation of wave overtopping on coastal structures [121]; extreme events such as tsunamis and storm surges, including the estimation of inundation zones and the associated changes in morphology; among many others that can be found in the literature [20]. Phase-resolving wave models come to fill this gap, allowing the description of the instantaneous wave properties necessary to describe all such phenomena. Once again, the additional price to enable such computations is in computational time: because frequency is not an independent variable anymore many points per wavelength are needed to obtain reasonably accurate results; moreover, if one aims to produce similar statistical estimates as with phase-averaged models then long simulations must be executed. This also highlights the need for efficient and robust phase-resolving wave models. The coupling of these models is the main object of study in this thesis.

1.2 Accurate phase-resolving models

The most accurate phase-resolving models for nearshore propagation solve the 3D Navier-Stokes or Euler equations under different formulations but, being too complex and costly in practice, especially for larger scale applications, approximate models are preferred. A fruitful approximation has been the reduction of the vertical dimension by using asymptotic equations valid in the shallow water

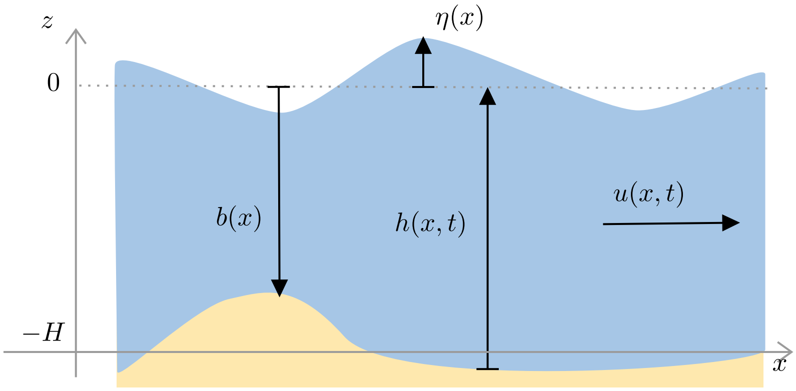

Figure 1.4: Sketch of some hydrodynamic variables usually involved in Boussinesq-type equations: $\eta(x,t)$ is the free-surface elevation; $u(x,t)$ is the depth-averaged horizontal velocity; $b(x)$ is the elevation of the bathymetry such that $b(x) < 0$ if underwater.

or long wave regime $\mu \ll 1$ from where one can deduce both the SV and B equations. This regime is also called the weakly-dispersive regime because for $\varepsilon \ll 1$ such that all $O(\varepsilon)$ terms are neglectable, the equations are linear and also admit sinusodial waves of the form

$$\eta_{BT}(x,t) = \cos(\kappa x - \omega_{BT}(\kappa)t) \tag{1.3}$$

for $\kappa > 0$, and with dispersion relations $\omega_{BT}(\kappa)$ satisfying

$$\omega_{BT}(\kappa) = \omega_{Airy}(\kappa) + O((H\kappa)^p), \qquad \text{some } p > 0 \tag{1.4}$$

This means that solutions of such models only make physical sense for sufficiently small $|H\kappa| = |2\pi\mu|$. Since this also means that the phase speed $c_p(\kappa) = \omega_{BT}(\kappa)/\kappa$ does not vary so much, we say that the dispersion is weak.

The simplest of these models is the SV or NSWE, which can be written as

$$\begin{aligned} &\partial_t \eta + \partial_x(hu) = 0 \\ &\partial_t u + u\partial_x u + g\partial_x \eta = 0 \end{aligned} \tag{1.5}$$

where, as shown in Figure 1.4, $\eta(x,t)$ is the free-surface elevation function, $u(x,t)$ the depth-averaged horizontal velocity, $h(x,t) = H + \eta(x,t) - b(x)$ the total water column height, with $b(x)$ the bathymetry variations over the reference depth H. It is possible to prove that $u\partial_x u = O(\varepsilon)$, so dicarding them and assuming $b(x) = 0$, one retrieves the linear wave equation or linear SV equation

$$\begin{aligned} &\partial_t \eta + H\partial_x u = 0 \\ &\partial_t u + g\partial_x \eta = 0 \end{aligned} \tag{1.6}$$

whose dispersion relation is

$$\omega_{SV}(\kappa) = \sqrt{gH}\kappa \tag{1.7}$$

Since the Taylor expansion of (1.2) is

$$\omega_{Airy}(\kappa) = \sqrt{gH}\kappa \left(1 - \frac{(\kappa H)^2}{3} + O((\kappa H)^4)\right) \tag{1.8}$$

we see that the SV equations contain only the leading order term of (1.8) for small $H\kappa$. This means that the SV model is not dispersive (in frequency) because waves of all frequencies propagate at the same speed; as a consequence the NSWE are only accurate for extremely small water depths, approximately in the range $|\kappa H| < \frac{1}{2}$ as can be confirmed in Figure 1.5. Moreover, in the nonlinear case, for $\varepsilon = O(1)$, the SV equations are hyperbolic and develop shock waves, thus producing discontinuous fronts over very short distances. This feature critically limits their ability to represent wave shoaling and secondary dispersive waves.

BT models such as the B equations themselves can be written as a pertubation of (1.5)

$$\begin{aligned} \partial_t \eta + H\partial_x u &= D_1(h, u, b) \\ \partial_t u + g\partial_x \eta &= D_2(h, u, b) \end{aligned} \tag{1.9}$$

where the terms D_1 and D_2 contain higher-order derivative terms of order $O(\varepsilon\mu)$, $O(\varepsilon\mu^2)$, $O(\mu^2)$ or higher depending on the case. BT models started gaining popularity after the developments of Peregrine in 1967 [99], where the first computations of wave shoaling on a plane beach using BT models were demonstrated, which was a huge improvement over the validity of the SV model [20]. Since then, a large variety of new BT models have been proposed and, by introducing new free parameters or more sofisticated methods such as layered models, their range of validity nowadays can extend up to deep waters. A complete presentation of the different models can be found in the reviews [78, 20].

The importance of linear wave dispersion, especially during the early stages of shoaling, naturally suggests the error in the linear dispersion relation as the most fundamental metric for model evaluation and comparison. In this sense, one BT model would be considered as an improvement of another whenever the residual

$$\begin{aligned} R(\kappa) &= \frac{\omega_{BT}(\kappa)}{\kappa} - \frac{\omega_{Airy}(\kappa)}{\kappa} \\ &= c_{BT}(\kappa) - c_{Airy}(\kappa) \end{aligned} \tag{1.10}$$

is smaller in some norm.

Examples of such models are the one-parameter families of models derived by Nwogu [95] or the more recent enhanced Green-Naghdi (eGN) model introduced in [15], each with dispersion relations given by

$$\begin{aligned} \omega_{Nwogu}(\kappa) &= \sqrt{gH}\kappa \left(\frac{1 - \left(\alpha + \frac{1}{3}\right)(\kappa H)^2}{1 - \alpha(\kappa H)^2} \right)^{1/2} \\ \omega_{eGN} &= \sqrt{gH}\kappa \left(\frac{1 + \left(\frac{\beta - 1}{3}\right)(\kappa H)^2}{1 + \frac{\beta}{3}(\kappa H)^2} \right)^{1/2} \end{aligned} \tag{1.11}$$

In the former, the velocity solved by the model is the one measured from the fixed height z_a from the bottom and $\alpha = (z_\alpha/h)^2/2 + (z_\alpha/h)$; while in the latter

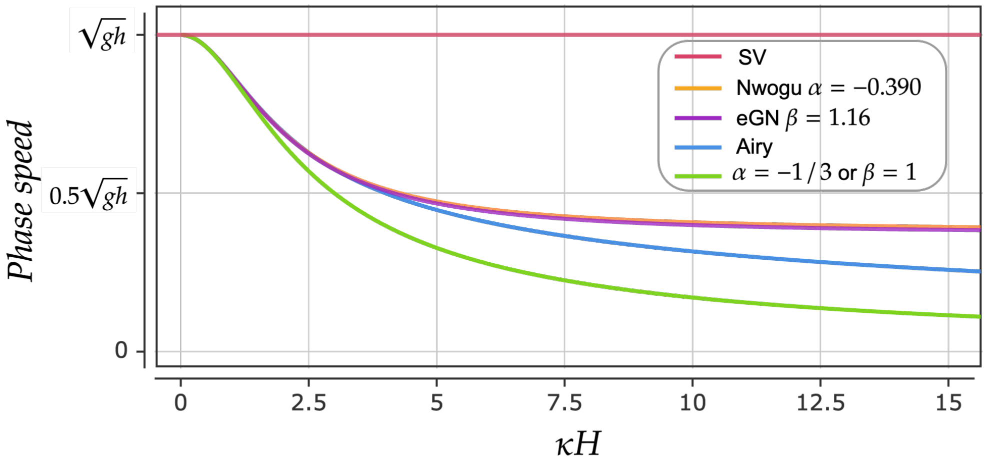

Figure 1.5: Phase speed $c_p(\kappa) = \omega(\kappa)/\kappa$ of different models plotted as a function of κH. From top to bottom in the plot: SV, Nwogu with $\alpha = -0.390$, eGN with $\beta = 1.16$, Airy model and the suboptimal choice of $\alpha = -1/3$ with Nwogu, which is equivalent to the eGN with $\beta = 1$.

the free-parameter β is introduced artificially by using asymptotic equivalences. In both cases, the choice of the free parameter is made as to minimize the residual (1.10) under some norm. For regular waves with only one Fourier mode the norm is just the modulus, however, for irregular waves the norm can be more ellaborate, normally chosen as a weighted average over a stablished range of $|\kappa H| \in [0, 4]$, giving more importance to the accuracy for smaller κH. More details can be found in [15] or [95], and references therein. Using this procedure, the researchers suggested values of

$$\alpha = -0.390, \quad \beta = 1.159 \tag{1.12}$$

which are plotted in Figure 1.5 for comparison, along with the case $\alpha = -1/3$, $\beta = 1$, on which both models turn into the classical Boussinesq equation. The relevance of minimizing (1.10) has to do with the mathematical justification of the model in a more abstract sense: minimizing the dispersion error indeed minimizes the error with respect to the "ideal" model. In the linear case the ideal model is the solution of the Airy equations, which includes the vertical dimension (as a 3D model). To see this more explicitly let us consider regular monochromatic wave solutions of the Airy and BT equations respectively

$$\eta_{Airy}(x,t) = e^{j\kappa(x - c_{Airy}(\kappa)t)}, \quad \eta_{BT}(x,t) = e^{j\kappa(x - c_{BT}(\kappa)t)}, \tag{1.13}$$

and let $R(\kappa) = c_{Airy}(\kappa) - c_{BT}(\kappa)$. Then, expanding the Taylor series of the exponential we can compute

$$\begin{aligned}
\eta_{BT}(x,t) - \eta_{Airy}(x,t) &= e^{j\kappa(x - c_{Airy}(\kappa)t)}(e^{j\kappa(c_{Airy}(\kappa) - c_B(\kappa))t} - 1) \\
&= \eta_{Airy}(x,t)(e^{j\kappa R(\kappa)t} - 1) \\
&= e^{j\kappa(x - c_{Airy}t)}(1 + (j\kappa Rt + O(|\kappa^2 R^2 t^2|)) - 1) \\
&= \eta_{Airy}(x,t)(j\kappa R(\kappa)t + O(|\kappa^2 R^2 t^2|))
\end{aligned} \tag{1.14}$$

Since in particular $|\eta_{Airy}| = 1$ we have that, for fixed t, the total error is controled at leading order by $\kappa R(\kappa) = \omega_{Airy}(\kappa) - \omega_{BT}(\kappa)$, and recalling (1.4) we obtain that

$$\eta_{BT}(x,t) - \eta_{Airy}(x,t) = O((H\kappa)^p) \tag{1.15}$$

The important point we can extract from here is that, for a collection of BT models with similar cost/efficiency, the consensus in the literature implied by the optimization of (1.10) is

The best (linear) model is the one closest to the 3D (linear Airy) model

This idea is at the core of the mathematical justification of more complex water wave models and will be the basis for the discussion throughout this whole document.

When nonlinear terms are retained, the analysis is much more technical but the goal is essentially the same: to prove that the remainder

$$R(\mu) = |\boldsymbol{W}_{3D} - \boldsymbol{W}_{BT}| \to 0, \quad \text{when } \mu \to 0 \tag{1.16}$$

with $\boldsymbol{W}_{BT} = (h_{BT}, u_{BT})$ and $\boldsymbol{W}_{3D} = (h_{3D}, u_{3D})$ the solutions of the BT and 3D models respectively. Such an analysis can be found in reference [78] for most BT models currently available. Different BT models (like the Nwogu and eGN model of the example) can differ in cost and complexity too, and these differences can come from the nonlinear terms, so their linearized equations may be exactly the same, *i.e.*, the analysis of Eq. 1.14 will not reveal any difference. For this reason the asymptotic rate $O(\mu^p)$ at which the remainder $R(\mu)$ in (1.16) goes to 0 is another useful metric of comparison. This rate is called the precision of the model. Additionally, when taking this limit, additional assumptions can be made on other asymptotic parameters such as ε to ensure a desired convergence. Table 1.1 summarizes some of the results justified in [78] for the NSWE, Nwogu and eGN equations. BT models are commonly defined with precisions of $O(\mu^4)$ but, as in the example, the model of Nwogu requires the small-amplitude assumption $\varepsilon = O(\mu^2)$ that turns $O(\varepsilon\mu^2)$ terms into $O(\mu^4)$ terms that can be discarded in the derivation and help improve the error estimates in (1.16); this assumption is called the weakly nonlinear regime. This is not the case with the eGN model where it is only assumed that $\varepsilon = O(1)$ (*i.e.,* its size is independent of μ but varies on a bounded range) so all those terms are retained. As a consequence the eGN model is able to represent the nonlinear stages of shoaling and other nonlinear phenomena more accurately than the Nwogu model.

When evaluating and comparing models, the precision must be understood in conjunction with the regime for ε and other metrics such as the linear dispersion. For example, if we consider the consistency error as a proxy for the precision of a model, Table 1.1 shows that all linear models are asymptotically just as accurate as the NSWE. As a rule of thumb one can navigate Table 1.1 by assuming that models towards the top left corner can replace those of the lower right corner if the right conditions are met: to the left, if sufficiently small μ (shallow water or long waves) is assured, and to the top for sufficiently small ε. On the opposite direction, towards the lower right corner of Table 1.1 one finds better accuracy at the price of additional computational cost and model complexity. Understanding these compromises is important in order to avoid

Nonlinearity \Precision	$O(\mu^2)$	$O(\mu^4)$
Weakly nonlinear $\varepsilon = O(\mu^2)$	Linear models*	Nwogu
Fully nonlinear $\varepsilon = O(1)$	SV	eGN

Table 1.1: Precision of SV, Nwogu and eGN models and their regimes reported in [78]. *For the linear case here we report only the consistency error, not necessarily the precision.

unnecessary computations that may not add relevant improvements to the results, as evidenced in [71]. Moreover, they are one of the important motivations behind coupling these models, as we will see in the next section.

1.3 Coupled phase-resolving models

Coupling different phase-resolving models has been mentioned as an idea for future work, for example, in references [72, 79]. The earliest case of coupling probably comes from tsunami early warning centers. Here the interest is to save computational time by using a linear SV model for far-field propagation, and a nonlinear SV model for the near-field propagation and inundation. Two examples of well-established tsunami software packages are the TUNAMI [63, 62] and MOST [115] models. In both cases the coupling was made in a *one-way* fashion using several telescopic nested grids, passing data from the largest to the smallest regions, with only the smallest ones using the nonlinear model, where the inundation is computed. As can be found in references [63, 62, 115], dispersion effects were first included by taking advantage of the truncation error of the numerical scheme and a carefully-chosen mesh size, which can be very restrictive in practice [85]. Nowadays it is beter understood that neglecting dispersion is a valid assumption for mega-earthquakes [50] even in the far field, where other effects such as the fluid's compressibility [1] or the sea-floor elasticity [122] can be more important, which can explain the good performance of MOST and TUNAMI in the operational setting. In the case of tsunamis triggered by medium-sized earthquakes or landslides, the waves are shorter and dispersion effects are not neglectable anymore. An example is found in [85], where the MOST model was coupled with the GloBouss software [98] to run the model of Nwogu [95] in the largest meshes, confirming important differences between the one-way BT-SV model and the purely SV model. In none of these cases was it examined whether the one-way communication of data or the specific transmission conditions applied to the boundaries of the nested grids affected the results. However, where field or laboratory measurements were available, the results proved to be satisfactorily accurate.

Especially in the last 15 years, the two-way coupling of SV and BT models has been very popular as a method to handle wave-breaking and run-up processes in the surf and swash zones shown in Figure 1.2. Unlike tsunami models, here both models are considered complementary not because of their comparative efficiency, but because the SV model can display superior accuracy compared to BT models, despite being asymptotically less accurate as in Table 1.1. Wave-breaking is in fact a complex phenomena that challenges important assumptions made in the derivation of BT models, such as the irrotationality of

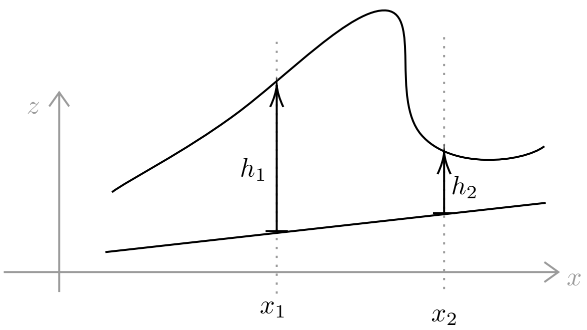

Figure 1.6: Variables of the volume of fluid moving at the same speed of the shock. Points 1 and 2 to the left and right of the shock (breaker front) are arbitrary as long as they move in time at the same speed of the shock. See [107] for more details.

the flow or the representation of the free surface as a single-valued function. To deal with the former, more sophisticated techniques have been proposed that add some mechanism to introduce the energy dissipation inside the BT equations (*e.g.,* the eddy viscosity by Zelt [128], the roller models introduced by Svendsen [108], the turbulent kinetic energy (TKE) by Nwogu [95] or the more recent depth-averaged large-eddy simulation model [66] of Kazakova & Richard, see the recent reviews [70, 66]).

Regarding the representation of the free-surface, it is true that no 2D (or depth-averaged) phase-resolving model would be able to capture the strong 3D features of a fully-formed plunging breaker, but some useful approximations can still be obtained. BT models derived from the irrotationality assumption are able to represent wave-amplitude growth due to shoaling, however, their main limitation is that this process does not finish by itself and the solution becomes singular in finite time. This has been noted since the seminal work of Peregrine [99] which is why traditional wave breaking mechanisms such as those of the previous paragraph have been applied to compensate these shoaling effects. On the other side, SV models are more robust and accurate in this part of the propagation, despite not being able to capture shoaling. Following references [107, 12], considering points x_1 and x_2 on each side of the jump as in Figure 1.6, one can demonstrate that the dissipation of the specific mechanical energy is given by

$$D_b = \frac{\rho g}{4}\left(\frac{g(h_1+h_2)}{2h_1h_2}\right)^{1/2}(h_2-h_1)^3 \tag{1.17}$$

with ρ the specific mass of the water, and h_1, h_2 the heights across the jump as in Figure 1.6. As shown in references [107, 12], after breaking has been detected, equation (1.6) gives an accurate approximation for wave-breaking dissipation without *ad-hoc* parametrizations [14, 15]. By itself, this is an important advantage over traditional approaches based on the eddy-viscosity or roller concepts and shows that indeed the SV model is the accurate choice over common BT models for wave-breaking propagation in the surf zone.

At first sight, this may seem in contradiction with Table 1.1 but it can be explained by the fact that the mathematical theory that supports the hierarchy

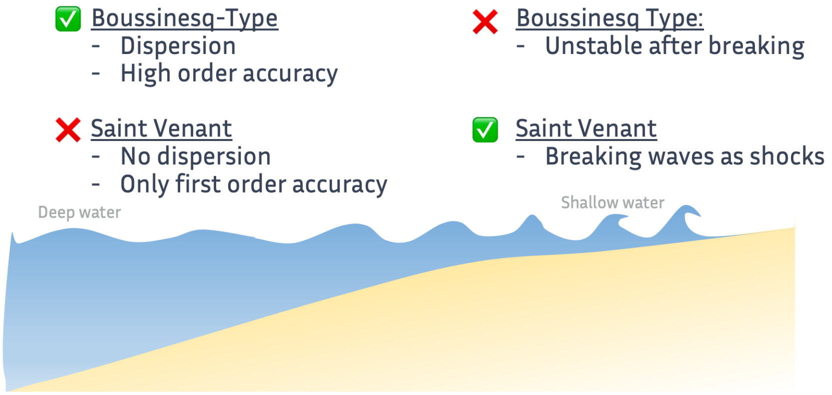

Figure 1.7: Summary of the complementary features of BT and SV models.

of Table 1.1 is only valid for

$$H \geq H_0 > 0, \quad \text{and} \quad t \leq T = O(\varepsilon^{-1}) \tag{1.18}$$

where the former indicates the abscence of the shoreline (vanishing depths) and the latter is the time until breaking (see refs. [78, 77] more details). Without these assumptions there is no theoretical notion of the hierarchy that relates SV and BT models as an approximation of the 3D model. This is an open problem in the literature [77, 78].

Regardless of the mathematically-proved properties, the previous evidence reveals that there exists a fortunate complementarity between SV and BT models, as highlighted in Figure 1.7. Such a complementarity was also a motivation for the one-way tsunami models mentioned earlier and it was also explored for a one-way coupled wave model in [23]. However, it was not until the work of Tonelli & Petti in 2009 [117] that a two-way coupled model started gaining traction; we will refer to this model as the *hybrid model* throughout the whole document. The main idea was to use a shock-capturing FV method for the hyperbolic terms and add dispersive terms (D_1 and D_2 in Equation (1.4)) discretized with another method, whenever a point is classified as non-breaking (by default), or to drop them when said point is classified as breaking. Since dispersive terms are of size $O(\mu^2)$ or higher, another argument is that these become neglectable in this part of the propagation, in the same spirit of the coupling of linear/nonlinear SV models presented before.

The hybrid model has found great success in the literature and among practicioners, being implemented on different software packages, many of which have well-established user-bases such as FUNWAVE-TVD [**funwavegpu**, 106], BOSZ [102], GeoClaw [74], Celeris [110, 111] and UHAINA [37]. The hybrid model was first proposed by Tonelli and Petti [117] for the BT model derived by Madsen and Sørensen [87] and a Finite Difference (FD) scheme for the dispersive terms.

In parallel, Tissier et al. [113] proposed the hybrid model for the fully nonlinear Boussinesq equations of Serre Green Naghdi (GN) [55]. The validation of the hybrid model has been conducted on multiple test cases involving wave breaking and runup of solitary waves [117, 118, 113], regular sinusoidal and cnoidal waves [118, 119, 113] and also irregular waves [120]; propagating on mildly-varying bathymetries with simple [117, 118], barred [119] and complex geometries in 1D and 2D [118, 119], even describing wave-current interaction and overtopping [121], among other phenomena. The comparisons with measurements have shown that the model is capable of accurately representing relevant properties such as mean wave setup and wave height decay. Moreover, Tonelli & Petti [121] showed that it can also satisfactorily represent wave-current interaction phenomena such as rip currents, the nonlinear transfer of energy between low and high frequency waves, and some wave-structure interactions.

The primary limitation of the hybrid model has not been its accuracy nor its computational cost, as was the case with other phase-resolving models, but rather the significant lack of consensus regarding its robustness and reliability. Oscillations have been noted from the conception of the hybrid model itself. Both Tonelli & Petti [117, 113] as well as Tissier [114] reported observing these oscillations but found no issues with mesh convergence. Similarly, Shi et al. [106] encountered persistent significant oscillations after wave breaking began, despite using a method designed to filter unphysical oscillations; no mesh-convergence problems were reported either. They also observed a discontinuity at the BT-SV interface and proposed, without providing proof, that it should decrease with μ. In [69], Kazolea, Delis & Synolakis proposed a 2D hybrid model for Nwogu's equations and, acknowledging the oscillations reported by Shi et al. in [106], they proposed a variation of the time-stepping algorithm that showed good results but without examining the mesh-convergence of the solution. In [80] Lannes & Marche applied the hybrid model on the eGN model in 2D, commenting that the BT-SV transition does not generate any disturbances and therefore no numerical filter is applied, but no mesh-convergence study was conducted. In [38] Filippini et al. described mesh-dependent spurious oscillations at the interface, whose size could be controlled with a modification in the discretization of the implicit part of the dispersive problem. In [74] the authors showed a proof of stability of the linear model and only observed small oscillations due to the BT-SV coupling at the dry front, not on the wave itself.

These isuses were not adressed in detail until 2018 when Kazolea & Ricchiuto [70] reported the first systematic mesh-convergence study of the hybrid model on multiple cases with weakly nonlinear and a fully nonlinear BT model, showing that mesh-sensitivity, oscilations and instabilities were permanent issue in both cases. Moreover, they observed that the numerical dissipation had a more important effect compared to the alternative TKE breaking closure that they studied too. These observations naturally discourage the use of the hybrid model in favor of other more classical approaches, which is what they recommended in the conclusions. Since then, the problem has continued to be reported in the literature. For example, in ref. [6] Bacigaluppi et al. conducted a mesh-converge study and found that the instabilities could be present or absent depending on the criteria chosen to detect broken waves, and that even in the stable case, some "flashes" or oscillations were observed. They attributed the instabilities to a mismatch of the energy transported across the interface. To this day, there is no agreement in the literature regarding which artifacts the hybrid model introduces (or not) in the solution, or to what extent they impact the mesh-convergence and stability of the numerical methods and the partial differential equations (PDEs) themselves. Understanding these issues is one of the objectives of this thesis.

1.4 The ideal coupled model

One reason that can explain this lack of consensus among researchers is the lack of an exact mathematical reference to compare the results with, or at least a precise notion of an ideal coupled model to use for model design. The performance of the coupled phase-resolving models has been assessed only with experimental or field measurements but, as Bonna, Chen & Saut highlighted [11], these are often contaminated with noise from other phenomena, making them inadequate for fully capturing the mathematical issues at hand. Even in the linear case, due to the heterogeneous nature of the hybrid model, there is no equivalent to the dispersion relation (1.2) that can be used to compare different models. Robustness, on the other hand, is a minimum requirement but does not say much about accuracy. For instance, while the one-way method used in tsunami modeling is robust, even if one somehow managed to adapt it for wave breaking it is unclear if it would inherently perform better than a hybrid model. On the physical principles front, Tissier et al. [114] decided against adding a transition zone that could blend the two equations instead of using a sharp interface, How can this choice be justified in mathematical terms? Moreover, if one proceeds as in the case of tsunami modeling and coupled two distinct Boussinesq-type equations like Nwogu and eGN using Table 1.1 as criteria, What considerations should one take into account to avoid non-physical artifacts?

Fortunately, the coupling of different types of PDEs has been an active field of research with several different applications, commonly found under the umbrella of heterogeneous domain decomposition methods, a field dedicated to "bridging (homogeneous) domain decomposition and mathematical modeling" [100]. Domain Decomposition methods (DDM) were born from the works of Schwarz when dealing with the proof of existence and uniqueness of the Laplace equation with Dirichlet boundary conditions in a domain of complex geometry [105], and later adapted by Lions [84] for parallel computing. The basic principle consists in splitting a complex problem into several related simpler problems that, when joined, produce the same solution as the original problem. In the case of Schwarz (homogeneous DDM) the complexity came from the geometry of the domain; for Lions it was the computational cost (time and memory) to solve large elliptic problems; in heterogeneous DDM the complexity comes from the changing character of the PDE.

One of the most notable examples in heterogeneous DDM is the coupling of the linear advection (A) and advection-diffusion (AD) equations, dating back to at least 1989 [48]. Reviews on the topic can be found in [100, 91] and a more recent and shorter one in [47]. In this case several coupling techniques have been proposed. Interestingly, among other models, also a "hybrid" model (the χ-*method* [19]) was proposed, where high-order derivative terms were discarded when their values fell below a threshold. In most of these cases the interest was not to simulate the interaction of two different physics (different fluids for example) but rather, to approximate the behavior of a viscous fluid, neglecting viscosity effects whereever they were not important. This notion motivated Dubach [31, Part II] in his PhD thesis to propose the optimization of the transmission conditions to minimize the error with respect to the most expensive AD model, from where the justification of other choices of transmission conditions that already existed was obtained. In fact, the optimal was found to be the transparent or absorbing boundary conditions studied by Halpern [58] and Engquist [33]. In the work by Dubach and others that followed later, this idea has been used to rank different coupling methods according to their performance [45], *i.e.,*. The important notion is that the ideal coupled model is the one closest to the most expensive model, as measured by the error of the solution.

Applied to the modeling of wave propagation, the previous principle cannot be applied so straightforwardly because, as discussed in Section 1.2, only in the shoaling zone or deeper waters the more expensive model is the most accurate. Instead, recalling the original criteria used to rank BT models of Section 1.2

The best coupled model is the one closest to the 3D model

in the sense of the error of its solution, *i.e.,* the one that minimizes

$$|\boldsymbol{W}_{coupled} - \boldsymbol{W}_{3D}|_E \tag{1.19}$$

with E some adequate Banach space. Before reaching the surf zone (under assumptions (1.18)) it is known that this 3D model corresponds to the free-surface Euler equations. One can also think of estimating this error by using an intermediate reference model as

$$|\boldsymbol{W}_{coupled} - \boldsymbol{W}_{3D}|_E \leq |\boldsymbol{W}_{coupled} - \boldsymbol{W}_{interm}|_E + |\boldsymbol{W}_{interm} - \boldsymbol{W}_{3D}|_E \tag{1.20}$$

with $\boldsymbol{W}_{interm}$ the solution of the intermediate reference model. For example, still before reaching the surf zone, this intermediate model could be the most accurate BT model according to the asymptotic hierarchy. In the linear case it could also be the Airy linear model itself. Inside the surf and swash zones however, as far as the current mathematical justification goes, there is no intermediate reference to be used.

Despite this limitation, thanks to a detailed inspection of the artifacts that will be described on Part I of this thesis, in Part II we will propose an intermediate reference model that will help quantify this error in some cases of coupling. This intermediate reference corresponds to the one way model, like the one that was used for tsunami modelling, and has the advantage that it characterizes the coupling error in terms of reflected waves generated by the interface. This idea will facilitate the mathematical justification of the linear hybrid model, and provides a way to compute a simple analytical metric that can be used to rank different coupled models, analogous to how the residual of the linear dispersion relation (1.4) is used to rank BT models. Moreover, this reference can easily be applied to the nonlinear case too through numerical experiments, thus bypassing the need for a more sofisticated solution, such as the 3D model or others.

1.5 Thesis objective and outline

The objective of this PhD thesis are:

Objective 1. To develop new coupled phase-resolving coastal wave models

Objective 2. To study and explain the source of any artifacts observed

Objective 3. To contribute to their mathematical justification

In terms of methods, a DDM approach has been followed throughout the whole document. More importantly, for the most part of the document, the contributions are inspired by the idea that the coupled model, as also do other phase-resolving models, can only aspire to be as similar as possible to the 3D reference model. Indeed, if it were not for the cost and complexity of the 3D model, in many situations the 3D model would be the prefered option.

The thesis is organized in two parts. Part I (chapters 2 to 4) is mainly dedicated to the theoretical and/or numerical study of new coupling methods. Part II (chapters 5 to 8) on the other side, focuses on developing a theoretical framework to analyze coupled linear models. This framework is demonstrated with the hybrid model but can be applied to other coupled models too.

Chapter 2 deals with the derivation of depth-averaged coupling conditions. Usually transmission conditions are obtained for each pair of models being coupled. Here we start from the other end and see if it is possible to derive them from the 3D reference model itself. This is done by applying the same steps of the derivation of the BT models. This is applied on linear discrete equations. The results show that, with the derived coupling conditions, when coupling the same BT models on both sides of the interface it is possible to recover a reference solution, but coupling linear BT and SV however, leads to instabilities of different nature than the hybrid model.

Chapter 3 studies a simple model found in the heterogeneous domain decomposition literature. In this case the heterogeneity is in the dimensionality of the problem, that couples a 1D with a 2D elliptic problem. The novelty of the current work is in the derivation of an improved 1D model that has the same mathematical structure as the one found in the literature, so by a simple transformation of the data, a better consistency error is obtained. The objective in this concrete example how this expensive model can be used to measure the accuracy of the coupled model, and more specifically, to learn how this improved model can affect the properties of the coupled model. Through an energy method an H^1 error estimate is derived. This estimate reveals that parameters such as the location of the interface do still have an influence in the solution and also that the error is asymptotically smaller than the one reported in the literature. Through numerical experiments it is confirmed that the improved model is more accurate, however, the original model showed super convergence and am accuracy that is similar to the newly improved model in some cases. This calls for a sharper error estimate with the first model and a characterization of other asymptotic regimes involved.

Since in Chapter 2 the model presented even more artifacts than the hybrid model, and in Chapter 3 the conclusions are more specifically related to the coupling of models with different dimensions, we turn back to the SV-BT coupled models in Chapter 4. The objective is to provide a better understanding, numerical evidence and more specific hypothesis regarding the three main problems observed in the literature, namely:

(I) Oscillations

(II) Instabilities

(III) Mesh-dependent solutions

that may be observed within the hybrid and some new coupling methods that will be introduced. To some level, this Chapter 4 can be considered as a sequel to the mesh-convergence study performed by Kazolea & Ricchiuto [70]. The discussion is performed around the propagation of a solitary wave on two different bathymetry profiles in 1D: the simple beach of [109] and a bathymetry of constant depth. Two BT models are tested: Nwogu [95], and the eGN [15, 38] that were mentioned in Section 1.2. Their discretization is done in a similar fashion as in [67, 38, 70], but implemented with a first order approximation to minimize the chances of observing oscillations. It is observed that, with a static interface the eGN-SV hybrid is stable with the usual CFL condition, while the Nwogu-SV hybrid is unstable unless a condition more stringent than $\Delta t = O(\Delta x^2)$ is imposed. For Nwogu-SV three new coupling techniques are proposed that, to some extent, improve its stability: artificial viscosity, an overlapping Schwarz Waveform Relaxation Method (SWRM) and an overlapping direct solver; their performance and calibration is discussed too. The SV-eGN hybrid with a static interface was stable for the mesh sizes and cases studied so we moved on to the dynamic interface for wave breaking. In this case the model presents large oscillations that are not necessarily unstable. Through a detailed inspection, we determined that the oscillations observed are not due to the moving interface nor the fact that it is computed alongside the simulation. In fact, the problem was that some artifacts introduced by the discretization are harmless while propagating on the SV subdomain but, when transmitted to the BT domain, become even larger than the wave itself. This was fixed by using a higher-order numerical method, and a more detailed explanation was left for Part II.

Part II aims to provide an extensible theoretical framework to characterize the artifacts found on previous chapters, at the same time of contributing to their mathematical justification, that is to say, to prove the well-posedness and aproximation error w.r.t. the 3D model. This chapter is the result of combining 4 main different techniques: the optimization of coupling conditions that lead to absorbing boundary conditions, first proposed by Dubach [31]; the reformulation of coupling conditions to equivalent transmission conditions, as proposed first by Pierre-Louis Lions [84], which is commonly used in Optimized Schwarz Methods [42]; the computation of the reflection coefficient used to study absorbing boundary conditions, as studied by Halpern [58] and Engquyst [33], and also in the study of half-line wave problems [35]; and the analytical techniques used on Schwarz Waveform Relaxation Methods by Martin [90], with the mathematical tools of Lions & Magenes [83] and Kreiss [76].

Part II begins with Chapter 5 that introduces its main objective: to provide a precise explanation of the artifacts characterized in Part I, and to contribute to the mathematical justification of the coupled models. Chapter 5 also introduces a discussion regarding the types of interfaces between the BT and SV subdomains of the hybrid model, that are classified depending on how the subdomains look like in the $x-t$ plane. These types are separated into 3 main simplifications: moving, vertical and horizontal interfaces. The expected physical effects that the vertical and horizontal interfaces have on wave propagation in the linear case are also discussed. The chapter closes by proposing a definition for the *coupling error*, given by the difference between a coupled model and the one-way model. A discussion is made on how this coupling error can be used for model evaluation, how it can characterize the unexpected artifacts (as opposed to the expected physical effects) in the solution, and how it contributes to quantifying the error w.r.t. the *ideal* model, the 3D model.

Chapter 6 recalls some properties of the homogeneous Cauchy problems of the SV and B equations. These are known results, but are reformulated in a way that will be useful for the coming chapters, using the anisotropic Sobolev spaces of the Appendix D. Using the definition of *weak-wellposedness* presented in [76], from these reformulated properties an explanation to the sensitivity of the eGN model that was observed on Chapter 4 of Part I is obtained. In simple terms, the problem is that mesh-dependent perturbations that have low energy in the SV model can have huge amounts of energy in the BT model, which can lead to a completely different solution on each mesh size. This is proved through an asymptotic analytical solution and demonstrated with numerical examples.

Chapter 7 deals with the problems on the half-line for the linear SV and B equations. Known results for the SV model are reformulated for later use as in Chapter 6, while the well-posedness of the B model is demonstrated. Previously, Johnston et al. [64] proved the existence and uniqueness of the B equations for classical solutions which lead to a compatibility condition as a requirement for the existence, and no characterization of the regularity and continuity was given. Here these results are extended to non-smooth solutions with a given regularity defined by using the anisotropic Sobolev spaces of the Appendix D, and the continuity is proved too. Additionally, the proofs show that no compatibility condition is required between the initial and boundary data. Moreover, the smoothing behavior of the dispersive boundary layer, first observed by Bresch, Lannes & Métivier [18], is also described for the linear case. Compared to the Cauchy problem, the half-line problem of the B equations is more robust in the sense that, roughly speaking, the L^2 norm of the solution is controlled by the L^2 norm of the boundary data, without involving its derivatives. This is evidence that it is the properties of the Cauchy problem of the B equations studied in Chapter 6, and not the transmission through the boundary, that are responsible for the mesh-convergence problems of the eGN model in Chapter 4.

Chapter 8 uses the results from Chapters 5 to 7 to analyze the linear hybrid B-SV model in the case of a vertical interface (in the $x - t$ plane). Following a domain decomposition approach, the chapter begins by defining the unique class of transmission conditions that allow to reformulate the hybrid model as a transmission problem between two half-line problems of different equations. First, the existence, uniqueness and regularity of the problem is proved using a Waveform Relaxation Method with an optimized version of the previous transmission conditions (transport-Dirichlet). This is done in the spirit of the original proof by Schwarz [105], although its application to parallel computing is also plausible, because both operators are local and the convergence is obtained in just 3 iterations. Then we proceed to study the coupling error, as defined in Chapter 5. It is demonstrated that indeed the coupling error can be understood as wave reflections that are generated at the interface; this notion is carefuly explained. A reflection coefficient is obtained and the effect of the directionality of the propagation is studied. This analysis allows us to prove the continuity for arbitary initial data in a specific topology. Due to the weakly-wellposedness of the Cauchy problem of the B equation, the continuity of the hybrid model only ensures control over the $n - th$ derivative of the solution w.r.t. the $n + 1 - th$

derivative of the initial data. Finally, we prove that the coupling error, that is to say, the size of the reflections, is of $O(\mu^2)$ but a control on the $n+2-th$ derivative of the initial data is required, which is due to the quadratic asymptotic behavior of the reflection coefficient.

Chapter 9 contains the conclusions and ideas for future work such as the extensions to 2D horizontal models, other BT equations and moving interfaces, among others.

Besides the chapters of the main body of this document, several appendices are attached. Appendices A to D recap some properties and theorems that were useful in the proofs presented in Part II. These appendices cover topics related to the Fourier and Laplace transforms, complex analysis, approximation theory, and the anisotropic Sobolev spaces and trace theorems introduced by Lions & Magenes [83]. Appendix E also contains an analysis of the differential equation involved in the implicit terms of the B equation, also used in the proofs of Part II.

Appendix F presents a more tangential ontribution that nonetheless can be interesting to some readers. Appendix F presents a proof for the continuity of the hybrid model that was attempted using the WRM but that found some challenges for the tools herein used. This proof consists in leveraging that the WRM converged in 3 iterations, to roll back to the initialization of the algorithm, estimating the traces with the solution of a given iteration, and then estimating the solution with the trace of a previous iteration, recursively until the initialization of the algorithm. The problem with this proof is that the assumptions of the theorems by Lions & Magenes were too strict to match the required topologies obtained in Chapter 6 and Chapter 7 over the 3 steps of the algorithm. To deal with this issue an assumption of smoothness was applied on the solution of the half line problem of the B equations, which is in any case too strong to be valid in its current form. This calls for either a better characterization of the smoothing properties of the dispersive boundary layer or to use a more flexible estimate for the continuity of the traces.

Part I

Towards new coupling methods

Chapter 2

Derivation of depth-averaged coupling conditions

In this chapter we explore a novel idea for coupling the linear Boussinesq equations (B)

$$\partial_t \zeta + \partial_x V = 0 \tag{2.1}$$

$$\partial_t V + \partial_x \zeta = \phi \tag{2.2}$$

$$-\frac{\mu}{3}\partial_x^2 \phi + \phi = -\frac{\mu}{3}\partial_x^3 \zeta \tag{2.3}$$

for $x < 0$ and $t \in]0, T[$, with the linear Saint-Venant equations (SV)

$$\partial_t \zeta + \partial_x V = 0 \tag{2.4}$$

$$\partial_t V + \partial_x \zeta = 0 \tag{2.5}$$

for $x > 0$, to represent the 1D propagation of waves in shallow water. Here ∂_t, ∂_x denote partial derivatives in the time and space variables t, x; $V(t, x)$ and $\zeta(t, x)$ stand for the vertically-averaged velocity and the free-surface level over its state at rest; $\phi(t, x)$ is an auxiliar variable for the elliptic part of the problem; and $\mu > 0$ is the asymptotic parameter characterizing the wave dispersion.

As stated in Chapter 1, Boussinesq-type (BT) equations such as the Green-Naghdi (GN) equations, have been coupled with the nonlinear Saint Venant equations (SV) to take advantage of their physical-modeling features: the dispersive terms in the GN equations can be used to accurately represent the phase and amplitude of waves in the shoaling zone, while shock-capturing well-balanced finite volume schemes for the SV equations can mimic the energy dissipation of wave-breaking and provide a robust handling of vanishing water depths without ad-hoc parametrizations. However, this coupled model has displayed a number of artifacts such as oscillations, mesh-convergence problems and instabilities [70].

To deal with this issue, the heterogeneity of the problem motivates us to use a "divide and conquer" strategy using domain decomposition methods (DDM) from a novel perspective. Usually, coupling conditions have been derived for each equation on a case-by-case basis (*e.g.*, [22, 65, 8, 10, 9, 129, 21]). Here we explore a different approach, based on the principle of Section 1.4 that

The best coupled model is the one closest to the 3D model

The idea is to start from this end of the problem, the 3D model, and derive the coupling conditions directly from it. Although we refer to this model as 3D, we will work only in the case of 1D propagation, which means that in fact it is 2D: 1D horizontal plus 1D in the vertical direction. Moreover, in principle the 3D model could be the Navier Stokes or free-surface Euler equations; here we will work with the linearized free-surface Euler equations with the formulation of Zakharov Craig and Sulem (ZCS) [127, 29, 28], that can also be found in [77]. They will be introduced later.

This strategy is applied following the steps of the derivation of the GN and SV equations [77, ch. 1 and 5], [15]. The idea is summarized in Figure 2.1, and it consists roughly on the following steps:

1. Start from a domain decomposition with coupling conditions adapted specifically for the 3D model

2. Take the depth average of the equations and coupling conditions

3. Apply the new coupling conditions to the depth-averaged models

In Section 2.1 we introduce the linearized ZCS formulation of the free-surface Euler equations and recall how to derive the B and SV equations, following the development of references [77, 15]. Then Section 2.2 introduces a discretization of the ZCS formulation, and derives discrete B and SV equations directly from the discrete 3D model. Section 2.3 presents a domain decomposition method with transmission conditions that are defined by taking advantage of the hyperbolic+elliptic structure of the problem. Section 2.4 then proceeds with the main step of this chapter, which is to take these coupling conditions and derive coupling conditions for the discrete B and SV equations. Section 2.5 explains how to use them for coupling B with B equations on each side of the interface, as also B with SV; numerical experiments are used to assess the performance of the new coupling condition on these two cases. Section 2.6 summarizes the conclusions from the previous observations.

2.1 Derivation of equations at the continuous level

In this section the derivation of the linear equations is recalled. In particular, first the Zakharov-Craig-Sulem formulation will be introduced along with an adimensionalization and linearization for small-amplitude waves, from where an asymptotic analysis will lead to the B and SV equations.

The derivation starts by considering an inviscid incompressible fluid, without surface-tension effects and under irrotational flow. Moreover, we will assume that the fluid is moving in one horizontal dimension. In this case, the movement of the fluid is governed by the following equations [77, 79]

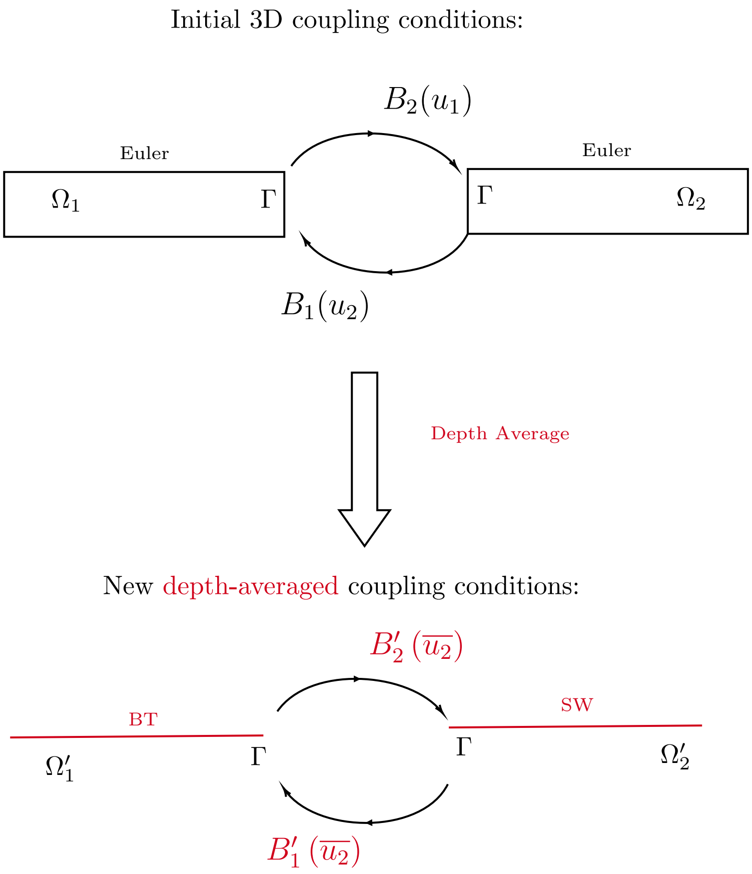

Figure 2.1: Depiction of the new strategy for deriving depth-averaged coupling conditions. Here Ω_1 and Ω_2 form a partition of the fluid domain Ω in the horizontal direction, where the Euler model is solved; Γ is the original interface used for decomposing the domain; B_1 and B_2 are the coupling conditions used to transmit information between subdomains using some traces u_1 and u_2 of the solution. Ω'_1 and Ω'_2 form a partition of the new "depth-averaged" domain; B'_1 and B'_2 are also the new depth-averaged coupling conditions used to couple the depth-averaged Boussinesq-type (BT) and Shallow Water (SW) equations.

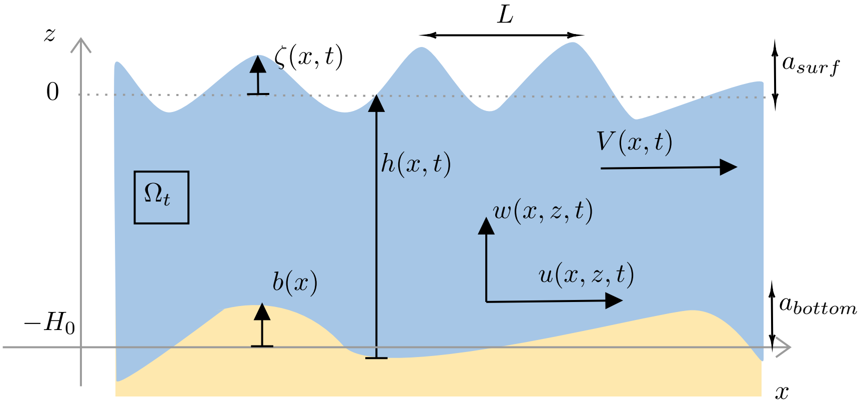

Figure 2.2: Sketch of variables used to describe the flow.

$$\begin{cases} \partial_t \zeta = G[\zeta, b]\psi \\ \partial_t \psi + \frac{1}{2}|\partial_x \psi|^2 + g\zeta - \dfrac{1}{2}\dfrac{(G[\zeta,b]\psi + \partial_x\psi\partial_x\zeta)^2}{1+|\partial_x\zeta|^2} = 0 \end{cases} \tag{2.6}$$

where, as shown in Figure 2.2, $\zeta(x,t)$ and $b(x,t)$ denote the free-surface elevation and the bathymetry functions, such that the region occupied by the fluid is

$$\Omega_t = \{-H_0 + b(x) \leq z \leq \zeta(x,t)\} \tag{2.7}$$

with $H_0 > 0$; also if $\boldsymbol{U}(x,z,t) = (u(x,z,t), w(x,z,t))$ is the pointwise fluid-velocity then $\psi = \Phi\,|_{z=\zeta}$ with $\Phi(x,z,t)$ the velocity-potential such that $\nabla\Phi(x,z,t) = \boldsymbol{U}(x,z,t)$; and G is the Dirichlet-to-Neumann operator

$$G[\zeta,b] : \psi \to \nabla\Phi\,|_{z=\zeta} \cdot \boldsymbol{N}, \quad \boldsymbol{N} = \begin{pmatrix} -\nabla\zeta \\ 1 \end{pmatrix} \tag{2.8}$$

with Φ satisfying

$$\begin{cases} \Delta\Phi = 0 & \text{in } \Omega_t \\ \Phi = \psi & \text{on } z = \zeta \\ \partial_{\boldsymbol{n}}\Phi = 0 & \text{on } z = -H_0 + b \end{cases} \tag{2.9}$$

and the normal vector

$$\boldsymbol{n} = \frac{\boldsymbol{N}_b}{|\boldsymbol{N}_b|}, \quad \boldsymbol{N}_b = \begin{pmatrix} \nabla b \\ -1 \end{pmatrix} \tag{2.10}$$

In this formulation the two main equations (2.6) correspond to the kinematic and dynamic boundary conditions of the fluid at the free surface, respectively. Additionally, in equation (2.9), the first line is due to the joint assumptions of incompressiblity and irrotationality; the second line is just the definition of ψ while the last one is the kinematic boundary condition at the sea bottom.

As can be found in [77], among other properties, the ZCS formulation makes explicit the fact that the knowledge of $\zeta(x,t)$ and $\psi(x,t)$ is enough to describe the movement of the fluid at every point (x,z,t), a fact that was noted in [127]; indeed, Φ can be computed *a posteriori* by solving (2.9) for each t. This is the main hint to derive depth-averaged models: if $G[\zeta, b]\psi$ is approximated in terms of ζ and ψ, then, the z dimension is automatically discarded. Moreover, it is more convenient to replace ψ by the vertically-averaged velocity too. It is also possible to derive the equations using other strategies, as was reviewed recently in [78], but the ZCS formulation is convenient for the development of the next sections.

To continue the analysis let us adimensionalize the equations, as in [77], with the change of variables

$$\begin{aligned} x' &= \frac{x}{L}, \qquad \zeta' = \frac{\zeta}{a_{surf}}, \qquad b' = \frac{b}{a_{bottom}} \\ \Phi' &= \frac{\Phi}{a_{surf}\frac{\sqrt{gH_0}}{\mu}}, \qquad t' = t\frac{\sqrt{gH_0}}{L} \end{aligned} \tag{2.11}$$

where L is a scale for the length of the waves, and μ is one of the adimensional parameters:

$$\varepsilon = \frac{a_{surf}}{H_0}, \quad \beta = \frac{a_{bottom}}{H_0}, \quad \mu = \frac{H_0^2}{L^2} \tag{2.12}$$

where ε and β are the nonlinearity and bathymetry parameters and μ is the shallowness parameter; the scale used to adimensionalize Φ can be obtained by studying the analytical solution (2.6) after linearizing around the state at rest $\zeta \approx 0$, $\boldsymbol{U} \approx 0$.

Remark 2.1. *The shallowness parameter μ must not be mistaken in this chapter. Indeed, here we use the squared form $\mu = H_0^2/L^2$ to facilitate the comparison with references [77, 15, 78].*

Given this change of variables the system (2.6) can be rewritten as

$$\partial_t \zeta = \frac{1}{\mu}\mathcal{G}[\varepsilon\zeta, \beta b]\psi \tag{2.13}$$

$$\partial_t \psi + \frac{\varepsilon}{2}|\nabla\psi|^2 + \zeta - \frac{\varepsilon\mu}{2}\frac{\left(\frac{1}{\mu}\mathcal{G}[\varepsilon\zeta, \beta b]\psi + \nabla\psi \cdot \nabla(\varepsilon\zeta)\right)^2}{1 + \mu|\nabla(\varepsilon\zeta)|^2} = 0 \tag{2.14}$$

with the adimensional Dirichlet-to-Neumann operator

$$\mathcal{G}[\varepsilon\zeta, \beta b]\psi = \partial_z \Phi|_{z=\varepsilon\zeta} - \mu\nabla\Phi|_{z=\varepsilon\zeta} \cdot \nabla(\varepsilon\zeta) \tag{2.15}$$

and the adimensional velocity potential Φ satisfying

$$\begin{cases} \mu\Delta\Phi + \partial_z^2\Phi = 0 & \text{in } \Omega_t = \{-1 + \beta b < z < \varepsilon\zeta\} \\ \Phi = \psi & \text{on } \{z = \varepsilon\zeta\} \\ \partial_z\Phi = \mu\nabla\Phi \cdot \nabla(\beta b) & \text{on } \{z = -1 + \beta b\} \\ \partial_x\Phi = 0 & \text{on } \{x = a \text{ or } x = b\} \end{cases} \tag{2.16}$$

Asymptotic models such as the SV and GN equations are written in terms of the vertically averaged veloctity

$$V = \frac{1}{h}\int_{z=-1+\beta b}^{\varepsilon\zeta} \nabla\Phi dz \tag{2.17}$$

where $h = \varepsilon\zeta - \beta b + 1$. Then, by means of vertical integration of (2.16), V can be related to $\mathcal{G}[\varepsilon\zeta, \beta b]$ by

$$\frac{1}{\mu}\mathcal{G}[\varepsilon\zeta, \beta b]\psi = -\nabla \cdot (hV) \tag{2.18}$$

from where (2.13) becomes exactly

$$\partial_t \zeta + \nabla \cdot (hV) = 0 \tag{2.19}$$

For the sake of clarity, we will assume throughout the document the small amplitude regime $\{\varepsilon = O(\mu), \beta = O(\mu)\}$ and discard all remaning $O(\mu)$ terms. In this regime $h = 1 + O(\varepsilon) + O(\beta) = 1 + O(\mu)$ and equations (2.19), (2.13), (2.14), (2.17) and (2.16) become

$$(ZCS): \begin{cases} \partial_t \zeta + \partial_x V = 0 \\ \partial_t \psi + \zeta = 0 \\ \\ V = \int_{z=-1}^{0} \nabla\Phi dz \\ \\ \mu\partial_x^2 \Phi + \partial_z^2 \Phi = 0 \quad \text{in } \Omega_t = \{-1 \leq z \leq 0\} \\ \Phi = \psi \quad \text{on } \{z = 0\} \\ \partial_z \Phi = 0 \quad \text{on } \{z = -1\} \end{cases} \tag{2.20}$$

where the $O(\mu)$ terms in the Laplace equation of (2.20) were not discarded, because they will allow to describe the non-hydrostatic effects in the equations using the vertically averaged velocity.

Following [79], now we look for asymptotic expansions for Φ of the form

$$\Phi = \sum_{j=0}^{k} \mu^j \Phi_j + O(\mu^{k+1}) \tag{2.21}$$

The procedure to obtain this expansion consists on substituting (2.21) on (2.20) sequentially for each k, discard $O(\mu^{k+1})$ terms and solve the resulting equation for Φ_k. For example, for $k = 0$, the asymptotic expansion is

$$\Phi = \Phi_0 + O(\mu) \tag{2.22}$$

which after replacing in equation (2.16) and discarding $O(\mu)$ terms, results in the problem

$$\begin{cases} \partial_z^2 \Phi_0 &= 0 \\ \Phi_0|_{z=\varepsilon\zeta} &= \psi \\ \partial_z \Phi_0|_{z=-1} &= 0 \end{cases} \tag{2.23}$$

whose solution is

$$\Phi_0 = \psi \tag{2.24}$$

For $k = 1$, using the second order asymptotic expansion

$$\Phi = \Phi_0 + \mu\Phi_1 + O(\mu^2) \tag{2.25}$$

similarly results in the system

$$\begin{cases} \partial_z^2 \Phi_1 &= -\partial_x \Phi_0 \\ \Phi_1|_{z=0} &= 0 \\ \partial_z \Phi_1|_{z=-1} &= 0 \end{cases} \tag{2.26}$$

whose solution is

$$\Phi_1 = \frac{1}{2}\partial_x^2\psi(1-(z+1)^2) \tag{2.27}$$

and leads to the second order expansion

$$\Phi = \psi + \mu\frac{1}{2}\partial_x^2\psi(1-(z+1)^2) + O(\mu^2) \tag{2.28}$$

As shown in [79], this procedure can be continued for arbitrary k, however, just the second order expansion (2.28) is enough in this work.

So far equation (2.28) allows us to discard the vertical dimension z, however, to take advantage of the exact relation (2.18) it is better to replace ψ with V. To do this we can substitute $\Phi = \Phi_0 + \mu\Phi_1 + O(\mu^2)$ from equation (2.28) into the third line of (2.20) to obtain

$$V = \partial_x\psi - \mu\mathcal{T}\partial_x\psi + O(\mu^2) \tag{2.29}$$

with $\mathcal{T}$ given by

$$\mathcal{T}(\cdot) = -\frac{1}{3}\partial_x^2(\cdot) \tag{2.30}$$

and, to isolate $\partial_x\psi$, at first order it is straightforward to do so from (2.29), as

$$\partial_x\psi = V + O(\mu) \tag{2.31}$$

At second order, we can substitute this first order approximation, equation (2.31), into the $\mathcal{T}\partial_x\psi$ term of equation (2.29), by regrouping $O(\mu^2)$ terms as

$$V = \partial_x\psi - \mu\mathcal{T}(V + O(\mu)) + O(\mu^2) \tag{2.32}$$

$$= \partial_x\psi - \mu\mathcal{T}V + O(\mu^2) \tag{2.33}$$

which leads to

$$\partial_x\psi = V + \mu\mathcal{T}V + O(\mu^2) \tag{2.34}$$

Now we are ready to substitute (2.34) back into the second line of (2.20) and discard $O(\mu^2)$ terms to obtain the momentum equation of the linearized Boussinesq equations

$$(1+\mu\mathcal{T})\partial_t V + \partial_x\zeta = 0 \tag{2.35}$$

which are equivalent to

$$\begin{cases} \partial_t V + \partial_x\zeta = \phi \\ (1+\mu\mathcal{T})\phi = \mu\mathcal{T}\partial_x\zeta \end{cases} \tag{2.36}$$

If now we continue discarding $O(\mu)$ terms we recover the momentum equation of the linear Saint-Venant equations

$$\partial_t V + \partial_x\zeta = 0 \tag{2.37}$$

Recapitulating, we have derived the following two systems of equations

$$(B)\begin{cases} \partial_t\zeta + \partial_x V &= 0 \\ \partial_t V + \partial_x\zeta &= 0 \\ (1+\mu\mathcal{T})\phi &= \mu\mathcal{T}\partial_x\zeta \end{cases}, \quad (SV): \begin{cases} \partial_t\zeta + \partial_x V &= 0 \\ \partial_t V + \partial_x\zeta &= 0 \end{cases} \tag{2.38}$$

We see that the B and SV equations are consistent with the ZCS equations (2.20) at orders $O(\mu^2)$ and $O(\mu)$ respectively. Additionally, because they derive from (2.20), both of them are consistent at $O(\mu)$ with the free-surface Euler equations in the Zakharov-Craig-Sulem formulation of (2.13), (2.14), (2.15) and (2.16), assuming the regime $\{\varepsilon = O(\mu), \quad \beta = O(\mu)\}$.

2.2 Derivation of equations at the discrete level

Now we will proceed to repeat the same process at the discrete level. For that, let us introduce a finite-difference discretization of equations (2.20), by defining $\zeta_i^n = \zeta(t^n, x_i)$, $\psi_i^n = \psi(t^n, x_i)$ as the nodal values on the uniform grid $x_i = i\Delta x$, $t^n = n\Delta t$, for $i \in \mathcal{N} = \{1...N_x - 2\}$ and $n = 1, 2, ...$ From equation (2.20) one obtains

$$\begin{cases} \dfrac{\zeta_i^{n+1} - \zeta_i^n}{\Delta t} + \dfrac{V_i^n - V_{i-1}^n}{\Delta x} = 0 \text{ for } i \in \mathcal{N} \\ \dfrac{\psi_i^{n+1} - \psi_i^n}{\Delta t} + \zeta_i^n = 0 \text{ for } i \in \mathcal{N} \end{cases} \tag{2.39}$$

where V_i^n is the discrete vertically-averaged velocity given by

$$V_i^n = \sum_{j=1}^{N_z - 1} \frac{\Phi_{i+1,j}^n - \Phi_{i,j}^n}{\Delta x} \Delta z \tag{2.40}$$

Boundary conditions at nodes $i = 0$ and $i = N_x - 1$ will be taken as $V_i^n = 0$ and $\zeta_0^n = \zeta_1^n$, $\zeta_{N_x-1}^n = \zeta_{N_x-2}^n$, following the recommendation of [124, eqs. (28), (37)]. In equation (2.40), $\Phi_{i,j}^n = \Phi(t^n, x_i, z_j)$ denotes the discrete velocity potential computed from

$$\mu \frac{\Phi_{i+1,j}^n + \Phi_{i-1,j}^n - 2\Phi_{i,j}^n}{\Delta x^2} + \frac{\Phi_{i,j+1}^n + \Phi_{i,j-1}^n - 2\Phi_{i,j}^n}{\Delta z^2} = 0$$
$$\text{for } i, j \in \mathcal{N} \times \{1, ..., N_z - 2\} \tag{2.41}$$

on a grid (x_i, z_j) such that $z_j = j\Delta z - 1$ and $z_{N_z-1} = 0$ and with boundary conditions

$$\begin{gathered} \Phi_{i,N_z-1}^n = \psi_i^n, \quad \Phi_{i,0} = \Phi_{i,1}, \\ \Phi_{0,j} = \Phi_{1,j}, \quad \Phi_{N_x-1,j} = \Phi_{N_x-2,j} \end{gathered} \tag{2.42}$$

Equations (2.39), (2.40), (2.41) and (2.42) form the discrete ZCS equations (dZCS).

To proceed with the derivation of the asymptotic equations, and for the sake of clarity, let us temporarily drop the time superscript n and introduce the asymptotic-degree superscript $(k) = (1), (2), \cdots$. Proceeding as in the continuous level, we look for an asymptotic expansion

$$\Phi_{i,j} = \sum_{q=0}^{k} \mu^q \Phi_{i,j}^{(q)} + O(\mu^{k+1}) \tag{2.43}$$

of the solution of the discrete Laplace equation (2.41). Substituting the first order expansion

$$\Phi_{i,j} = \Phi_{i,j}^{(0)} + O(\mu)$$

into equation (2.41) and discarding $O(\mu)$ terms leads to the problem

$$\begin{cases} \Phi_{i,j+1}^{(0)} + \Phi_{i,j-1}^{(0)} - 2\Phi_{i,j}^{(0)} = 0 \\ \Phi_{i,0}^{(0)} = \Phi_{i,1}^{(0)} \\ \Phi_{i,N_z-1}^{(0)} = \psi_i \end{cases} \tag{2.44}$$

for $j \in i, j \in \mathcal{N} \times \{1, ..., N_z - 2\}$. The characteristic polynomial of this equation is

$$t^2 - 2t + 1 = 0 \tag{2.45}$$

and its two roots are equal to 1, so the solution must have the form

$$\Phi^0_{i,j} = c_1(i) + c_2(i)j \text{ for } 0 \leq j \leq N_z - 1 \tag{2.46}$$

From the boundary condition at the bottom, $j = 0$ we extract $c_2(j) = 0$ and from the boundary condition at the surface $j = N_z - 1$, $c_1(i) = \psi_i$. Thus we have that $\Phi^0_{i,j} = \psi_i$ and the first order expansion is

$$\Phi_{i,j} = \psi_i + O(\mu) \tag{2.47}$$

Similarly, at second order, replacing $\Phi_{i,j} = \Phi^{(0)}_{i,j} + \mu\Phi^{(1)}_{i,j} + O(\mu^2)$ into (2.41) leads to

$$\begin{cases} \dfrac{\Phi^{(1)}_{i,j+1} + \Phi^{(1)}_{i,j-1} - 2\Phi^{(1)}_{i,j}}{\Delta z^2} = -\dfrac{\psi_{i+1} + \psi_{i-1} - 2\psi_i}{\Delta x^2} \\ \Phi^{(0)}_{i,0} = \Phi^{(0)}_{i,1} \\ \Phi^{(0)}_{i,N_z-1} = 0 \end{cases} \tag{2.48}$$

Since the right hand side of the first line of (2.48) does not depend on j, the left-hand side evaluated at j and $j-1$ must be equal:

$$\Phi^{(1)}_{i,j+1} + \Phi^{(1)}_{i,j-1} - 2\Phi^{(1)}_{i,j} = \Phi^{(1)}_{i,j} + \Phi^{(1)}_{i,j-2} - 2\Phi^{(1)}_{i,j-1} \tag{2.49}$$

which is the same as the recurrence relation

$$\Phi^{(1)}_{i,j+1} - 3\Phi^{(1)}_{i,j} + 3\Phi^{(1)}_{i,j-1} - \Phi^{(1)}_{i,j-2} = 0 \tag{2.50}$$

whose characteristic polynomial is

$$t^3 - 3t^2 + 3t + 1 = 0 \tag{2.51}$$

and has three roots equal to 1, thus $\Phi^1_{i,j}$ must have the form

$$\Phi^{(1)}_{i,j} = c_1(i) + c_2(i)j + c_3(i)j^2 \tag{2.52}$$

Replacing $\Phi_{i,j} = \Phi^{(0)}_{i,j} + \mu\Phi^{(1)}_{i,j} + O(\mu^2)$ into the vertical boundary conditions, $j = 0, N_z - 1$ in equation (2.48) we deduce that $c_1 + c_2(N_z - 1) + c_3(N_z - 1)^2 = 0$ and $c_2 + c_3$=0 respectively. This means that $c_2 = -c_3$ and $c_1 = c_3(N_z - 1) - c_3(N_z - 1)^2$. Replacing this back into (2.52) gives

$$\begin{aligned} \Phi^{(1)}_{i,j} &= c_3(N_z - 1) - c_3(N_z - 1)^2 - c_3 i + c_3 j^2 \\ &= c_3(j^2 - j - (N_z - 1)(N_z - 2)) \end{aligned} \tag{2.53}$$

To compute c_3, notice that, using (2.52)

$$\begin{aligned} \Phi^{(1)}_{i,j+1} + \Phi^{(1)}_{i,j-1} - 2\Phi^{(1)}_{i,j} &= c_1 + c_2(j+1) + c_3(j+1)^2 \\ &+ c_1 + c_2(j-1) + c_3(j-1)^2 \\ &- 2(c_1 + c_2 j + c_3 j^2) \\ &= 2c_3 = -\frac{\Delta z^2}{\Delta x^2}(\psi_{i+1} + \psi_{i-1} - 2\psi_i) \end{aligned} \tag{2.54}$$

where the last equality comes from equation (2.48). This means that

$$c_3 = -\frac{\Delta z^2}{2\Delta x^2}(\psi_{i+1} + \psi_{i-1} - 2\psi_i) \tag{2.55}$$

and since now we have found c_1, c_2 and c_3, the discrete asymptotic expansion of second order is

$$\Phi_{i,j} = \psi_i - \mu\frac{\Delta z^2}{2\Delta x^2}(\psi_{i+1} + \psi_{i-1} - 2\psi_i)(j^2 - j - (N_z - 1)(N_z - 2)) + O(\mu^2) \tag{2.56}$$

We can substitute the first order expansion (2.47) into (2.40) and use the fact that $1 = (N_z - 1)\Delta z$ to obtain

$$\begin{aligned} V_i &= \frac{1}{(N_z - 1)\Delta z \Delta x}((N_z - 1)\Delta z \psi_{i+1} - (N_z - 1)\Delta z \psi_i) + O(\mu) \\ &= \frac{\psi_{i+1} - \psi_i}{\Delta x} + O(\mu) \end{aligned} \tag{2.57}$$

which gives us the first order expansion:

$$\frac{\psi_{i+1} - \psi_i}{\Delta x} = V_i + O(\mu) \tag{2.58}$$

For the second order approximation, from (2.56) we obtain

$$\begin{aligned} V_i &= \frac{\psi_{i+1} - \psi_i}{\Delta x} \\ &- \frac{\mu \Delta z^2}{2(N_z - 1)\Delta x^3}\left[(\psi_{i+2} + \psi_i - 2\psi_{i+1}) - (\psi_{i+1} + \psi_{i-1} - 2\psi_i)\right] \\ &\times \sum_{j=1}^{N_z - 1}(j^2 - j - (N_z - 1)(N_z - 2)) + O(\mu^2) \end{aligned} \tag{2.59}$$

also

$$\sum_{j=1}^{N_z - 1} j^2 = N_z(N_z - 1)(2N_z - 1)/6 \tag{2.60}$$

$$\sum_{j=1}^{N_z - 1} j = N_z(N_z - 1)/2 \tag{2.61}$$

thus

$$\sum_{j=1}^{N_z - 1}(j^2 - j - (N_z - 1)(N_z - 2)) = -\frac{1}{3}(N_z - 1)(2N_z - 3)(N_z - 2) \tag{2.62}$$

So the second order asymptotic expansion for V_i is

$$\begin{aligned} V_i &= \frac{\psi_{i+1} - \psi_i}{\Delta x} \\ &+ \frac{\mu \Delta z^2}{3\Delta x^3}(N_z - \frac{3}{2})(N_z - 2) \\ &\times \left[(\psi_{i+2} + \psi_i - 2\psi_{i+1}) - (\psi_{i+1} + \psi_{i-1} - 2\psi_i)\right] \\ &+ O(\mu^2) \end{aligned} \tag{2.63}$$

but $(N_z - 1)\Delta z = 1$, so

$$\begin{aligned} V_i = &\frac{\psi_{i+1} - \psi_i}{\Delta x} \\ &+ \frac{\mu}{3\Delta x^3}(1 - \Delta z/2)(1 - \Delta z) \\ &\times [(\psi_{i+2} + \psi_i - 2\psi_{i+1}) - (\psi_{i+1} + \psi_{i-1} - 2\psi_i)] \\ &+ O(\mu^2) \end{aligned} \tag{2.64}$$

which can also be re-arranged as

$$\begin{aligned} V_i = &\frac{\psi_{i+1} - \psi_i}{\Delta x} \\ &+ \frac{\mu}{3\Delta x^2}(1 - \Delta z/2)(1 - \Delta z) \\ &\times \left[\frac{\psi_{i+2} - \psi_{i+1}}{\Delta x} + \frac{\psi_i - \psi_{i-1}}{\Delta x} - 2\frac{\psi_{i+1} - \psi_i}{\Delta x}\right] \\ &+ O(\mu^2) \end{aligned} \tag{2.65}$$

We can now substitute the first order approximation (2.58) into (2.65) to obtain

$$V_i = \frac{\psi_{i+1} - \psi_i}{\Delta x} + \frac{\mu}{3}(1 - \Delta z/2)(1 - \Delta z)\frac{V_{i+1} + V_{i-1} - 2V_i}{\Delta x^2} + O(\mu^2) \tag{2.66}$$

from where we can isolate $\frac{\psi_{i+1} - \psi_i}{\Delta x}$

$$\frac{\psi_{i+1} - \psi_i}{\Delta x} = V_i - \frac{\mu}{3}(1 - \Delta z/2)(1 - \Delta z)\frac{V_{i+1} + V_{i-1} - 2V_i}{\Delta x^2} + O(\mu^2) \tag{2.67}$$

Remark 2.2. *In this discrete setting, equations* (2.65) *and* (2.67) *are the analogous of the asymptotic expansions for* V *and* $\partial_x \psi$ *in the regime of the Boussinesq equations* $\varepsilon = O(\mu)$. *In fact, these are consistent with equations* (2.29) *and* (2.34) *up to an* $O(\Delta x, \Delta z)$ *term. Moreover, one can substitute* $z_j = -1 + \Delta z j$ *and use the fact that* $\Delta z(N_z - 1) = 1$ *to obtain*

$$\begin{aligned} \Phi_{i,j} &= \psi_i - \mu\frac{1}{2}\frac{\psi_{i+1} + \psi_{i-1} - 2\psi_i}{\Delta x^2}(j^2 - j - (N_z - 1)(N_z - 2)) + O(\mu^2) \\ &= \psi_i + \frac{\mu}{2}\frac{\psi_{i+1} + \psi_{i-1} - 2\psi_i}{\Delta x^2}(1 - (z_j + 1)^2 - z_j \Delta z) + O(\mu^2) \end{aligned} \tag{2.68}$$

which is consistent at $O(\Delta z)$ *with* (2.28), *for constant* μ.

Applying a forward finite-difference operator into equation (2.39) one obtains

$$\frac{(\psi_{i+1}^{n+1} - \psi_i^{n+1})/\Delta x - (\psi_{i+1}^n - \psi_i^n)/\Delta x}{\Delta t} + \frac{\zeta_{i+1}^n - \zeta_i^n}{\Delta x} = 0 \tag{2.69}$$

defining the TV_i operator as

$$TV_i = -\frac{1}{3}\frac{V_{i+1} + V_{i-1} - 2V_i}{\Delta x^2} \tag{2.70}$$

and the modified dispersion parameter

$$\nu = \mu(1 - \Delta z/2)(1 - \Delta z) \tag{2.71}$$

Then we can use the asymptotic expansion (2.67) and discard terms of size $O(\mu^2)$ to obtain the discrete equation

$$(1 + \nu T)\left(\frac{V_i^{n+1} - V_i^n}{\Delta t}\right) + \frac{\zeta_{i+1}^n - \zeta_i^n}{\Delta x} = 0 \tag{2.72}$$

which, as at the continous level, is equivalent to

$$\begin{aligned} \frac{V_i^{n+1} - V_i^n}{\Delta t} + \frac{\zeta_{i+1}^n - \zeta_i^n}{\Delta x} &= \phi_i \\ (1 + \nu T)\phi_i &= \nu T\left(\frac{\zeta_{i+1}^n - \zeta_i^n}{\Delta x}\right) \end{aligned} \tag{2.73}$$

and if we discard all $O(\mu)$ terms

$$\frac{V_i^{n+1} - V_i^n}{\Delta t} + \frac{\zeta_{i+1}^n - \zeta_i^n}{\Delta x} = 0 \tag{2.74}$$

Using the first line of (2.39), we can now assemble the discrete Boussinesq (dB) and Saint-Venant (dSV) equations

$$(dB) \quad \begin{cases} \dfrac{\zeta_i^{n+1} - \zeta_i^n}{\Delta t} + \dfrac{V_i^n - V_{i-1}^n}{\Delta x} = 0 \\ \dfrac{V_i^{n+1} - V_i^n}{\Delta t} + \dfrac{\zeta_{i+1}^n - \zeta_i^n}{\Delta x} = \phi_i \\ (1 + \nu T)\phi_i = \nu T\left(\dfrac{\zeta_{i+1}^n - \zeta_i^n}{\Delta x}\right) \end{cases} \tag{2.75}$$

$$(dSV) \quad \begin{cases} \dfrac{\zeta_i^{n+1} - \zeta_i^n}{\Delta t} + \dfrac{V_i^n - V_{i-1}^n}{\Delta x} = 0 \\ \left(\dfrac{V_i^{n+1} - V_i^n}{\Delta t}\right) + \dfrac{\zeta_{i+1}^n - \zeta_i^n}{\Delta x} = 0 \end{cases} \tag{2.76}$$

2.3 Domain decomposition of the Euler equations

Let $(\zeta_i^n, V_i^n, \Phi_{i,j}^n)$ be the solution of the dZCS system. We will call this solution the monodomain solution. We will now introduce coupling conditions to derive from them new coupling conditions for the dB and dSV equations.

Let us decompose the domain in two components with a vertical interface located at $i = l \in \mathcal{N}$. To do this let $\zeta_{i,s}^{n+1}$, $\psi_{i,s}^{n+1}$, $\Phi_{i,j,s}^{n+1}$, $V_{i,s}^n$ be the values of the unknowns on each subdomain $s = 1, 2$. These variables are computed from equations (2.39), (2.40), (2.41), but with i in $\mathcal{N}_s$ instead of $\mathcal{N}$, where

$$\mathcal{N}_1 = \{1, .., l - 1\}$$

$$\mathcal{N}_2 = \{l, ..., N_x - 2\}$$

equation (2.41) is solved with $i \in \mathcal{N}_1$ for $s = 1$ and $i \in \mathcal{N}_2 \setminus \{l\}$ for $s = 2$. To obtain the same monodomain solution, equations (2.39) are complemented with Dirichlet transmission conditions

$$\begin{aligned} \zeta^n_{l,1} &= \zeta^n_{l,2}, & V^n_{l,1} &= V^n_{l,2} & \psi^n_{l,1} &= \psi^n_{l,2} \\ \zeta^n_{l-1,2} &= \zeta^n_{l-1,1}, & V^n_{l-1,2} &= V^n_{l-1,1} & \psi^n_{l-1,2} &= \psi^n_{l-1,1} \end{aligned} \tag{2.77}$$

while (2.41) is complemented with Neumann and Dirichlet transmission conditions

$$\begin{aligned} &\frac{\Phi^n_{l,j,1} - \Phi^n_{l-1,j,1}}{\Delta x} - \frac{\Delta x}{2\mu \Delta z^2}\left(\Phi^n_{l,j+1,1} + \Phi^n_{l,j-1,1} - 2\Phi^n_{l,j,1}\right) && (2.78) \\ &= \frac{\Phi^n_{l+1,j,2} - \Phi^n_{l,j,2}}{\Delta x} + \frac{\Delta x}{2\mu \Delta z^2}\left(\Phi^n_{l,j+1,2} + \Phi^n_{l,j-1,2} - 2\Phi^n_{l,j,2}\right) && \\ &\Phi^n_{l,j,2} = \Phi^n_{l,j,1} && (2.79) \end{aligned}$$

which include an $O(\Delta x)$ term that ensures that the monodomain solution is preserved exactly at the discrete level [46]. Merging the two coupled solution as

$$\Phi^n_{i,j,*} = \begin{cases} \Phi^n_{i,j,1} & i \leq l \\ \Phi^n_{i,j,2} & i > l \end{cases} \tag{2.80}$$

this scheme satisfies

$$\Phi^n_{i,j,*} = \Phi^n_{i,j} \tag{2.81}$$

i.e., the coupled solution $\Phi^n_{i,j,*}$ is exactly the same as the monodomain solution. These coupling conditions lead to what is known in the DDM literature as the Neumann-Dirichlet method. This method consists on obtaining $\Phi^n_{i,j,*}$ from the limit of the sequence $(\Phi^{n,k}_{i,j,1}, \Phi^{n,k}_{i,j,2})^{\infty}_{k=0}$ when $k \to \infty$. This sequence is defined by an arbitrary initial guess for $k = 0$ and by the iterative subproblems for $k \geq 1$

$$\begin{cases} \mu \dfrac{\Phi^{n,k}_{i+1,j,1} + \Phi^n_{i-1,j,1} - 2\Phi^n_{i,j,1}}{\Delta x^2} + \dfrac{\Phi^{n,k}_{i,j+1,1} + \Phi^n_{i,j-1,1} - 2\Phi^n_{i,j,1}}{\Delta z^2} = 0 \\[2ex] \dfrac{\Phi^{n,k}_{l,j,1} - \Phi^{n,k}_{l-1,j,1}}{\Delta x} - \dfrac{\Delta x}{2\mu\Delta z^2}\left(\Phi^{n,k}_{l,j+1,1} + \Phi^{n,k}_{l,j-1,1} - 2\Phi^{n,k}_{l,j,1}\right) \\ \quad = \dfrac{\Phi^{n,k-1}_{l+1,j,2} - \Phi^{n,k-1}_{l,j,2}}{\Delta x} + \dfrac{\Delta x}{2\mu\Delta z^2}\left(\Phi^{n,k-1}_{l,j+1,2} + \Phi^{n,k-1}_{l,j-1,2} - 2\Phi^{n,k-1}_{l,j,2}\right) \\[2ex] \Phi^n_{i,N_z-1} = \psi^n_i, \quad \Phi_{i,0} = \Phi_{i,1}, \quad \Phi_{0,j} = \Phi_{1,j}, \quad \Phi_{N_x-1,j} = \Phi_{N_x-2,j} \\[2ex] \qquad\qquad i, j \in \mathcal{N}_1 \times \{1, ..., N_z - 1\} \end{cases}$$

$$\begin{cases} \mu \dfrac{\Phi^{n,k}_{i+1,j,2} + \Phi^n_{i-1,j,2} - 2\Phi^n_{i,j,2}}{\Delta x^2} + \dfrac{\Phi^{n,k}_{i,j+1,2} + \Phi^n_{i,j-1,2} - 2\Phi^n_{i,j,2}}{\Delta z^2} = 0 \\ \\ \Phi^n_{l,j,2} = \Phi^n_{l,j,1} \\ \\ \Phi^n_{i,N_z-1} = \psi^n_i, \quad \Phi_{i,0} = \Phi_{i,1}, \quad \Phi_{0,j} = \Phi_{1,j}, \quad \Phi_{N_x-1,j} = \Phi_{N_x-2,j} \\ \\ i,j \in \mathcal{N}_2 \times \{1,...,N_z-1\} \end{cases}$$

As shown in [40, eq. (2.5) with $\theta = 1$], this algorithm converges if $L_1 < L_2$, with

$$L_1 = l\Delta x$$

$$L_2 = (N_x - l)\Delta x$$

Now let us verify that the coupled solution recovers the monodomain solution $\zeta^n_i, V^n_i, \psi^n_i, \Phi^n_{i,j}$. This can be proved by induction. Let us reconstruct

$$\begin{aligned} \zeta^n_{i,*} &= \zeta^n_{i,1} \quad i \le l \\ \zeta^n_{i,*} &= \zeta^n_{i,2} \quad i > l \end{aligned} \tag{2.82}$$

$$\begin{aligned} V^n_{i,*} &= V^n_{i,1} \quad i \le l \\ V^n_{i,*} &= V^n_{i,2} \quad i > l \end{aligned} \tag{2.83}$$

$$\begin{aligned} \psi^n_{i,*} &= \psi^n_{i,1} \quad i \le l \\ \psi^n_{i,*} &= \psi^n_{i,2} \quad i > l \end{aligned} \tag{2.84}$$

At $n = 0$, if we assume that

$$\zeta^n_{i,*} = \zeta^n_i, \quad V^n_{i,*} = V^n_i \tag{2.85}$$

then, from (2.81) we already know that $\Phi^n_{i,j,*} = \Phi^n_{i,j}$ too, hence

$$\psi^n_{i,*} = \psi^n_i \tag{2.86}$$

at $n = 0$. Now we can proceed inductively, assuming that (2.85),(2.86) and (2.81) hold at timestep n, then for interior nodes $i \in \mathcal{N}_s$, $s = 1, 2$, the solution at $n + 1$ is obtained explicitly from the same data at step n (for the monodomain and subdomain's solutions) from equations (2.39). Since the Dirichlet-like boundary conditions (2.77) make the reconstruction of (2.83), (2.82) and (2.84) unambiguous, this leads to conclude that (2.85) and (2.86) hold at $n+1$ too. Moreover, assuming assuming $L_1 < L_2$ and taking the limit solution when $k \to \infty$ of the Laplace problems (2.82) and (2.82), because in the surface boundary condition is $\Phi^{n,*}_{i,j} = \psi^n_i$ the right hand side is the data of the monodomain solution at step n, from the convergence of the Neumann-Dirichlet method, then also (2.81) holds at $n + 1$.

2.4 Derivation of depth-averaged coupling conditions

Additional coupling conditions for V_i^n and ζ_i^n are not necessary because they are already given by the original coupling conditions of the ZCS equations, in section 2.3. The coupling conditions that are missing in this case are for the variable ϕ_i^n in eq. (2.75), which will be derived here. This also means that the domain decomposition of dSV-dSV models does not require any additional information, which leaves us only the cases of dB-dB and dB-dSV coupling.

We can multiply equation (2.79) by Δz and use the notation $D_x^+ f_i = (f_{i+1} - f_i)/\Delta x$, $D_z^+ f_j = (f_{j+1} - f_j)/\Delta z$ to rewrite it as

$$\begin{aligned} &D_x^+ \Phi^1_{l-1,j} \Delta z - \frac{\Delta x}{2\mu} \left(D_z^+ \Phi^1_{l,j} - D_z^+ \Phi^1_{l,j-1} \right) \\ &= D_x^+ \Phi^2_{l,j} \Delta z + \frac{\Delta x}{2\mu} \left(D_z^+ \Phi^2_{l,j} - D_z^+ \Phi^2_{l,j-1} \right) \end{aligned} \tag{2.87}$$

now we can add them from $j = 1$ to $j = N_z - 2$ as

$$\begin{aligned} &\sum_{j=1}^{N_z-2} D_x^+ \Phi^1_{l-1,j} \Delta z - \frac{\Delta x}{2\mu} \left(\sum_{j=1}^{N_z-2} D_z^+ \Phi^1_{l,j} - \sum_{j=1}^{N_z-2} D_z^+ \Phi^1_{l,j-1} \right) \\ &= \sum_{j=1}^{N_z-2} D_x^+ \Phi^2_{l,j} \Delta z + \frac{\Delta x}{2\mu} \left(\sum_{j=1}^{N_z-2} D_z^+ \Phi^2_{l,j} - \sum_{j=1}^{N_z-2} D_z^+ \Phi^2_{l,j-1} \right) \end{aligned} \tag{2.88}$$

but because of the definition of $V_i = \sum_{j=1}^{N_z-1} D_x^+ \Phi_{i,j} \Delta z$ we can replace

$$\begin{aligned} \sum_{j=1}^{N_z-2} D_x^+ \Phi_{i,j} \Delta z &= \sum_{j=1}^{N_z-1} (D_x^+ \Phi_{i,j}) \Delta z - D_x^+ \Phi_{i,N_z-1} \Delta z \\ &= V_i - D_x^+ \Phi_{i,N_z-1} \Delta z \end{aligned} \tag{2.89}$$

to obtain the equation

$$\begin{aligned} &V_{l-1} - D_x^+ \Phi_{l-1,N_z-1} \Delta z - \frac{\Delta x}{2\mu} \left(\sum_{j=1}^{N_z-2} D_z^+ \Phi^1_{l,j} - \sum_{j=1}^{N_z-2} D_z^+ \Phi^1_{l,j-1} \right) \\ &= V_l - D_x^+ \Phi_{l,N_z-1} \Delta z + \frac{\Delta x}{2\mu} \left(\sum_{j=1}^{N_z-2} D_z^+ \Phi^2_{l,j} - \sum_{j=1}^{N_z-2} D_z^+ \Phi^2_{l,j-1} \right) \end{aligned} \tag{2.90}$$

We can evaluate the remaining sums telescopically and use the boundary condition $D_z^+ \Phi_{i,0} = 0$:

$$\begin{aligned} \sum_{j=1}^{N_z-2} D_z^+ \Phi_{i,j} - \sum_{j=1}^{N_z-2} D_z^+ \Phi_{i,j-1} &= D_z^+ \Phi_{i,N_z-2} - D_z^+ \Phi_{i,0} \\ &= D_z^+ \Phi_{i,N_z-2} \end{aligned} \tag{2.91}$$

which results in the equation

$$\begin{aligned} &V^1_{l-1} - D^+_x \Phi^1_{l-1,N_z-1}\Delta z - \frac{\Delta x}{2\mu} D^+_z \Phi_{l,N_z-2} \\ &= V^2_l - D^+_x \Phi^2_{l,N_z-1}\Delta z + \frac{\Delta x}{2\mu} D^+_z \Phi^2_{l,N_z-2} \end{aligned} \tag{2.92}$$

or using the notation for backward differences $D^-_z f_j = (f_j - f_{j-1})/\Delta z$:

$$\begin{aligned} &V^1_{l-1} - D^+_x \Phi^1_{l-1,N_z-1}\Delta z - \frac{\Delta x}{2\mu} D^-_z \Phi^1_{l,N_z-1} \\ &= V^2_l - D^+_x \Phi^2_{l,N_z-1}\Delta z + \frac{\Delta x}{2\mu} D^-_z \Phi^2_{l,N_z-1} \end{aligned} \tag{2.93}$$

So far these equations have been obtained exactly, without requiring approximations. To proceed with the derivation and clear all remaining terms that are not ζ or V, we will now introduce some approximations, using relations from the continuous level. Starting with the vertical derivatives $D_z\Phi$ in the last equation, we can use the definition of the Dirichlet-to-Neumann operator $\mathcal{G}\psi_i$ from (2.15) to obtain

$$\begin{aligned} \frac{1}{\mu} D^-_z \Phi_{i,N_z-1} &= \frac{1}{\mu}\partial_z \Phi_{|x=x_i,z=0} + O(\frac{\Delta z}{\mu}) \\ &= \frac{1}{\mu}\mathcal{G}\psi_i + O(\varepsilon) + O(\frac{\Delta z}{\mu}) \\ &= -\partial_x(hV)_{|x=x_i} + O(\varepsilon, \frac{\Delta z}{\mu}) \\ &= -\partial_x V_{|x=x_i} + O(\varepsilon, \frac{\Delta z}{\mu}) \end{aligned} \tag{2.94}$$

where in the last line we have used that $h = 1 + O(\varepsilon)$. If we replace this back into eq. (2.93)

$$\begin{aligned} &V^1_{l-1} - D^+_x \Phi^1_{l-1,N_z-1}\Delta z + \frac{\Delta x}{2}\partial_x V^1_l \\ &= V^2_l - D_x \Phi^2_{l,N_z-1}\Delta z - \frac{\Delta x}{2}\partial_x V^2_l + O(\varepsilon, \Delta z/\mu) \end{aligned} \tag{2.95}$$

Now we can use the first order asymptotic approximation for Φ of eq. (2.47), $D_x\Phi_{i,N_z-1} = V_i + O(\mu)$, to obtain

$$\begin{aligned} &V^1_{l-1}(1 - \Delta z) + \frac{\Delta x}{2}\partial_x V^1_l \\ &= V^2_l(1 - \Delta z) - \frac{\Delta x}{2}\partial_x V^2_l + O(\varepsilon, \Delta z/\mu, \mu\Delta z) \end{aligned} \tag{2.96}$$

So to have $O(\mu)$ consistency with the discrete domain decomposition of the Laplace equation we need the regime $\varepsilon = O(\mu)$ and $\Delta z = O(\mu^2)$.

To use this formula for domain decomposition of an asymptotic shallow water model let us replace $\partial_x V^1_l$ in eq. (2.96) with a backward finite difference D^-_x

in the left-hand-side of the equation and a forward finite difference D_x^+ in the right-hand-side. Then, eq. (2.96) becomes

$$V_{l-1}^1(1-\Delta z)+\frac{1}{2}(V_l^1-V_{l-1}^1)=V_l^2(1-\Delta z)-\frac{1}{2}(V_{l+1}^2-V_l^2) \tag{2.97}$$

which can also be written as

$$\frac{1}{2}(V_l^1+V_{l-1}^1)-V_{l-1}^1\Delta z=\frac{1}{2}(3V_l^2-V_{l+1}^2)-V_l^2\Delta z \tag{2.98}$$

since for the elliptic equation we need to write this formula in terms of ϕ, we can do so by using the relation $\phi_i = D_t^+ V_i^n + D_x^+\zeta_i^n$ from eq. (2.75). If we replace this we obtain that

$$\begin{aligned}\frac{1}{2}(\phi_{l,1}^n+\phi_{l-1,1}^n)-\phi_{l-1,1}^n\Delta z &= \frac{1}{2}(3\phi_{l,2}^n-\phi_{l+1,2}^n)-\phi_{l,2}^n\Delta z\\ &-\left(\frac{3\Delta x^2}{2}T(D_x^+\zeta_l^n)-(D_x^+\zeta_l^n-D_x^+\zeta_{l-1}^n)\Delta z\right)\end{aligned}$$

which leaves us with the problem for $\phi_{i,1}$ with transmission conditions:

$$\begin{cases}(1+\nu T)\phi_{i,1}^n = \nu T D_x^+\zeta_i\\ \phi_{0,1}^n=\phi_{Left}\\ \frac{1}{2}(\phi_{l,1}^n+\phi_{l-1,1}^n)-\phi_{l-1,1}^n\Delta z = \frac{1}{2}(3\phi_{l,2}^n-\phi_{l+1,2}^n)-\phi_{l,2}^n\Delta z\\ \quad -\left(\frac{3\Delta x^2}{2}T(D_x^+\zeta_l^n)-(D_x^+\zeta_l^n-D_x^+\zeta_{l-1}^n)\Delta z\right)\end{cases} \tag{2.99}$$

and for subdomain $s=2$

$$\begin{cases}(1+\nu T)\phi_{i,1}^n = \nu T D_x^+\zeta_i\\ \phi_{l,2}^n=\phi_{l,1}^n\\ \phi_{N_x-1,2}^n=\phi_{Right}\end{cases} \tag{2.100}$$

2.5 Numerical evaluation of the coupling conditions

As mentioned at the beginning of the previous section, only two cases are interesting: dB-dB and dB-dSV coupling. This is because the coupling conditions of the parent ZCS model, (2.77) are still applicable for ζ and u, but ψ is not a variable anymore. Instead, ϕ needed new coupling conditions. The evolution of ζ and V is made as

$$\begin{aligned}\zeta_i^{n+1} &= \zeta^n+\Delta t D_x^- V_i\\ V_i^{n+1} &= V^n+\Delta t D_x^+\zeta_i+\Delta t\phi_i^n\end{aligned} \tag{2.101}$$

but Φ_i computed on different ways depending on whether it is the dB-dB or the dB-dSV case. We present the implementation of both cases and their results separately.

2.5.1 Homogeneous case: dB-dB coupling

In the dB-dB case we use an additive domain decomposition method, that means that, given ζ_i^n, V_i^n, we define a $(\phi_{i,1}^{n,k}, \phi_{i,2}^{n,k})_{k=0}^{\infty}$, defined by an initial guess $\phi_{i,1}^{n,0}, \phi_{i,2}^{n,0}$ and, for $k \geq 1$, from the algorithm:

$$\begin{cases} (1+\nu T)\phi_{i,1}^{n,k+1} = \nu T D_x^+ \zeta_i^n \\ \phi_{0,1}^{n,k+1} = \phi_{Left} \\ \frac{1}{2}(\phi_{l,1}^{n,k+1} + \phi_{l-1,1}^{n,k+1}) - \phi_{l-1,1}^{n,k+1}\Delta z = \frac{1}{2}(3\phi_{l,2}^{n,k} - \phi_{l+1,2}^{n,k}) - \phi_{l,2}^{n,k}\Delta z \\ \qquad - \left(\frac{3\Delta x^2}{2} T(D_x^+\zeta_l^n) - (D_x^+\zeta_l^n - D_x^+\zeta_{l-1}^n)\Delta z\right) \end{cases} \tag{2.102}$$

$$\begin{cases} (1+\nu T)\phi_{i,1}^{n,k+1} = \nu T D_x^+ \zeta_i^n \\ \phi_{l,2}^{n,k+1} = \phi_{l,1}^{n,k} \\ \phi_{N_x-1,2}^{n,k+1} = \phi_{Right} \end{cases} \tag{2.103}$$

Then, for sufficiently large k, if the algorithm converges, we reconstruct ϕ_i^n from

$$\phi_i^n = \begin{cases} \phi_{i,1}^{n,k} & i \leq l \\ \phi_{i,2}^{n,k} & i > l \end{cases} \tag{2.104}$$

In this homogeneous case, coupling dB with dB, we only need to verify that the previous algorithm converges to the monodomain solution $\phi_i^\star$ from

$$\begin{cases} (1+\nu T)\phi_i^\star = \nu T D_x^+ \zeta_i^n, & i = 1..N_x - 2 \\ \phi_0 = \phi_L \\ \phi_{N_x-1} = \phi_R \end{cases} \tag{2.105}$$

With this purpose, we test the algorithm with data

$$\zeta_i^n = -\frac{1}{6}x_i^3 \tag{2.106}$$

to see whether it converges or not when $k \to \infty$, and, if so, compare this solution with the monodomain's $\phi^\star$. The other parameters of the problem are $\phi_L = 0$, $\phi_R = -0.5$, $\mu = 3$, $\Delta x = 0.05$, $\Delta z = 2.5 \times 10^{-5}$, the domain is $\Omega =]0, 1[$, and the interface is located at $x_0 = 0.4$.

Figure 2.3 (top image) shows the estimation of the L^2 norm of $\phi_i^{n,k} - \phi_i^\star$ as a function of k. Clearly the algorithm diverges. To fix this situation let us notice that, in the limit, the reconstructed solution satisfies

$$\frac{1}{2}(\phi_l^n + \phi_{l-1}^n) - \phi_{l-1}^n\Delta z = \frac{1}{2}(3\phi_l^n - \phi_{l+1}^n) - \phi_l^n\Delta z \tag{2.107}$$

which can be rewritten as

$$\begin{aligned} \frac{\phi_l^n - \phi_{l-1}^n}{\Delta x} + 2\frac{\Delta z}{\Delta x}\phi_{l-1}^n = \frac{\phi_{l+1}^n - \phi_l^n}{\Delta x} + 2\frac{\Delta z}{\Delta x}\phi_l^n \\ +3\Delta x T(D_x^+\zeta_l^n) - 2\frac{(D_x^+\zeta_l^n - D_x^+\zeta_{l-1}^n)}{\Delta x}\Delta z \end{aligned} \tag{2.108}$$

and defined as coupling conditions

$$\begin{aligned}\frac{\phi_{l,1}^{n}-\phi_{l-1,1}^{n}}{\Delta x}+2\frac{\Delta z}{\Delta x}\phi_{l-1,1}^{n}=&\frac{\phi_{l+1,2}^{n}-\phi_{l,2}^{n}}{\Delta x}+2\frac{\Delta z}{\Delta x}\phi_{l,2}^{n}\\&+3\Delta xT(D_x^+\zeta_l^n)-2\frac{(D_x^+\zeta_l^n-D_x^+\zeta_{l-1}^n)}{\Delta x}\Delta z\end{aligned}\tag{2.109}$$

Using (2.109) instead of (2.108) in the algorithm of eq. (2.102) and eq. (2.103), the convergence results are shown in Figure 2.3 (bottom image). Now the algorithm converges after about 50 iterations. However, although small, the difference with the monodomain solution does not reduce to machine-zero values, but it remains close to 10^{-4} . The explanation to why the method converges now, is that the transmission condition eq. (2.109), replaced in the algorithm eq. (2.102) and eq. (2.103), also corresponds to a discrete Neumann-Dirichlet method, as was mentioned for the velocity potential Φ in section 2.3. Because we chose the length of the domains $L_1 = 0.4$ and $L_2 = 0.6$, we know the algorithm converges [46]. However, one must notice that eq. (2.109) contains terms of size $O(\Delta x, \Delta z/\Delta x)$ that are indeed small, but, at the discrete level, do not allow to recover the exact monodomain solution [46].

These results show that the proposed method of depth-averaged coupling conditions can define a convergent domain decomposition method after some manipulations, but in this case, the limit does not respect the exact solution at the discrete level, which was an important feature of the original domain decomposition method. This is due to small terms that are propagated through the steps of the derivation.

2.5.2 Heterogeneous case: dB-dSV coupling

In the dB-dSV we impose $\phi_{i,2}^n = D_t^+V_i^n + D_x\zeta_i^n = 0$ for $i \geq l+1$, to have the SV equations in that part of the domain, which means that an iterative algorithm is not necessary anymore. Using the derived coupling conditions in the Neumann form of eq. (2.109), we now have

$$\begin{cases}(1+\nu T)\phi_{i,1}^n=\nu TD_x^+\zeta_i^n\\ \phi_{0,1}^n=\phi_{Left}\\ \dfrac{\phi_{l,1}^{n}-\phi_{l-1,1}^{n}}{\Delta x}+2\dfrac{\Delta z}{\Delta x}\phi_{l-1,1}^{n}=\\ \qquad 3\Delta xT(D_x^+\zeta_l^n)-2\dfrac{(D_x^+\zeta_l^n-D_x^+\zeta_{l-1}^n)}{\Delta x}\Delta z\\ \phi_{l,1}^n=\phi_{l,2}^n\end{cases}\tag{2.110}$$

One can notice that the third line of (2.110) satisfies

$$\frac{\phi_{l,1}^{n}-\phi_{l-1,1}^{n}}{\Delta x}=\frac{\phi_{l+1,2}^{n}-\phi_{l,2}^{n}}{\Delta x}+O(\Delta x)\tag{2.111}$$

but from the dSV equation

$$\phi_{l+1,2}^n=0$$

and with the Dirichlet boundary condition, last line in eq. (2.110), we arrive to

$$\phi_{l,1}^n=\frac{1}{2}\phi_{l-1,1}^n+O(\Delta x)\tag{2.112}$$

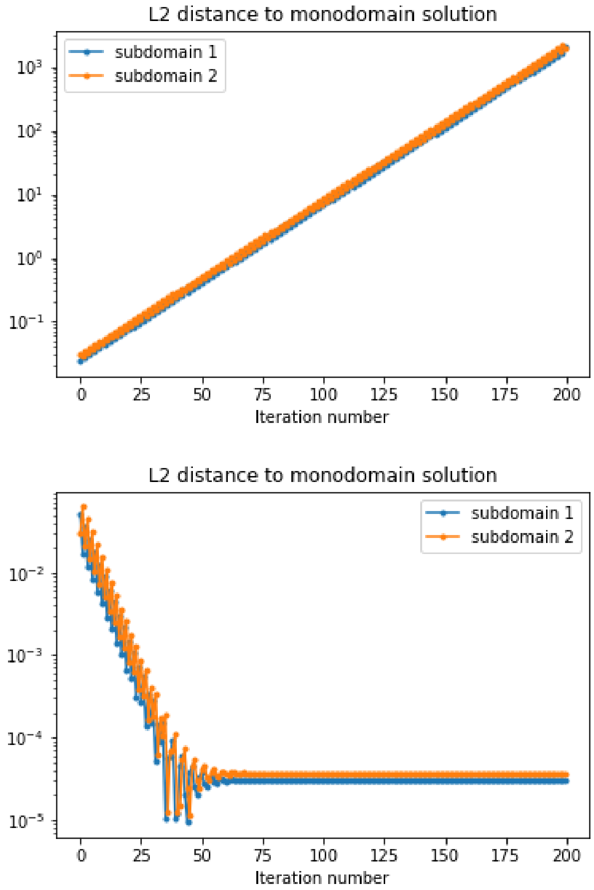

Figure 2.3: L^2 distance to monodomain of the solution on each subdomain as a function of the iteration number when using (2.108) and (2.109) respectively.

for $\Delta z = O(\Delta x^2)$. Through this formula, we can interpret the transmission condition as a kind of smoother transition from nonzero ϕ to zero ϕ across the interface. In particular, this is made through a linear interpolation in the following sequence:

$$\begin{array}{cccc} \text{Node } i\text{:} & l-1 & l & l+1 \\ \text{Value } \phi_i^n\text{:} & \phi_{l-1,1}^n, & \frac{1}{2}\phi_{l-1,1}^n + O(\Delta x^2), & 0 \end{array} \tag{2.113}$$

To test this heterogeneous DDM we propagate a solitary wave

$$\begin{aligned} \zeta(x,t) &= sech^2(x - t + x_0) \\ V(x,t) &= \zeta(t,x)/(1+\varepsilon\zeta(x,t)) \end{aligned} \tag{2.114}$$

and modify the source terms of the equation so that it is an exact solution at the continuous level. Here the parameters are $x_0 = -3$, $\varepsilon = 0.2$, the domain is $(x,t) \in]-11,11[\times]-3,3[$, and the interface is located at $x = 0$.

The idea of adding this (commonly known as) manufactured solution is that any disturbances on the wave profile will be due to the coupling conditions. Figure 2.4 shows the results for different mesh sizes and instants. It is clear that once the wave crosses the interface mesh-dependent variations of the free-surface propagate on both sides of the interface in an anti-symmetrical fashion. Moreover, the amplitude of these waves increases as the mesh is refined, but the model does not exhibit any instabilities this far. This is similar to the results reported by [70] and calls for a more detailed inspection and analysis of the artifacts that appear at the continuous and discrete levels.

2.6 Conclusions

In this chapter we have derived coupling conditions for coupling Boussinesq with Boussinesq equations (B-B), or Boussinesq with Saint-Venant equations (B-SV) in the linear case. The derivation started from the linear discrete ZCS equations, for which coupling conditions for domain decomposition were proposed, based on the Dirichlet-to-Neumann domain decomposition method for the elliptic part of the problem that exactly preserves the monodomain solution at the discrete level. Then, the derivation consisted on repeating the same steps of the derivation of Boussinesq-type models on these Neumann-Dirichlet conditions. We found that indeed such a task is possible, and that the performance of the new coupling conditions is different in the B-B case than in the B-SV case. In the B-B coupling we found that the resulting conditions also corresponded to Dirichlet-to-Neumann on the elliptic part of the B model, but the preservation of the exact solution at the discrete level was lost due to small $O(\Delta x)$ terms, although the difference was small. This was attributed to small terms that were propagated throughout the steps of the derivation. In the B-SV case we found that the coupling conditions induce a smoother transition of the elliptic variable across the interface plus $O(\Delta x)$ terms. However, the numerical experiments display a mesh-dependent artifact that propagates in both directions from the interface with larger amplitudes on smaller mesh sizes. The computations do not show instabilities.

The previous results suggest further analysis of the coupling conditions, in order to identify the source of these artifacts and possible solutions. Since these

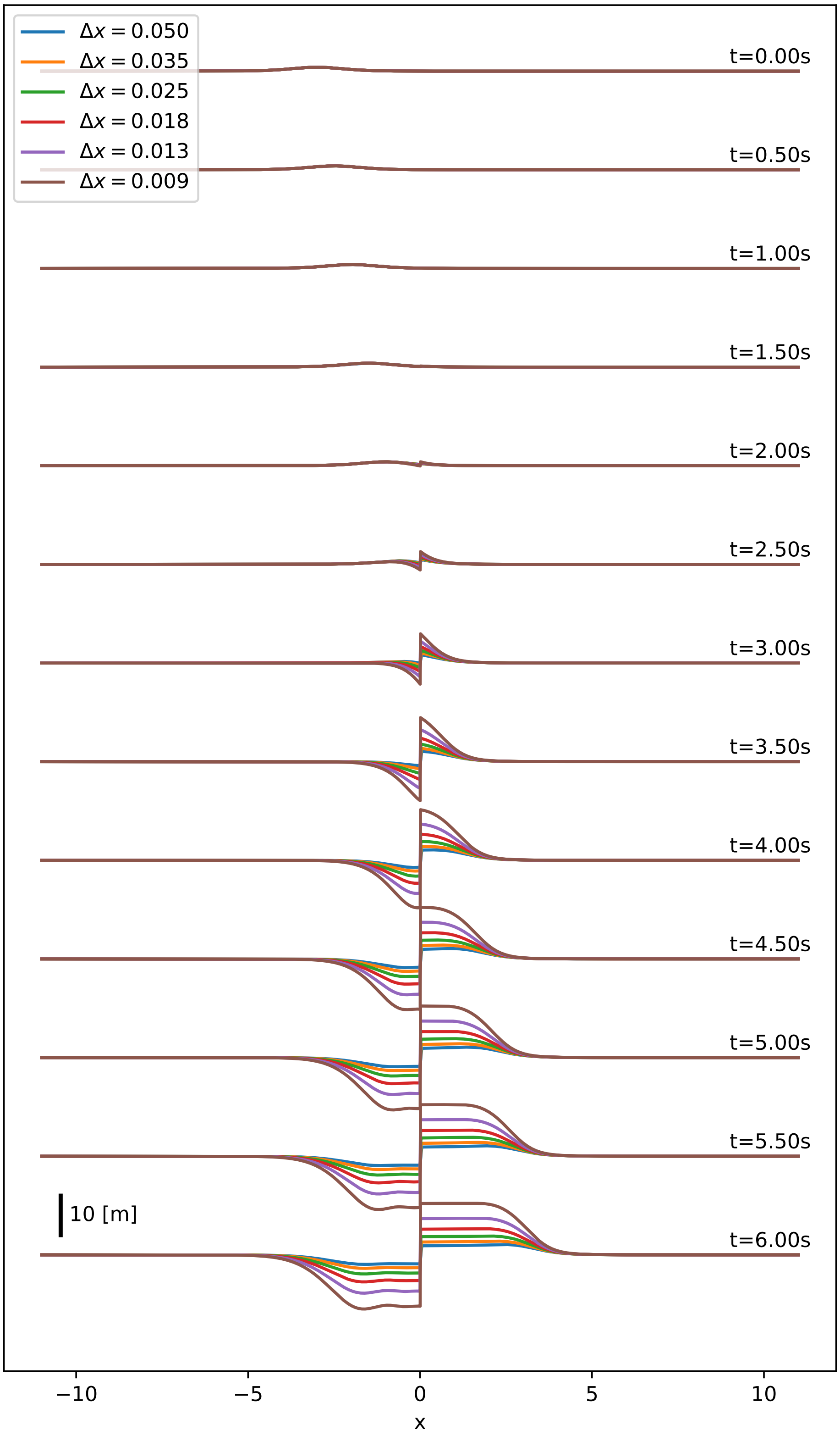

Figure 2.4: Free surface of the manufactured solitary wave computed with the new coupling conditions. The Boussinesq model is used in $x < 0$, and the Saint-Venant model on $x > 0$. Results are shown at different instants and mesh sizes.

artifacts have also been observed in the literature [70] we postpone the analysis of the method herein proposed for now. Instead, next Chapter 3 studies with an example how the 3D (expensive) model can be used to understand the precision of a coupled model, and a particular higher-order model of an averaged equation that, contrary to the BT models, does not require additional computational cost nor complexity. Then, in Chapter 8 we retake the conversation about the artifacts in coupled models, like those observed in here, but using the hybrid and other coupled models including nonlinear terms. There we identify strong numerical evidence that support more specific hypothesis about their source and characteristics.

Chapter 3

Evaluating the accuracy of a coupled model: a 1D/2D improved dimensionally heterogeneous case

As was stated in Chapter 1, the reference solution one should aim to use to evaluate the performance of the coupled phase-resolving models is the "expensive (3D) model". Examples of such models are the free-surface Euler or Navier stokes equations. The goal of this chapter is to study with a specific example how this expensive model can be used to measure the accuracy of the coupled model. With this purpose in mind, we build upon a simple model, derived by Tayachi et al. [112] for coupling 1D with 2D equations, and we report some results that we obtained that allowed us to obtain an improved version of the 1D model that has higher order accuracy at practically no additional cost. We also are interested in understanding the effect that this improved equation that we derived has on the overall accuracy of the coupled model.

The target 2D model to approximate is given by the following elliptic boundary value problem

$$\begin{cases} -(\partial_x^2 u + \partial_z^2 u) = F \text{ in } \Omega \\ \partial_n u = 0 \text{ in } \Gamma_T \\ \partial_n u + \kappa u = 0 \text{ in } \Gamma_B \\ u(x,z) = \gamma_1(x,z) \text{ in } \Gamma_L \\ u(x,z) = \gamma_2(x,z) \text{ in } \Gamma_R \end{cases} \tag{3.1}$$

where $\Omega \subset \mathbb{R}^2$, and Γ_T, Γ_B, Γ_L and Γ_R are a partition of $\partial\Omega$, standing respectively for the top, bottom, left and right boundaries, as depicted in figure Figure 3.1; $F(x,z)$ is a known source term ; and $\gamma_1(x,z)$, $\gamma_2(x,z)$ are used to impose Dirichlet boundary conditions on Γ_L and Γ_R.

To make sense of this problem as a 1D/2D dimensionally heterogeneous problem let us assume that the leftmost part of the domain is a rectangle of dimensions $L \times H$, *i.e.*, $\Omega \cap \{x < L\} =]0, L[\times]0, H[$ (see Figure 3.2), as depicted in Equation (3.3). The idea is to take advantage of this configuration by splitting the domain into

$$\Omega_{1D} =]0, L_1[\times]0, H[, \quad \Omega_{2D} = \Omega \cap \{x > L_1\} \tag{3.2}$$

with $L_1 < L$, and then approximating the original solution $u(x, z)$ by $u_1(x)$ and $u_{2D}(x, z)$, with

$$u_1(x) : \Omega'_{1D} = [0, L_1] \mapsto \mathbb{R}$$

obtained from a problem with reduced dimension (1D) and

$$u_{2D}(x, z) : \Omega_{2D} \mapsto \mathbb{R}$$

solved with the same equations and corresponding boundary conditions as (3.1). To be able to perform this simplification the key assumption is that the rectangle is very narrow, *i.e.*,

$$\varepsilon = \frac{H}{L} \ll 1$$

This idea was proposed and studied by Tayachi et al. in [112], where the following 1D model was derived

$$\begin{cases} -u_1''(x) + \dfrac{\kappa}{H} u_1(x, 0) = \overline{F}, \quad x \in \Omega'_{1D} \\ u_1(0) = \overline{\gamma_1(0, \cdot)} \end{cases} \tag{3.3}$$

with

$$\overline{F}(x) = \frac{1}{H} \int_0^H F(x, z) dz, x \in \Omega'_{1D} \tag{3.4}$$

Tayachi et al. shown that the first equation of (3.3) was consistent at $O(\varepsilon^2)$ with the 2D equation (3.1). Moreover, they showed that the relative size of the slack in Ω_{2D} was important, with the slack measured by $(L - L_1)/L$. Also, to couple (3.3) and (3.1) the researchers looked for coupling conditions that would ensure the conservation of the averaged values and derivatives:

$$\begin{aligned} \overline{u}_1(L_1) &= \overline{u}_2(L_1) \\ \partial_x \overline{u}_1(L_1) &= \partial_x \overline{u}_2(L_1) \end{aligned} \tag{3.5}$$

which was finally implemented with the Robin boundary conditions

$$\begin{aligned} (\partial_x + \lambda) u_1(L_1) &= (\partial_x + \lambda) \overline{u}_2(L_1) \\ (-\partial_x + \lambda) u_2(L_1, z) &= (-\partial_x + \lambda) \overline{u}_1(L_1) \quad z \in]0, H[\end{aligned} \tag{3.6}$$

using a multiplicative Schwarz iterative scheme[1]. With this scheme, it was shown in [112], among other observations, that the solution of the coupled model is $O(\varepsilon^2)$ accurate in $x > L_1$, that the slack $x \in [L - L_1, L]$ can be necessary, and that the iterative Schwarz used to discretize it can converge in 2 iterations for a specific choice of λ.

In the present work we have derived an improved equation that is consistent at $O(\varepsilon^4)$ with (3.1). This equation can be written as

---

[1] This scheme will be introduced in Section 3.2

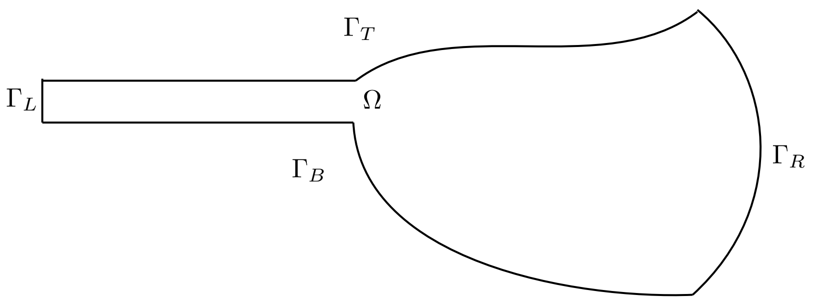

Figure 3.1: Diagram depicting the domain Ω and its boundaries Γ_T, Γ_R, Γ_B and Γ_L.

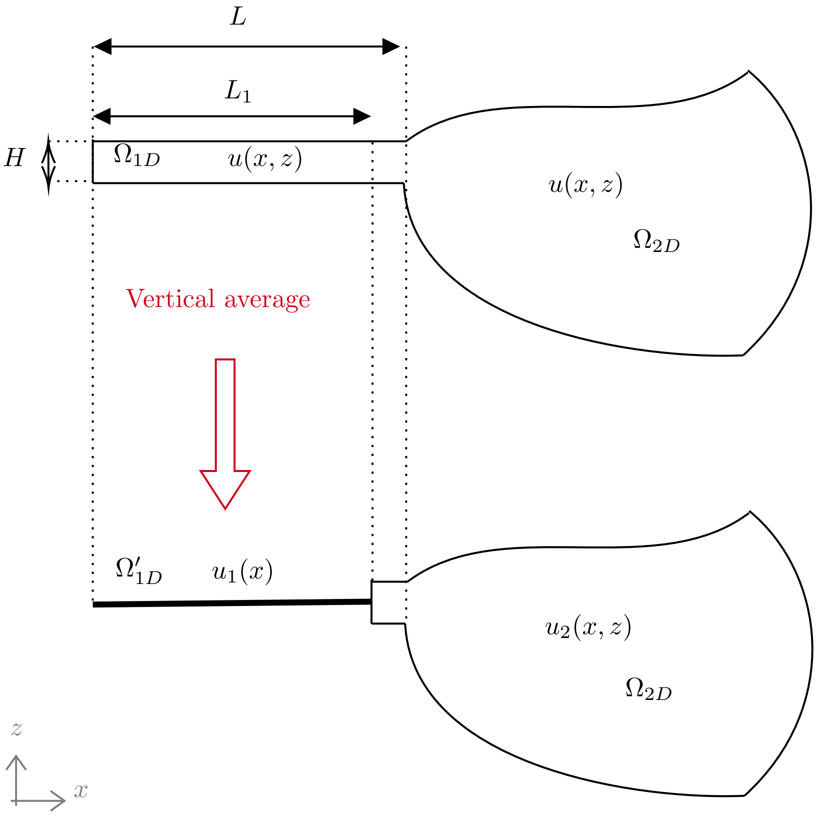

Figure 3.2: Representation of the vertical averaging performed to solve $u_1(x)$ and $u_2(x,z)$ on each sudomain, instead of $u(x,z)$ in the whole domain.

$$- u'' + \frac{\kappa^\star}{H} u = \overline{F}^\star \tag{3.7}$$

where

$$\begin{aligned} \kappa^\star &= \left(1 + \frac{1}{3}\kappa L\right)^{-1} \kappa \\ \overline{F}^\star &= \left(1 + \frac{1}{3}\kappa L\right)^{-1} \left(\overline{F} + \frac{\kappa}{H}\overline{\mathcal{F}}\right) \\ \overline{\mathcal{F}}(x) &= \frac{1}{H} \int_0^H \int_0^z \int_s^H F(x,z')dz'dsdz \end{aligned} \tag{3.8}$$

and is coupled with (3.1) in Ω_{2D} using the same coupling conditions (3.6). This enhanced model has the advantage that it satisfies the same underlying differential equation, with modifications in F and κ achieved through straightforward transformations of the original data (Eq. (3.8)). This means that the increase from second to fourth order accuracy in the truncation error is obtained with minimal to none increase in complexity and computational cost.

Section 3.1 presents the derivation of the models. Section 3.2 presents the new coupled model and a domain-decomposition method used to solve it. Then, in Section 3.3, error estimates for the new model are derived, demonstrating that it is $O(\varepsilon^4)$ accurate, which is at a higher rate than the $O(\varepsilon^2)$ obtained in [112]. Section 3.4 shows numerical experiments that verify that the error is indeed improved with the new model in all cases, however, the $O(\varepsilon^2)$ model can reach higher convergence rates in some situations too. Finally, Section 3.5 shows the conclusions and ideas to continue this research.

3.1 Model derivation for the infinite strip

Let us assume in this section that $\Omega = \mathbb{R}\times]0,H[$, the infinite strip of height H, and adimensionalize the equation (3.1) by applying the change of variables [25]

$$\begin{aligned} &\widetilde{u} = u/U \quad \widetilde{x} = x/L \\ &\widetilde{z} = z/H \quad \widetilde{F} = \frac{L^2}{U}F \\ &\widetilde{\kappa} = \frac{L^2}{H}\kappa \end{aligned} \tag{3.9}$$

so $\Omega = \mathbb{R}\times]0,1[$, and L, U are scaling factors for the horizontal direction and u . After dropping the tildes, problem (3.1) becomes

$$\begin{cases} -(\varepsilon^2\partial_x^2 u + \partial_z^2 u) = \varepsilon^2 F \text{ in } \Omega \\ \partial_z u = 0 \text{ at } z = 1 \\ -\partial_z u + \varepsilon^2 \kappa u = 0 \text{ at } z = 0 \\ u = \gamma_1/U \text{ at } x = 0 \end{cases} \tag{3.10}$$

where $\varepsilon = H/L$ is the narrowness parameter of the problem.

Integrating equation (3.10) from $z = 0$ to $z = 1$

$$- \left(\varepsilon^2\partial_x^2\overline{u}(x) + \partial_z u(x,1) - \partial_z u(x,0)\right) = \varepsilon^2\overline{F}(x), \quad \text{in } \mathbb{R} \tag{3.11}$$

and using the boundary conditions at $z = 1$ and $z = 0$ in (3.10)

$$-\overline{u}''(x) + \kappa u(x, 0) = \overline{F}(x) \text{ in } \mathbb{R} \tag{3.12}$$

Equation (3.12) is the exact equation satisfied by $\overline{u}$, describing how the averaged value is affected by the bottom trace and bounary condition term $\kappa u(x, 0)$ and the source terms $\overline{F}$.

Remark 3.1. *As in the derivation of the Saint-Venant or Boussinesq equations, the depth-averaged model transforms boundary conditions in Γ_B and Γ_T into terms of the equation itself. In the current case this corresponds to the term $\kappa u(x, 0)$ in* (3.12)

However, as it is written right now, equation (3.12) cannot be solved unless also $u(x, 0)$ is known. The derivation of the asymptotic equations is done as was done for the Boussinesq-type models [15, 77] in Chapter 2. It consists in expressing $u(x, 0)$ in terms of $\overline{u}$ by expanding the vertical variations in a power series of ε

$$u = u_0 + \varepsilon^2 u_1 + \varepsilon^4 u_2 + O(\varepsilon^6) \tag{3.13}$$

which at second order is simply

$$u(x, z) = u_0(x, z) + O(\varepsilon^2) \tag{3.14}$$

Substituting this expression back into (3.10) and discarding $O(\varepsilon^2)$ terms leads to the problem

$$\begin{aligned} \partial_z^2 u_0 &= 0 \text{ for } z \in (0, 1) \\ \partial_z u_0 &= 0 \text{ at } z = 1 \\ -\partial_z u_0 &= 0 \text{ at } z = 0 \\ u_0 &= \gamma_1 / U \text{ at } x = 0 \end{aligned} \tag{3.15}$$

whose solution can be written as $u_0(x, z) = u_0(x, 0)$. Discarding $O(varepsilon^2)$ terms, the second order approximation is

$$u(x, z) = u_0(x, 0) + O(\varepsilon^2) = u(x, 0) + O(\varepsilon^2) = \overline{u}(x) + O(\varepsilon^2) \tag{3.16}$$

because it is constant in the vertical direction. Substituting back into (3.12) results in the second order model in dimensionless form

$$-\bar{u}'' + \kappa \bar{u} = \bar{F} \text{ in } \mathbb{R} \tag{3.17}$$

At the next (fourth) order we can substitute $u = u_0 + \varepsilon^2 u_1 + O(\varepsilon^4)$ into the adimensionalized equations (3.10) and discard $O(\varepsilon^4)$ terms to obtain the problem for $u_1(x, \cdot)$:

$$\begin{aligned} -\partial_z^2 u_1(x, \cdot) &= \partial_x^2 u_0 + F \text{ in } \mathbb{R} \\ \partial_z u_1(x, 1) &= 0 \\ \partial_z u_1(x, 0) &= -\kappa u_0(x, 0) \end{aligned} \tag{3.18}$$

Integrating the first equation in (3.18) from z to 1, using the fact that u_0 does not depend on z, and the boundary condition at $z = 1$ we obtain

$$\begin{aligned} \partial_z u_1(x,z) - \partial_z u_1(x,1) &= \partial_x^2 u_0(x,0)(1-z) + \int_z^1 F(x,dz')dz' \\ \partial_z u_1(x,z) &= \partial_x^2 u_0(x,0)(1-z) + \int_z^1 F(x,dz')dz' \end{aligned} \tag{3.19}$$

So integrating now from 0 to z and rearranging

$$u_1(x,z) = u_1(x,0) + \frac{1}{2}\partial_x^2 u_0(x,0)[1-(1-z)^2] + \int_0^z \int_s^1 F(x,z')dz'ds \tag{3.20}$$

so the fourth order expansion (3.13) is

$$u(x,z) = u_0(x,0) + \varepsilon^2 \left\{ u_1(x,0) + \frac{1}{2}\partial_x^2 u_0(x,0)[1-(1-z)^2] + \mathcal{F}(x,z) \right\} + O(\varepsilon^4) \tag{3.21}$$

with $\mathcal{F}(x,z) = \int_0^z \int_s^1 F(x,z')dz'ds$. We can evaluate this expresion at $z = 0$ to obtain

$$u(x,0) = u_0(x,0) + \varepsilon^2 u_1(x,0) + O(\varepsilon^4) \tag{3.22}$$

which in turn means that

$$u_0(x,0) + \varepsilon^2 u_1(x,0) = u(x,0) + O(\varepsilon^4) \tag{3.23}$$

and replaced back into (3.21) results in

$$u(x,z) = u(x,0) + \varepsilon^2 \left(\frac{1}{2}\partial_x^2 u_0(x,0)[1-(1-z)^2] + \mathcal{F}(x,z) \right) + O(\varepsilon^4) \tag{3.24}$$

Now we can take the average of (3.24) as

$$\overline{u}(x) = u(x,0) + \varepsilon^2 \left\{ \frac{1}{2}\partial_x^2 u_0(x,0)[(1 - \int_0^1 (1-z)^2)dz] + \overline{\mathcal{F}}(x) \right\} + O(\varepsilon^4) \tag{3.25}$$

but $\int_0^1 (1-z)^2 dz = 1/3$ so

$$\overline{u}(x) = u(x,0) + \varepsilon^2 \left\{ \frac{1}{3}\partial_x^2 u(x,0) + \overline{\mathcal{F}}(x) \right\} + O(\varepsilon^4) \tag{3.26}$$

now, because of the second order asymptotic expansion (3.16) we have that

$$\begin{aligned} \varepsilon^2 \partial_x^2 u_0(x,0) &= \varepsilon^2 \partial_x^2 (\overline{u}(x) + O(\varepsilon^2)) \\ &= \varepsilon^2 \overline{u}''(x) + O(\varepsilon^4) \end{aligned} \tag{3.27}$$

so we obtain

$$\overline{u}(x) = u(x,0) + \varepsilon^2 \left\{ \frac{1}{3}\overline{u}''(x) + \overline{\mathcal{F}}(x) \right\} + O(\varepsilon^4) \tag{3.28}$$

from where it is easy to isolate $u(x,0)$ as

$$u(x,0) = \overline{u}(x) - \varepsilon^2 \left\{ \frac{1}{3}\overline{u}''(x) + \overline{\mathcal{F}}(x) \right\} + O(\varepsilon^4) \tag{3.29}$$

we can plug this back into (3.12) and re arrange as:

$$-\partial_x^2\overline{u}+\kappa\left(\overline{u}(x,z)-\varepsilon^2\left\{\frac{1}{3}\overline{u}''(x)+\overline{\mathcal{F}}(x)\right\}\right)=\overline{F}+O(\varepsilon^4) \tag{3.30}$$

$$-\left(1+\frac{1}{3}\kappa\varepsilon^2\right)\partial_x^2\overline{u}+\kappa\overline{u}=\kappa\varepsilon^2\overline{\mathcal{F}}+\overline{F}+O(\varepsilon^4) \tag{3.31}$$

so the fourth order equation can be written as

$$-\left(1+\frac{1}{3}\kappa\varepsilon^2\right)\overline{u}''+\kappa\overline{u}=\kappa\varepsilon^2\overline{\mathcal{F}}+\overline{F} \tag{3.32}$$

For the sake of completeness, we can rewrite the asymptotic expansion (3.24) in terms of $\overline{u}$ only, by substituting (3.29) into (3.24) and using (3.27), as

$$\begin{aligned}u(x,z)&=\overline{u}(x)-\varepsilon^2\left(\frac{1}{3}\overline{u}''(x)+\overline{\mathcal{F}}(x)\right)\\&\quad+\varepsilon^2\left\{\frac{1}{2}\overline{u}''(x)[1-(1-z)^2]+\mathcal{F}(x,z)\right\}+O(\varepsilon^4)\\&=\overline{u}(x)+\frac{\varepsilon^2}{2}\overline{u}''(x)\left(\frac{1}{3}-(z-1)^2\right)+\varepsilon^2\left(\mathcal{F}(x,z)-\overline{\mathcal{F}}(x)\right)+O(\varepsilon^4)\end{aligned} \tag{3.33}$$

Equation (3.33) is now written as the vertical average $\overline{u}$ plus $O(\varepsilon^2)$, zero-average fluctuations of u across z due to internal and external effects.

One can recover both expressions (3.32) and (3.33) in variables with dimensions. For (3.32), because of the double integral in $\tilde{\mathcal{F}}$:

$$\overline{\tilde{\mathcal{F}}}(x,z)=\frac{L^2}{U}\frac{1}{H^2}\overline{\mathcal{F}}(x,z) \tag{3.34}$$

substituting this into equation (3.32) we derive the fourth order equation as

$$-\left(1+\frac{1}{3}\varepsilon^2\tilde{\kappa}\right)\overline{u}+\tilde{\kappa}\overline{\tilde{u}}''=\tilde{\kappa}\varepsilon^2\overline{\tilde{\mathcal{F}}}+\overline{\tilde{F}} \tag{3.35}$$

$$-\left(1+\frac{1}{3}\frac{H^2}{L^2}\frac{L^2}{H}\kappa\right)\frac{L^2}{U}\overline{u}''+\frac{L^2}{H}\kappa\frac{1}{U}\overline{u}=\frac{L^2}{H}\kappa\frac{H^2}{L^2}\frac{L^2}{U}\frac{1}{H^2}\overline{\mathcal{F}}+\overline{F} \tag{3.36}$$

$$-\left(1+\frac{1}{3}\kappa H\right)\overline{u}''+\frac{\kappa}{H}\overline{u}=\frac{\kappa}{H}\overline{\mathcal{F}}+\overline{F} \tag{3.37}$$

recalling that

$$\overline{\mathcal{F}}(x)=\frac{1}{H}\int_0^H\int_0^z\int_s^H F(x,z')dz'dsdz \tag{3.38}$$

To simplify the equation one let us denote

$$\begin{aligned}\kappa^\star&=\left(1+\frac{1}{3}\kappa H\right)^{-1}\kappa\\\overline{F}^\star&=\left(1+\frac{1}{3}\kappa H\right)^{-1}\left(\overline{F}+\frac{\kappa}{H}\overline{\mathcal{F}}\right)\end{aligned} \tag{3.39}$$

then fourth-order equation (3.37) can be written as

$$-\overline{u}'' + \frac{\kappa^\star}{H}\overline{u} = F^\star \tag{3.40}$$

and if one had repeated the same process with the second order equation, it becomes

$$-\overline{u}'' + \frac{\kappa}{H}\overline{u} = F \tag{3.41}$$

which means that one can obtain a higher-order equation by solving the same equation and simply transforming the data κ and F.

3.2 The new coupled model

Going back now to the case where $\Omega \cap \{x < L\} =]0, L[\times]0, H[$, the fourth order coupled problem consists in finding functions $\overline{u}_1$ and u_2 such that

$$\left\{ \begin{aligned} -\frac{d^2}{dx^2}\overline{u}_1 + \frac{\kappa^\star}{H}\overline{u}_1 &= \overline{F}^\star \text{ in }]0, L_1[\\ \overline{u}_1(0) &= \overline{\gamma_1} \\ \frac{d}{dx}\overline{u}_1(L_1) + \lambda\overline{u}_1(L_1) &= \gamma_{21} \\ \\ -(\partial_x^2 u_2 + \partial_z^2 u_2) &= F \text{ in } \Omega_2 \\ \partial_n u_2 &= 0 \text{ on } \Gamma_T \\ \partial_n u_2 + \kappa u_2 &= 0 \text{ on } \Gamma_B \\ u_2(x,z) &= \gamma_2(x,z) \text{ on } \Gamma_R \\ -\partial_x u_2(L_1, z) + \lambda u_2(L_1, z) &= \gamma_{21}(z) \text{ on } \Gamma \\ \\ \gamma_{21} &= \partial_x \overline{u}_2(L_1, \cdot) + \lambda \overline{u}_2(L_1, \cdot) \\ \gamma_{12}(z) &= -\frac{d}{dx}\overline{u}_1(L_1) + \lambda\overline{u}_1(L_1) \end{aligned} \right. \tag{3.42}$$

to solve this system a multiplicative Schwarz scheme is implemented, defined by the algorithm:

$$\left\{\begin{aligned} -\frac{d^2}{dx^2}\overline{u}_1^{k+1} + \frac{\kappa^\star}{H}\overline{u}_1^{k+1} &= \overline{F}^\star \text{ in }]0, L_1[\\ \overline{u}_1^{k+1}(0) &= \overline{\gamma_1} \\ \frac{d}{dx}\overline{u}_1^{k+1}(L_1) + \lambda\overline{u}_1^{k+1}(L_1) &= \gamma_{21}^k \\ \\ -(\partial_x^2 u_2^{k+1} + \partial_z^2 u_2^{k+1}) &= F \text{ in } \Omega_2 \\ \partial_n u_2^{k+1} &= 0 \text{ on } \Gamma_T \\ \partial_n u_2^{k+1} + \kappa u_2^{k+1} &= 0 \text{ on } \Gamma_B \\ u_2^{k+1}(x,z) &= \gamma_2(x,z) \text{ on } \Gamma_R \\ -\partial_x u_2^{k+1}(L_1,z) + \lambda u_2^{k+1}(L_1,z) &= \gamma_{21}^k(z) \text{ on } \Gamma \\ \\ \gamma_{21}^k &= \partial_x \overline{u}_2^k(L_1,\cdot) + \lambda\overline{u}_2^k(L_1,\cdot) \\ \gamma_{12}^k(z) &= -\frac{d}{dx}\overline{u}_1^k(L_1) + \lambda\overline{u}_1^k(L_1) \end{aligned}\right. \tag{3.43}$$

for $k \geq 1$, and initialized with $\gamma_{21}^0 \in \mathbb{R}$ and $\gamma_{12}^0(z) = c \in \mathbb{R}$. Since the new fourth order equation is formally the same differential equation as the second order model derived by Tayachi et al. [112] and the transmission conditions are the same too, the algorithm (3.43) has the same convergence properties of those derived by Tayachi et al. in [112]. We quote without proving the following theorem and remark from reference [112], to which the reader is referred for further details

Theorem 3.1. *For each $\lambda > 0$, the sequence $(\overline{u}_1^k, u_2^k)_{k=0}^\infty$ of the Schwarz algorithm converges in $H^1(\Omega_1) \times H^1(\Omega_2)$ to $(\overline{u}_1^\lambda, u_2^\lambda)$ that satisfies constraints*

$$\overline{u}_1(L_1) = \overline{u}_2(L_1) \tag{3.44}$$

$$\frac{d}{dx}\overline{u_1}(L_1) = \partial_x \overline{u}_2(L_1) \tag{3.45}$$

Remark 3.2. *The Schwarz algorithm converges in 2 iterations if one chooses $\lambda = \lambda_{opt} = r^\star \coth(r^\star L_1)$ with $r^\star = \sqrt{\kappa^\star / L_1}$. In that case, the transmission operator*

$$\partial_x + \lambda_{opt} \tag{3.46}$$

is the exact absorbing operator of the averaged equation (3.40)

3.3 Error analysis

In this section the error of (3.42) in Ω_2 is analyzed, regarding the main question of this chapter.

Theorem 3.2. *Let $\lambda > 0$, $0 < L_1 < L$, and $(\overline{u}_1, u_2)$ be the solution to the second order coupled model* (3.42) [2]*, there exists constants $M_1(\lambda) > 0$ and*

---

[2] Obtained by replacing $\kappa^\star = \kappa$ and $F^\star = F$ on (3.42)

$M_2 > 0$, such that if $\varepsilon \to 0$ then

$$||u_{|\Omega_2} - u_2||^2_{H^1(\Omega_2)} \leq M_1(\lambda)(1+\delta^2)\frac{\varepsilon^4}{\delta^2} + M_2\varepsilon^8 \tag{3.47}$$

with $\delta = \frac{L-L_1}{L}$ the relative length of the part of Ω_2 contained in the rectangular portion of the domain.

Proof. The function $u_{|\Omega_2} - u_2$ is solution to the system

$$\begin{aligned} -\Delta(u-u_2) &= 0 \text{ in } \Omega_2 \\ \partial_n(u-u_2) &= 0 \text{ on } \Gamma_T \cap \partial\Omega_2 \\ \partial_n(u-u_2) + \kappa(u-u_2) &= 0 \text{ on } \Gamma_B \cap \partial\Omega_2 \\ u - u_2 &= 0 \text{ on } \Gamma_R \end{aligned} \tag{3.48}$$

multiplying the first equation by $u - u_2$ and using the boundary conditions on $\partial\Omega_2 - \Gamma$ we obtain

$$\int_{\Omega_2} |\nabla(u-u_2)|^2 dxdz + \int_{\Gamma_B\cap\partial\Omega_2} \kappa|u-u_2|^2 ds = \int_\Gamma \partial_n(u-u_2)(u-u_2) \tag{3.49}$$

Let $I = \int_\Gamma \partial_n(u-u_2)(u-u_2)dz$ then with $K = \max(1, 1/\kappa)$ we have

$$||u_{|\Omega_2} - u_2||^2_{H^1(\Omega_2)} \leq KI \tag{3.50}$$

so to the idea of the proof is to expand I on different terms and obtain estimates for them. Since the outer normal of Ω_2 in Γ is $n = (-1, 0)^T$, and because of the Robin boundary condition in Γ we can write I as

$$\begin{aligned} I &= \int_\Gamma -\partial_x(u-u_2)(u-u_2)dz \\ &= \int_\Gamma -\partial_x u(u-u_2) - (-u_1' + \lambda u_1 - \lambda u_2)(u-u_2)dz \\ &= \int_\Gamma -\partial_x u(u-u_2) - (-u_1' + \lambda u_1 + \lambda u - \lambda u - \lambda u_2)(u-u_2)dz \\ &= \int_\Gamma (-\partial_x u + \lambda u)(u-u_2)dz - \int_\Gamma (-u_1' + \lambda u_1)(u-u_2)dz - \lambda\int_\Gamma (u-u_2)^2 dz \\ &= A + B + C \end{aligned} \tag{3.51}$$

and we can expand A as

$$\begin{aligned} A = \int_\Gamma (-\partial_x u + \lambda u)(u-u_2)dz &= \int_\Gamma (-\partial_x u + \lambda u)(u-\overline{u})dz \\ &+ \int_\Gamma (-\partial_x u + \lambda u)(\overline{u}-u_1)dz \\ &+ \int_\Gamma (-\partial_x u + \lambda u)(u_1-u_2)dz \\ &= A_1 + A_2 + A_3 \end{aligned} \tag{3.52}$$

Let the fluctuation of u at L_1 be $v(L_1, z) = u(L_1, z) - \overline{u}(L_1)$ for $0 \leq z \leq H$. We know from its definition that

$$\begin{aligned} \int_\Gamma v dz = \int_0^H v(L_1, z) dz = 0 \\ \int_\Gamma \partial_x v dz = \int_0^H \partial_x v(L_1, z) dz = 0 \end{aligned} \tag{3.53}$$

and because of either (3.16) or (3.33) that $v = O(\varepsilon^2)$ and $\partial_x v = O(\varepsilon^2)$. We can use this to evaluate A_1

$$\begin{aligned} A_1 &= \int_\Gamma (-\partial_x u + \lambda u)(u - \overline{u}) dz \\ &= \int_\Gamma (-\overline{u}' + \lambda \overline{u} - \partial_x v + \lambda v) v dz \\ &= (-\overline{u}' + \lambda \overline{u}) \int_\Gamma v dz + \int_\Gamma (-\partial_x v + \lambda v) v dz \\ &= \int_\Gamma (-\partial_x v + \lambda v) v dz = O(\varepsilon^4) \end{aligned} \tag{3.54}$$

or more precisely, that there exists $M_1(\lambda) > 0$ and $\varepsilon_1^2 > 0$ such that for every $\varepsilon^2 \in (0, \varepsilon_1^2)$

$$|A_1| \leq M_1(\lambda) \varepsilon^4 \tag{3.55}$$

For A_2 we will just evaluate the integral since $(\overline{u} - u_1)$ does not depend on z and use as

$$\begin{aligned} A_2 &= \int_\Gamma (-\partial_x u + \lambda u)(\overline{u} - u_1) dz \\ &= H(-\overline{u}' + \lambda \overline{u})(\overline{u} - u_1) \end{aligned} \tag{3.56}$$

For A_3, because of the Robin boundary conditions we have that $\overline{u}_2(L_1) = u_1(L_1)$, so

$$\begin{aligned} A_3 &= \int_\Gamma (-u + \lambda u)(u_1 - u_2) dz \\ &= \int_\Gamma (-u + \lambda u)(\overline{u}_2 - u_2) dz \end{aligned} \tag{3.57}$$

now we can use (3.16) or (3.33) inside $\Omega_2 \cap [L_1, L]$ to write u_2 as

$$u_2 = \overline{u}_2 + v_2 \text{ in } \Omega_2 \cap [L_1, L] \tag{3.58}$$

with v_2 the fluctuation of u_2 inside the rectangle $\Omega_2 \cap [L_1, L]$, such that $\overline{v}_2 = 0$. On this case the characteristic length can be chosen as $L - L_1$ so the narrowness parameter is $\varepsilon^2 = H/(L - L_1)$. Also because of (3.33) we know that $v_2 = O(\varepsilon_2^2)$ and $\partial_x v_2 = O(\varepsilon_2^2)$. As with A_1, we can now write A_3 using the fluctuations v and v_2 as

$$\begin{aligned} A_3 &= \int_\Gamma (-\overline{u}' + \lambda \overline{u} - \partial_x v + \lambda v) v_2 dz \\ &= \int_\Gamma (-\partial_x v + \lambda v) v_2 dz \\ &= O(\varepsilon^2) O(\varepsilon_2^2) \end{aligned} \tag{3.59}$$

however $\varepsilon_2 = \varepsilon/\delta$ with $\delta = (L - L_1)/L$ the relative length of the rectangle used for the asymptotic expansion of u_2. We have deduced that

$$A_3 = O\left(\frac{\varepsilon^4}{\delta^2}\right) \tag{3.60}$$

For B we can replace and

$$B = -\int_\Gamma (-u_1' + \lambda u_1)(u - u_2) dz = -H(-u_1' + \lambda u_1)|_{x=L_1} (\overline{u} - \overline{u}_2)|_{x=L_1} \tag{3.61}$$

however $\overline{u}_2(L_1) = u_1(L_1)$ so we can write (fixing $x = L_1$)

$$\begin{aligned} B &= -H(-u_1' + \lambda u_1)(u - u_1) \\ &= -H\left[-(u_1 - \overline{u})' + \lambda(u_1 - \overline{u})\right](\overline{u} - u_1) \\ &\quad - H(-\overline{u}' + \lambda \overline{u})(\overline{u} - u_1) \\ &= B_1 + B_2 \end{aligned} \tag{3.62}$$

First let us notice that $B_2 + A_2 = 0$, while for B_1,

$$\begin{aligned} B_1 &= -H(-(u_1 - \overline{u})' + \lambda(u_1 - \overline{u}))(\overline{u} - u_1) \\ &= -H(u_1 - \overline{u})'(u_1 - \overline{u}) + H\lambda(u_1 - \overline{u})^2 \\ &= B_{1\alpha} + B_{1\beta} \end{aligned} \tag{3.63}$$

For $B_{1\beta}$ we can use that $\overline{u}_1(L_1) = \overline{u}_2(L_1)$ and the Cauchy-Schwarz to write

$$\begin{aligned} B_{1\beta} &= H\lambda(u_1 - \overline{u})^2 \\ &= H\lambda(\overline{u_2} - \overline{u})^2 \\ &= \frac{H\lambda}{H^2}\left(\int_\Gamma \overline{u}_2 - \overline{u}\right)^2 \\ &\leq \frac{\lambda}{H}\int_0^H 1 dz \int_\Gamma (\overline{u}_2 - \overline{u})^2 dz = \lambda \int_\Gamma (\overline{u}_2 - \overline{u})^2 dz = -C \end{aligned} \tag{3.64}$$

thus $B_{1\beta} + C \leq 0$.

We can analyze $B_{1\alpha}$ by using the fourth order 1D equation (3.37) for $\overline{u}_1$ by writing it as

$$-\overline{u}_1'' + r^2\left(\overline{u}_1 - \frac{H^2}{3}\overline{u}_1'' - \overline{\mathcal{F}}\right) = \overline{F} \text{ in }]0, L_1[\tag{3.65}$$

whereas if we write the exact averaged equation (3.3) as

$$-\overline{u}'' = \overline{F} - r^2 u(x, 0) \tag{3.66}$$

and add $r^2\left(\overline{u}-\frac{H^2}{3}\overline{u}''-\overline{\mathcal{F}}\right)$ to both sides of the equation, we obtain that

$$-\overline{u}''+r^2\left(\overline{u}-\frac{H^2}{3}\overline{u}''-\overline{\mathcal{F}}\right)=\overline{F}-r^2\left(u(x,0)-\left(\overline{u}-\frac{H^2}{3}\overline{u}''-\overline{\mathcal{F}}\right)\right) \tag{3.67}$$

in $]0,L_1[$. We can now substract (3.67) from (3.65) to obtain the equation for $\overline{u}_1-\overline{u}$

$$-(\overline{u}_1-\overline{u})''+r^2\left(\overline{u}_1-\overline{u}-\frac{H^2}{3}(\overline{u}_1-\overline{u})''\right)=r^2\left(u(x,0)-\left(\overline{u}-\frac{H^2}{3}\overline{u}''-\overline{\mathcal{F}}\right)\right) \tag{3.68}$$

which in turn can be rewritten as

$$-(\overline{u}_1-\overline{u})''+\alpha r^2(\overline{u}_1-\overline{u})=\alpha r^2 R(x) \tag{3.69}$$

with $\alpha=(1+\frac{r^2H^2}{3})^{-1}$ and $R(x)=u(x,0)-\left(\overline{u}(x)-\frac{H^2}{3}\overline{u}''(x)-\overline{\mathcal{F}}(x)\right)$. We can multiply this equation by $\overline{u}_1-\overline{u}$, integrate it between 0 and L_1 and use integration by parts

$$\int_0^L(\overline{u}_1'-\overline{u}')^2dx-(\overline{u}_1'-\overline{u}')(\overline{u}_1-\overline{u})|_0^L+\alpha r^2\int_0^L(\overline{u}_1-\overline{u})^2dx=\alpha r^2\int_0^L(\overline{u}_1-\overline{u})dx \tag{3.70}$$

But because of the boundary condition at $x=0$, $\overline{u}_1(0)-\overline{u}(0)=0$, we can isolate $B_{1\alpha}$ as

$$\begin{aligned}B_{1\alpha}&=-H(u_1-\overline{u})'(u_1-\overline{u})|_{x=L_1}\\&=H\alpha r^2\int_0^L R(\overline{u}_1-\overline{u})dx-H\mathcal{Q}(\overline{u}_1-\overline{u})\\&=B_{1\alpha_1}+B_{1\alpha_2}\end{aligned} \tag{3.71}$$

with $\mathcal{Q}(\overline{u}_1-\overline{u})=\int_0^L(\overline{u}_1'-\overline{u}')^2dx+\alpha r^2\int_0^L(\overline{u}_1-\overline{u})^2dx\geq 0$ so $B_{1\alpha_2}\leq 0$. For $B_{1\alpha_1}$ we can apply the inequality

$$ab\leq\frac{a^2}{2}+\frac{b^2}{2} \tag{3.72}$$

as

$$\begin{aligned}B_{1\alpha_1}&=H\alpha r^2\int_0^L R(\overline{u}_1-\overline{u})dx\\&\leq H\alpha r^2\int_0^L\frac{R^2}{2}dx+H\alpha r^2\int_0^L\frac{(\overline{u}_1-\overline{u})^2}{2}dx\\&=B_{1\alpha_1'}+B_{1\alpha_1''}\end{aligned} \tag{3.73}$$

Because of (3.29) $R=O(\varepsilon^4)$ so $B_{1\alpha_1'}=O(\varepsilon^8)$. Also, we can add $B_{1\alpha_1''}$ and $B_{1\alpha_2}$ together to show that

$$\begin{aligned}B_{1\alpha_1''}+B_{1\alpha_2}&=H\alpha r^2\int_0^L\frac{(\overline{u}_1-\overline{u})^2}{2}dx-H\mathcal{Q}(\overline{u}_1-\overline{u})\\&=-H\int_0^L(\overline{u}_1'-\overline{u}')^2dx-\frac{H\alpha r^2}{2}\int_0^L(\overline{u}_1-\overline{u})^2\leq 0\end{aligned} \tag{3.74}$$

So far we have proved that with $K = \max(1/\kappa, 1)$

$$\begin{aligned}
||u_{|\Omega_2} - u_2||^2_{H^1(\Omega_2)} &\leq KI = K(A + B + C)\\
&\leq K(A_1 + A_2 + A_3 + B_{1\alpha_1'} + B_{1\alpha_1''}\\
&\qquad + B_{1\alpha_2} + B_{1\beta} + B_2 + C)\\
&= K(A_1 + A_3 + B_{1\alpha_1'} + (A_2 + B_2)\\
&\qquad + (B_{1\alpha_1''} + B_{1\alpha_2}) + (B_{1\beta} + C))\\
&\leq K(A_1 + A_3 + B_{1\alpha_1'})
\end{aligned} \tag{3.75}$$

since $A_2 + B_2 = 0$, $B_{1\alpha_1''} + B_{1\alpha_2} \leq 0$ and $B_{1\beta} + C < 0$. Also, $A_1 = O(\varepsilon^4)$ and $A_3 = O(\varepsilon^4/\delta^2)$ involve λ but $B_{1\alpha_1'} = O(\varepsilon^8)$ does not, so we can conclude that there exists $\varepsilon_0^2 > 0$, $M_1(\lambda) > 0$ independent of ε^2 but depending on λ, and $M_2 > 0$ independent of λ and ε^2, such that for any $\varepsilon^2 \in (0, \varepsilon_0^2)$

$$||u_{|\Omega_2} - u_2||^2_{H^1(\Omega_2)} \leq M_1(\lambda)\frac{\varepsilon^4}{\delta^2}(1 + \delta^2) + M_2\varepsilon^8 \tag{3.76}$$

□

Theorem 3.2 shows that the coupled model (3.42) provides an $O(\varepsilon^2/\delta)$ approximation of (3.1), which is greater than the $O(\varepsilon/\delta)$ estimate provided in [112]. The next section is devoted to numerical experiments that verify this observation.

3.4 Numerical experiments

In this section we show numerical results to verify and illustrate the performance of the fourth order coupled model and compare it with the second order model. All computations have been performed using the software package Freefem++ [59] using algorthm (3.43).

The test case consits in a domain made of a rectangle connected to a funnel shape as in Fig. 3.3. The domain is forced by a source term $F(x, z) = F \in \mathbb{R}$, constant in Ω, and homogeneous Dirichlet boundary conditions $\gamma_1 = \gamma_2 = 0$. The model is discretized with a P_2 finite element method to help with a faster mesh-convergence in the comparisons, using a uniform triangular mesh of size ≈ 0.005, unless stated otherwise. The geometrical parameters of the problem (depicted in figure 3.3) are: L, the length of the rectangle; L_1, the length of Ω_1; H, the height of the rectangle; and l, the horizontal length of the funnel. The only other physical parameters are F and κ.

3.4.1 Exact solution in the rectangular domain

Since the source term is constant, the solution to the second order problem (3.41) $\overline{u}_1$ can be computed explicitly at each iteration of the Schwarz algorithm as:

$$\overline{u}_1^{k+1}(x) = K_1 e^{rx} + K_2 e^{-rx} + \frac{F}{r^2} \tag{3.77}$$

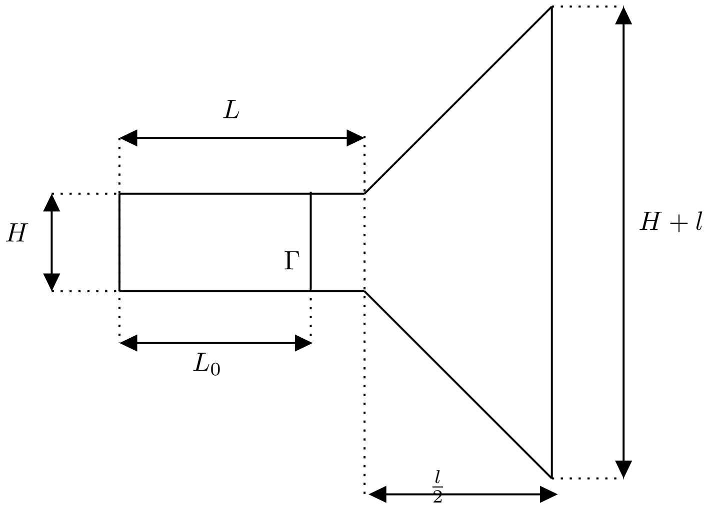

Figure 3.3: Domain configuration for numerical experiments.

where $r = \sqrt{\kappa/H}$ is the positive root of the characteristic polynomial and

$$\begin{aligned} K_1 &= \frac{\gamma_{21}^k - \frac{F}{r^2}\left(\lambda_1 e^{-rL} + \lambda - e^{-rL}\right)}{2\cosh(rL) + 2\sinh(rL)} \\ K_2 &= -K_1 - \frac{F}{r^2} \end{aligned} \tag{3.78}$$

from where we can compute $\overline{\gamma}_{12}^{k+1}$ as

$$\overline{\gamma}_{12}^{k+1} = K_1 e^{rL}(\lambda - r) + K_2 e^{-rL}(\lambda + r) + F\frac{\lambda}{r^2} \tag{3.79}$$

For the fourth order model $\overline{\gamma}_{12}$ can be computed from (3.79) by using the change of variables of equation (3.39). On this case this means that one must substitute r and F by r' and F' given by

$$\begin{aligned} r^\star &= \sqrt{\kappa^\star/H} \\ F^\star &= \alpha F + \frac{\kappa^\star}{H}\overline{\mathcal{F}} \end{aligned} \tag{3.80}$$

where $\alpha = (1 + \frac{1}{3}\kappa L)^{-1}$, $\kappa^\star = \alpha\kappa$ and we have used $\overline{F} = F$. Also

$$\mathcal{F}(x, z) = \int_0^z \int_s^H F dz' ds = \frac{1}{2}F\left(H^2 - (H - z)^2\right) \tag{3.81}$$

and

$$\overline{\mathcal{F}}(x) = \frac{1}{H}\int_0^H \mathcal{F}(x, z)dz = \frac{1}{3}H^2 F \tag{3.82}$$

from where we obtain

$$F' = \alpha F + \frac{\kappa^\star H}{3}F \tag{3.83}$$

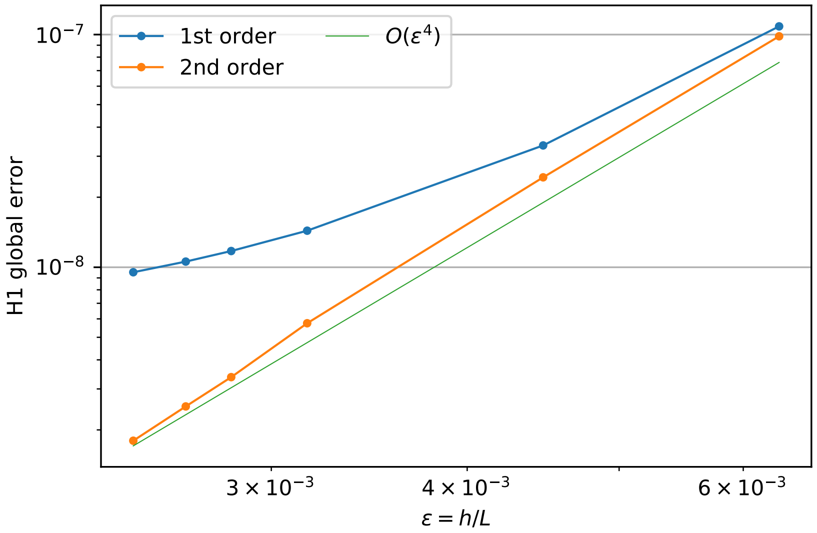

Figure 3.4: H^1 norm of $u_{|\Omega} - u_2^{\lambda}$ with λ from Remark 3.2 (page 59), $L = 2$, $L_1 = 1.5$ and $\kappa = 0.001$.

	Case 1	**Case 2**
Second order	1.65	3.8
Fourth order	4.54	4.5

Table 3.1: Convergence rates computed from the 5 first points of Figures 3.4 and 3.5 as the slope of the least-squares regression of said points.

3.4.2 Comparison varying the narrowness of the 1D domain

For the comparison we consider two cases with the same $\kappa = 0.001$, and $l = 3$ but with $L_1 = 1.5$ and $L = 2$ (Case 1); and $L_1 = 19.5$, $L = 20$ (Case 2). Figures 3.4 and 3.5 show the values of $||u_{|\Omega_2} - u_2^{\lambda}||_{H^1(\Omega_2)}$ for Case 1 and Case 2 respectively. From these results one can confirm that the error of the fourth order model is smaller than the second order model. To compare the convergence rate as $\varepsilon \to 0$ the empirical rates computed with the first 5 points of each line are displayed in Table 3.1. For both cases it is observed that the convergence rates of both models are greater than the theoretical ones. Moreover, in Case 2, the convergence rate of the second order model almost approaches the fourth order model's, which suggests that, in some cases, the use of the higher order model does not imply an improvement in the asymptotic convergence rate, although the error is still improved in magnitude. These results are complementary to the previous Theorem 3.2, suggesting that sharper estimates, involving additional interactions between l, L, L_1 and other scales, could explain these observations.

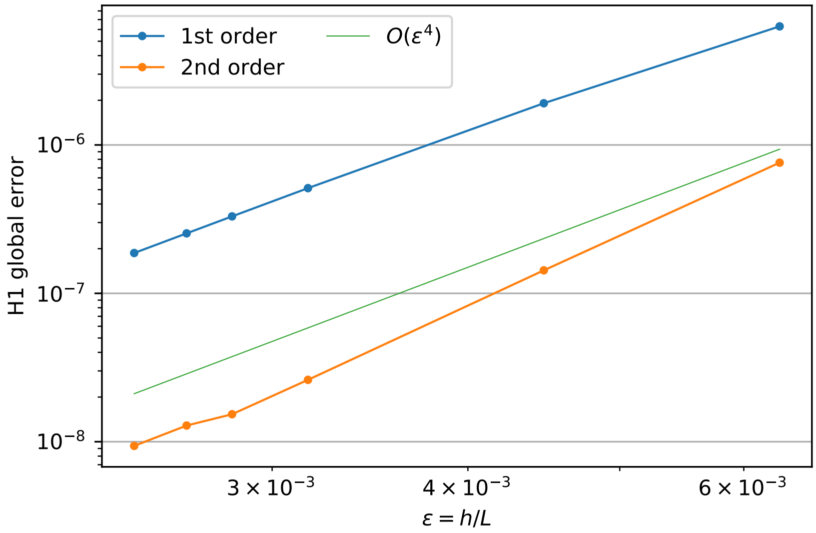

Figure 3.5: H^1 norm of $u_{|\Omega} - u_2^\lambda$ with λ from equation Remark 3.2 (page 59), $L = 20$, $L_1 = 19.5$ and $\kappa = 0.001$.

3.5 Conclusion

In this chapter, we have studied the approximation of a 2D elliptic model by employing a coupled 1D-2D model, with the aim of understanding how to use the expensive 2D model to measure the accuracy of the coupled model, and also, to discern the impact that improving the averaged equation has on the coupled model's overall precision. Building upon the work by Tayachi et al. (2014) [112], where a second-order model was derived, we derived a new 1D averaged model whose truncation error is of fourth order, $O(\varepsilon^4)$. This improvement is analogous to how Boussinesq-type models are asymptotically more accurate than the Saint-Venant model, as for example, in the derivation shown in Figure 3.2. The most prominent feature of the new 1D model is that no additional computational cost is required to compute the solution because, in fact, the differential equation is formally the same, except for a simple transformation of the problem's data. This is in contrast with Boussinesq-type equations, that are more complex and costly than the Saint-Venant equations.

The H^1 norm of the error of this model in the 2D part of the domain corroborates that the fourth-order model has indeed an $O(\varepsilon^4)$ accuracy. Moreover, in all cases studied, the numerical validation showed that the 4th order model is indeed closer to the 2D model than the 2nd order counterpart. Moreover, the numerical results showed super convergence, with convergence rates higher than those expected.

An intriguing finding from this study is that the convergence rates of the second-order model can also be very close to those of the fourth-order model, which can be counterintuitive. It hints that the 2nd order model might have a similar precision as the 4th order model in some cases, which could allow to save computational resources. This could be explained by understanding other asymptotic regimes involving scales such as the 2D domain size and the boundary condition data κ. Future studies should focus on deriving sharper error estimates using these considerations, but will not be considered on this PhD thesis.

In the next chapter we will take a different approach and present some results that were obtained directly with new and old coupled Boussinesq-type/ Saint-Venant coupled models. This will lead to the analysis of Part II, where we will resume the discussion regarding the relevance of using the 3D model as the reference solution for measuring the coupled model's accuracy.

Chapter 4

Artifacts, mesh-convergence and new coupling methods in the nonlinear regimes

4.1 Introduction

The two-way coupling of Boussinesq-type (BT) and Saint-Venant (SV) equations in the nonlinear regime is not a new endeavour. Recalling some of the facts mentioned in the introductory Chapter 1, such a coupling was first reported almost 15 years ago now in [117, 113] as a technique for computing wave breaking on phase-resolving wave models. Since then its use for wave breaking has been extensively validated [117, 118, 119, 120, 15, 114], extended to other weakly and fully nonlinear BT models [67, 38] and to 2D equations [69]. Despite its success, three important problems have been observed, namely

(I) Oscillations

(II) Instabilities

(III) Mesh-dependent solutions

The first of these problems, (I) Oscillations, was already reported in [118] and [114], in the form of small waves that were not sensitive to the mesh size and did not affect the performance of the model. However, in [38] it was reported that some oscillations on the BT-SV interface could grow as the mesh was refined while in [70], it was observed that some of these oscillations lead to either a blow up of the solution (problem II), and/or to important differences between different mesh sizes (problem III), depending on the BT model used. Moreover, it is possible to observe some of these problems with new coupling methods, such as the one introduced in Chapter 2. These observations raise fundamental questions about the reliability of the hybrid and other coupled models, among others:

(I) Oscillations: Are the short oscillations that have been reported a part of the solution or a problem of the discretization?

(II) Instabilities: What causes them? Are they coming from the continous or the discrete level? How to fix them?

(III) Mesh dependent solutions: What causes the large variations in the solution when changing the mesh size? Is it related to the instabilities?

Answering these questions is of paramount importance to ensure the efficiency and robustness of coupled depth-averaged models (BT and/or SV). This is equally valid when one seeks to couple the equations for the purpose of enhanced computational efficiency in intermediate to deep waters as it is for computing wave-breaking dynamics in the surf zone with depth-averaged models.

The main goal of this chapter is to provide numerical evidence and new hypotheses regarding problems (I) to (III), with special attention on identifying and explaining the source of the artifacts that are observed in the computations. This is done for the hybrid models and also for new coupling techniques that will be proposed. The discussion is performed around the propagation of a solitary wave on two different bathymetry profiles in 1D: the classical case of a simple beach [109] and a bathymetry of constant depth. Two BT models are tested: the weakly nonlinear BT equations of Nwogu [95], and a frequency-enhanced version of the Green-Naghdi system [15, 38]. Their discretization is done in a similar fashion as in [67, 38, 70].

This chapter is organized as follows: in Section 4.2 the wave propagation models are presented. Then, Section 4.3 introduces the discrete schemes used to integrate them, including the moving interface used for wave breaking. In Section 4.4 new coupling techniques applied to the model of Nwogu are introduced. These techniques consist in adding an artificial viscosity or an overlapping region, instead of a simple interface. Section 4.5 presents results and discussions with Nwogu's models, including how the new coupling techniques can improve the stability of Nwogu's hybrid model. Section 4.6 presents the results obtained with Green-Naghdi's model. The discussion is different, because no instabilities are observed but still a mesh-dependent solution is obtained with the variable breaking criteria. Finally, the conclusions are presented in Section 4.7.

4.2 Wave propagation models

This section introduces the two BT models that are used throughout this chapter. These are: the weakly dispersive model of Nwogu [95] and a frequency-enhanced version of the Gren-Naghdi model [80].

4.2.1 The weakly dispersive model of Nwogu

The first model considered in this chapter corresponds to the equations of Nwogu [95] written in conservative form [68] as

$$\partial_t \boldsymbol{U}^\star + \partial_x \boldsymbol{F}(\boldsymbol{U}) = \boldsymbol{S}_b + \boldsymbol{S}_d \tag{4.1}$$

where

$$\boldsymbol{U}^* = \begin{pmatrix} H \\ P \end{pmatrix}, \quad \boldsymbol{U}^a = \begin{pmatrix} H \\ Hu^a \end{pmatrix}, \qquad \boldsymbol{F}(\boldsymbol{U}^a) = \begin{pmatrix} Hu^a \\ H(u^a)^2 + \frac{1}{2}gH^2 \end{pmatrix} \tag{4.2}$$

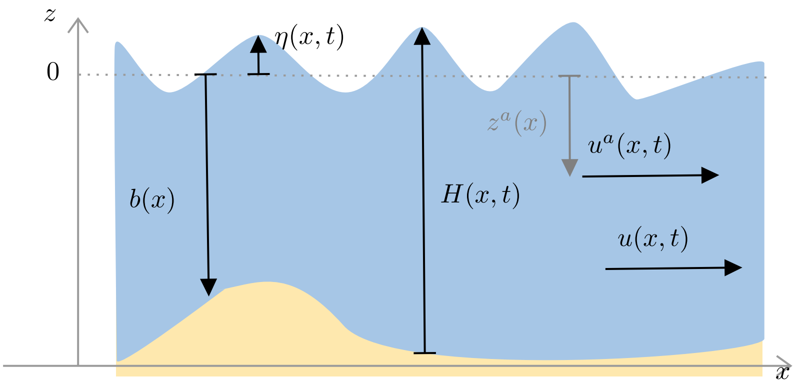

Figure 4.1: Sketch of variables: $b(x)$ is the still water depth; $\eta(x,t)$ is the free-surface elevation over the still level; $H(x,t) = b(x) + \eta(x,t)$ the total water depth; $u^a(x,t)$ is the horizontal fluid velocity at height $z^a(x)$ from the surface (negative if below the still level) used in Nwogu's model; $u(x,t)$ is the depth averaged horizontal velocity in the GN model.

As shown in Figure 4.1, x and t are the space and time coordinates; $b(x)$ is the still water depth; $\eta(x,t)$ is the free-surface elevation over the still level; $H(x,t) = b(x) + \eta(x,t)$ the total water depth; $u^a(x,t)$ is the horizontal fluid velocity at height $z^a(x)$ from the surface (negative if below the still level); $z^a(x) = \alpha b(x)$ with $\alpha = -0.531$ chosen to optimize the linear dispersion properties of the model [95]; and $P(x,t)$ an auxiliary variable containing dispersive terms, and that satisfies the elliptic problem

$$P = Hu^a + Hz^a \left(\frac{z^a}{2} \partial_x^2 u^a + \partial_x^2 (bu^a) \right) \tag{4.3}$$

The second order derivatives in P are the only dispersive terms on which the time derivative is applied. Also, the source terms for the bathymetry and the explicit part of the dispersive terms in equation (4.1) are

$$\boldsymbol{S}_b = \begin{pmatrix} 0 \\ -gH\partial_x b \end{pmatrix} \quad \boldsymbol{S}_d = \begin{pmatrix} -\psi_C \\ \psi_M - u\psi_C \end{pmatrix} \tag{4.4}$$

with $b(x)$ the elevation of the bathymetry with the same reference frame as η and

$$\begin{aligned} \psi_M &= -\partial_t H z^a \left(\frac{z^a}{2} \partial_x^2 u^a + \partial_x^2 (bu^a) \right) \\ \psi_C &= \partial_x \left[\left(\frac{(z^a)^2}{2} - \frac{b^2}{6} \right) b \partial_x^2 u^a + \left(z^a + \frac{b}{2} \right) b \partial_x^2 (bu^a) \right] \end{aligned} \tag{4.5}$$

4.2.2 The fully-nonlinear model of Green-Naghdi

The second model considered corresponds to the frequency-enhanced fully nonlinear equations of Green Naghdi [55] (GN). As in [70], these are written in the form presented in [38, 4, 15, 77] as

$$\partial_t \boldsymbol{U} + \partial_x \boldsymbol{F}(\boldsymbol{U}) = \boldsymbol{S}_b(\boldsymbol{U}) + \boldsymbol{\Phi} \tag{4.6}$$

where

$$\boldsymbol{U} = \begin{pmatrix} H \\ Hu \end{pmatrix}, \quad \boldsymbol{\Phi} = \begin{pmatrix} 0 \\ H\phi \end{pmatrix} \tag{4.7}$$

with u the depht-averaged horizontal velocity in 1D (shown in Figure 4.1, 71) and ϕ satisfies

$$\phi + \alpha \mathcal{T}(\phi) = \mathcal{T}(w) - \mathcal{Q} \tag{4.8}$$

with $w = g\partial_x(H + b)$, and $\mathcal{T}$ is a linear elliptic operator with the self-adjoint form [4]

$$\mathcal{T}(\cdot) = S_1^*(HS_1(\cdot)) + S_2^*(HS_2(\cdot)), \tag{4.9}$$

that in 1D can be written as

$$S_1(\cdot) = \frac{H}{\sqrt{3}}\partial_x(\cdot) - \frac{\sqrt{3}}{2}\partial_x b(\cdot), \quad S_2(\cdot) = -\frac{1}{2}\partial_x b(\cdot). \tag{4.10}$$

and the quadratic term $\mathcal{Q}$ in (4.8) is given by

$$\begin{aligned} \mathcal{Q} = {} & 2H\partial_x H(\partial_x u)^2 + \frac{4H^2}{3}\partial_x u \partial_x^2 u + H\partial_x b(\partial_x u)^2 + H\partial_x^2 b u \partial_x u \\ & + \left[\partial_x^2 b \partial_x H + \frac{1}{2}\partial_x^2 H + \partial_x b \partial_x^2 b\right] u^2 \end{aligned} \tag{4.11}$$

As shown in [80], choosing $\alpha = 1.159$ optimizes the error of the linear dispersion relation.

4.3 Discretization

Writing the equations in the form $\boldsymbol{U}' = \mathcal{N}\boldsymbol{U}$ the integration in time is done with the first order forward Euler scheme

$$\boldsymbol{U}^{n+1} = \boldsymbol{U}^n + \Delta t \mathcal{N} \boldsymbol{U}^n \tag{4.12}$$

or with the third order stability-preserving Runge-Kutta scheme [54]

$$\begin{aligned} \boldsymbol{U}^{(1)} &= \boldsymbol{U}^n + \Delta t \mathcal{N} \boldsymbol{U}^n \\ \boldsymbol{U}^{(2)} &= \frac{3}{4}\boldsymbol{U}^n + \frac{1}{4}\boldsymbol{U}^{(1)} + \frac{1}{4}\mathcal{N}\boldsymbol{U}^{(1)} \\ \boldsymbol{U}^{n+1} &= \frac{1}{3}\boldsymbol{U}^n + \frac{2}{3}\boldsymbol{U}^{(2)} + \frac{2}{3}\mathcal{N}\boldsymbol{U}^{(2)} \end{aligned} \tag{4.13}$$

where $\boldsymbol{U}^n$ represents the solution at timestep n with timestep size Δt^n computed with the standard condition

$$\Delta t^n = CFL \frac{\Delta x}{\max_i(\sqrt{gH_i^n} + |u_i^n|)} \tag{4.14}$$

with $CFL \in]0, 1[$. The space discretization is done as in [70] by using a finite volume (FV) scheme in space, with a shock-capturing scheme for the hyperbolic fluxes $\boldsymbol{F}$ and bathymetry source term $\boldsymbol{S}_b$, and finite differences (FD) or finite element (FE) scheme for the dispersive terms of Nwogu's and Green-Naghdi's model respectively. The convienence of using different schemes (FD and FE) for the dispersive terms is simply to reuse the code base of the models already developed in [70]. Since the study of the questions (I) to (III) involve a mesh-convergence study of the models, the hyperbolic fluxes and time integration are approximated at first order. This choice is based on the fact that Godunov's upwind method is the simplest scheme that prevents spurious oscillations in the hyperbolic models, due to its known dissipativity and monotonicity-preserving properties [82]. Only in the case of the GN model a fourth-order scheme for $\boldsymbol{F}$ and $\boldsymbol{S}_b$ is also applied along with the third-order Runge Kutta time-integration scheme. This will be useful later in the discussion.

The FV scheme used was specifically designed to preserve steady states at rest on problems with variable bathymetries. This feature is also called the $C-$property or well-balanced property in the literature [24]. The scheme is implemented on a uniform 1D Cartesian mesh with cells $C_i = [x_{i-1/2}, x_{i+1/2}]$, for i from 1 to N_x, such that $\Delta x = |C_i|$ is constant and $\bigcup_i C_i = \overline{\Omega} = [a, b]$, with Ω the computational domain.

The overall steps to compute the solution on each timestep and for each model are depicted in Figure 4.2. In what follows the details of this scheme are recalled for the case of non-vanishing depths, *i.e.,* when there exists $H_0 > 0$ suh that $H \geq H_0$ in the whole domain and all times. Since the development of such methods is not the main focus of this work, the reader is directed to [67] for more details, in particular regarding the well-balancing properties with vanishing depths, emerging topographies, or the conservation of mass, among other properties.

4.3.1 FV spatial discretization

The FV scheme is applied by integrating the equations on $C_i \times [t^n, t^{n+1}]$, with $t^{n+1} - t^n = \Delta t$ the timestep size to obtain

$$\frac{\Delta \boldsymbol{U}_i^n}{\Delta t} = -\frac{1}{\Delta x}\left(\boldsymbol{F}_{i+1/2}^n - \boldsymbol{F}_{i-1/2}^n\right) + \frac{1}{\Delta x}\Delta \boldsymbol{S}_{bi}^n + \frac{1}{\Delta x}\overline{\boldsymbol{S}}_{di}^n \tag{4.15}$$

With $\boldsymbol{U}_i^n = \int_{C_i} \boldsymbol{U}^n dx$, the cell-average of $\boldsymbol{U}^n$ at cell C_i; $\boldsymbol{F}_{i+1/2}^n$, the numerical flux at the cell interface $i + 1/2$ and timestep n; and $\Delta \boldsymbol{S}_{bi}^n$, $\overline{\boldsymbol{S}_{di}^n}$ the numerical topography and dispersive source terms.

The fluxes $\boldsymbol{F}_{i+1/2}^n$ are evaluated by solving the Riemann problem for the left and right states of interface $i + 1/2$, $\boldsymbol{U}_{i+1/2}^L$ and $\boldsymbol{U}_{i+1/2}^R$. In the first order Godunov scheme these correspond to the upwinding

$$\boldsymbol{U}_{i+1/2}^L = \boldsymbol{U}_i^n, \quad \boldsymbol{U}_{i+1/2}^R = \boldsymbol{U}_{i+1}^n \tag{4.16}$$

The Riemann problem is solved with the solver of Roe [101]. Defining $\Delta_{i+1/2}(\cdot) = (\cdot)_{i+1/2}^R - (\cdot)_{i+1/2}^L$ and $\boldsymbol{F}_{i+1/2}^{R,L} = \boldsymbol{F}(\boldsymbol{U}_{i+1/2}^{R,L})$, results in the numerical fluxes

$$\begin{aligned}\boldsymbol{F}_{i+1/2} &= \frac{1}{2}\left(\boldsymbol{F}_{i+1/2}^R + \boldsymbol{F}_{i+1/2}^L\right) - \frac{1}{2}\left|A_{i+1/2}\right|\Delta_{i+1/2}\boldsymbol{U} \\ &= \frac{1}{2}\left(\boldsymbol{F}_{i+1/2}^R + \boldsymbol{F}_{i+1/2}^L\right) - \frac{1}{2}\left[X\left|\Lambda\right|X^{-1}\right]_{i+1/2}\Delta_{i+1/2}\boldsymbol{U}\end{aligned} \tag{4.17}$$

where $A_{i+1/2}$ is the Roe average Jacobian matrix $\frac{\partial \boldsymbol{F}(\boldsymbol{U})}{\partial \boldsymbol{U}}$, diagonalized by the right and left eigenvector matrices $X_{i+1/2}$ and $X^{-1}_{i+1/2}$, with $\Lambda_{i+1/2}$ the diagonal matrix with the eigenvalues in the diagonal. The Roe average Jacobian matrix between the states $\boldsymbol{U}^R_{i+1/2}$ and $\boldsymbol{U}^L_{i+1/2}$ is given by

$$A_{i+1/2} = \begin{bmatrix} 0 & 1 \\ \tilde{c}^2_{i+1/2} - \tilde{u}^2_{i+1/2} & 2\tilde{u}_{i+1/2} \end{bmatrix}, \tag{4.18}$$

where the average velocity $\tilde{u}$ and celerity $\tilde{c}$ are:

$$\tilde{u}_{i+1/2} = \frac{u^L\sqrt{H^L} + u^R\sqrt{H^R}}{\sqrt{H^L} + \sqrt{H^R}} \quad \text{and} \quad \tilde{c}_{i+1/2} = \sqrt{\frac{g\left(H^R + H^L\right)}{2}}, \tag{4.19}$$

the eigenvalues of $A_{i+1/2}$ are $\lambda^{1,2}_{i+1/2} = \tilde{u}_{i+1/2} \pm \tilde{c}_{i+1/2}$, with corresponding eigenvectors $r^1_{i+1/2} = \begin{bmatrix} 1 \\ \lambda^1_{i+1/2} \end{bmatrix}$ and $r^2_{i+1/2} = \begin{bmatrix} 1 \\ \lambda^2_{i+1/2} \end{bmatrix}$.

The topography source term is discretized so that steady states at rest are preserved at the discrete level. This is done by balancing the Roe fluxes as

$$\Delta \boldsymbol{S}_{bi} = \boldsymbol{S}^-_{bi+1/2} + \boldsymbol{S}^+_{bi-1/2} \tag{4.20}$$

where

$$\begin{aligned} \boldsymbol{S}^+_{bi+1/2} &= \frac{1}{2}\left[X(I + \left|\Lambda^{-1}\right|\Lambda)X^{-1}\right]_{j+1/2} \tilde{\boldsymbol{S}}_{bi+1/2} \\ \boldsymbol{S}^-_{bi+1/2} &= \frac{1}{2}\left[X(I - \left|\Lambda^{-1}\right|\Lambda)X^{-1}\right]_{j+1/2} \tilde{\boldsymbol{S}}_{bi+1/2}, \end{aligned} \tag{4.21}$$

with

$$\tilde{\boldsymbol{S}}_{bi+1/2} = \begin{bmatrix} 0 \\ -g\frac{H^L+H^R}{2}(b^R - b^L) \end{bmatrix}_{i+1/2}. \tag{4.22}$$

With this scheme, when the water is at rest, it is ensured that the advective numerical flux terms equal the source term $\Delta \boldsymbol{F}^n_i = \Delta \boldsymbol{S}'_{bi}$, so at each mesh cell: $u = 0$ and $b^R - b^L = -(h^R - h^L)$.

4.3.2 Dispersive terms

The dispersive term of Nwogu's model ψ_C in (4.5) is obtained by cell-averaging as

$$\begin{aligned} \left(\overline{\psi_C}\right)_i &= \frac{1}{\Delta x}\int_{C_i} \psi_C dx \\ &= \Bigg\{\Bigg[\left(\frac{z^2_{ai+1/2}}{2} - \frac{b^2_{i+1/2}}{6}\right) b_{i+1/2}\partial^2_x u_{i+1/2} \\ &\qquad + \left(z_{ai+1/2} + \frac{b_{i+1/2}}{2}\right) b_{i+1/2}\left(b_{i+1/2}\partial^2_x u_{i+1/2}\right)\Bigg] \\ &\quad - \Bigg[\left(\frac{z^2_{ai-1/2}}{2} - \frac{b^2_{i-1/2}}{6}\right) b_{i-1/2}\partial^2_x u_{i-1/2} \\ &\qquad + \left(z_{ai-1/2} + \frac{b_{i-1/2}}{2}\right) b_{i-1/2}\partial^2_x\left(b_{i-1/2}u_{i-1/2}\right)\Bigg]\Bigg\} \end{aligned} \tag{4.23}$$

and evaluating the face values as

$$u_{i+1/2} = \frac{7(u_{i+1} + u_i) - (u_{i+2} + u_{i-1})}{12} + O(\Delta x^4), \tag{4.24}$$

$$\partial_x^2 u_{i+1/2} = \frac{(u_{i+2} + u_{i-1}) - (u_{i+1} + u_i)}{2\Delta x^2} + O(\Delta x^2). \tag{4.25}$$

which can be derived by expanding u on Taylor series on cells $i-1$ to $i+2$, evaluating at $x_{i+1/2}$ and solving the linear system [73].

For the momentum equation of Nwogu's equation (4.1), second derivatives in cell centers are discretized as

$$\partial_x^2 u_i = \frac{1}{\Delta x^2}(u_{i-1} - 2u_i + u_{i+1}) + O(\Delta x^2) \tag{4.26}$$

so ψ_M in (4.5) is computed as

$$(\psi_M)_i = \partial_t H_i \left(\frac{z_{ai}}{2} \partial_x^2 u_i + \partial_x^2 (bu)_i \right)$$

with $\partial_t H_i$ obtained from the mass equation as

$$\partial_t H_i = \frac{\Delta H_i^n}{\Delta t} = -\partial_x (Hu)_i^n - (\psi_C)_i^n \tag{4.27}$$

The elliptic equation of Nwogu's model (4.3) is solved for u_i^{n+1} after computing P_i^{n+1}, as depicted in Fig. 4.2, by solving the tri-diagonal system

$$H_i(A_i u_{i-1}^{n+1} + B_i u_i^{n+1} + C_i u_{i+1}^{n+1}) = P_i^{n+1}, \quad i = 1...N_x \tag{4.28}$$

where

$$\begin{aligned} A_i &= \frac{z_{ai}}{\Delta x^2}\left(\frac{z_{ai}}{2} + b_{i-1}\right) \\ B_i &= \frac{z_{ai}}{\Delta x^2}\left(\frac{z_{ai}}{2} + b_{i+1}\right) \\ C_i &= 1 - \frac{z_{ai}}{\Delta x^2}\left(\frac{z_{ai}}{2} + 2b_i\right) \end{aligned} \tag{4.29}$$

For the GN system (4.6) the dispersive equation (4.8) is discretized using P^1 continuous finite elements. By using the self-adjoint property of the operator $H + \alpha H \mathcal{T}$ and dividing by H, the variational form of (4.8) is

$$\begin{aligned} &\int_\Omega (v\phi + S_1(v) H S_1(\phi) + S_2(\phi) H S_2(\phi)) dx \\ &= \int_\Omega S_1(v) H S_1(w) + S_2(v) H S_2(w) + Q(v) dx, \quad v \in H_0^1(\Omega) \end{aligned} \tag{4.30}$$

from where the expressions of the system to obtain the projection on the P^1 space can be deduced. The full expressions can be found in [38] however, because of the choice of P^1 elements, the problem also consists also of a tridiagonal symmetric positive-definite matrix as (4.28). Finally, once ϕ_i is obtained, the cell average can be computed as

$$\overline{\mathbf{\Phi}}_i = \frac{1}{8} \begin{pmatrix} 0 \\ \phi_{i-1} + 6\phi_i + \phi_{i+1} \end{pmatrix} \tag{4.31}$$

So the solver can finally be iterated as in Figure 4.2.

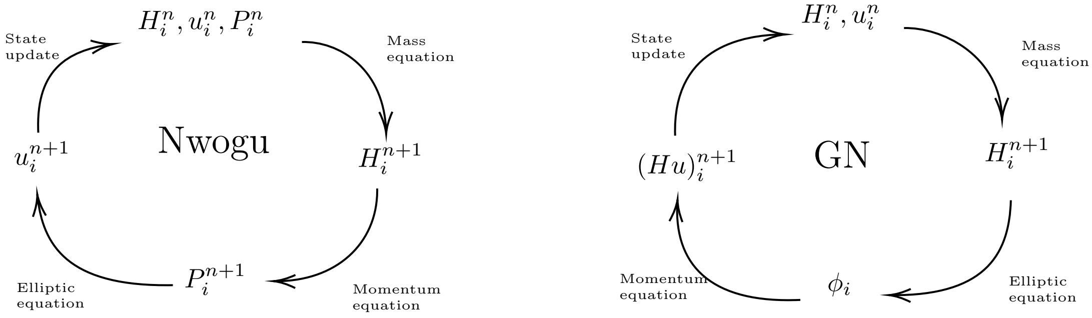

Figure 4.2: Diagram depicting the iteration loop of the numerical solver of Nwogu's (left) and Green-Naghdi (right) models (4.1). Arcs represent subroutines. Nodes represent the output of such subroutines, not necessarily obtained from the output of the upstream node, but a combination of some or all of those values and the current state at step n. More details can be found in [70] and references therein.

4.3.3 Boundary conditions

For the boundary conditions the elliptic problems are complemented with the closed-wall boundary conditions

$$u_0 = 0, \quad u_{N_x+1} = 0 \tag{4.32}$$

while for computing the other derivative terms two additional rows of ghost cells are added and filled with mirrored values as

$$\begin{aligned} u_{Nx+2}^{n+1} &= u_{Nx-1}^{n+1}, & H_{Nx+2}^{n+1} &= H_{Nx-1}^{n+1}, \\ u_{Nx+1}^{n+1} &= 0, & H_{Nx+1}^{n+1} &= H_{Nx}^{n+1}, \\ u_0^{n+1} &= 0, & H_0^{n+1} &= H_1^{n+1}, \\ u_{-1}^{n+1} &= u_2^{n+1}, & H_{-1}^{n+1} &= H_2^{n+1} \end{aligned} \tag{4.33}$$

whose justification has recently been revisited in [27]. These ghost cells are defined during the *State update* stage in Figure 4.2, so information at step $n+1$ is already known at that point. Naturally, the equations (4.33) are not exactly absorbing, however, all numerical experiments are chosen with computational domains that are large enough so that the waves never reach the boundaries.

4.3.4 Moving interface for wave breaking

For modeling the propagation of breaking waves the procedure detailed in [69] and [114] is used. The first step consists in detecting breaking waves as the set of points (x, t) where either of the following criteria is satisfied

$$\begin{aligned} |\partial_t H(x,t)| &\geq \gamma \sqrt{gH(x,t)} \\ |\partial_x \eta(x,t| &\geq \tan \varphi_c \end{aligned} \tag{4.34}$$

throughout this document values of $\gamma = 0.6$ and $\varphi_c = \pi/6$ are used [70]. The second step consists in grouping flagged cells and enlarging the breaking regions to account for a typical roller length [114, 69]. The last step is the cessation criteria, on which cells are unflagged, *i.e.,* not considered as breaking anymore, whenever

$$F_r = \sqrt{\frac{(2h_2/h_1+1)^2-1}{8}} \leq Fr_c \tag{4.35}$$

with h_1 and h_2 the heights at the front and behind the shock waves, and $Fr_c = 1.3$. This is based on the analogy between broken waves and bores. The interested reader can consult reference [114] for more details.

4.3.5 Higher order discretization

A fourth order scheme is also used with the Green-Naghdi model. This is implemented by changing the reconstruction of the left and right states $\boldsymbol{U}_{i+1/2}^{L,r}$ of eq. (4.16) and then correcting the topography term $\Delta \boldsymbol{S}_{bi}$ of eq. (4.20) to balance steady states at rest. This strategy is reproduced from [67] and we recall it here for the sake of completeness of the presentation.

The fourth order reconstruction of the left and right states at each interface $\boldsymbol{U}_{i+1/2}^{L,R}$ is done with a fourth-order Monotonic Upstream-centered Scheme for Conservation Laws (MUSCL) scheme given by Yamamoto et al. [126]. All variables, the total water depth H, the horizontal averaged velocity u and the topography b are computed for the left and right values at the interface $i+1/2$ according to:

$$H_{i+1/2}^{L} = H_i + \frac{1}{6}\left(\varphi(r_1)\Delta H_{i-1/2}^{*} + 2\varphi\left(\frac{1}{r_1}\right)\Delta^{*} H_{i+1/2}\right) \tag{4.36}$$

$$H_{i+1/2}^{R} = H_{i+1} - \frac{1}{6}\left(2\varphi(r_2)\Delta^{*} H_{i+1/2} + \varphi\left(\frac{1}{r_2}\right)\Delta^{*} H_{i+3/2}\right) \tag{4.37}$$

Here φ is the van Leer nonlinear slope limiter function [32].

$$\varphi(r_i) = \frac{r_i + |r_i|}{1+|r_i|}, \quad \text{with } r_1 = \frac{\Delta^{*} H_{i+1/2}}{\Delta^{*} H_{i-1/2}}, \quad r_2 = \frac{\Delta^{*} H_{i+3/2}}{\Delta^{*} H_{i+1/2}} \tag{4.38}$$

with $\Delta^{*}(\cdot)$ from

$$\Delta^{*} H_{i_1/2} = \Delta H_{i+1/2} - \frac{1}{6}\left(\Delta\overline{H}_{i+3/2} - 2\Delta\overline{H}_{i+1/2} + \Delta\overline{H}_{i-1/2}\right) \tag{4.39}$$

and

$$\begin{aligned} \Delta\overline{H}_{i-1/2} &= \text{minmod}(\Delta H_{i-1/2}, \Delta H_{i+1/2}, \Delta H_{i+3/2}) \\ \Delta\overline{H}_{i+1/2} &= \text{minmod}(\Delta H_{i+1/2}, \Delta H_{i+3/2}, \Delta H_{i-1/2}) \\ \Delta\overline{H}_{i+3/2} &= \text{minmod}(\Delta H_{i+3/2}, \Delta H_{i-1/2}, \Delta H_{i+1/2}) \\ \Delta H_{i+1/2} &= H_{i+1} - H_i \end{aligned} \tag{4.40}$$

and the minmod limiter given by

$$\text{minmod}(a,b,c) = \text{sign}(a)\max(|a|, 2\text{sign}(a)b, 2\text{sign}(a)c) \tag{4.41}$$

Since we have changed the reconstruction across the cell interfaces, (4.20) requires a correction term to enable the preservation of steady states at rest at the discrete level, avoiding unphysical oscillations. To be able to do this, a correction term is added to eq. (4.20) as

$$\Delta \boldsymbol{S}_{bi} = \boldsymbol{S}^{-}_{bi+1/2} + \boldsymbol{S}^{+}_{bi-1/2} + \boldsymbol{S}^{\star}_{b}(\boldsymbol{U}^{L}_{i+1/2}, \boldsymbol{U}^{R}_{i-1/2}) \tag{4.42}$$

with the new term given by

$$\boldsymbol{S}^{\star}_{b}(\boldsymbol{U}^{L}_{i+1/2}, \boldsymbol{U}^{R}_{i-1/2}) = \begin{pmatrix} 0 \\ -g\dfrac{H^{R}_{i-1/2} + H^{L}_{i+1/2}}{2}(b^{R}_{i-1/2} - b^{L}_{i+1/2}) \end{pmatrix} \tag{4.43}$$

According to [61, 94], this ensures the preservation of the stady states at rest exactly at the discrete level, as mentioned in [67].

4.4 New coupling methods for Nwogu's -Saint Venant coupling

In this section, we explore three different techniques to assess their impact on the stability of the coupled SV-Nwogu model with a set interface. The first technique involves adding an artificial viscous source term to the momentum equation. This approach is inspired by findings in [70], which showed that incorporating an eddy viscosity term in Nwogu's model enhanced stability in scenarios where the hybrid model faltered. Unlike the approach in [70] where viscous terms were applied across Nwogu's entire model, here, they are specifically added around the interface of the hybrid model. This strategy draws on the concept of stabilizing dissipative terms used in numerical schemes for hyperbolic equations, like the Lax-Wendroff method [82, sec. 6.1], and the parabolic regularization technique for assessing the soundness of nonlinear equations [104, 5].

The other two techniques involve creating an overlapping region by using two interfaces, one for each model, instead of a single interface. This overlapping method is inspired by the classical Schwarz method for domain decomposition and parallel processing, which was originally developed by Schwarz for the Laplace equations [105, 43]. The second technique used consists in the Schwarz Waveform Relaxation method (SWRM), where each subdomain is solved iteratively, utilizing as boundary conditions the trace results computed by its neighbor on a previous iteration. The third and last technique consists in a direct overlapping solver where the same two interfaces are used but the result is obtained without iterations, in a more similar fashion to the hybrid model.

Inspired by domain decomposition methods, other non-overlapping techniques could be used with both, the direct solver or the SWRM. For example, using different boundary conditions such as Robin, Neumann, or even pseudo-differential operators (See [42] for examples). However, since the study of initial boundary value problems has only recently begun to be addressed in the literature [65, 81, 78], this work focuses solely on Dirichlet operators. The implementation is takes advantage of ghost cells, which facilitates the tranmission of the data between subdomains.

4.4.1 Artificial viscosity

The artificial viscosity source term $\boldsymbol{S}_\nu$ is added by solving

$$\partial_t \boldsymbol{U}^\star + \partial_x \boldsymbol{F}(\boldsymbol{U}) = \boldsymbol{S}_b + \boldsymbol{S}_d + \boldsymbol{S}_\nu \tag{4.44}$$

instead of (4.1). The source term is inspired by the viscous SV equations [88] and given by

$$\boldsymbol{S}_\nu = \begin{pmatrix} 0 \\ \chi_W(x - x_{interface+})\nu \partial_x(H\partial_x u) \end{pmatrix} \tag{4.45}$$

where χ_W is the indicator function

$$\chi_W(x) = \begin{cases} 1 & |x| \leq W \\ 0 & |x| > W \end{cases} \tag{4.46}$$

with W the width of the viscous term around the interface of Ω_+; $x_{interface+} = 9.5m$ is the location of the interface of the subdomain Ω_+; and $\nu > 0$ is the artificial viscosity parameter. Notice that if $\nu = 0$ then the viscosity term is deactivated and the solver is the same as the hybrid modelwith a fixed interface, whereas if $W = 0$ then the viscous term is activated but is only computed at $x_{interface}$. Given these definitions the goal is to observe the effects that varying ν and W has on the stability and artifacts of the solution.

The discretization of this source term is made by computing its cell average as

$$\overline{\boldsymbol{S}_f}_i = \frac{\nu}{\Delta x} \begin{pmatrix} 0 \\ \nu \chi_L(x - 9.5)(H_{i+1/2}\partial_x u_{i+1/2} - H_{i-1/2}\partial_x u_{i-1/2}) \end{pmatrix} \tag{4.47}$$

and then computing the face values by using the finite difference [73]

$$\partial_x u_{i+1/2} = \frac{15u_{i+1} - u_i - (u_{i+2} - u_{i-1})}{12\Delta x} + O(\Delta x^4) \tag{4.48}$$

4.4.2 An overlapping Schwarz Waveform Relaxation Method

The overlapping region is added to the domain $\Omega =]a, b[$ by defining subdomains $\Omega_- =]a, c + L[$ and $\Omega_+ =]c, b[$ with $a < c < b$ and $L > 0$ such that $\Omega_- \cap \Omega_+ =]c, c + L[$. The overlapping problem consists in finding $\boldsymbol{U}_\pm = (H_\pm, H_\pm u_\pm) : \Omega_\pm \times]0, T[\to \mathbb{R}^2$ such that

$$\begin{aligned} \mathcal{N}_\pm \boldsymbol{U}_\pm = 0, \quad & \text{in } \Omega_\pm \times]0, T[\\ \boldsymbol{U}_\pm(0, \cdot) = \boldsymbol{U}_0 \quad & \text{in } \Omega_\pm \end{aligned} \tag{4.49}$$

with $\mathcal{N}_\pm$ either $\mathcal{N}_{Nwogu}$ or $\mathcal{N}_{SV}$, so that $\mathcal{N}_{Nwogu}\boldsymbol{U} = 0$ if and only if $\boldsymbol{U} = (H, u)$ satisfies (4.1), and $\mathcal{N}_{SV}\boldsymbol{U} = 0$ if and only if $\boldsymbol{U}$ satifies the same (4.1) but with $S_d = 0$ and $P = Hu$, in other words, $\boldsymbol{U}$ satisfies the Saint-Venant equations.

The SWRM relies on closing system (4.49) by defining tranmission conditions B_-,B_+ such as:

$$\begin{aligned} B_- \boldsymbol{U}_-(c + L, \cdot) = B_- \boldsymbol{U}_+(c + L, \cdot) \\ B_+ \boldsymbol{U}_+(0, \cdot) = B_+ \boldsymbol{U}_-(0, \cdot) \end{aligned}, \quad \text{in }]0, T[\tag{4.50}$$

and then obtaining the solution by running the algorithm

$$\begin{aligned}
\mathcal{N}_-\boldsymbol{U}_-^{k+1} &= 0, \quad \text{in } \Omega_-\times]0,T[\\
\boldsymbol{U}_-^{k+1}(0,\cdot) &= \boldsymbol{U}_0 \quad \text{in } \Omega_-\\[1em]
\mathcal{N}_+\boldsymbol{U}_+^{k+1} &= 0, \quad \text{in } \Omega_+\times]0,T[\\
\boldsymbol{U}_+^{k+1}(0,\cdot) &= \boldsymbol{U}_0 \quad \text{in } \Omega_+\\[1em]
B_-\boldsymbol{U}_-^{k+1}(c+L,\cdot) &= B_-\boldsymbol{U}_+^{k}(c+L,\cdot) \quad \text{in }]0,T[\\
B_+\boldsymbol{U}_+^{k+1}(0,\cdot) &= B_+\boldsymbol{U}_-^{k}(0,\cdot) \quad \text{in }]0,T[
\end{aligned} \tag{4.51}$$

for $k \geq 1$ integer, starting from the initial guess for the traces $\boldsymbol{U}_+^0(0,\cdot)$, $\boldsymbol{U}_-^0(c+L,\cdot)$.

The SWRM is implemented at the discrete level using the scheme presented in Section 4.3 to approximate the operators $\mathcal{N}_-$ and $\mathcal{N}_+$. Each domain is discretized on a uniform mesh of size Δx and with total interior cells of N_- and N_+ for Ω_- and Ω_+, and an overlap of M cells, as denoted in Figure 4.3; Δx, N_-, N_+ and M satisfy

$$\Delta x = \frac{c+L-a}{N_-} = \frac{b-c}{N_+} = \frac{L}{M} \tag{4.52}$$

Denoting the coordinates of the cell centers by

$$x_{-,i} = a + (i-1)\Delta x, \quad x_{+,i} = c + (i-1)\Delta x \tag{4.53}$$

then, as depicted in Figure 4.3, by construction

$$\begin{aligned}
x_{+,1} = x_{-,N_--M} &= c\\
x_{-,N_--M} = x_{+,M} &= c+L-\Delta x
\end{aligned} \tag{4.54}$$

Let $\boldsymbol{U}_{\pm,i}^{n,k} = (H_{\pm,i}^{n,k}, (Hu)_{\pm,i}^{n,k})$ be the approximate solution at iteration k of algorithm (4.51) in domain $\Omega_\pm$ at node i and timestep n. Using the discrete scheme presented on Section 4.3, algorithm (4.51) is complemented with the transmission conditions

$$\begin{aligned}
u_{-,N_-+1}^{n,k+1} &= u_{+,M+1}^{n,k}, & u_{+,0}^{n,k+1} &= u_{-,N_--M-1}^{n,k},\\
u_{-,N_-+2}^{n,k+1} &= u_{+,M+2}^{n,k}, & u_{+,-1}^{n,k+1} &= u_{-,N_--M-2}^{n,k},\\
H_{-,N_-+1}^{n,k+1} &= H_{+,M+1}^{n,k}, & H_{+,0}^{n,k+1} &= H_{-,N_--M-1}^{n,k},\\
H_{-,N_-+2}^{n,k+1} &= H_{+,M+2}^{n,k}, & H_{+,-1}^{n,k+1} &= H_{-,N_--M-2}^{n,k}
\end{aligned} \tag{4.55}$$

As denoted in Figure 4.3, these transimssion conditions subtitute (4.33) and (4.32) on their respective boundaries, and they simply copy the information from interior cells at iteration k into the ghost cells of the neighbor's ghost cells with identical x coordinate at iteration $k+1$ on each timestep n, similar to a Dirichlet operator at the continuous level.

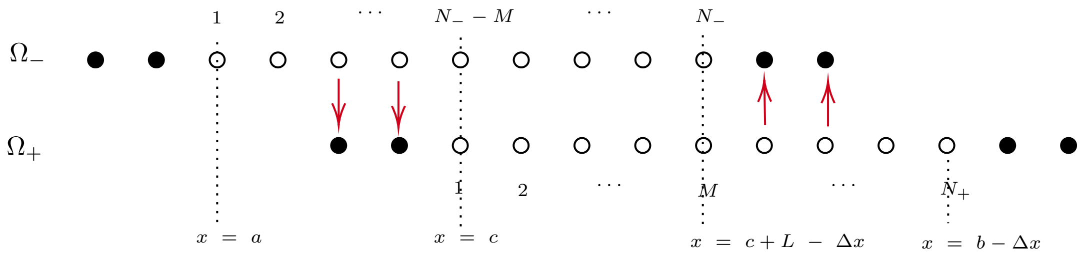

Figure 4.3: Distribution and enumeration of cell centers in the overlapping algorithms. White circles correspond to interior cells; black circles to ghost cells. Red arrows indicate data transmitted from one domain into the ghost cells of the neighbor domain.

4.4.3 A direct overlapping solver

One disadvantage of the SWRM is that it requires computing the solution several times on each subdomain in order to obtain a solution. One way to achieve optimal convergence is to prevent data to travel from the locations of one interface to the other, for example, from $x = c + L$ in Ω_- to $x = c$. In the small-amplitude hyperbolic case, with an argument similar to that used in [46], one can prove that by choosing L and T such that

$$\max_{x,t} \sqrt{gH} \leq \frac{L}{T} \tag{4.56}$$

the algorithm converges in just two iterations. This happens because waves generated by the non-converged traces do not reach the neighbor's interface location. This means that either a large L or a small T will lead to an optimal number of iterations. To cover the whole duration, the simulation can be run on time windows $T_1, T_2, ..T_N$ satisfying criteria (4.56) [46]. Moreover, the choice of the initial guess can also accelerate the convergence or, in the worst case, make the algorithm unstable on early iterations. This will be shown on the numerical results of the next section.

Since reducing the time window size T improves the convergence of the algorithm, another strategy is studied here, in which the smallest possible timewindow $T = \Delta t$ is used. In this case the overlap is implemented more similarly to the hybrid model by directly assigning the ghost cells on each timestep as

$$\begin{aligned}
u^{n+1}_{-,N_-+1} &= u^{n+1}_{+,M+1}, \quad u^{n+1}_{+,0} = u^{n+1}_{-,N_--M-1}, \\
u^{n+1}_{-,N_-+2} &= u^{n+1}_{+,M+2}, \quad u^{n+1}_{+,-1} = u^{n+1}_{-,N_--M-2}, \\
H^{n+1}_{-,N_-+1} &= H^{n+1}_{+,M+1}, \quad H^{n+1}_{+,0} = H^{n+1}_{-,N_--M-1}, \\
H^{n+1}_{-,N_-+2} &= H^{n+1}_{+,M+2}, \quad H^{n+1}_{+,-1} = H^{n+1}_{-,N_--M-2}
\end{aligned} \tag{4.57}$$

where $\boldsymbol{U}^n_{\pm,i} = (H^n_{\pm,i}, H^n_{\pm,i} u^n_{\pm,i})$ is the approximation provided by the scheme of Section 4.3 to $\boldsymbol{U}_-, \boldsymbol{U}_+$, the solutions of

$$\begin{aligned} \mathcal{N}_-\boldsymbol{U}_- &= 0, \quad \text{in } \Omega_-\times]0,T[\\ \boldsymbol{U}_-(0,\cdot) &= \boldsymbol{U}_0 \quad \text{in } \Omega_- \\ \\ \mathcal{N}_+\boldsymbol{U}_+ &= 0, \quad \text{in } \Omega_+\times]0,T[\\ \boldsymbol{U}_+(0,\cdot) &= \boldsymbol{U}_0 \quad \text{in } \Omega_+ \end{aligned} \tag{4.58}$$

with the enumeration shown in Figure 4.3. Notice that (4.57) is an explicit equation because the update of the ghost cells is performed during the *State update* stage shown in Figure 4.2, so values on all interior cells at step $n+1$ are all known at that point.

One can wonder whether this method provides the same solution as the SWRM or not. The following Proposition shows that if $T = \Delta t$ then the solution is indeed the same. Numerical results of the next section will show that for larger T the solutions can be different and, in particular, that the limit of the SWRM can be stable in situations where the direct solver is unstable (same mesh size, initial condition, etc).

Proposition 4.1. *Let $\boldsymbol{U}_i^0$ be the initial condition known for every integer i. Let $\boldsymbol{U}_{\pm,i}^{n,k+1}$ and $\boldsymbol{U}_{\pm,i}^{n}$ denote the solutions of the SWRM and the direct method respectively, on domain $\Omega_\pm$, node i, timestep n and iteration $k+1$. If $T = \Delta t$ then for every $n \geq 0$, $k \geq 0$ integers*

$$\begin{aligned} \boldsymbol{U}_{-,i}^{n+1,k+1} &= \boldsymbol{U}_{-,i}^{n+1} \quad -1 \leq i \leq N_- + 2 \\ \boldsymbol{U}_{+,i}^{n+1,k+1} &= \boldsymbol{U}_{+,i}^{n+1} \quad -1 \leq i \leq N_+ + 2 \end{aligned} \tag{4.59}$$

Proof. The proof consists in making explicit the fact that $T = \Delta t$ is just one timestep of the discrete scheme, so after one iteration all results only depend on the initial condition, which is what the direct solver does too.

Without loss of generality we will assume that $N_- = N_+ = N$. Since at $n = 0$ the initial condition must satisfied, then we have

$$\begin{aligned} \boldsymbol{U}_{-,i}^{n,k+1} &= \boldsymbol{U}_i^0, \quad -1 \leq i \leq N+2 \\ \boldsymbol{U}_{+,i}^{n,k+1} &= \boldsymbol{U}_{N-M+i-1}^0, \quad -1 \leq i \leq N+2 \\ \\ \boldsymbol{U}_{-,i}^{n} &= \boldsymbol{U}_i^0, \quad -1 \leq i \leq N+2 \\ \boldsymbol{U}_{+,i}^{n} &= \boldsymbol{U}_{N-M+i-1}^0, \quad -1 \leq i \leq N+2 \end{aligned} \tag{4.60}$$

for every integer $k \geq 0$. Let also $g_{\pm,1}^n$ and $g_{\pm,2}^n$ be the initial guess of the traces used to initialize (4.51), *i.e.,* such that for $k = 0$

$$\begin{aligned} \boldsymbol{U}_{-,N+1}^{n+1,k+1} &= g_{-,1}^{n+1} \quad \boldsymbol{U}_{+,-1}^{n+1,k+1} = g_{+,1}^{n+1} \\ \boldsymbol{U}_{-,N+2}^{n+1,k+1} &= g_{-,2}^{n+1} \quad \boldsymbol{U}_{+,0}^{n+1,k+1} = g_{+,2}^{n+1} \end{aligned} \tag{4.61}$$

according to the enumeration of Figure 4.3. Let $\mathcal{S}^-$ and $\mathcal{S}^+$ denote the discrete stepping operators, such that

$$
\begin{aligned}
\boldsymbol{U}_{-,i}^{n+1,k+1} &= \mathcal{S}^{-}(\boldsymbol{U}_{-,\cdot}^{n,k+1})[i], &\text{for } 1 \leq i \leq N\\
\boldsymbol{U}_{+,i}^{n+1,k+1} &= \mathcal{S}^{+}(\boldsymbol{U}_{+,\cdot}^{n,k+1})[i], &\text{for } 1 \leq i \leq N\\
\\
\boldsymbol{U}_{-,i}^{n+1} &= \mathcal{S}^{-}(\boldsymbol{U}_{-,\cdot}^{n})[i], &\text{for } 1 \leq i \leq N\\
\boldsymbol{U}_{+,i}^{n+1} &= \mathcal{S}^{+}(\boldsymbol{U}_{+,\cdot}^{n})[i], &\text{for } 1 \leq i \leq N
\end{aligned}
\tag{4.62}
$$

for every $k \geq 0$. Then because of the initial condition (4.60)

$$
\begin{aligned}
\boldsymbol{U}_{-,i}^{n+1,k+1} &= \mathcal{S}^{-}(\boldsymbol{U}_{\cdot}^{0})[i], &\text{for } 1 \leq i \leq N\\
\boldsymbol{U}_{+,i}^{n+1,k+1} &= \mathcal{S}^{+}(\boldsymbol{U}_{N-M+(\cdot)-1}^{0})[i], &\text{for } 1 \leq i \leq N\\
\\
\boldsymbol{U}_{-,i}^{n+1} &= \mathcal{S}^{-}(\boldsymbol{U}_{\cdot}^{0})[i], &\text{for } 1 \leq i \leq N\\
\boldsymbol{U}_{+,i}^{n+1} &= \mathcal{S}^{+}(\boldsymbol{U}_{N-M+(\cdot)-1}^{0})[i], &\text{for } 1 \leq i \leq N
\end{aligned}
\tag{4.63}
$$

from where we deduce that for all interior nodes both solutions are the same

$$
\begin{aligned}
\boldsymbol{U}_{-,i}^{n+1,k+1} &= \boldsymbol{U}_{-,i}^{n+1} \quad 1 \leq i \leq N\\
\boldsymbol{U}_{+,i}^{n+1,k+1} &= \boldsymbol{U}_{+,i}^{n+1} \quad 1 \leq i \leq N
\end{aligned}
\tag{4.64}
$$

while for the ghost cells on the interface of Ω_{-} using (4.55)

$$
\begin{aligned}
\boldsymbol{U}_{-,N+1}^{n+1,k+1} &= \boldsymbol{U}_{+,M}^{n+1,k} \quad (\text{ Eq. } (4.55))\\
&= \mathcal{S}^{+}(\boldsymbol{U}_{N-M+(\cdot)-1}^{0})[M] \quad (\text{ Eq. } (4.63), \text{ line } 2)\\
&= \boldsymbol{U}_{+,M}^{n+1} \quad (\text{ Eq. } (4.63), \text{ line } 4\ )\\
&= \boldsymbol{U}_{-,N+1}^{n+1} \quad (\text{ Eq. } (4.57)\ )
\end{aligned}
\tag{4.65}
$$

and the same arguments lead to $\boldsymbol{U}_{-,N+2}^{n+1,k+1} = \boldsymbol{U}_{-,N+2}^{n+1}$. Finally, for the interface of Ω_{+}

$$
\begin{aligned}
\boldsymbol{U}_{+,0}^{n+1,k+1} &= \boldsymbol{U}_{+,N-M-1}^{n+1,k} \quad (\text{ Eq. } (4.55))\\
&= \mathcal{S}^{-}(\boldsymbol{U}_{\cdot}^{0})[N-M-1] \quad (\text{ Eq. } (4.63), \text{ line } 1)\\
&= \boldsymbol{U}_{-,N-M-1}^{n+1} \quad (\text{ Eq. } (4.63), \text{ line } 3\ )\\
&= \boldsymbol{U}_{+,0}^{n+1} \quad (\text{ Eq. } (4.57)\ )
\end{aligned}
\tag{4.66}
$$

and similarly one obtains $\boldsymbol{U}_{+,-1}^{n+1,k+1} = \boldsymbol{U}_{+,-1}^{n+1}$. Repeating this argument inductively leads to the conclusion. □

4.4.4 Software

The solver of Section 4.3 is a modified version of the Fortran codes used in [70]. The Schwarz iteration loop of algorithm (4.51) is implemented using Bash scripts that call the Fortran executables and save (read) ghost-cells data into (from) CSV files, as depicted in Figure 4.4.

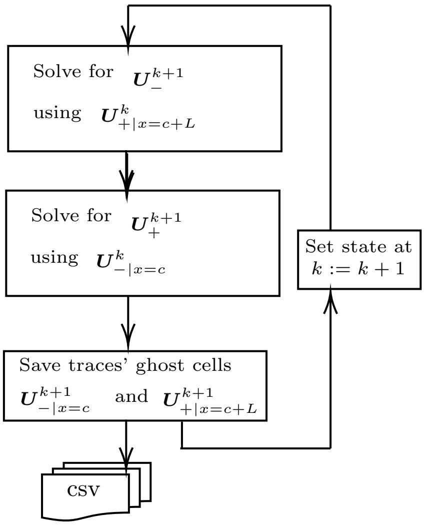

Figure 4.4: Data flow of the iteration loop of the SWRM implemented in Bash. The solver stages use a modified version of the Fortran code used in [67].

From an implementation point of view this has some advantages. Firstly, the modularity gained by having two independent code-bases allows to have a clear separation of concerns between the hydrodynamic solver and the SWRM process, which makes the model non-intrusive. In fact the only footprint on the original source code is the set of new subroutines for input/output and boundary conditions that are required, but otherwise, the original solvers remain untouched. This is an advantage over the alternative choice of storing the solutions of each subdomain on different arrays initialized at runtime, which would require a major refactoring of the code and a more abstract and complex programming pattern, which in turn would require more complex tests to ensure the mantainability of the code over time. The main comparative disadvantage is that since input/output operations are done to csv files, these tasks slow down computations and take additional memory, which could be a big issue in 2D solvers for large scale scenarios. Moreover, the current implementation is sequential but could very well be adapted for parallel computing. Being a 1D prototype-stage code none of these issues are a big concern at the moment, but improvements are of course possible. For example, besides improving the input/output format, for a more mature implementation it could be possible to use a bidirectional communication channel from each subdomain process to a middleware service. This middleware could, on one side, coordinate the communications between the two subdomain solvers, and on the other, be in charge of queing and saving the data asynchronously, without interrupting the iteration loop. Another choice is to implement the algorithm using a software framework such as OpenPalm[1]. This would allow us to enjoy the benefits of modularity offered by the method, at the same time of scaling-up the computations efficiently.

---

[1] OpenPalm can be found at `https://www.cerfacs.fr/globc/PALM_WEB/`

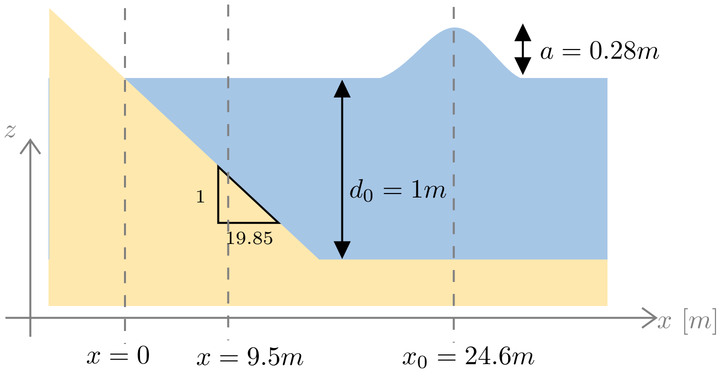

Figure 4.5: Configuration of the test case of a solitary wave on a simple beach.

4.5 Results with Nwogu's- Saint Venant coupled models

In this section the hybrid model and the new coupling methods presented in Section 4.4 are examined through numerical experiments. The results are presented and discussed separately for each method.

4.5.1 Nwogu's hybrid model

In this section we inspect the artifacts that appear in the solution of the hybrid Nwogu-SV model on some test cases. The test cases are two, and consist in the propagation of a solitary wave over two types of bathymetries: (1) a bathymetry of constant-depth and (2) a simple beach with a slope shown in Figure 4.5, which was proposed in the experiments of reference [109]. The computational domain is $\Omega = [-20m, 80m]$ and the hybrid model is configured with a static interface at $x = 9.5m$ such that the SV model is solved on cells at $x < 9.5m$ and Nwogu's model is solved on $x \geq 9.5n$. The initial condition is given by the left-propagating solitary wave of the Green-Naghdi equations

$$\begin{aligned} H_0(x) &= d_0 + b(x) + Asech^2\left(\kappa(x - x_0)/2\right) \\ u_0(x) &= -c\left(1 - \frac{d_0}{H_0(x) - b(x)}\right) \end{aligned} \tag{4.67}$$

with $\kappa = \sqrt{\frac{3A}{(A+d_0)d_0^2}}$ and $c = \sqrt{gd_0(A + d_0)}$, and $H_0(x) = u_0(x) = 0$ whenever $b(x) > 0$. The other parameters are $A = 0.28m$, $d_0 = 1m$ and $x_0 = 24.6$; the duration of the simulations is $T = 7s$ unless stated otherwise. Two bathymetries are studied: the flat bottom $b(x) = -1$ and the simple beach

$$b(x) = \begin{cases} -x/19.85 & x \leq 19.85 \\ -1 & x > 19.85 \end{cases} \tag{4.68}$$

The objective is to observe the artifacts and instabilities that appear on both scenarios with different mesh sizes. In all these experiments only the first order scheme is used. The coarsest mesh is chosen with mesh size $\Delta x_0 = 0.025m$ and $CFL = 0.3$ for which the flat-bottom case is unstable and the simple-beach case is stable. When refining the mesh to $\Delta x_1 = \Delta x_0/2$ with the same CFL the simple-beach case becomes unstable too. These instabilities show up at the interface $x = 9.5m$, as can be seen in Figure 4.6. It is observed that the instabilities consist in oscillations of similar length as the mesh size and that they are located on the cells of the dispersive domain that are closest to the interface. These oscillations grow rapidly and end up generating negative water depths.

To stabilize the algorithm the mesh size Δx is kept constant and the CFL number is halfed until a stable result is obtained. Once a stable CFL is found the mesh is reduced by half too; if with the new mesh size the model is also unstable then the process is restarted. Tables 4.1 and 4.2 show the registry of this process. It is assumed that once a stable CFL is found for a given mesh, all coarser meshes will be stable too. One can observe that in neither case it was possible to keep the CFL number constant when refining the mesh. In both the flat bottom and simple beach cases one is forced to reduce the CFL number on a greater proportion than the ratio of coarser-to-current mesh, which indicates a stability condition more stringent than $\Delta t = O(\Delta x^2)$.

Figures 4.7 and 4.8 show the results of the stable configurations on several instants. One can observe that the only visible artifact is a short wave of smaller amplitude propagating upstream on the dispersive domain. This wave has a constant wavelength on all mesh sizes and gets sharper as the resolution is increased. This suggests that these waves are an artifact of the differential equation and not of the discrete scheme. Moreover, they resemble reflected waves as the ones obtained from a change in the bathymetry [30], except that now they are produced artifically by the interface. To visualize this more clearly Figure 4.9 compares the hybrid Nwogu's model with the Nwogu's model solved on every point, displaying also their difference. One can observe that indeed, there is a perturbation propagating upstream to the right of the interface.

Fortunately, because the amplitude of the reflections is small with respect to the local depth one has $Fr \approx 1 < Fr_c$ in (4.35) so even if the gradient is large it will not be considered as a breaking wave. For example, Figure 4.10 shows the results obtained with mesh Δx_2 on the simple-beach case along with the values of $|\partial_x \eta|$ and $|\partial_t H|$ and thresholds for wave-breaking detection of Section 4.3.4. It is clear that the main front indeed satisfies the wave breaking criteria because the gradients in space and time surpass in magnitude their respective thresholds. Moreover, one can see that $|\partial_t \eta|$ slightly surpasses the threshold (4.34). However, in this case $h_1 = 0.634m$ and $h_2 = 0.6523m$ which results in $Fr = 1.0205$ according to (4.35); since $Fr < Fr_c$ it does not qualify as an active breaker.

So far it has been deduced that the hybrid model with the equations of Nwogu and with a fixed interface requires a stringent stability condition to provide a mesh-convergent solution, but a solution indeed exists. Moreover, the main artifact of this solution is a mesh-independent reflected wave, small enough to not to be mistaken as a breaking wave. Further analysis fall outside the scope of this chapter and will be left for the next Part II.

Mesh size | CFL	**0.3**	**0.125**	**0.06**	**0.03**	**0.015**	**0.075**
$\Delta x_0 = 0.025m$	Unstable	Stable				
$\Delta x_1 = \Delta x_0/2$		Unstable	Unstable	Stable		
$\Delta x_2 = \Delta x_0/4$				Unstable	Unstable	Stable

Table 4.1: Registry of unstable and stable cases for different mesh sizes varying the CFL number. Solitary wave over flat-bottom case. Empty cells represent cases that were not computed, assuming that they were either stable (towards the upper right corner) or unstable (towards the lower left corner).

cfl	**0.3**	**0.15**	**0.075**	**0.037**	**0.018**	**0.009**
$\Delta x_0 = 0.025m$	Stable					
$\Delta x_1 = \Delta x_0/2$	Unstable	Stable				
$\Delta x_2 = \Delta x_0/4$		Unstable	Unstable	Stable		
$\Delta x_3 = \Delta x_0/8$				Unstable	Unstable	Stable

Table 4.2: Registry of unstable and stable cases for different mesh sizes varying the CFL number. Solitary wave on a simple beach case.

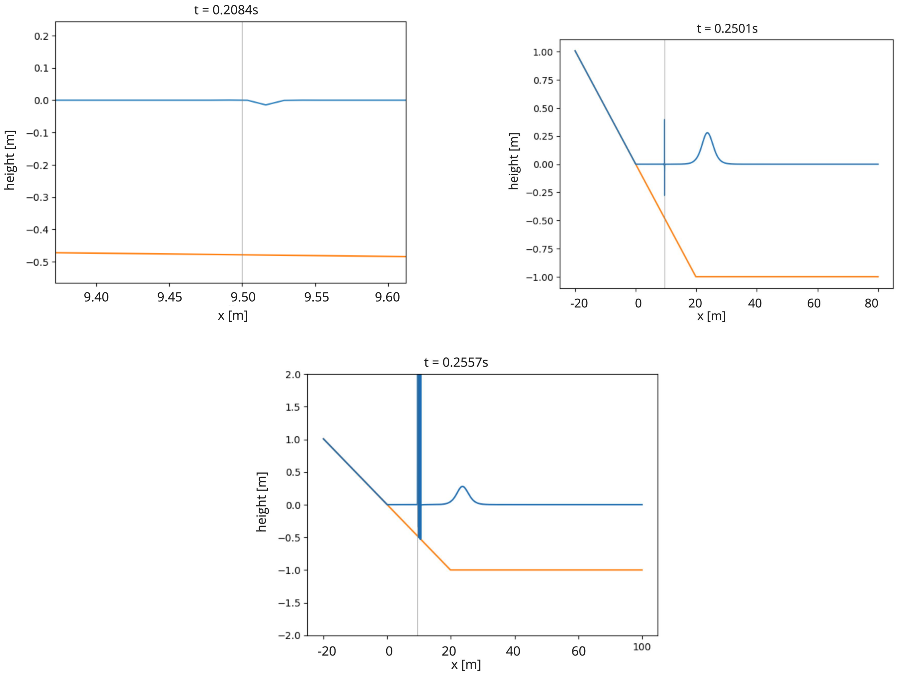

Figure 4.6: Evolution of the small oscillation that ends up exploding into negative water depths. Using Nwogu-SV hybrid model with mesh $\Delta x_0/2$ and $CFL = 0.3$.

4.5.2 Nonoverlapping interface with artificial viscosity

To see the impact that the viscosity has on the solution we study the case with a flat-bottom $b(x) = -1$ and use as reference the two meshes $\Delta x_0 = 0.0250m$ and $\Delta x_1 = \Delta x_0/2 = 0.0125m$ with CFL=0.3 and CFL=0.125 respectively, which

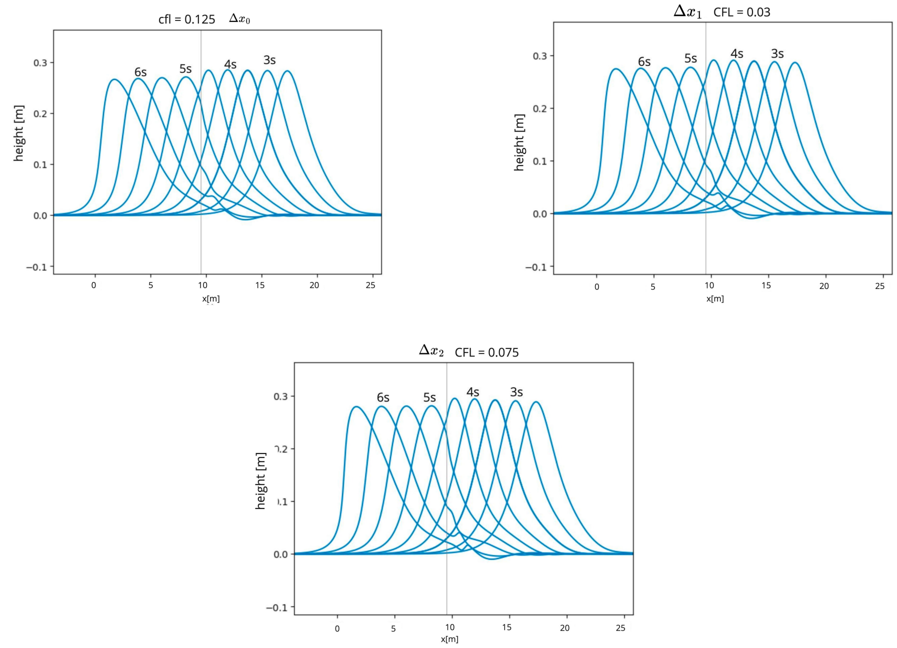

Figure 4.7: Results obtained with the Nwogu's model for different mesh sizes with the stable CFL numbers on the flat-bottom solitary wave case.

were unstable in the hybrid model (see Table 4.1). Starting with a viscosity of $\nu = 0.1$ and a width of $W = 1m$ the CFL is varied and the simulations are run until they reach $T = 10s$, or a negative depth is observed. Figure 4.11 shows the durations reached by the simulations as a function of the CFL number on both meshes. It is observed that the additional viscosity indeed stabilizes the computations in both mesh sizes. Moreover, larger values of CFL can also stabilize the model, however, the increase in CFL is small and covers a more narrow range on the first mesh. Figure 4.12 shows the sensitivity to the ν parameter on each mesh with the initial CFL. One can see that in both meshes the model is stable only on a finite interval of ν, which is smaller with Δx_0 than Δx_1. Figure 4.13 shows the duration of the model as a function of the width $\boldsymbol{W}$. The mesh Δx_0 proves to be more restrictive yet again. However, introducing viscosity in only a few cells suffices to secure the model's stability for both Δx_0 and Δx_1 meshes. Figure 4.14 and 4.15 show snapshots of the free surface computed on each mesh and for different values of W. One can verify that indeed the smaller width turns into a smaller dissipation, but most importantly that the difference in peaks between the largest width $W = 1$ and the smallest $W = 0$ (just one cell with viscous source term) is less than 1%, so it is not very sensitive once W is sufficiently small. These results show that the stability of the model could be improved by adding artificial dissipation in just a few cells around the interface, without significantly affecting the wave propagation. Finally, the only artifact that remains is the reflected wave that was observed with the hybrid model too. However, the choice of ν has to be made carefully, which calls for a more precise characterization of the stability condition. Since the scope of this part is just the identification of such features,

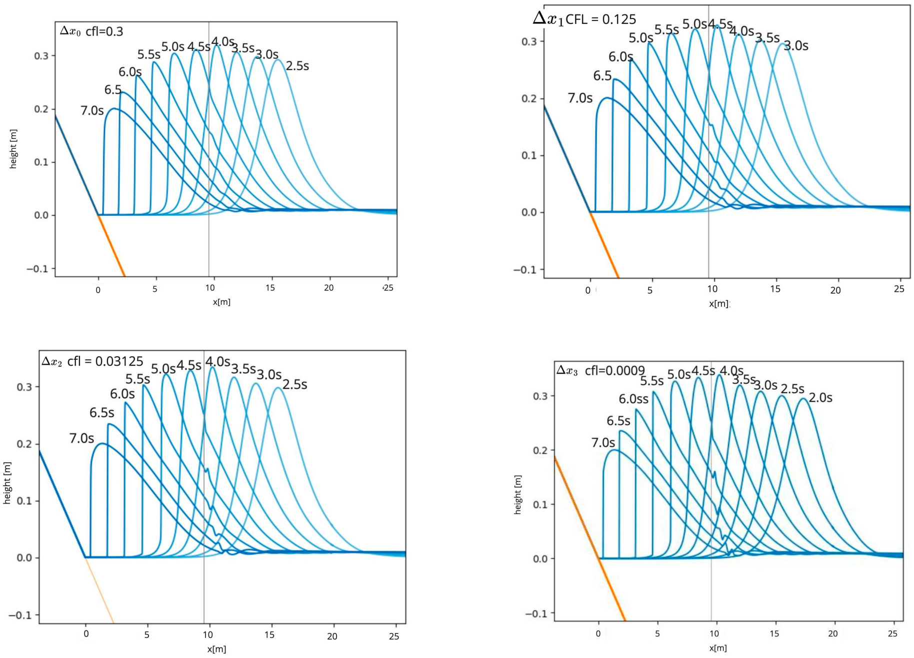

Figure 4.8: Results obtained with the Nwogu's model for different mesh sizes with the stable CFL numbers on the Synolakis' solitary wave case.

this characterization is left as future research.

4.5.3 Overlapping SWRM solver

In this section the overlapping models presented in Section 4.4 are tested on the case of the propagation of a solitary wave over a plane beach [109]. The computational domains are $\Omega =]-20, 80[$, $\Omega_- =]-20, 9.5[$, $\Omega_+ =]9.5 + L, 80[$, *i.e.*, $a = -20m$, $b = 80m$ and $c = 9.5m$, with L to be chosen later. The bathymetry is the simple beach profile of equation (4.68).

The computed results of the overlapping strategies are compared with the hybrid in terms of the mesh sizes. The main difference in the configuration of the algorithms is that a constant Δt is used for the whole duration until $T = 5s$, instead of the variable timestep of (4.14). This is done to ensure that no interpolation is performed to iterate the algorithm later. To achieve this we start from the coarsest mesh is $\Delta x_0 = 0.025m$ and $\Delta t_0 = 0.0013s$, which ensure that $\Delta t \leq \Delta t^n$ for all n, with Δt^n from (4.14). On this configuration the hybrid model is still stable at $T = 5s$ as shown in Figure 4.16. Then, refining to $\Delta t_1 = \Delta t_0/2$ and $\Delta x_1 = \Delta x_0/2$ the hybrid model becomes unstable, blowing up very early in the simulation right at the interface, as shown in Figure 4.17. This is the starting point for the comparison.

Verification with the homogeneous coupling: The implementation of the overlapping SWRM with the transmission conditions given by (4.55) is validated in the homogeneous-coupling case. This is done by verifying the convergence

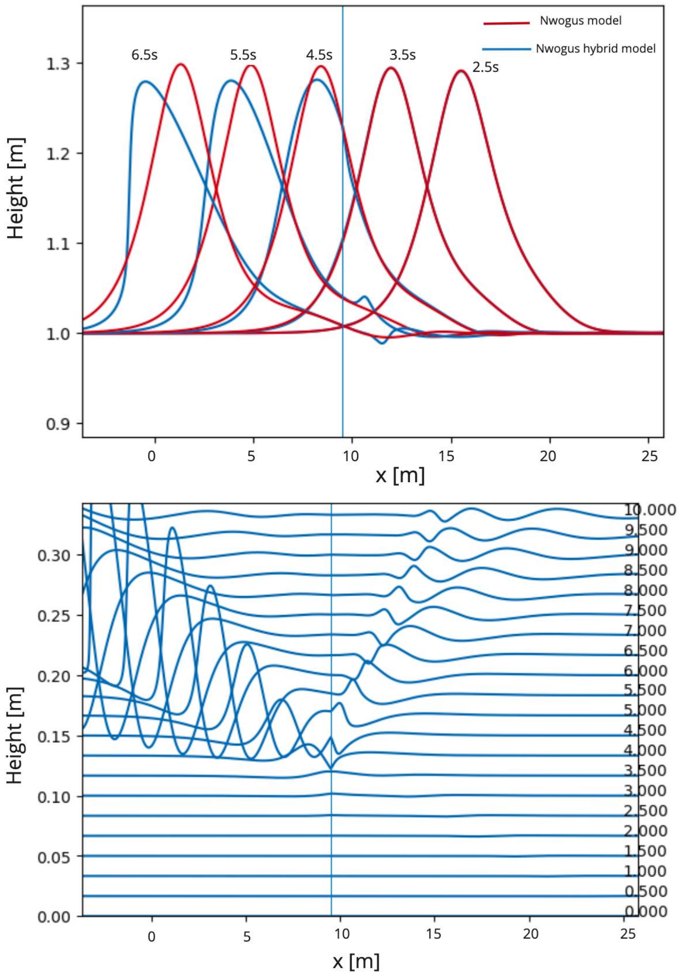

Figure 4.9: Comparison of the hybrid Nwogu's model and the Nwogu's model used everywhere in the domain with the finest mesh on the flat-bottom case. Top picture shows snapshots of the free surface of both models. Bottom picture shows the difference hybrid minus Nwogu's model.

of the algorithm when $\mathcal{N}_{-} = \mathcal{N}_{+} = \mathcal{N}_{Nwogu}$ and comparing the result with the monodomain solution, *i.e.*, the solution of the problem with $\mathcal{N}_{Nwogu}W = 0$ solved in Ω; an overlap of $L = 10m$ and the coarse mesh are used in the computations.

Figures 4.18 and 4.19 show the L^2 norm of the difference of two successive iterations (iteration i minus $i-1$) for the two variables H and Hu respectively. These results show that the algorithm has converged on the third iteration already. Such a fast convergence is due to the large overlapping region, which is something expected for an overlapping Schwarz scheme [46]. Figure 4.20 shows the computed free-surface elevation at $T = 5s$ of the converged overlapping SWRM with for the SV-Nwogu coupling and the monodomain solution, verifying that indeed the same result is achieved. These findings confirm the

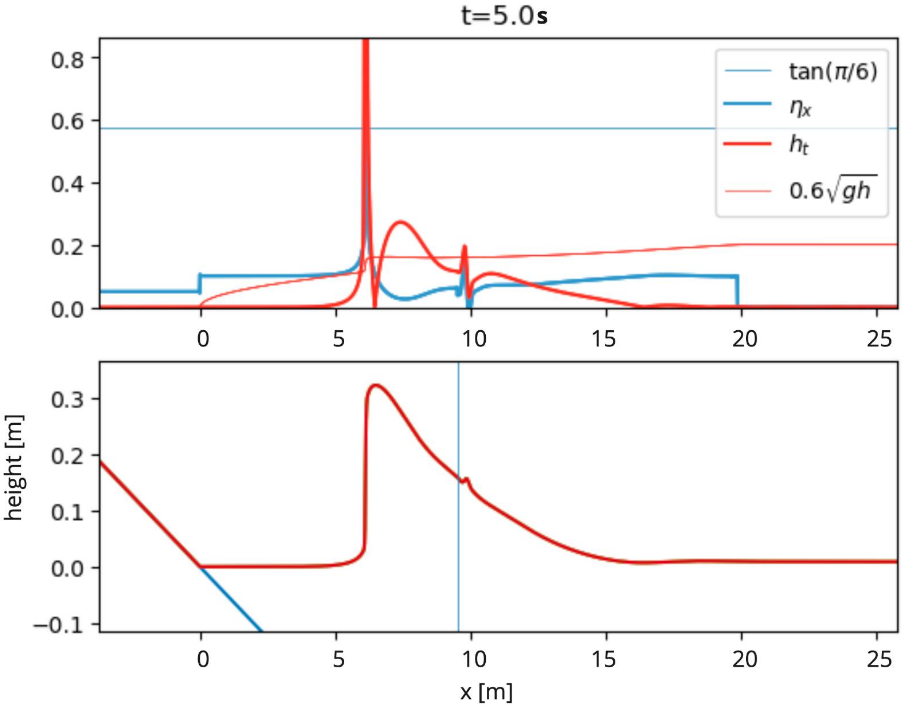

Figure 4.10: Values at $t = 5.0s$ of the magnitudes of the gradients $\partial_t H$, $\partial_x \eta$ and wave-breaking thresholds of section 4.3.4 (top figure) and wave heights (bottom) obtained with the hybrid model using Nwogu's equations for the simple beach case with mesh Δx_2.

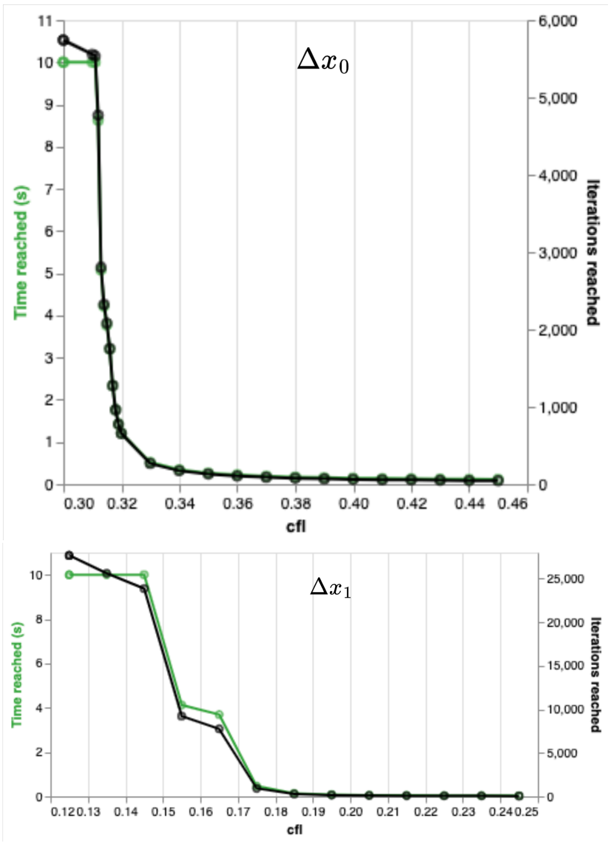

Figure 4.11: Time T and number of iterations reached by the simulations before a negative depth was detected as a function of the CFL number on meshes Δx_0 and Δx_1, artificial viscosity of $\nu = 0.1$ and a viscous width of $W = 1m$.

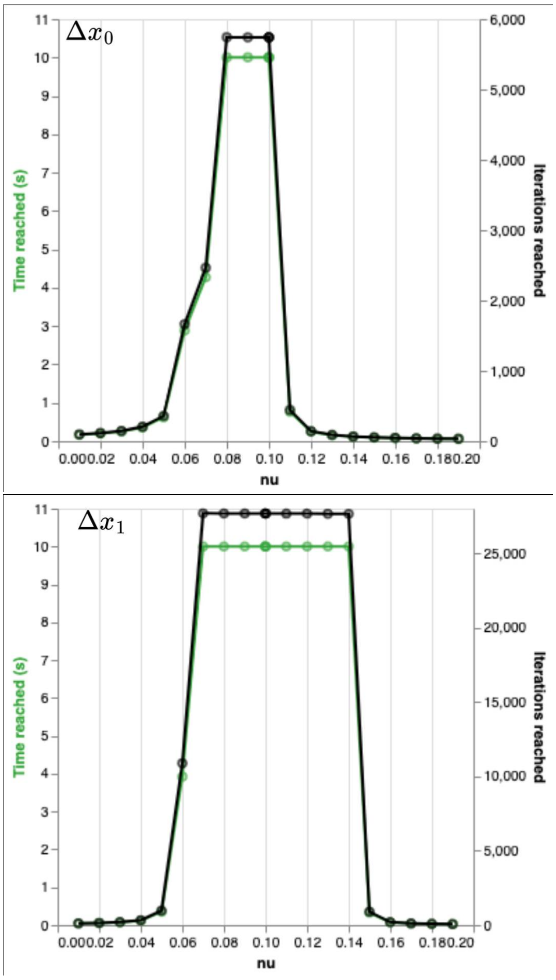

Figure 4.12: Time T and number of iterations reached by the simulations before a negative depth was detected as a function of the artificial viscosity ν on for mesh size Δx_0 and CFL=0.3 (top) and mesh size Δx_1 and CFL=0.125 (bottom); artificial viscosity of $\nu = 0.1$; and a viscous width of $W = 1m$.

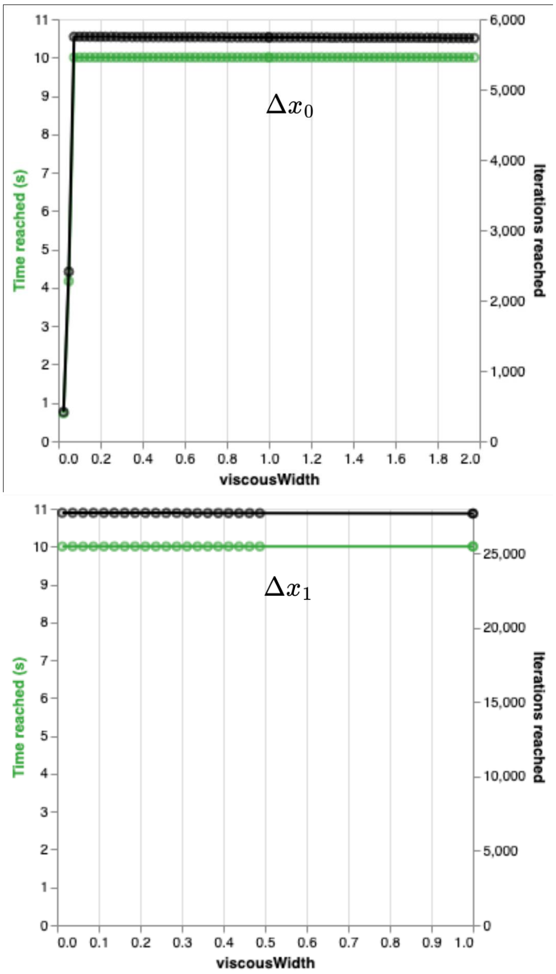

Figure 4.13: Time T and number of iterations reached by the simulations before a negative depth was detected as a function of the viscous width W on meshes Δx_0 and Δx_1 with CFL=0.3 (top) and CFL=0.125 (bottom); and artificial viscosity of $\nu = 0.1$.

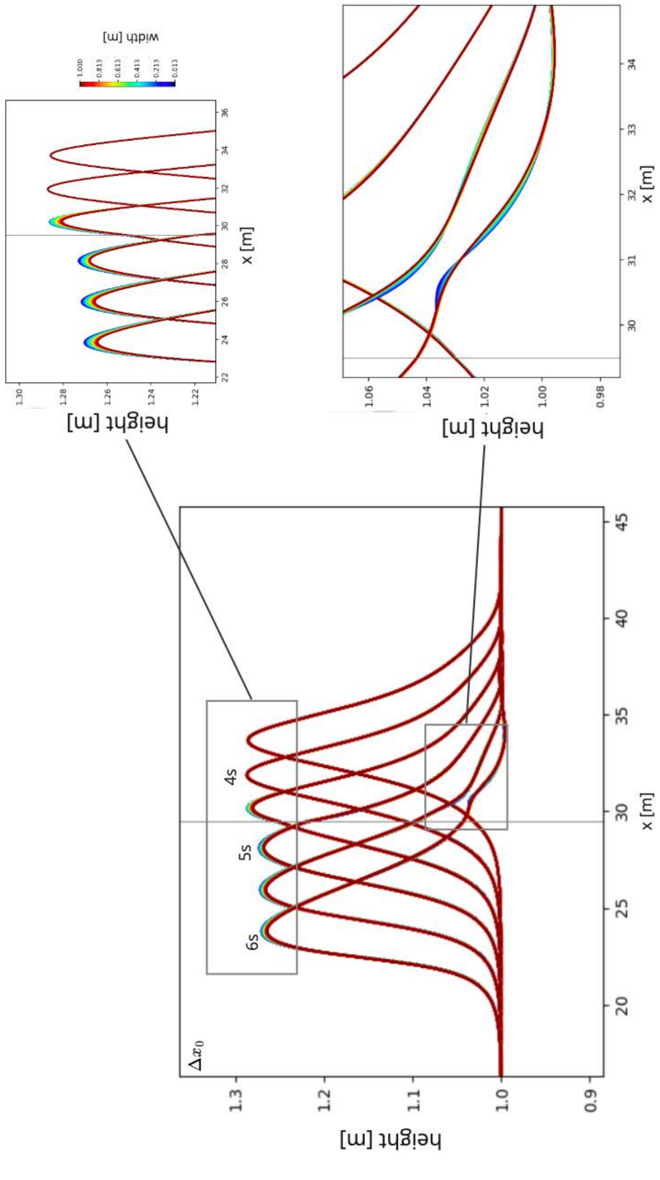

Figure 4.14: Snapshots of the free surface computed with mesh Δx_0 and for different values of W encoded in the color scale. Figure is rotated for better readability.

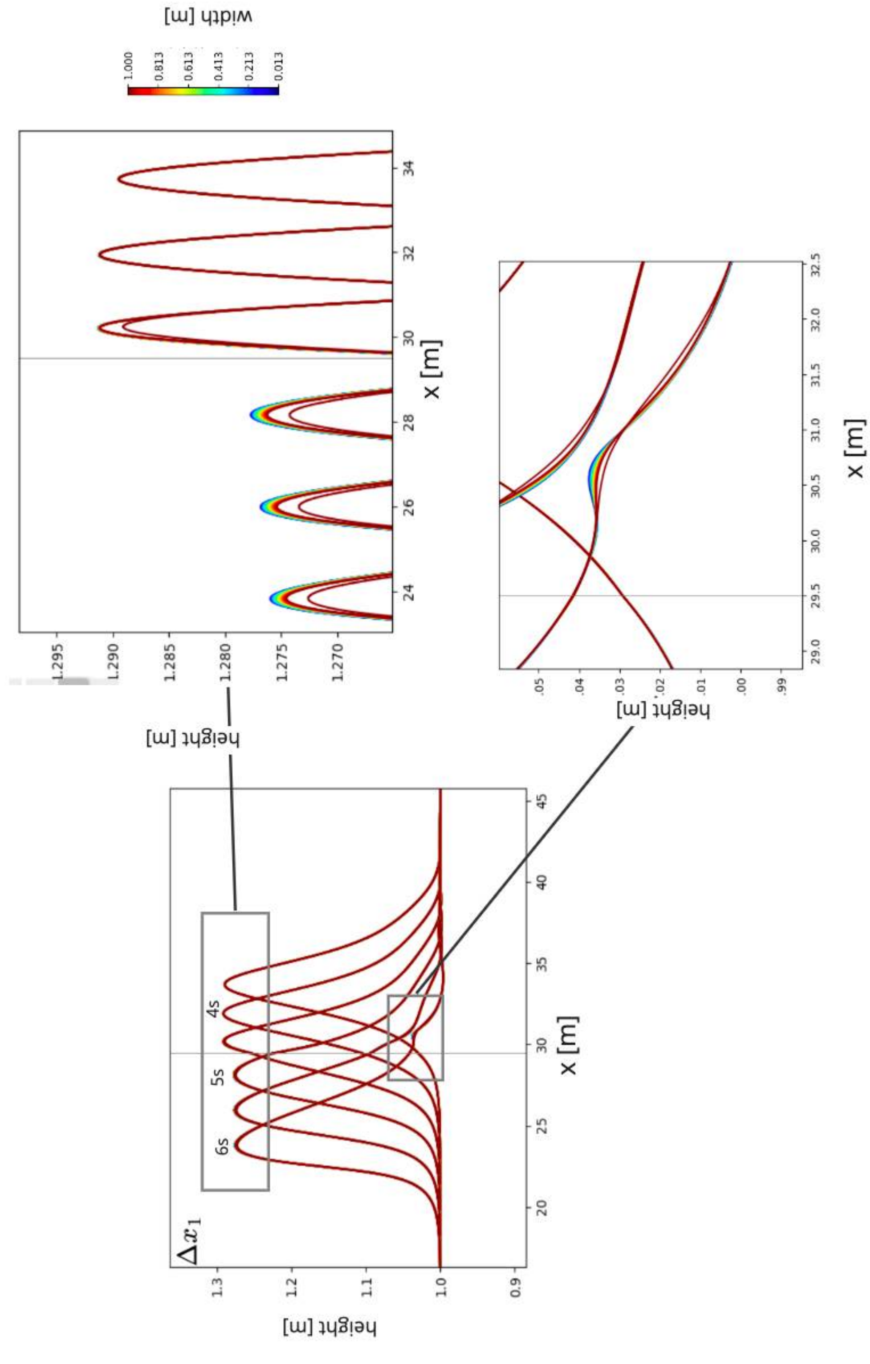

Figure 4.15: Snapshots of the free surface computed with mesh Δx_1 and for different values of W encoded in the color scale. Figure is rotated for better readability.

hypothesis that the transmission conditions (4.55) are a feasible strategy for domain decomposition of the Nwogu's model.

Mesh-convergence of the heterogeneous SV-Nwogu coupling Given that the transmission conditions (4.55) work properly in the homogeneous case (Nwogu-Nwogu coupling), now they are applied on the heterogeneous case $\mathcal{N}_- = \mathcal{N}_{SV}$ and $\mathcal{N}_+ = \mathcal{N}_{Nwogu}$. Specifically, the objective now is to see whether it is possible to obtain a mesh-convergent solution with the overlapping model, while paying attention to any artifacts that may be observed in the solution. A summary of the stability of the different cases is provided in Figure 4.32.

For the coarse mesh Δt_0, Δx_0 and an overlap of $L = 10m$ the SWRM converges in 1 iteration in Ω_- and in 2 iterations in Ω_+, as shown in Figures 4.22 and 4.23. This is explained by the wave speed, as was observed in [46]: because the interface at $x = c + L$ is far enough from $x = c$, where the initial guess is forced at, the trace $\boldsymbol{U}^1(c + L, \cdot)$ is unaffected and has reached limit of the SWRM for the time window chosen. This also means that, when solving for $\boldsymbol{U}_-^1$, the trace $\boldsymbol{U}_+^1(c+L, \cdot)$ already has the converged values. Similarly, because the algorithm is sequential and the trace $\boldsymbol{U}_-^1(c, \cdot)$ has converged, the solution $\boldsymbol{U}_+^2$ is the limit of the algorithm too. Figure 4.21 shows the free surface given by this limit for several instants during the propagation. It is observed that the shock develops as expected in Ω_-, however, in Ω_+ some oscillations appear at the interface $x = c + L$. This could be either due to a dispersive boundary layer such as the one observed in the classical Boussinesq model in [81, 18], or due to artifacts introduced by the discretization.

To distinguish discrete from PDE artifacts that appear in the solution the mesh-convergence study is continued. Refining the mesh to $\Delta t_1 = \Delta t_0/2$ and $\Delta x_1 = \Delta x_1/2$ renders the SWRM unable to converge due to instabilities in the interface of the dispersive domain. These instabilities could be explained by an incompatibility issue between the wave propagated by the dispersive domain and the incoming of the hyperbolic domain. This could be explained for example by the compatibility constraints needed to proof the local well-posedness of the solution in the transmission problem described in [18]. To fix this, smaller overlap sizes are tried. Since the overlap was already very large in comparison to the wave itself, this is the simplest way to make the data more compatible at $x = c$ and facilitate the convergence of the algorithm. Values of $L = 5m, 1m$ and $0.5m$ are tried, with only the latter providing a convergent algorithm. Figures 4.24 and 4.25 show that the convergence of the SWRM is achieved at 15 iterations. Such a number of iterations is expected because now both interfaces are very close so the algorithm is far from satisfying (4.56). Figure 4.26 shows the converged solution, including the values of the ghost cells. The only artifacts that appear are some height differences in the boundaries of the overlapping region and a small negative bump traveling upstream in the dispersive domain Ω_+.

When refining the mesh to $\Delta x_2 = \Delta x_0/4$, $\Delta t_2 = \Delta t_0/4$ the algorithm converges already in 15 iterations and the solution (Figure 4.27) displays similar artifacts as with the mesh $\Delta x_1, \Delta t_1$. Refining further to $\Delta x_3 = \Delta x_0/8$ and $\Delta t_3 = \Delta t_0/8$ causes the solution $\boldsymbol{U}_+^2$ to blowup at $t \approx 4.8s$, when the wave crosses the interface of the dispersive domain. This is similar to the instability with the large overlap $L = 10m$ explained earlier, that appeared due to the incompatibility of the interface data. Since the overlap is now reasonably small compared to the support of the wave, to fix this problem, the algorithm (4.51) is now initialized using the traces obtained with the limit of the previous mesh size, $\Delta t_2, \Delta x_2$, interpolated linearly to a resolution of Δt_3. Figures 4.28 and 4.29 show that the method reaches an iteration error in the L^2 norm of 10^{-12} at iteration 15 already with the new interpolated initial guess. This supports the hypothesis that the convergence problem is due to compatibility issues like those found on the dispersive boundary layer of the classical Boussinesq equations [18].

Figure 4.30 shows the evolution of the free surface for mesh Δx_4. Once again, these results also display the reflection that propagates upstream in the dispersive domain and the oscillations at the boundary, but with less dissipation than with the other meshes. Furthermore, Figure 4.31 compares the results with meshes Δx_1, Δx_2 and Δx_3. One can observe that the wavelength of these oscillation decreases proportionally to the mesh size but the solution approaches a limit. This suggests that these oscillations are a discrete artifact that will disappear in the limit $\Delta x \to 0$.

These observations suggest that the overlapping model with the SWRM is approaching a mesh convergent solution while mantaining a constant ratio of $\Delta t/\Delta x$, which was not possible with the hybrid model. Also, this converged solution displays a reflected wave that is similar to the hybrid's. However, special care has to be taken with the calibration of the overlap size and the initial guess, which calls for additional research at the discrete level.

4.5.4 Overlapping direct solver

Unlike the SWRM solver, the direct solver is stable for the whole duration $T = 6s$ with a mesh size Δx_1 when using overlaps of $L = 10m$, $L = 5m$, $L = 1m$ and $L = 0.5m$. For the sake of comparison with the SWRM the convergence study is made with the latter. This is also convenient to only have duplicate values on a tiny region of the domain. A summary of the stability results is displayed in Figure 4.32.

Using an overlap of $L = 0.5m$ the direct overlapping solver is stable for mesh sizes $\Delta x_0, \Delta x_1$ and Δx_2 with the same Δt as the SWRM. For the finest mesh Δx_3 with timestep size Δt_3 the solver became unstable at the dispersive interface around $3.8s$ in the computations, but taking a timestep size of $\Delta t_3/2$ stabilized it.

Figure 4.34 shows the free surface elevation with the finest mesh. Compared to the results of the SWRM (displayed on Figure 4.33), the differences between both solvers, the direct and SWRM overlapping solvers, are minor but non-zero. Moreover, as with the SWRM, the main artificial features displayed by the results of the direct solver are small right-propagating waves inside the dispersive domain Ω_+; and shorter oscillations very close to the dispersive boundary.

To examine these shorter oscillations, Figure 4.34 shows a close-up view of the solution around the overlap. As with the SWRM, short oscillations are observed on the boundary, and their wavelengths decrease proportionally to the mesh-size Δx. This suggests that they are an artifact introduced by the discretization, and not by the dispersive boundary layer or other continuous-level phenomena.

Fgure 4.35 shows a larger region that includes the waves propagating inside the domain on different meshes. Unlike the short waves observed right at the

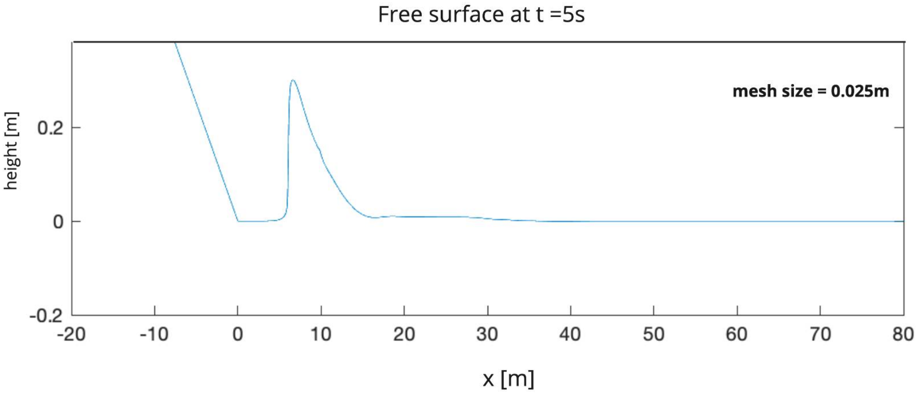

Figure 4.16: Last step reached by the Nwogu's solver with the static interface with the coarse mesh $\Delta x = 0.025m$ and CFL=0.3. The solver is able to reach $T = 5s$.

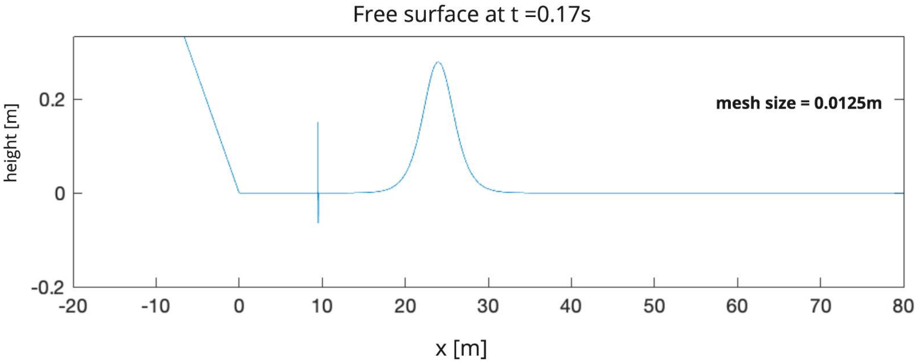

Figure 4.17: Some steps before the last one reached by the Nwogu's solver with the static interface with the coarse mesh $\Delta x = 0.0125m$ and CFL=0.3. The solver only reaches around $T = 0.17s$, then it turns unstable at the interface.

dispersive boundaries these waves do not change in wavelength when refining and their amplitude increases slightly with the finest meshes, due to the decrease in numerical diffusion. Moreover, they also match the description of wave reflections introduced by the interface also observed in the previous methods.

4.6 Results with Green-Naghdi coupled models

4.6.1 Green-Naghdi's hybrid model

Figure 4.36 shows the computed free surface using the hybrid model of Green-Naghdi with a static interface located at $x = 9.5$ on the solitary wave case with the simple-beach bathymetry of Figure 4.5, Equation (4.68). The mesh size is chosen as $\Delta x_0 = 0.025m$, $\Delta x_k = \Delta x_0 2^{-k}$, $k = 1, 2, 3$, $CFL = 0.3$ in all of them and the first-order FV method is used for the hyperbolic fluxes. One can observe that, unlike with Nwogu's model, for the range of mesh sizes explored

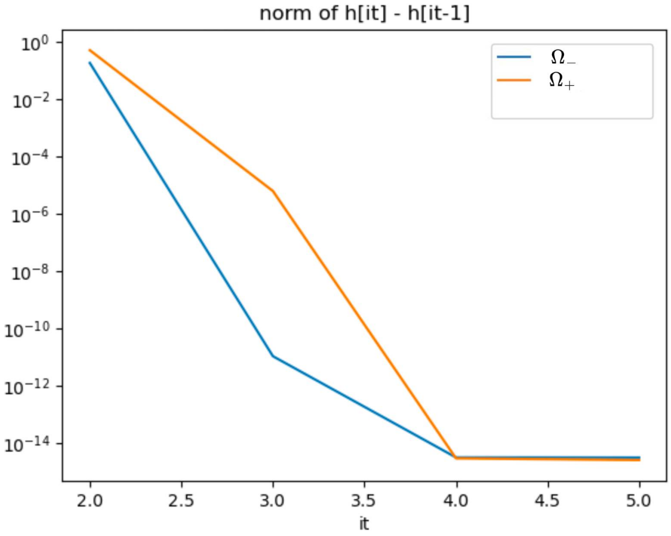

Figure 4.18: L^2 norm of the difference in H of iterations it and $it-1$ on each subdomain in the homogeneous coupling algorithm.

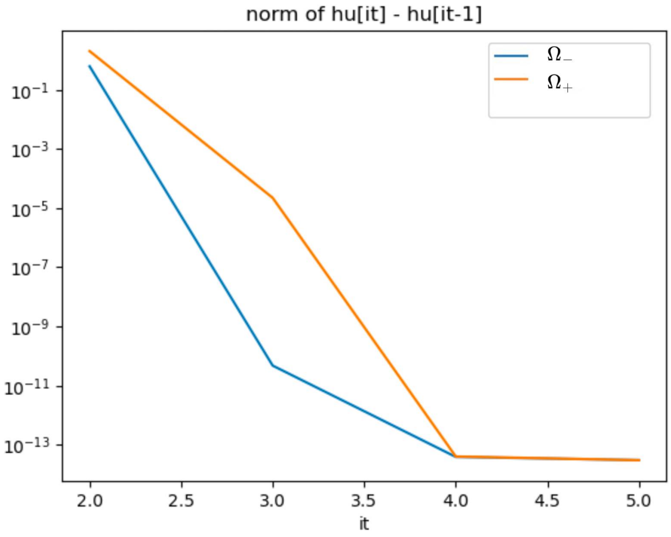

Figure 4.19: L^2 norm of the difference in Hu of iterations it and $it-1$ on each subdomain in the homogeneous coupling algorithm.

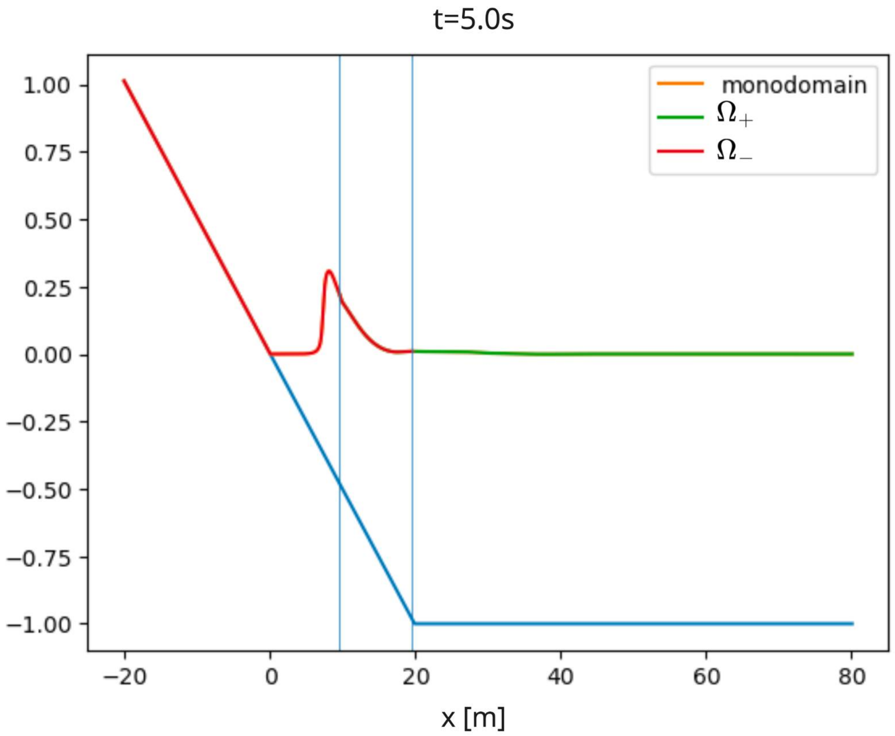

Figure 4.20: Free-surface elevation at $T = 5s$ of the converged overlapping SWRM and the monodomain solution with the Nwogu model that verifies that the same solution is obtained. Here $L = 10$ and the coarse mesh $\Delta x = 0.025m$ is used. Vertical lines denote the artificial boundaries.

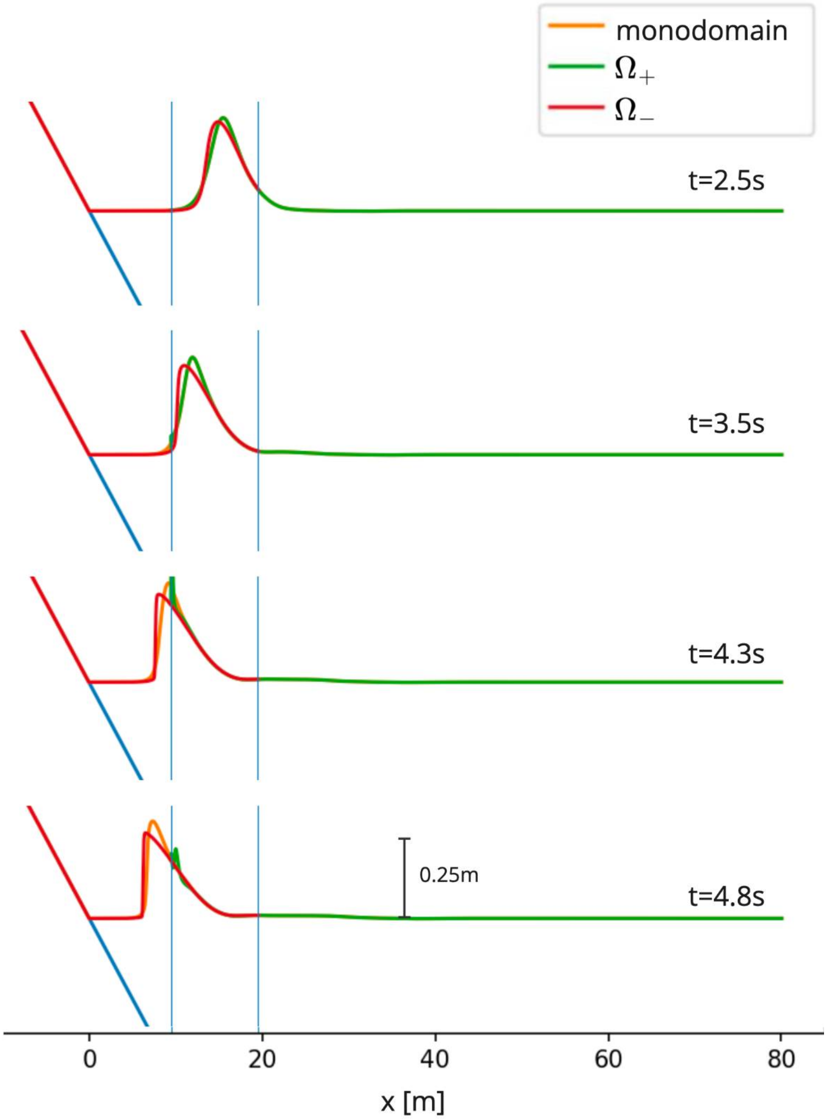

Figure 4.21: Free-surface computed with the coupled SWRM overlapping model and the Nwogu monodomain solution, for overlap of $L = 10m$ length and the coarse mesh $\Delta x = 0.025m$. Vertical lines denote the artificial boundaries.

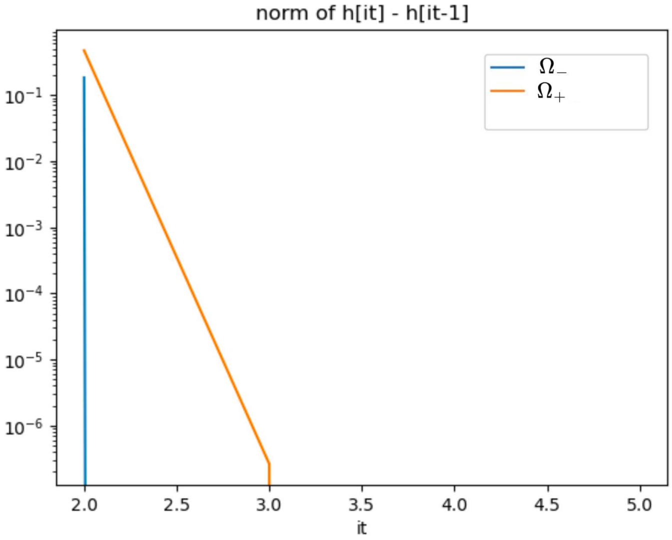

Figure 4.22: L^2 norm of the difference in H of iterations it and $it-1$ on each subdomain in the heterogeneous coupling algorithm and coarse mesh.

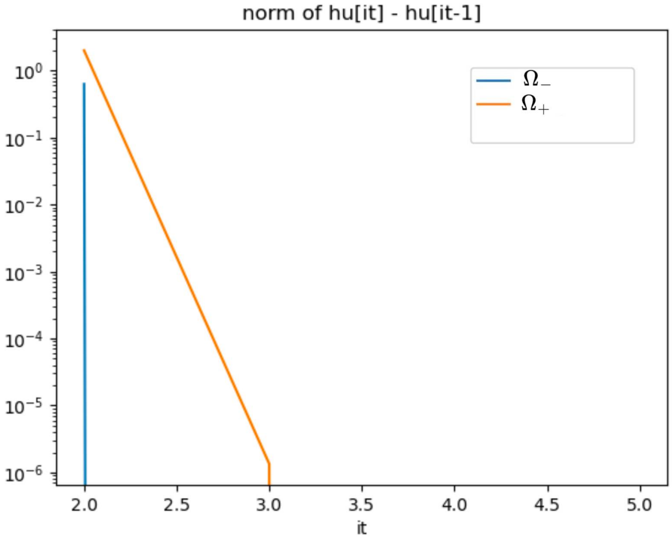

Figure 4.23: L^2 norm of the difference in Hu of iterations it and $it-1$ on each subdomain in the heterogeneous coupling algorithm and coarse mesh.

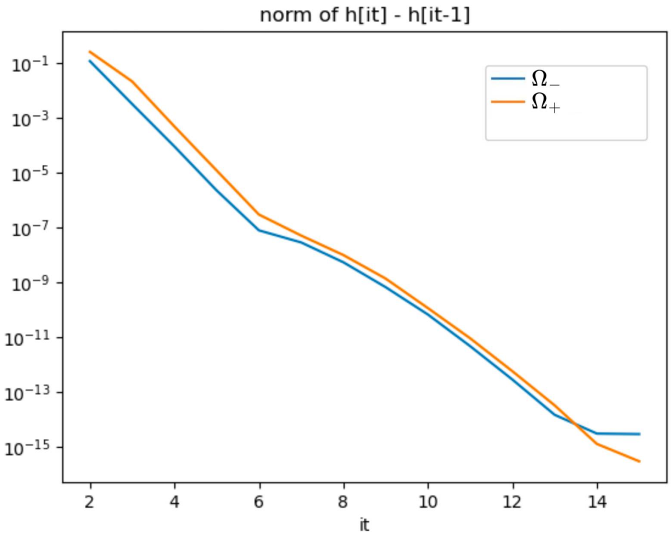

Figure 4.24: L^2 norm of the difference in H of iterations it and $it-1$ on each subdomain in the heterogeneous coupling algorithm and fine mesh $\Delta t_1, \Delta x_1$, with overlap $L = 0.5m$

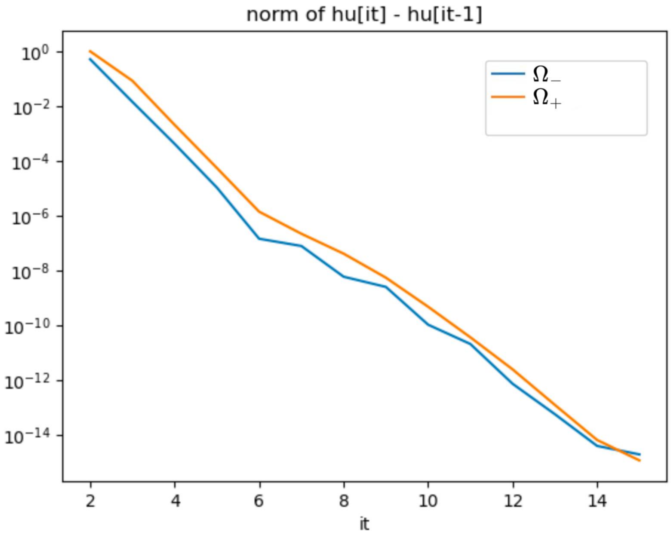

Figure 4.25: L^2 norm of the difference in Hu of iterations it and $it-1$ on each subdomain in the heterogeneous coupling algorithm and fine mesh $\Delta t_1, \Delta x_1$, with overlap $L = 0.5m$

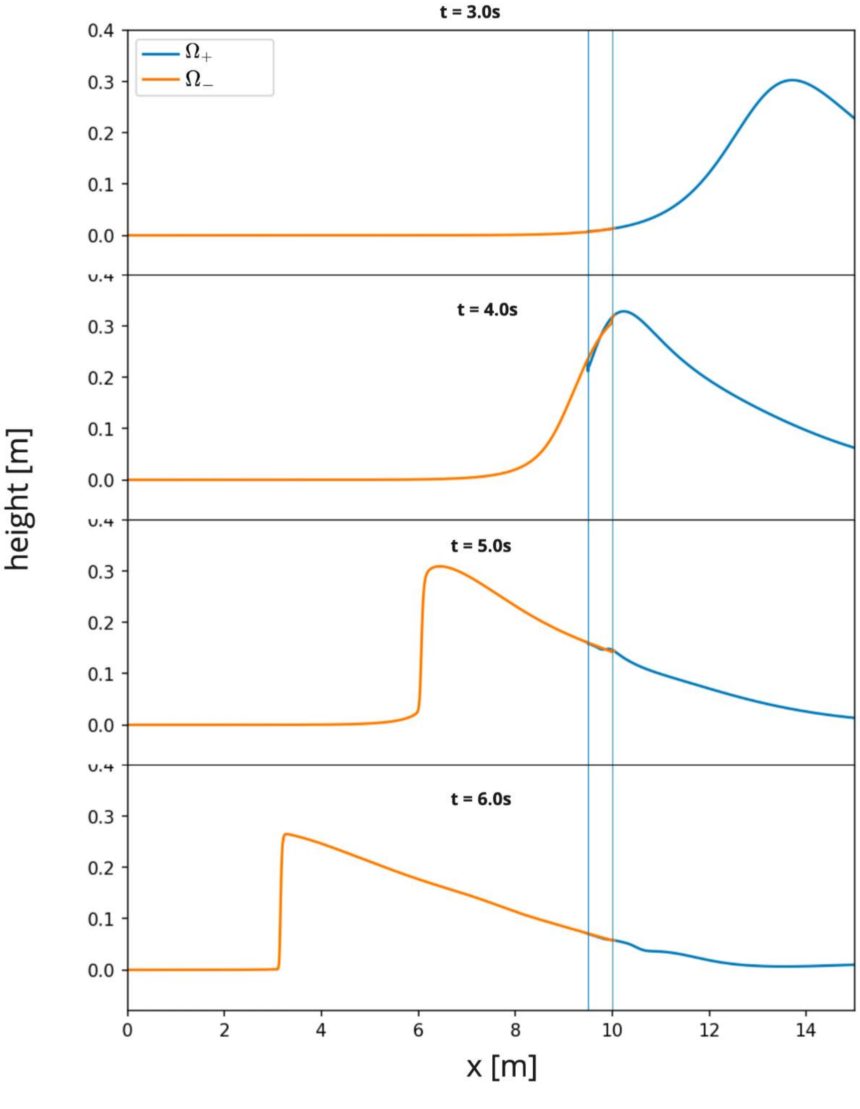

Figure 4.26: Solution of the coupled overlapping model computed with the SWRM for $L = 0.5$ and a mesh $\Delta t_1 = \Delta t_0/2$ and $\Delta x_1 = \Delta x_0/2$. Vertical lines denote the artificial boundaries.

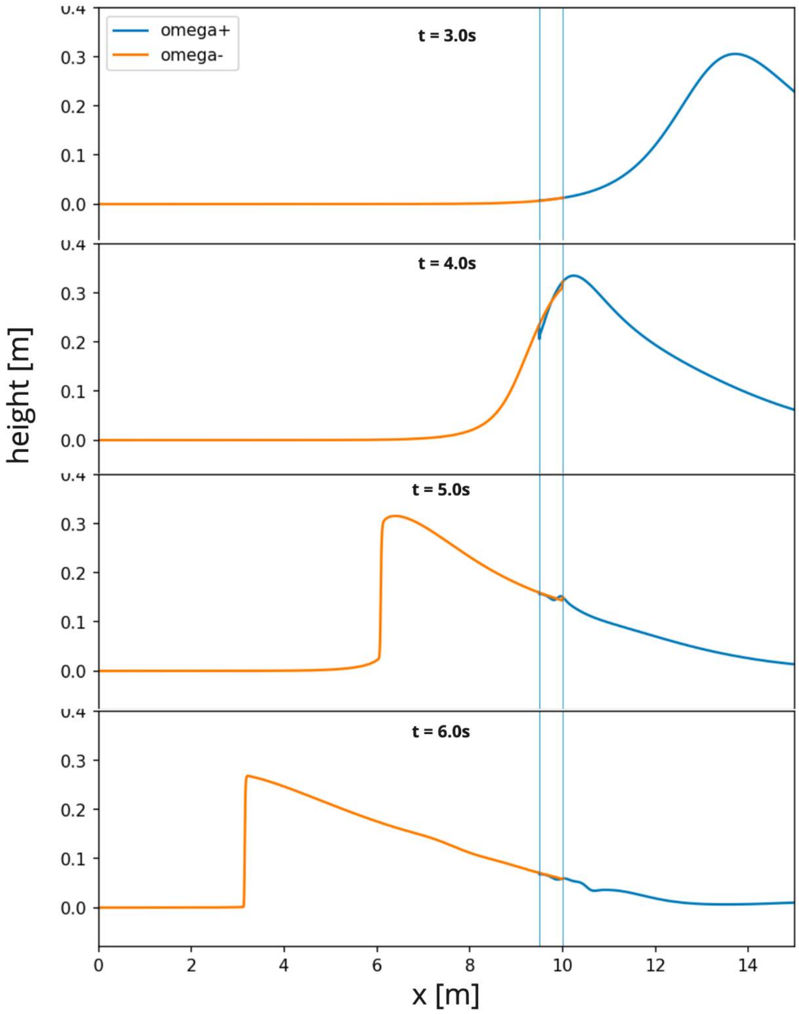

Figure 4.27: Solution of the coupled overlapping model computed with the SWRM for $L = 0.5$ and a mesh $\Delta t_2 = \Delta t_0/4$ and $\Delta x_2 = \Delta x_0/4$. Vertical lines denote the artificial boundaries.

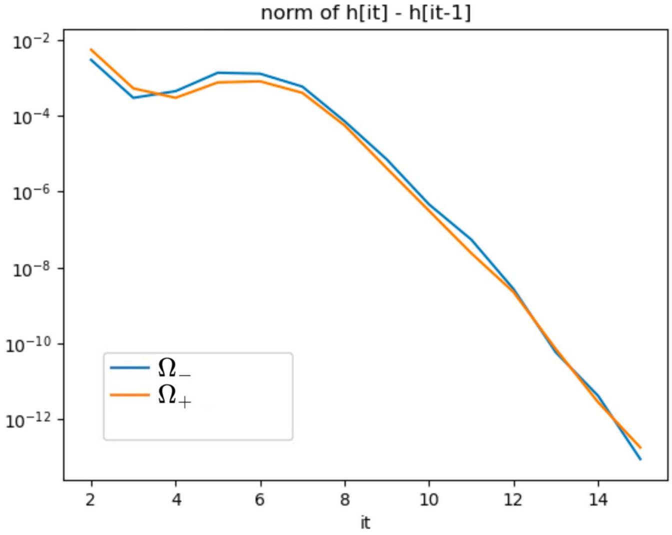

Figure 4.28: L^2 norm of the difference in H of iterations it and $it-1$ on each subdomain in the heterogeneous coupling algorithm and fine mesh $\Delta t_3, \Delta x_3$, with overlap $L = 0.5m$ and initial traces interpolated from the converged solution of mesh Δt_2, Δx_2

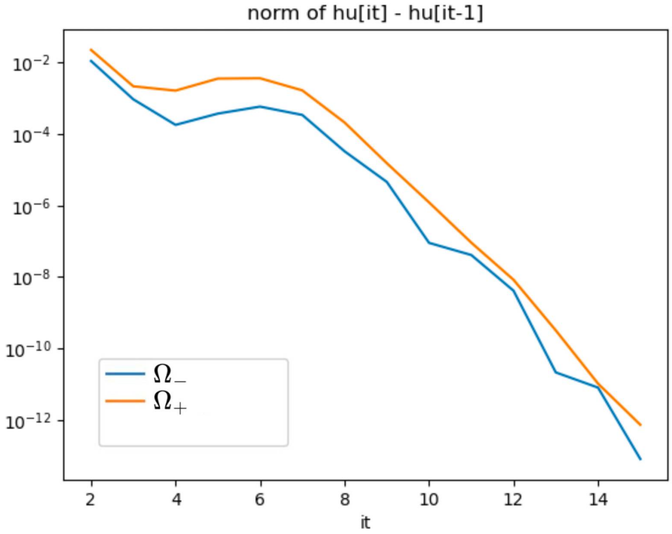

Figure 4.29: L^2 norm of the difference in Hu of iterations it and $it-1$ on each subdomain in the heterogeneous coupling algorithm and fine mesh $\Delta t_3, \Delta x_3$, with overlap $L = 0.5m$ and initial traces interpolated from the converged solution of mesh Δt_2, Δx_2

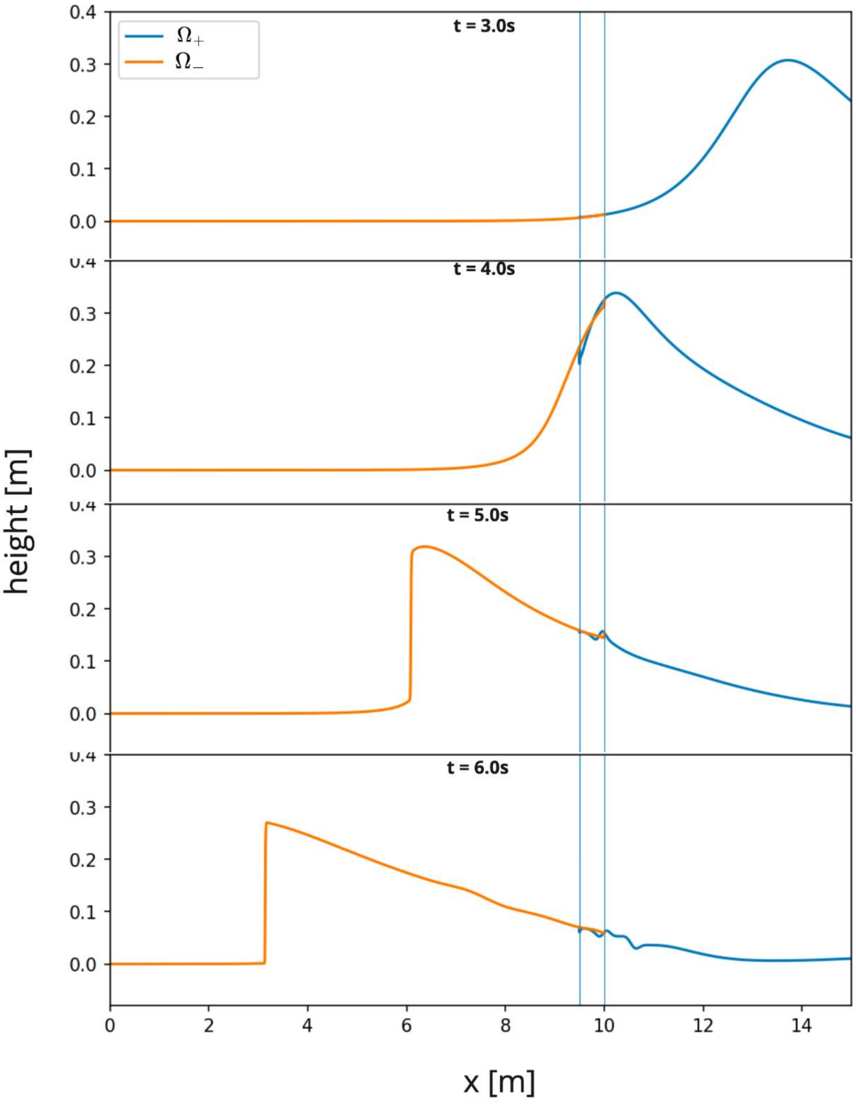

Figure 4.30: Solution of the coupled overlapping model computed with the SWRM for $L = 0.5$ and a mesh $\Delta t_3 = \Delta t_0/8$ and $\Delta x_3 = \Delta x_0/8$. Vertical lines denote the artificial boundaries.

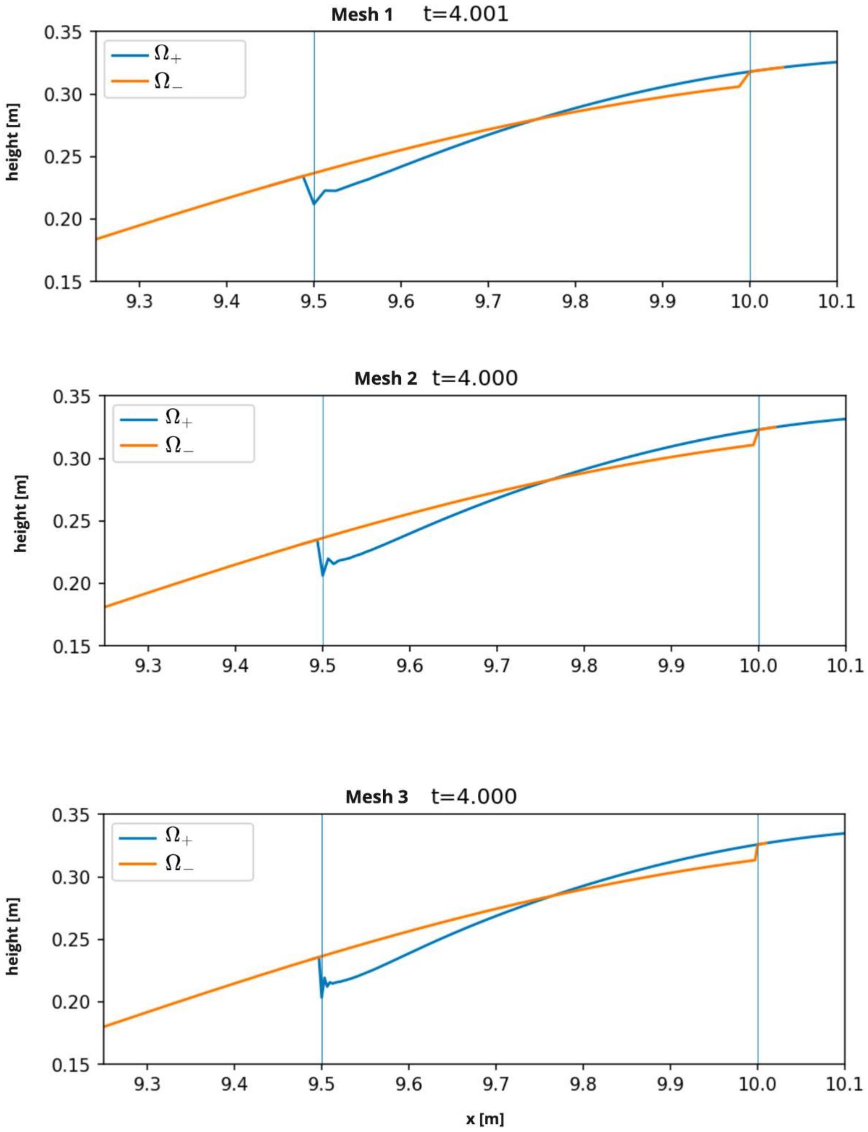

Figure 4.31: Zoom-in around the overlap region with Mesh 1 (Δx_1), Mesh 2(Δx_2) and Mesh 3 (Δx_3)

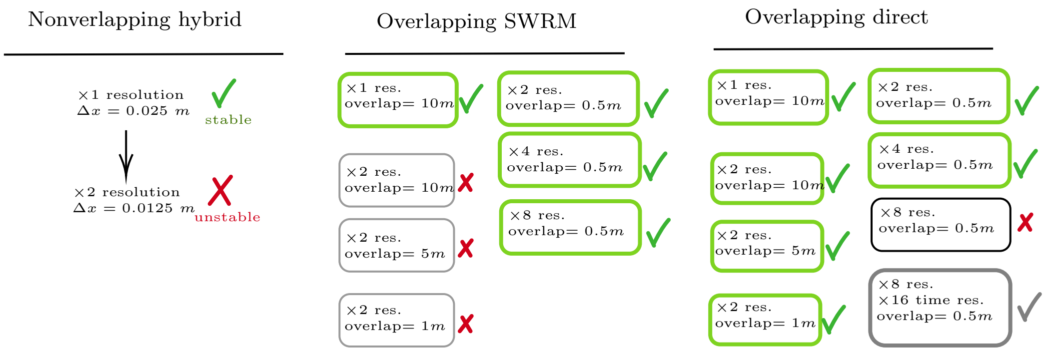

Figure 4.32: Summary of results with the hybrid, overlapping SWRM and direct overlapping solvers.

and a duration of $T = 10s$ the GN model remains stable. This is consistent with the results obtained in [70]. Additionally, unlike Nwogu's hybrid model, no reflected wave is visible in the computations.

Since there are no visible artifacts in the previous results the mesh-convergence with the variable breaking criteria (4.34) is examined. Figures 4.37, 4.38 and 4.39 show snapshots of the free surface and SV subdomains at different times. These results are computed with mesh sizes Δx_0, Δx_1 and Δx_2 using the variable breaking criteria of (4.34). One can observe that even though the model is stable, mesh-dependent oscillations appear after 7s, spoiling the convergence of the solution. Moreover, some of these oscillations are detected as breaking waves.

4.6.2 Offline breaking criteria using coarse mesh results

In order to reduce the sources of variability, next an ”offline” breaking criteria is introduced, obtained by computing the wave-breaking regions from a coarse mesh Δx_0, and then using it on the finer meshes. Figure 4.40 shows in black lines the curves in the $x - t$ plane of the minimum and maximum values of $x(t)$ respectively, where the SV model was used in the results shown in 4.37. The offline breaking criteria consists in approximating these points with least-squares linear regressions, and obtaining the subdomains of the wetted part of the $x - t$ plane as

$$\begin{aligned} Q_{SV} &= \{(x,t) : x_L(t) \leq x \leq x_R(t), t_0 \leq t \leq t_f \quad H(x,t) > 0\} \\ Q_{GN} &= \{(x,t) : (x,t) \notin Q_{SV}, \quad H(x,t) > 0\} \end{aligned} \tag{4.69}$$

which in this case gives $x_L(t) = -2.75t + 29.40$, $x_R(t) = -2.95t + 22.07$, $t_0 = 5.68s$ and $t_f = 7.23s$. Figures 4.41 and 4.42 show a close-up view of the results computed with the offline method and with mesh sizes Δx_0, Δx_1 and Δx_2. It is clear that the mesh-convergence problem still persists. Moreover, from these results it is possible to observe a spurious wave-packet whose wavelength decreases with Δx appearing at $t = 7s$ for x close but greater than $x_R(t)$. This wavepacket then evolves and grows becoming the large spurious waves observed at $t = 7.5s$.

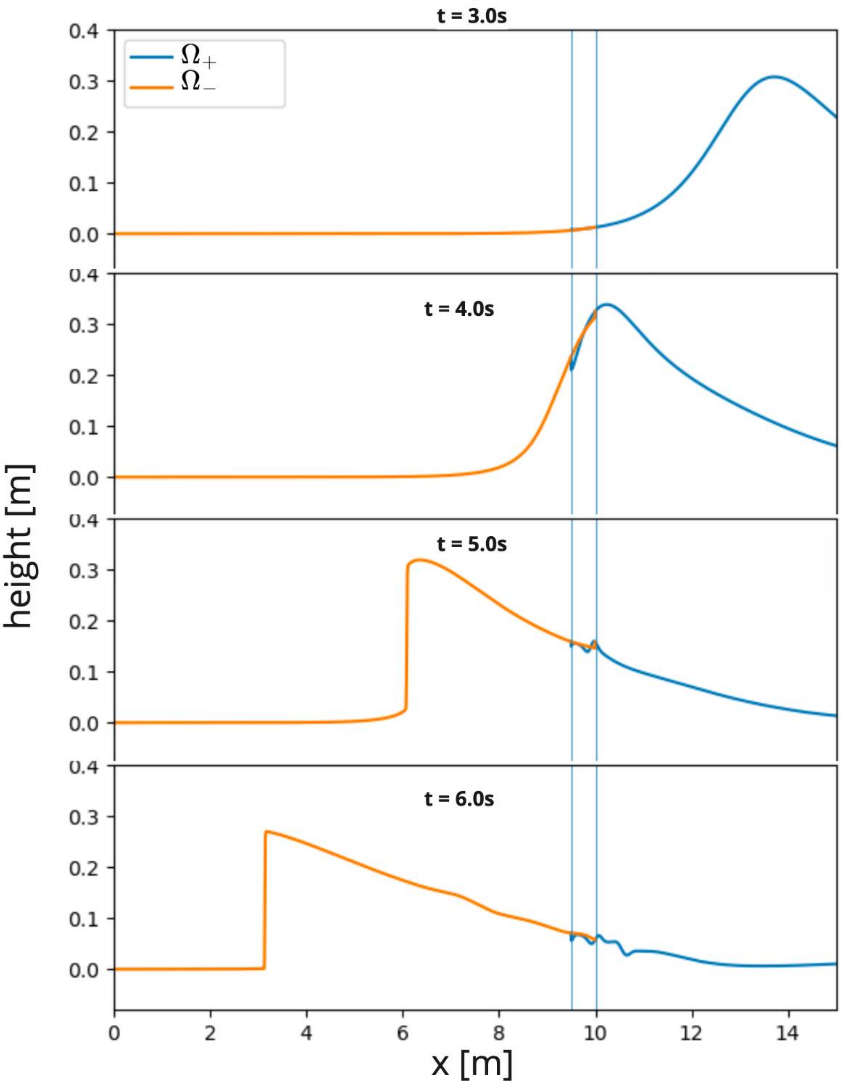

Figure 4.33: Solution of the coupled overlapping model computed with the direct solver, $L = 0.5$ and mesh $\Delta x_3 = \Delta x_0/8$, $\Delta t_3 = \Delta t_0/16$. Vertical lines denote the artificial boundaries.

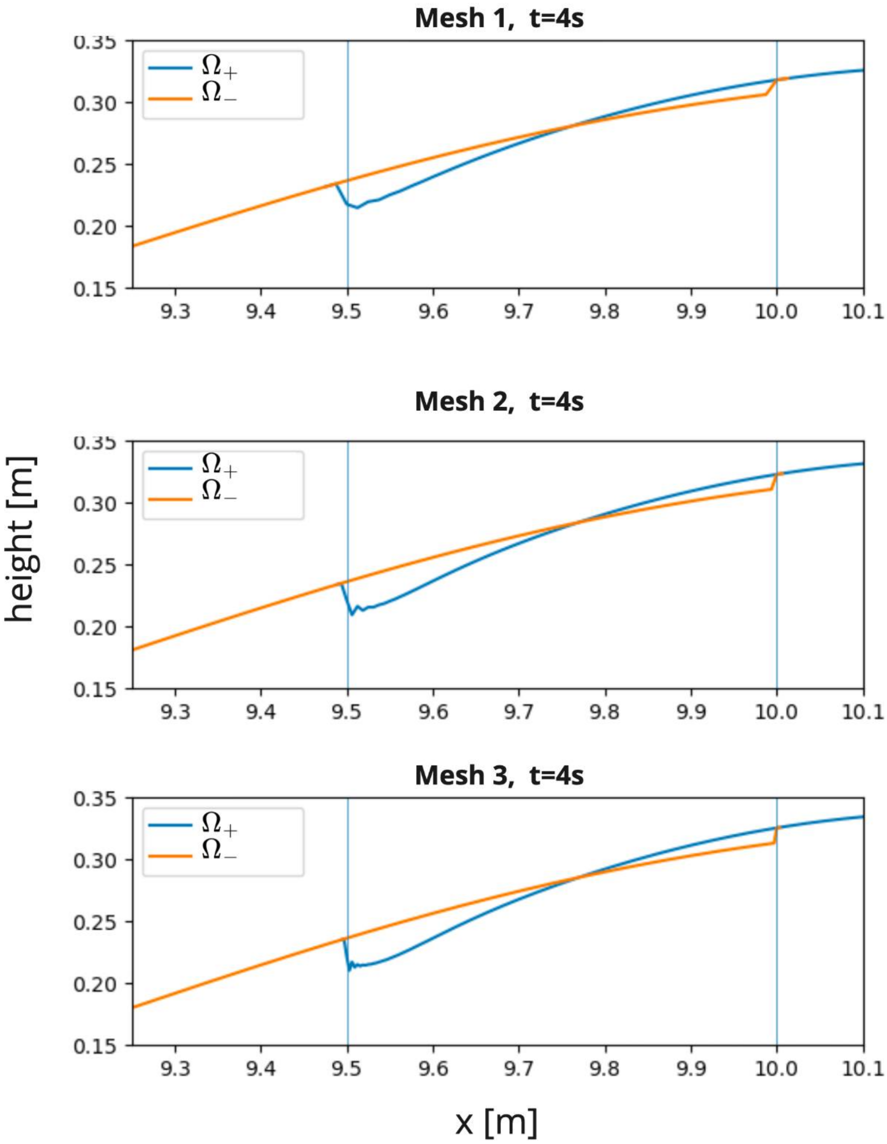

Figure 4.34: Using the direct overlapping method, the figures show a zoom-in view around the overlap with Mesh 1 (Δx_1, top), Mesh 2(Δx_2, middle) and Mesh 3 (Δx_3, bottom).

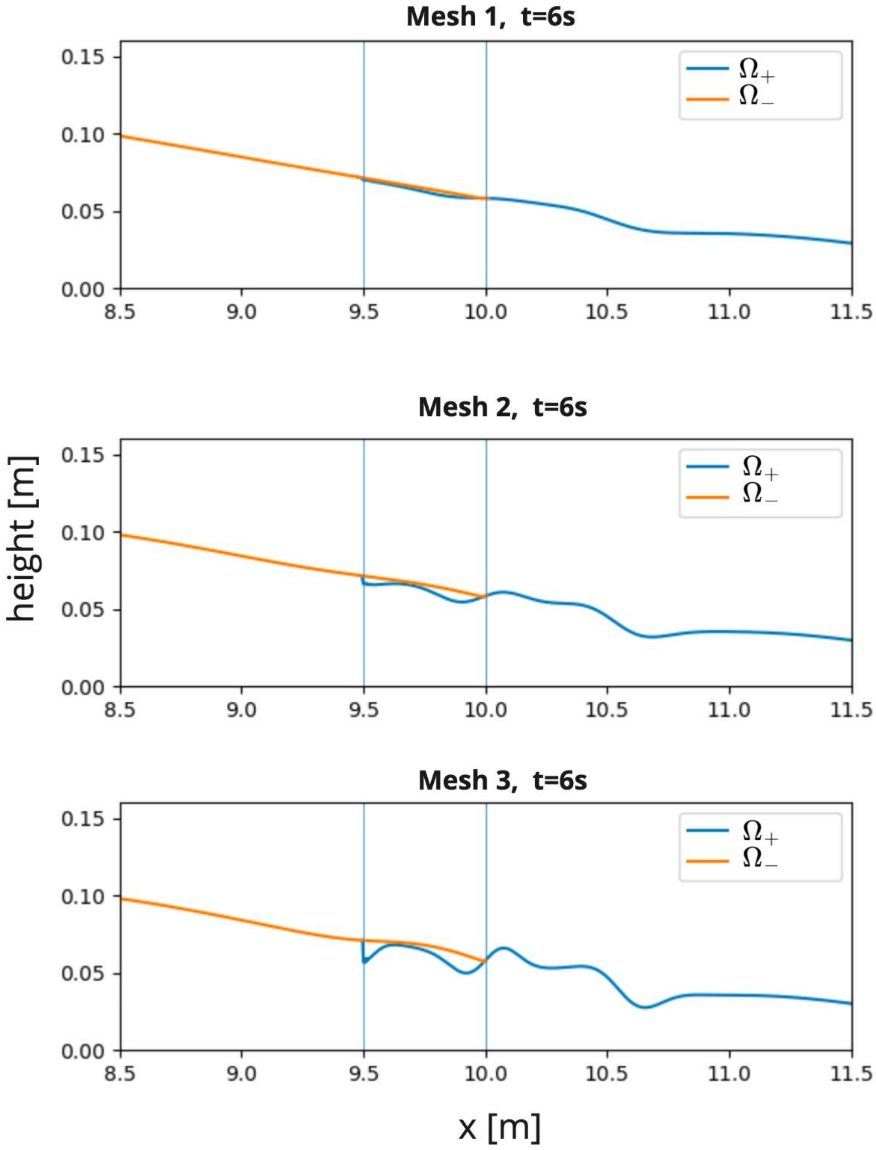

Figure 4.35: Zoom-in around the overlap on a larger region. Results computed with the direct overlapping model on Mesh 1 (Δx_1, top), Mesh 2(Δx_2, middle) and Mesh 3 (Δx_3, bottom)

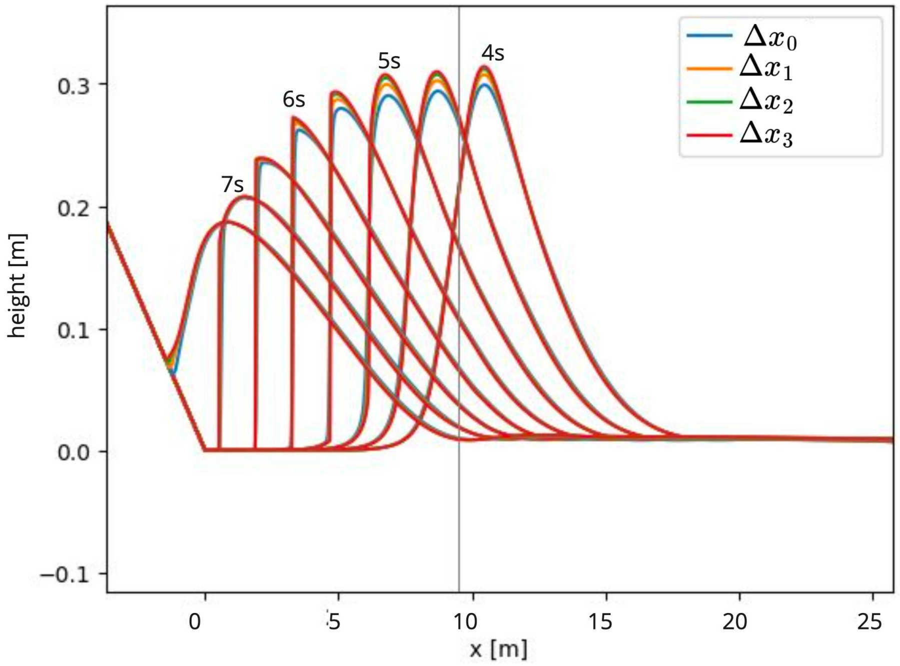

Figure 4.36: Snapshots of the free surface computed with the hybrid Green-Naghdi model with a static interface located at $x = 9.5m$ and $CFL = 0.3$, on the solitary wave case with the simple-beach bathymetry.

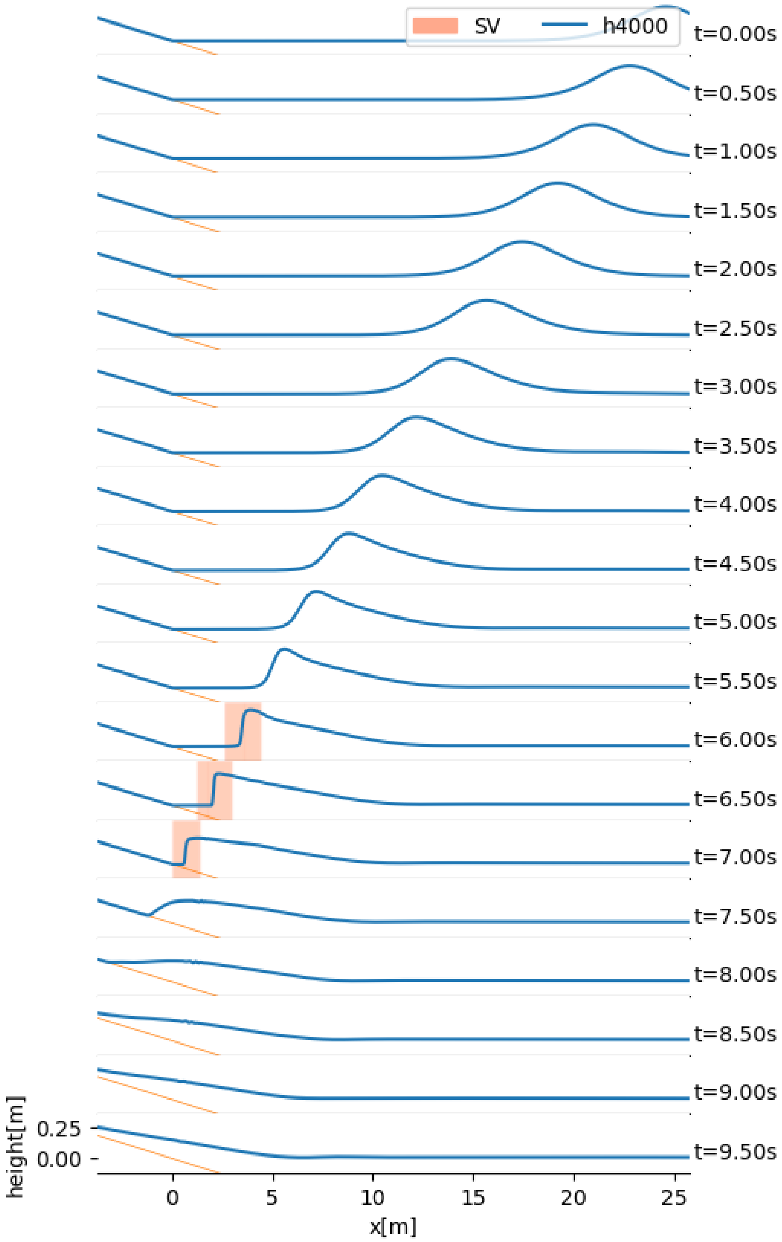

Figure 4.37: Snapshots of the free surface at different times computed with mesh size Δx_0 using the variable breaking criteria

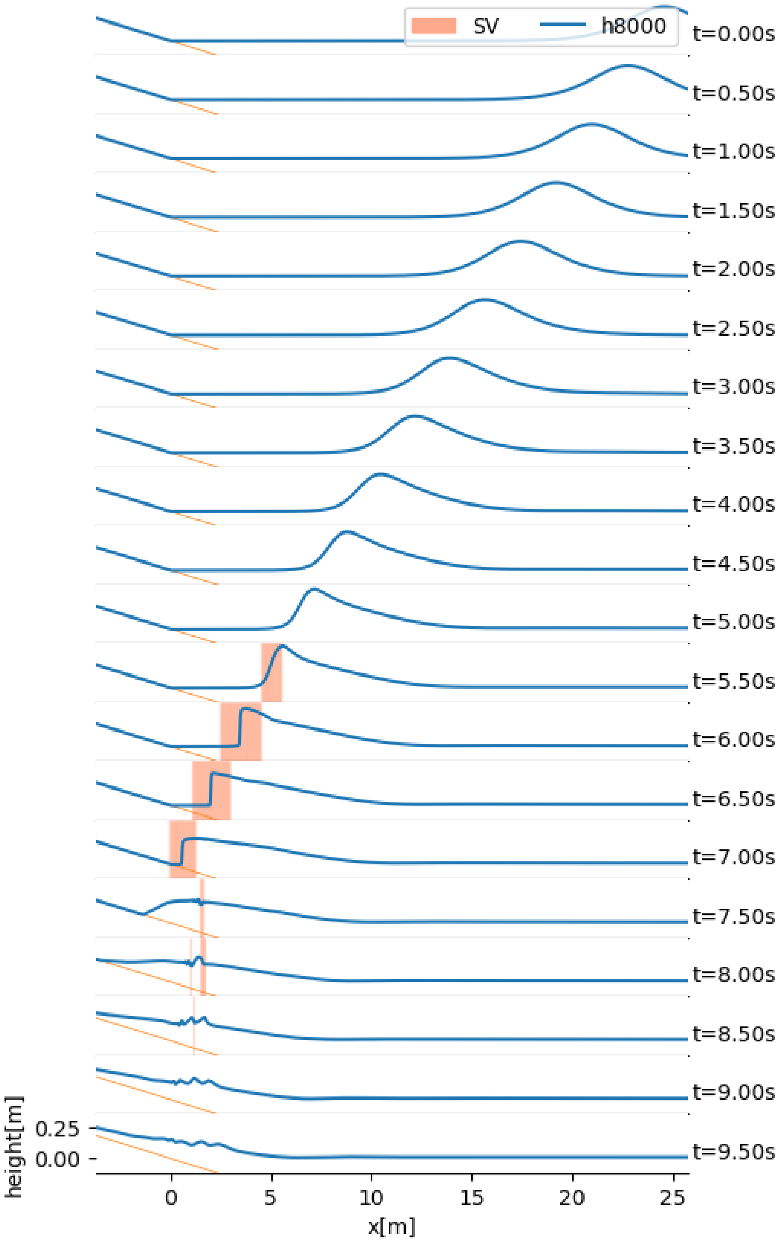

Figure 4.38: Snapshots of the free surface at different times computed with mesh size Δx_1 using the variable breaking criteria

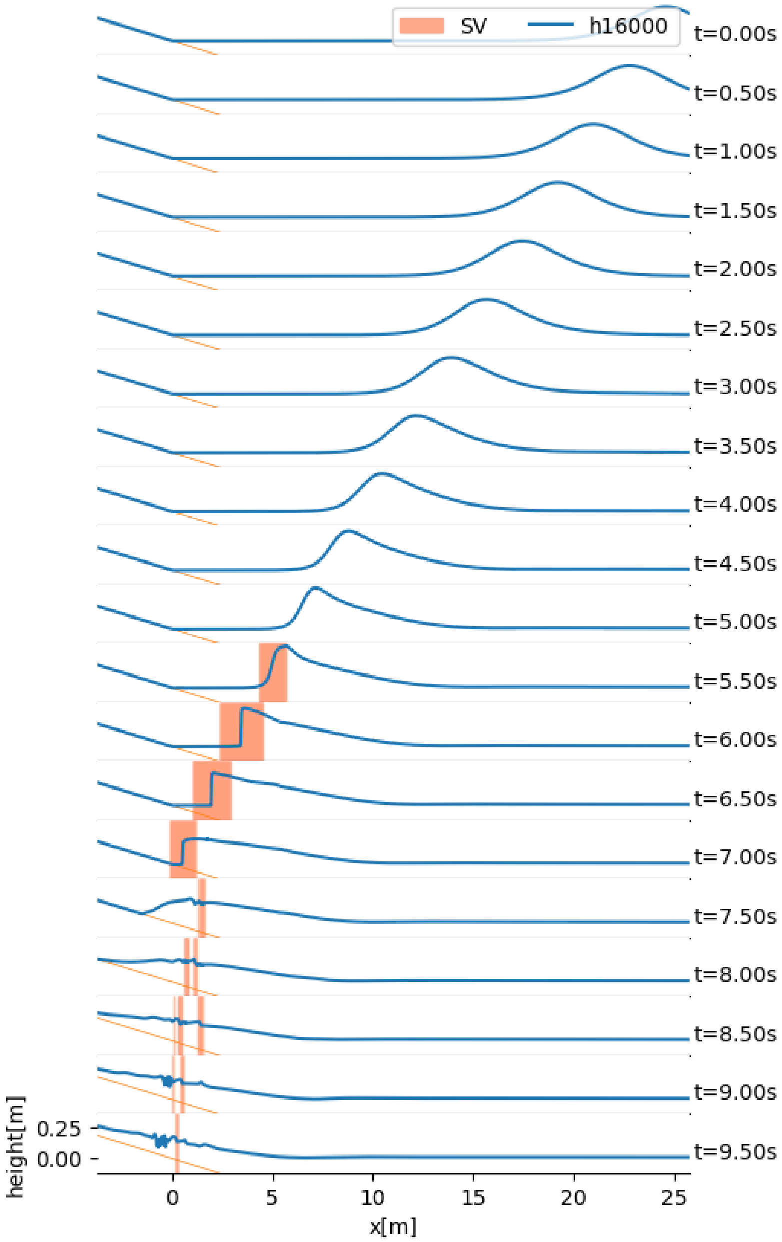

Figure 4.39: Snapshots of the free surface at different times computed with mesh size Δx_2 using the variable breaking criteria

4.6.3 Deep inspection of the moving-interface problem

To clarify how these unexpected waves arise, Figure 4.43 shows the free surface just before the large, unexpected waves begin to form, zooming in on a small bump that later turns into these waves. In the right column of Figure 4.43, we observe this bump originating as a small irregularity within the SV domain, which then continues moving offshore, albeit more slowly than $x_R(t)$. As it moves within the GN model's subdomain the bump increases in size. This indicates that the SV model initially creates the bump, and the GN model contributes to its growth. To verify the SV model's role in forming the initial bump, we rerun the simulations with the same initial conditions and parameters, but this time using only the SV model across the entire domain. Figure 4.44 displays the free surface computed at $t = 7s$, highlighting the wave's peak with different mesh sizes ($\Delta x = \Delta x_0 2^{-k}, k = 0, .., 4$), and indeed shows a tiny irregularity at the wave's leading edge. This issue doesn't occur when we use a flat bottom and apply the SV equations throughout, as Figure 4.45 demonstrates, which aligns with the expected behavior of the Finite Volume scheme's monotonicity-preserving nature. Figure 4.46 presents results from the SV model using the fourth-order scheme of 4.3.5 with only the SV model computed on the simple-beach scenario. Now the free surface is free from irregularities. Back again to the hybrid model with the breaking criteria of Section 4.3.4, Figure 4.47 shows the results using the fourth order scheme on several meshes, to be compared with Figures 4.41 and 4.42. Additionally, Figure 4.48 shows the results with the finest mesh Δx_3 and the fourth-order scheme. Clearly, the model is now able to approach a mesh-independent solution. This highlights that while the SV model can handle small mesh-specific issues without significant problems, these can become much larger when transmitted to the GN model. As it was just demonstrated, in the present scheme these artifacts were introduced by the first-order topography discretization.

Next chapters will address the question of why and how this transmission problem works from a theoretical point of view, and why the BT model (GN in the current case) can be sensitive to small perturbances while the SV model is not.

4.7 Conclusions

In this chapter the performance of the coupled models Nwogu-SV and GN-SV have been examined with the goal of understanding the source of the artifacts that have previously been observed in the literature. As pointed out in the introduction, understanding such features is important to ensure the efficiency and robustness of these models. The performance has been assessed on the case of a propagating solitary wave over either a simple beach profile or a bathymetry of constant depth by conducting a mesh-convergence study. To conclude, the main observations have been grouped using the questions of the beginning of this chapter:

(I) Oscillations: Are the short oscillations that have been reported a part of the solution or a problem of the discretization? The best explanation from the data that was obtained is that these oscillations are reflected

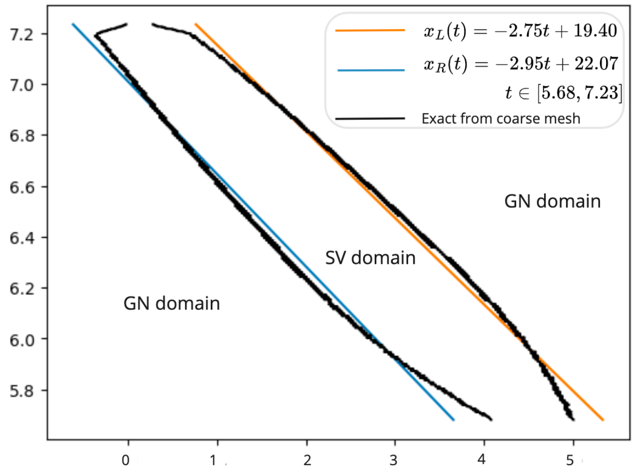

Figure 4.40: Boundaries of the SV domain where wave breaking is simulated. Black line denotes the boundary obtained from the variable breaking criteria on the coarse mesh Δx_0. The other lines are the linear regressions that approximate this region, and that are used to define the offline criteria.

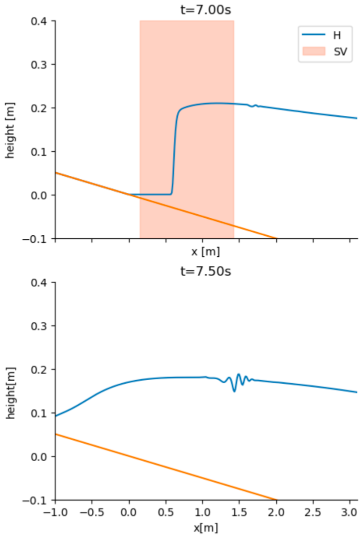

Figure 4.41: Close-up view of the results computed with the offline method with mesh size Δx_0

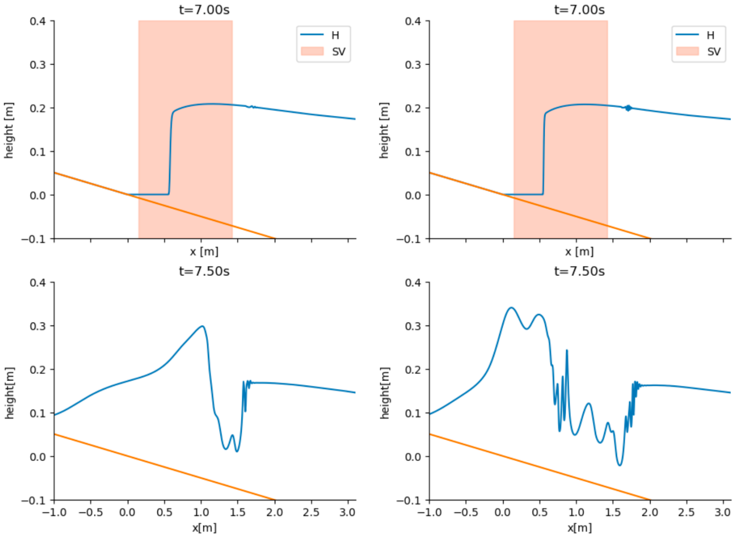

Figure 4.42: Close-up view of the results computed with the offline method with mesh size Δx_1, left column, and Δx_2 , right column.

waves generated by the interface. On the Nwogu-SV case, in all four methods (hybrid, viscosity, overlapping SWRM and overlapping direct) these waves were observed with a wavelength that was independent of the mesh size, and only when the wave crossed the interface, which demonstrates that this should be an expected feature at the continuous level. Unlike the Nwogu-SV models, the GN-SV hybrid did not display such features in a noticeable manner. Further analysis is required and will be shown in Part II of this document.

(II) Instabilities: What causes them? Are they coming from the continous or the discrete level? How to fix them? Using the Nwogu-SV model with an interface put on a fixed location, it was possible to replicate the instabilities observed in [70] when using a stability condition like $\Delta t = O(\Delta x)$. Regarding the cause, the data suggests that the instabilities are due to the inhability of the numerical scheme to handle the Nwogu-SV transition. The main observation is that the algorithm is stable if one imposes a stability condition more stringent than $\Delta t = O(\Delta x^2)$. On this case it was possible to retrieve a mesh-convergent solution, hence the instabilities are not a feature of the continuous problem, but of the discrete one. Attempting to fix these instabilities new coupling techniques were tried, for the Nwogu-SV model with a fixed interface, namely: the artificial viscosity; an overlapping Schwarz Waveform Relaxation Method; and an overlapping direct solver. It was found with the artificial viscosity method that, although a stability condition more restrictive than $\Delta t = O(\Delta x)$ seemed required, indeed the new viscous term could improve the stability of the model. Using the overlapping method, it was found that the SWRM was more stable than the direct method for small overlap sizes, and that in this case it was possible to maintain a linear stability condition $\Delta t = O(\Delta x)$, which reinforces the idea that a different numerical scheme must be designed. This stability condition comes with two drawbacks: the choice of

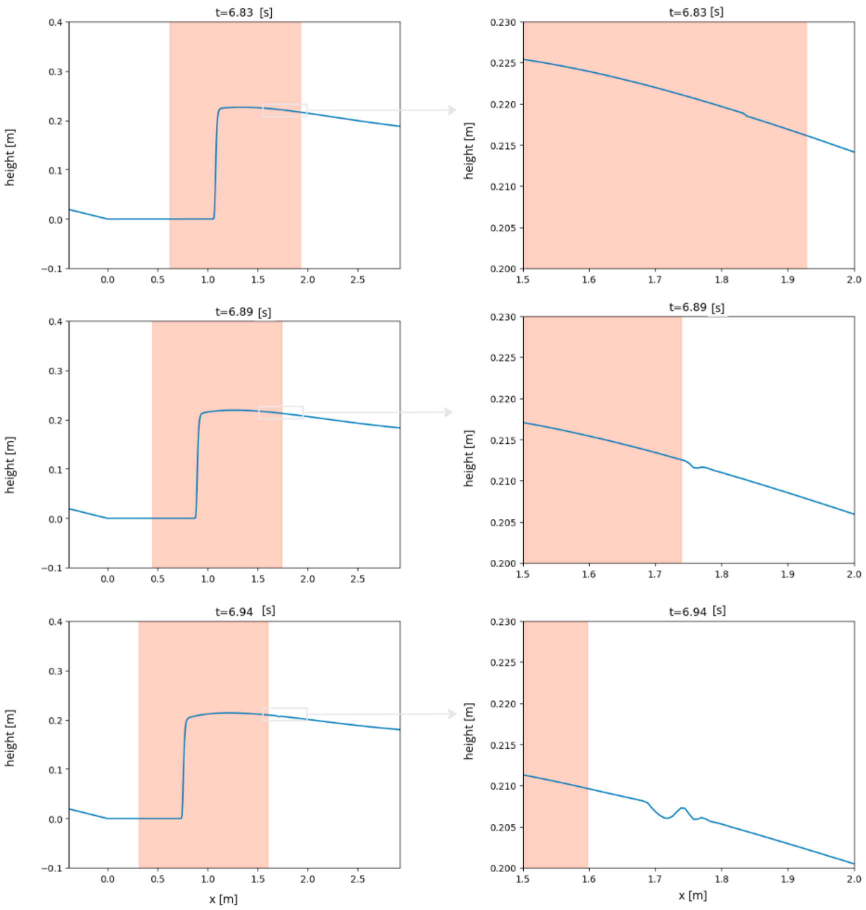

Figure 4.43: Computed free surface right before the big spurious waves develop. View of the breaking front (left) and close up view of the original spurious wave (right).

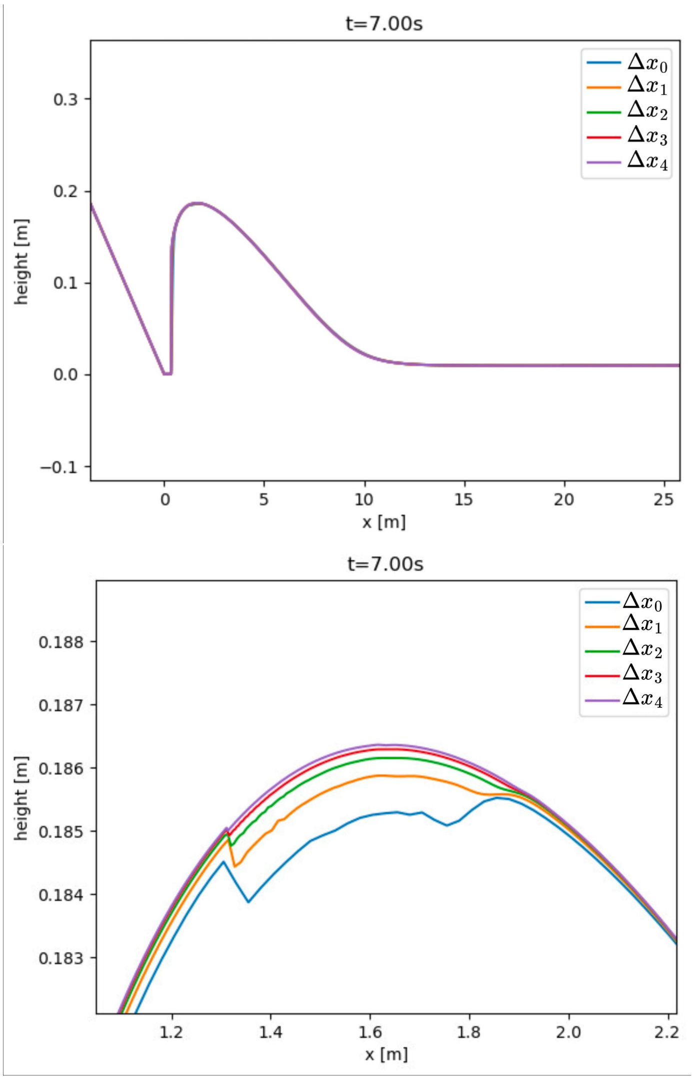

Figure 4.44: Free surface computed with the SV model on the case of a solitary wave on a simple beach. Mesh sizes are $\Delta x_k = \Delta x_0 \times 2^{-k}, k = 0, .., 4$, $\Delta x_0 = 0.025m$

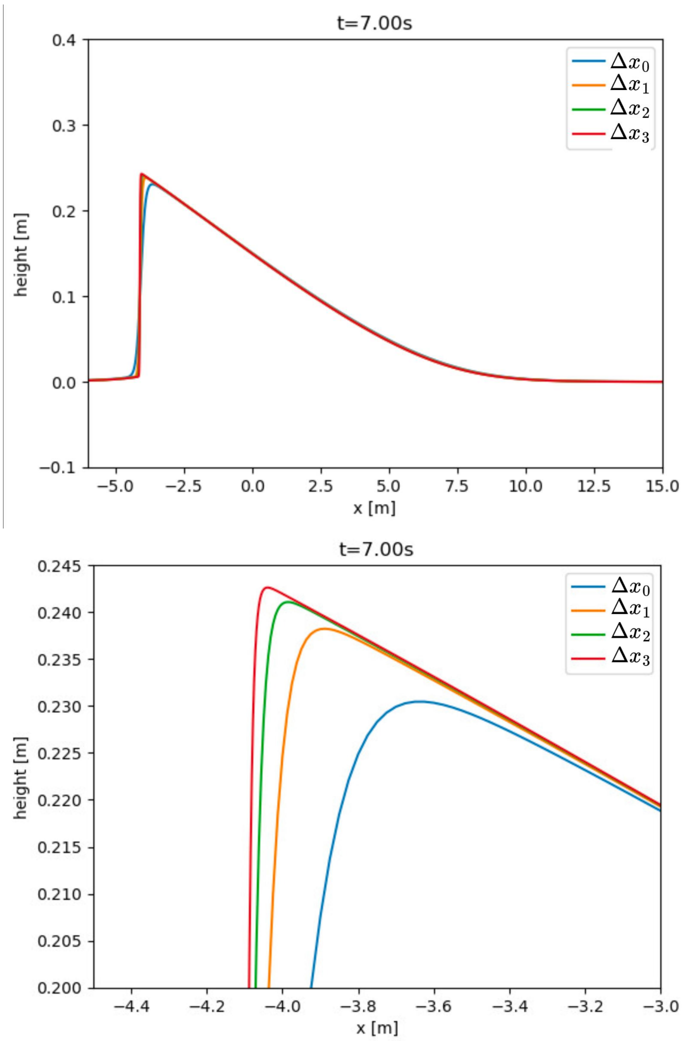

Figure 4.45: Free surface computed with the SV model FV fluxes on the case of a solitary wave propagating on a flat bathymetry . Mesh sizes are $\Delta x_k = \Delta x_0 \times 2^{-k}, k = 0, .., 4,\ \Delta x_0 = 0.025m$

a compatible initialization for the algorithm; and the added cost, with respect to the hybrid model, of iterating the algorithm until convergence. Unlike the Nwogu-SV model, the GN-SV hybrid did not present stability problems. For this reason none of the proposed new coupling techniques were tried on it.

(III) Mesh convergence: What causes the large variations in the solution when changing the mesh size? Is it related to the instabilities? The large variations were verified using the moving interface for wave breaking in the GN-SV hybrid model. By defining the GN and SV subdomains in the $x-t$ plane in an offline fashion, that is to say, given as a parameter in the simulation instead of computed along, the oscillations still persisted, hence it is not the variability nor the uncertainty of the GN and SV domains that causes it. Through a detailed inspection it was determined that the cause is that some artifacts introduced by the discretization are harmless while propagating on the SV subdomain but, when transmitted to the BT domain, become even larger than the wave itself. In this particular case, this was triggered by a tiny discontinuity coming from the low order discretization of the topography, so the problem was fixed by using a higher-order numerical method. Regarding its relation with the instabilities, in all cases the model was stable, did not blow up. However, the large size of the waves evidently risks producing negative depths maybe in other settings; this is a hypothesis that was not studied. Again, further analysis is required and will be continued in Part II.

The next Part II will be devoted to provide a theoretical framework on which these hypothesis can be studied more precisely. This will be applied to the linear Boussinesq and Saint-Venant equations. Regarding the previous three questions, it will be demonstrated that the hybrid model with a static interface is well-posed, hence it is stable; that the oscillations that are observed are indeed reflections that can be quantified precisely, even considering their directionality; and that the mesh convergence problem has to do with how the Cauchy problem of the SV model is more robust to small perturbations on the initial data than the Boussinesq model. In simple terms, the problem is that mesh-dependent perturbations that have low energy in the SV model can have huge amounts of energy in the BT model, which can lead to a completely different solution on each mesh size. Interestingly, the half-line problems have the opposite behaviors: the Boussinesq equations will be shown to be more robust than the half-line problem of the Saint-Venant equations, in the sense that the solution will have improved regularity, and will not have at all the energy issue of the Cauchy problems. This highlights the importance of understanding the different mechanisms that can be used to transmit information across subdomains (initial conditions, boundary conditions, etc).

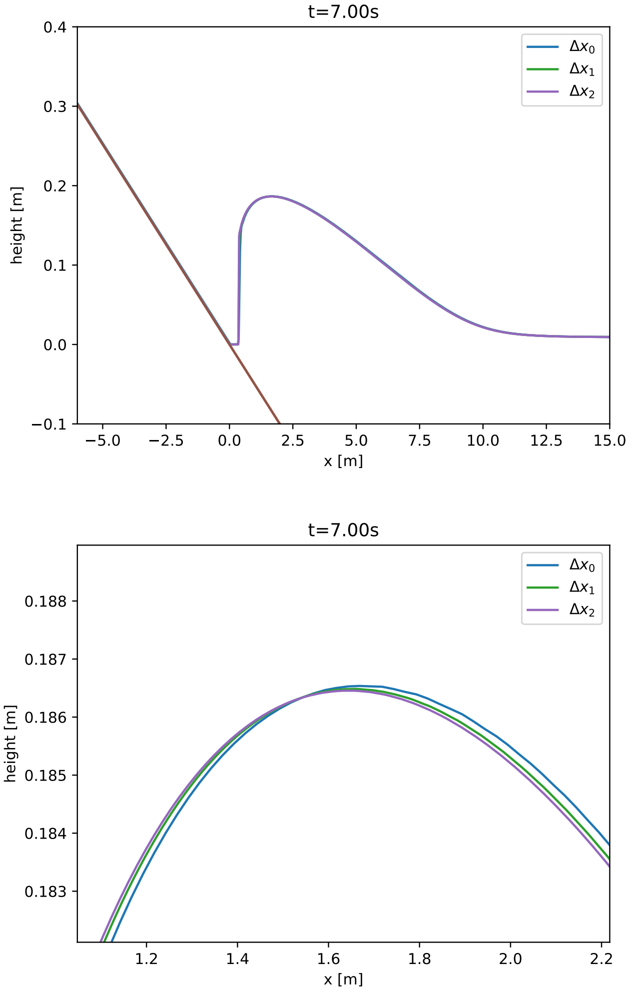

Figure 4.46: Free surface computed with the SV model and 4th order scheme for hyperbolic fluxes, on the case of a solitary wave on a simple beach. Mesh sizes are $\Delta x_k = \Delta x_0 \times 2^{-k}, k = 0, .., 4$, $\Delta x_0 = 0.025m$

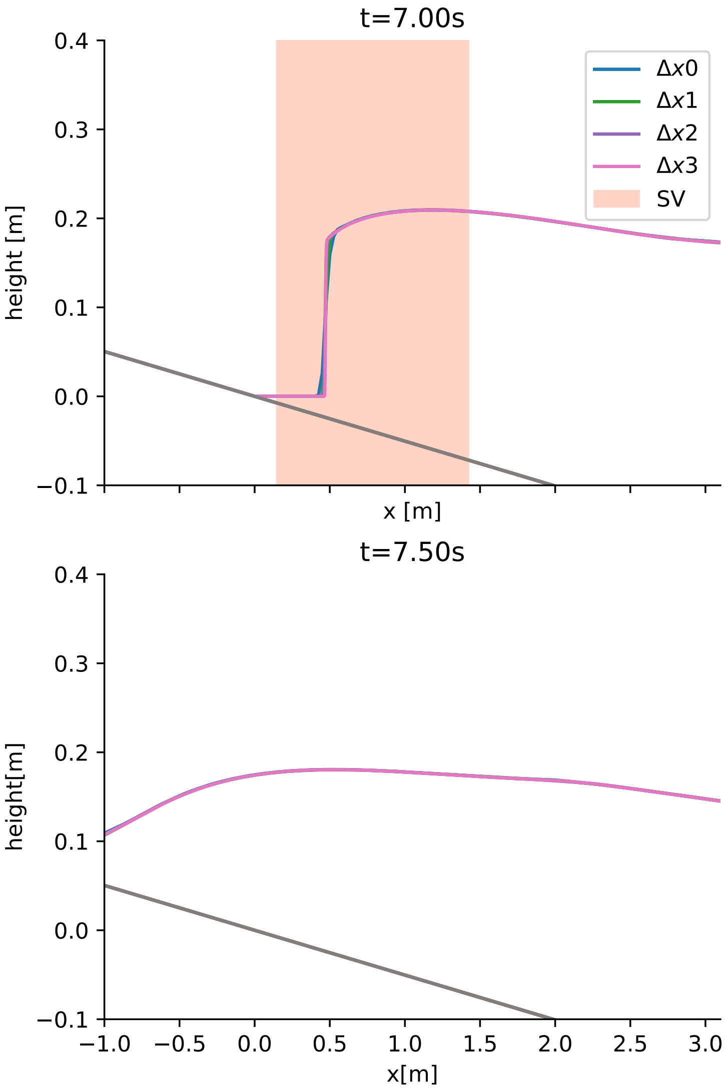

Figure 4.47: Free surface at $t = 7.0s$ and $7.5s$ computed with the fourth order scheme wih mesh sizes Δx_0 to Δx_3. Compared to Figures 4.41 and 4.42 no spurious waves are observed on any mesh.

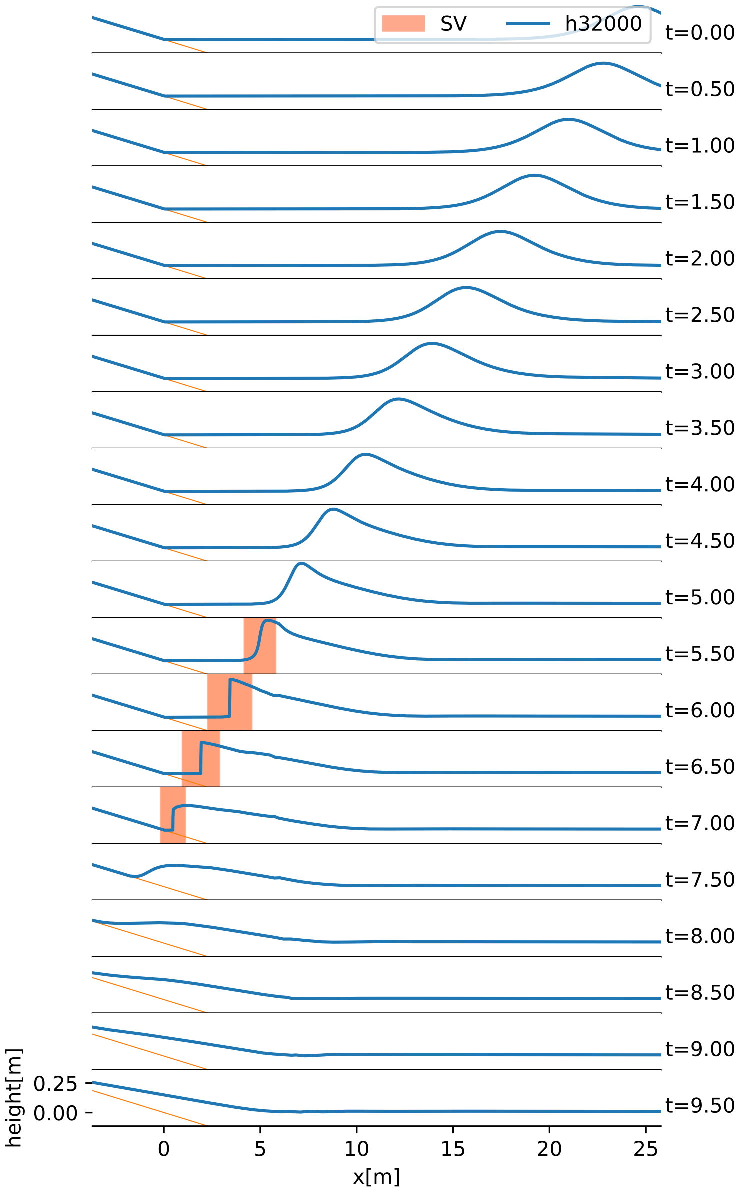

Figure 4.48: Results with the fourth order scheme and mesh Δx_3 at all times.

Part II

A theoretical framework to analyze linear coupled models of waves

Chapter 5

Coupled phase-resolving linear models

Part II of this thesis has two objectives. The first one is **to provide a precise explanation of the artifacts reported in Part I**, that is to say, to answer the following questions:

(I) Oscillations: Are the short oscillations that have been reported (in the literature and on Chapter 4) part of the solution or a problem of the discretization?

(II) Instabilities: What causes them? Are they coming from the continous or the discrete level? How to fix them?

(III) Mesh-dependence: What causes the large variations in the solution when changing the mesh size? Is that related to the instabilities?

The second objective is **to contribute to the mathematical justification of the coupled models** by studying the behavior of

$$\boldsymbol{W} - \boldsymbol{W}_{3D} \tag{5.1}$$

where $\boldsymbol{W}$ denotes the solution of coupling two phase-resolving coastal wave models and $\boldsymbol{W}_{3D}$ is the solution of the reference 3D model. We only analyze the coupling of Saint-Venant and Boussinesq equations, although the rationale is the same for other Boussinesq-type models. As was discussed in Chapter 1, the 3D model can be the Airy equations in the linear case, or the free-surface Euler or Navier-Stokes equations in the nonlinear case. This is because they can provide the most accurate solution to the problem of water waves but are normally too complex or expensive to compute.

In this chapter we introduce the framework on which these two objectives will be tackled: the linearized equations. Section 5.1 introduces the mathematical equations of the models to be coupled. Section 5.2 discusses the types of interfaces and subdomains involved in the coupling, and the expected physical effects that these should have on the flow, as opposed to the unexpected artifacts of Chapter 4. Section 5.3 proposes the one-way coupled model to measure and separate the *coupling error* from other types of error that can be involved

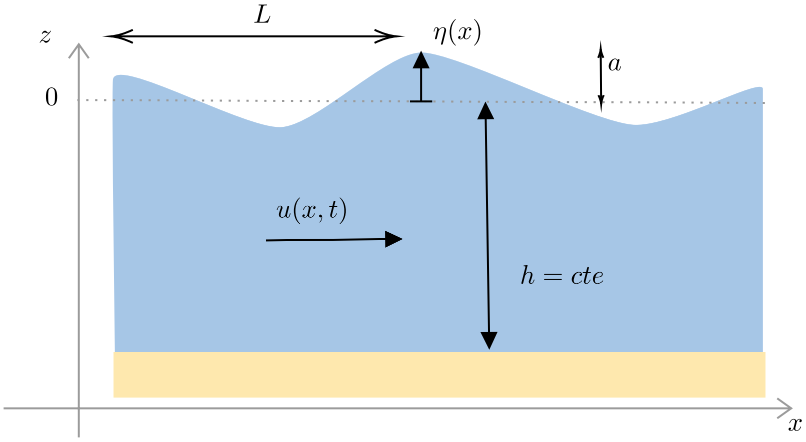

Figure 5.1: Sketch of variables and scales.

when computing (5.1). An interesting remark is that this definition of the *coupling error* is abstract and pragmatical enough to be able to compute it in the nonlinear case with numerical methods. This can facilitate the comparison and prototyping of different coupling strategies, regardless of their theoretical complexity. Finally, 5.4 summarizes some conclusions.

5.1 Linear coupled models

Let $\Omega = \mathbb{R}$, $T > 0$ and $Q = \Omega \times]0, T[$. Let Q_{SV} and Q_B be such that $\overline{Q}_{SV} \cup \overline{Q}_B = \overline{Q}$. We aim to find $\boldsymbol{W}(x,t) = (\eta(x,t), u(x,t))$ such that it solves the linear Saint-Venant (SV) equations

$$\begin{aligned} \partial_t \eta + h \partial_x u &= 0 \\ \partial_t u + g \partial_x \eta &= 0 \end{aligned} \quad \text{in } Q_{SV} \tag{5.2}$$

and the linear Boussinesq (B) equations

$$\begin{aligned} \partial_t \eta + h \partial_x u &= 0 \\ \left(1 - \frac{h^2}{3} \partial_x^2\right) \partial_t u + g \partial_x \eta &= 0 \end{aligned} \quad \text{in } Q_B \tag{5.3}$$

with initial data

$$\eta(\cdot, 0) = \eta_0, \quad u(\cdot, 0) = u_0 \text{ in } \Omega \tag{5.4}$$

As shown in Figure 5.1, η represents the free-surface elevation, u the depth-averaged horizontal velocity, $h > 0$ is the constant depth, and also g is the gravitational acceleration. The main property of these models is the dispersion relation. This can be obtained by substituting $\boldsymbol{W} = e^{j(\kappa x - \omega t)} \Phi$, with $\boldsymbol{\Phi}(\kappa) = (1, \Phi)^t \in \mathbb{C}^2$, from where one obtains that there are two solutions for each model, such that

$$\begin{aligned} \omega_{SV}(\kappa) &= \pm \sqrt{gh} \kappa, \quad \Phi_{SV} = \pm 1 \\ \omega_B(\kappa) &= \pm \sqrt{gh} \frac{\kappa}{\sqrt{1 + \frac{1}{3} h^2 \kappa^2}}, \quad \Phi_B = \pm \sqrt{1 + \frac{1}{3} h^2 \kappa^2} \end{aligned} \tag{5.5}$$

for each respective operator. The two solutions for each equation reflect the bidirectional nature of the propagation of waves.

Defining the phase celerities

$$c_{SV}(\kappa) = \frac{\omega_{SV}(\kappa)}{\kappa}, \quad c_B(\kappa) = \frac{\omega_B(\kappa)}{\kappa} \tag{5.6}$$

one can see that $c_{SV} = \sqrt{gh}$ is constant, so waves of all lengths propagate at the same speed, and c_B is a monotonous decreasing function of $|h\kappa|$ with limit equal to 0, so waves of different lengths are dispersed and the longest ones propagate to a speed close to c_{SV} while the shortest ones move arbitrarily slow. Also, a fact that is less talked about in the literature, is that for $\eta \neq 0$ the ratio $\Phi = \eta/u$ in the SV model is $\Phi_{SV} = 1$, whereas in the B model it becomes $\Phi_B = \sqrt{1 + \frac{1}{3}h^2\kappa^2}$, which indicates that, with the B model, u grows arbitrarily large with κ. This issue will be studied with more precision in Chapter 6 in terms of the weak well-posedness of the solution.

To simplify the analysis it is useful to work with adimensional variables

$$\begin{aligned} x' &= \frac{x}{L}, \quad t' = t\frac{\sqrt{gh}}{L}, \\ \eta' &= \frac{\eta}{a}, \quad u' = \frac{u}{\frac{a}{h}\sqrt{gh}} \end{aligned} \tag{5.7}$$

where L and a are characteristic scales for the wavelength and amplitude, also shown in Figure 5.1. Defining $\mu^2 = h^2/3$ and

$$A = \begin{pmatrix} 0 & 0 \\ 0 & \mu^2 \end{pmatrix}, \quad B = \begin{pmatrix} 0 & 1 \\ 1 & 0 \end{pmatrix} \tag{5.8}$$

one can write the problem more compactly as: Find $\boldsymbol{W}(x,t)$ such that

$$\begin{cases} \mathcal{L}_{SV}\boldsymbol{W} = 0 & \text{in } Q_{SV} \\ \mathcal{L}_B\boldsymbol{W} = 0 & \text{in } Q_B \\ \boldsymbol{W}(\cdot,0) = \boldsymbol{W}_0 & \text{in } \Omega \end{cases} \tag{5.9}$$

where $\mathcal{L}_B = (I - A)\partial_t + B\partial_x$ and $\mathcal{L}_{SV} = \partial_t + B\partial_x$. In this case their dispersion relations become

$$\begin{aligned} \omega_{SV}(\kappa) &= \pm\kappa, \quad \phi_{SV} = \pm 1, \\ \omega_B(\kappa) &= \pm\frac{\kappa}{\sqrt{1+\mu^2\kappa^2}}, \quad \phi_B = \pm\sqrt{1+\mu^2\kappa^2} \end{aligned} \tag{5.10}$$

Clearly, this system needs a more precise definition of what Q_{SV} and Q_B are, and a statement about what to do at the interfaces $\partial Q_{SV} \cap \partial Q_B$. We discuss this in the next section.

5.2 Subdomains and expected features

We will make the simplification that Q_{SV} and Q_B are non-overlapping subdomains, *i.e.,* $Q_{SV} \cap Q_B = \emptyset$. Figure 5.2 shows three useful simplifications. The

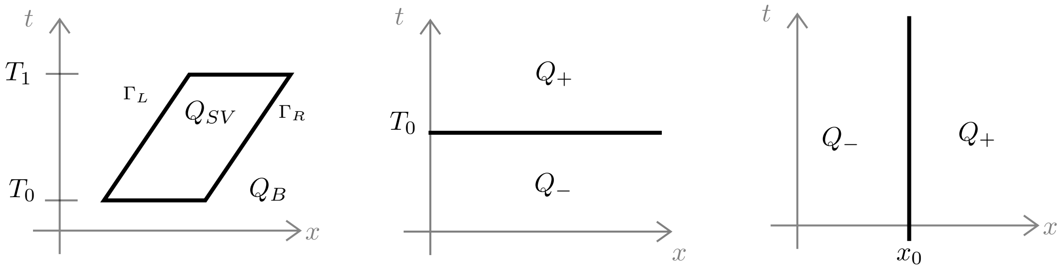

Case (a) Case (b) Case (c)

Figure 5.2: Three types of partitions of the upper $x-t$ plane to define the subdomains Q_- and Q_+, where different models are used: Case (a) dynamic interfaces, Case (b) horizontal (temporal) interface, Case (c) vertical (spatial) interface.

first one is similar to the breaking of a single wave, with Q_B being the whole upper $x-t$ plane with a hole in Q_{SV}, defined to surround the evolution of the breaker (case (a) in Figure 5.2). In this case, data is transmitted between the two models by two main mechanisms: as an initial condition at $t = T_0$ and $t = T_1$, and through the boundaries on Γ_L and Γ_R. This motivates the study of two other related simplifications, cases (b) and (c) in Figure 5.2, corresponding to a horizontal and a vertical interface in the $x-t$ plane. In this case one can have either $Q_- = Q_B$ and $Q_+ = Q_{SV}$ or $Q_- = Q_{SV}$ and $Q_+ = Q_B$. We will also denote $\mathcal{L}_-$ and $\mathcal{L}_+$ the SV and B operators to coincide with the choice of Q_- and Q_+.

5.2.1 Effects of the horizontal interface

For a horizontal interface, let us define the family of operators $(\mathcal{T}_\pm(t))_{t\geq 0}$ such that

$$\mathcal{T}_\pm(t)\boldsymbol{W}_0 = \boldsymbol{W}(\cdot,t), \quad t \geq 0 \tag{5.11}$$

is the solution of the Cauchy problems

$$\begin{cases} \mathcal{L}_\pm \boldsymbol{W} = 0, & \text{in } Q \\ \boldsymbol{W}(\cdot,0) = \boldsymbol{W}_0, & \text{in } \Omega \end{cases} \tag{5.12}$$

which we assume for now that are well-posed[1]. In this case, transmitting the data from one model to the other without additional transformations, the solution of the coupled problem (5.9) can be written as

$$\boldsymbol{W}(\cdot,t) = \begin{cases} \mathcal{T}_-(t)\boldsymbol{W}_0, & 0 \leq t \leq T_0 \\ \\ \mathcal{T}_+(t-T_0)\mathcal{T}_-(T_0)\boldsymbol{W}_0, & t \geq T_0 \end{cases} \tag{5.13}$$

that is to say, one computes the solution with model $\mathcal{L}_-$ until T_0 and applies the result as an initial condition on model $\mathcal{L}_+$ for a duration of $t - T_0$, until

---

[1] This will be studied on Chapter 6.

reaching the desired t. Because of this property, the transmission of data can only be made in *one way*, forward in time.

To understand the expected effect of this coupling, we use (5.10) to describe the velocity profile in the form

$$u(x,t) = A(t)e^{j(\kappa x - \omega(\kappa,t)x)} \tag{5.14}$$

which leads to

$$u(x,t) = \begin{cases} e^{j\kappa x} & t = 0 \\ e^{j(\kappa x - \omega_- t)}, & 0 < t \leq T_0 \\ e^{j(\omega_+ - \omega_-)T_0} e^{j(\kappa x - \omega_+ t)} & T_0 < t \end{cases} \tag{5.15}$$

Equation (5.15) reveals that to change the phase speed and obtain a continuous solution at $t = T_0$, a phase-jump of size $(\omega_+ - \omega_-)T_0$ has to be introduced. However, the solution has an interesting property: for the whole duration, the **wavenumber κ remains unchanged**, which means that the Fourier spectrum of the solution **only changes its phase, not its magnitude**. This same analysis applies for η, but the discussion about the factor $\phi = u/\eta$ is more subtle and related to the weak-wellposedness issue of the model, which will be discussed later on Chapter 6.

5.2.2 Effects of the vertical interface: the one-way model

In the case of a vertical interface the general solution requires more work, however, in the same spirit as the horizontal case we can assume that the initial data $\boldsymbol{W}_0$ is supported on Ω_- and study the solution of the *one-way* model

$$\boldsymbol{W}^\star = \begin{cases} \boldsymbol{W}^\star_{cauchy,-} & \text{in } Q_- \\ \boldsymbol{W}^\star_{half,+} & \text{in } Q_+ \end{cases} \tag{5.16}$$

where

$$\begin{cases} \mathcal{L}_- \boldsymbol{W}^\star_{cauchy,-} = 0, & \text{in } Q_- \\ \boldsymbol{W}^\star_{cauchy,-}(\cdot,0) = \boldsymbol{W}_0 & \text{in } \Omega_- \end{cases} \tag{5.17}$$

and

$$\begin{cases} \mathcal{L}_+ \boldsymbol{W}^\star_{half,+} = 0, & \text{in } Q_+ \\ \boldsymbol{W}^\star_{half,+}(\cdot,0) = 0 & \text{in } \Omega_+ \\ u^\star_{half,+}(0,\cdot) = u^\star_{cauchy,-}(0,\cdot) & \text{on }]0,T[\end{cases}, \tag{5.18}$$

In this case, substituting solutions of the form

$$u^\star_{cauchy,-}(x,t) = e^{j(\kappa_- x - \omega_-(\kappa_-)t)}, \quad u^\star_{half,+}(x,t) = e^{j(\kappa_+ x - \omega_+(\kappa_+)t)} \tag{5.19}$$

with positive $\kappa_\pm$, $\omega_\pm$, the one-way transmission condition at $x = 0$ of (5.18) implies that

$$\omega_-(\kappa_-) = \omega_+(\kappa_+) \tag{5.20}$$

In the case where $Q_- = Q_B$ and $Q_+ = Q_{SV}$ eq. (5.20) can be written as

$$\kappa_+ = \frac{\kappa_-}{\sqrt{1 + \mu^2 \kappa_-^2}} < \kappa_- \tag{5.21}$$

which reveals that when a wave crosses the interface and arrives into Ω_+ it gets stretched-out, increasing its wavelength. This is an artificial refraction induced by the change in the dispersion of the media on which the waves propagates.

On the opposite direction, when $Q_- = Q_{SV}$ and $Q_+ = Q_B$ there is also an artificial refraction and, for the same reason as before, the waves are compressed. However, since in this case the wavelength changes according to

$$\kappa_+ = \frac{\kappa_-}{\sqrt{1-\mu^2\kappa_-^2}} > \kappa_-, \quad \text{if } \mu\kappa_- < 1 \tag{5.22}$$

we now also have to deal with the new constraint that $\mu\kappa_- < 1$. This constraint comes from the fact that the range of ω_{SV} is $\mathbb{R}$, but the range of ω_B is $]-\frac{1}{\mu}, \frac{1}{\mu}[$ so the transformation given by

$$\begin{array}{cccc} \mathbb{R} \to &]-\frac{1}{\mu}, & \frac{1}{\mu}[& \to \mathbb{R} \\ \kappa_- \mapsto & \omega_-(\kappa_-) = & \omega_+(\kappa_+) & \mapsto \kappa_+ \end{array} \tag{5.23}$$

only works for $\mu\kappa_- < 1$. This issue will also be studied in detail on Chapter 7, where it will be shown that the B model has a dispersive boundary layer with a time-smoothing effect that filters out all frequencies that fall outside the range of ω_+. Such a dispersive boundary layer was observed for the first time by Bresch et al. [18] and mentioned later by Lannes & Weynans [81].

We have deduced that the **directionality** of the propagation is important and that in the SV to B direction the interface has two effects, **refraction** in space and **smoothing** in time, while in the B to SV case it is only refraction.

5.3 Coupling error and reference solution

Now we continue with a discussion on how to measure the error

$$\boldsymbol{W} - \boldsymbol{W}_{3D} \tag{5.24}$$

where $\boldsymbol{W}$ is the solution of the coupled model and $\boldsymbol{W}_{3D}$ the solution of the reference (expensive) 3D model, on the case of a horizontal and vertical interface in the $x-t$ plane (Figure 5.2).

5.3.1 Horizontal interface

In the case of a horizontal interface, for a domain without vanishing depths and for $t \leq T_0$, the error (5.24) has already been quantified for most BT models in [77, 78]. In this case, the 3D model is the free-surface Euler equations. For $t \geq T_0$ let $(\mathcal{T}_{3D}(t))_{t\geq 0}$ such that

$$\boldsymbol{W}_{3D}(\cdot, t) = \mathcal{T}_{3D}(t)\boldsymbol{W}_0 \tag{5.25}$$

and also let

$$\boldsymbol{W}_a(\cdot, t) = \left\{ \begin{array}{cc} \mathcal{T}_{3D}(t)\boldsymbol{W}_0 & t \leq T_0 \\ \mathcal{T}_+(t-T_0)\mathcal{T}_{3D}(T_0)\boldsymbol{W}_0 & t \geq T_0 \end{array} \right. \tag{5.26}$$

Then we can estimate

$$|\boldsymbol{W}(\cdot,t) - \boldsymbol{W}_{3D}(\cdot,t)|_E \leq |\boldsymbol{W}(\cdot,t) - \boldsymbol{W}(\cdot,t)_a|_E + |\boldsymbol{W}(\cdot,t)_a - \boldsymbol{W}_{3D}(\cdot,t)|_E \tag{5.27}$$

with $|\cdot|_E$ a norm on a suitable Banach space E. These terms correspond to

- $\boldsymbol{W}(\cdot,t)-\boldsymbol{W}(\cdot,t)_a$: The error propagated from T_0 until t, due to the wrong initial condition at $t = T_0$. This error can be estimated by setting E as the space where the BT model is continuous w.r.t the initial data.
- $\boldsymbol{W}(\cdot,t)_a-\boldsymbol{W}(\cdot,t)_{3D}$: The model error, of the Cauchy problem from T_0 to $t > T_0$. This is obtained from the justification in [77].

So, using $\boldsymbol{W}_a$, the error (5.24) can be estimated from the **existing results** about the continuity an justification of the **Cauchy problems** of each model.

5.3.2 Vertical interface

For the case of a vertical interface, here we will show that one can use the one-way coupling solution $\boldsymbol{W}^\star$ from (5.16) to isolate the error induced by the coupling conditions from other types of errors. We will explain here that this is clear in the case where $\boldsymbol{W}_0$ is supported on Ω_-. This is regardless of whether the model is linear or nonlinear. For the more general case of arbitrarily supported data one has to use two coupled models and a density argument that we outline here too.

Let us recall the solution of the one way model

$$\boldsymbol{W}^\star = \begin{cases} \boldsymbol{W}^\star_{cauchy,-} & \text{in } Q \\ \boldsymbol{W}^\star_{half,+} & \text{in } Q_+ \end{cases} \tag{5.28}$$

where

$$\begin{cases} \mathcal{L}_-\boldsymbol{W}^\star_{cauchy,-} = 0, & \text{in } Q \\ \boldsymbol{W}^\star_{cauchy,-}(\cdot,0) = \boldsymbol{W}_0 & \text{in } \Omega \end{cases} \tag{5.29}$$

and

$$\begin{cases} \mathcal{L}_+\boldsymbol{W}^\star_{half,+} = 0, & \text{in } Q_+ \\ \boldsymbol{W}^\star_{half,+}(\cdot,0) = 0 & \text{in } \Omega_+ \\ u_{half,+}(0,\cdot) = u_{cauchy,-}(0,\cdot) & \text{on }]0,T[\end{cases} , \tag{5.30}$$

and define $\boldsymbol{W}^{\star\star}$ as the solution of the one-way coupling between the 3D model and the $\mathcal{L}_+$ model:

$$\boldsymbol{W}^{\star\star} = \begin{cases} \boldsymbol{W}_{3D} & \text{in } Q_- \\ \boldsymbol{W}^{\star\star}_{half,+} & \text{in } Q_+ \end{cases} \tag{5.31}$$

with $\boldsymbol{W}^{\star\star}_{half,+}$ the solution of the half line problem on Q_+

$$\begin{cases} \mathcal{L}_+\boldsymbol{W}^{\star\star}_{+.half} = 0, & \text{in } Q_+ \\ \boldsymbol{W}^{\star\star}_{+.half}(\cdot,0) = 0 & \text{in } \Omega_+ \\ u_{half,+}(0,\cdot) = u^{3D}(0,\cdot) & \text{on }]0,T[\end{cases} , \tag{5.32}$$

Notice that $\boldsymbol{W}^{\star\star}_{half,+}$ is computed using the **best boundary data** $u^{3D}(0,\cdot)$.

Using these definitions we can separate the error in three parts as

$$\boldsymbol{W} - \boldsymbol{W}^{3D} = (\boldsymbol{W} - \boldsymbol{W}^\star) + (\boldsymbol{W}^\star - \boldsymbol{W}^{\star\star}) + (\boldsymbol{W}^{\star\star} - \boldsymbol{W}^{3D}) \tag{5.33}$$

Let us now explore why it makes sense to refer to the first term as the **coupling error**. For clarity in our explanation, we will describe the terms in reverse order, starting from the last one and moving to the first.

- $\boldsymbol{W}^{\star\star} - \boldsymbol{W}^{3D}$: This is the **half-line model error** of the operator $\mathcal{L}_+$. To see this notice from (5.32) that

$$\boldsymbol{W}^{\star\star} - \boldsymbol{W}^{3D} = \begin{cases} 0 & \text{in } Q_- \\ \boldsymbol{W}^{\star\star}_{half,+} & \text{in } Q_+ \end{cases} \tag{5.34}$$

and since $\boldsymbol{W}^{\star\star}_{half,+}$ is only using data from the 3D model it does not carry errors from the other parts of the domain. It seems also that the most intuitive way to improve this error is by improving the operator $\mathcal{L}_+$, although the boundary condition (5.32) could also influence the results. Such problems for BT equations have only recently been studied in the literature for arbitrary boundary data [81, 18].

- $\boldsymbol{W}^{\star} - \boldsymbol{W}^{\star\star}$: Is the **Cauchy model error** of the $\mathcal{L}_-$ operator. To see this notice also that

$$\boldsymbol{W}^{\star} - \boldsymbol{W}^{\star\star} = \begin{cases} \boldsymbol{W}^{\star}_{cauchy,-} - \boldsymbol{W}_{3D} & \text{in } Q_- \\ \boldsymbol{W}^{\star}_{half,+} - \boldsymbol{W}^{\star\star}_{half,+} & \text{in } Q_+ \end{cases} \tag{5.35}$$

so for Q_- the comparison is w.r.t. to the best solution and for Q_+ the comparison is w.r.t. the same half-line model $\mathcal{L}_+$ but using the best possible data on the boundary, $u_{3D}(0,\cdot)$. In other words, in Q_- this type of error indicates the precision the Cauchy problem of model $\mathcal{L}_-$, while for Q_+ it represents the part of this error that is carried by $\mathcal{L}_+$. Again, the most natural way of improving this error is by replacing $\mathcal{L}_-$ by a better model.

- $\boldsymbol{W} - \boldsymbol{W}^{\star}$ is the **coupling error**. In this case we have

$$\boldsymbol{W} - \boldsymbol{W}^{\star} = \begin{cases} \boldsymbol{W}_- - \boldsymbol{W}^{\star}_{cauchy,-} & \text{in } Q_- \\ \boldsymbol{W}_+ - \boldsymbol{W}^{\star}_{half,+} & \text{in } Q_+ \end{cases} \tag{5.36}$$

so for Q_- this error measures the absorbing ability of the coupling conditions for the operator $\mathcal{L}_+$, while in Q_+ it describes how these errors propagate with the model $\mathcal{L}_+$.

Remark 5.1. *The reader can notice that, in the case of propagation far from the shore where the hierarchy of BT and SV models is clear, one can estimate*

$$|\boldsymbol{W} - \boldsymbol{W}_{3D}| \leq |\boldsymbol{W} - \boldsymbol{W}_{expensive}| + |\boldsymbol{W}_{expensive} - \boldsymbol{W}_{3D}| \tag{5.37}$$

with $\boldsymbol{W}_{expensive}$ *the solution to the most accurate/expensive BT model. Then, the second term can be estimated from the justification of the cauchy problem of said model, and the first term can be obtained by replacing* $\boldsymbol{W}_{3D}$ *with* $\boldsymbol{W}_{expensive}$ *in the definitions of the coupling, half-line and Cauchy errors just introduced.*

Even though the half-line model error and the Cauchy model error are also affected by the choice of transmission conditions, the one that more directly describes the artificial effects added by the coupling method is the **coupling error**. The other types of error are also affected by the transmission conditions, however, they seem more related to the specific understanding of the problems on the whole and half lines. Notice also that none of these definitions has used the assumption of linearity, so the same observations apply regardless of the nonlinearity of the equations.

The effects described by the coupling error are artifacts that appear on top of those of described previously on Section 5.2.2. In fact, this reveals that indeed the one-way model is the best coupled model in this simplified setting where waves indeed propagate in only one direction in Q_+ if they are initially supported on Q_-. However, in more complex situations such as variable bathymetries and 2D geometries, where significant waves propagate in the opposite direction this is not necessarily true.

As mentioned in the previous bullet points, the coupling error measures the absorbing ability of the interface. This is what motivated us to look for methods for quantifying reflected waves, something that is usually done for absorbing boundary conditions, as in the pioneering works of Halpern [58] and Engquist & Majda [33].

One important limitation of the one-way model is the assumption that the initial data is supported on one side of the interface. In Chapter 8 this limitation is removed by approximating the initial condition $\boldsymbol{W}_0$ as the sum of two functions $\boldsymbol{W}_0^L$ and $\boldsymbol{W}_0^R$, each supported to the left and right of the interface, as shown in Figure 5.3. This approximation can be done arbitrarily thanks to a density argument that is proved in the appendix C. The reference solution in this case is the superposition of two coupled models:

$$\boldsymbol{W}^{\star\star\star} = \boldsymbol{W}_L^\star + \boldsymbol{W}_R^\star \tag{5.38}$$

where $\boldsymbol{W}_L^\star$ is the solution of the one-way coupling (5.16) initialized with $\boldsymbol{W}_0^L$ as in (8.89); and $\boldsymbol{W}_R^\star$ is the solution of the one-way coupling initialized with $\boldsymbol{W}_0^R$, but solved in the opposite direction, *i.e.*,

$$\boldsymbol{W}_R^\star = \begin{cases} \boldsymbol{W}_{cauchy,+} & \text{in } Q_+ \\ \boldsymbol{W}_{half,-} & \text{in } Q_- \end{cases} \tag{5.39}$$

where

$$\begin{cases} \mathcal{L}_+ \boldsymbol{W}_{cauchy,+} = 0, & \text{in } Q_+ \\ \boldsymbol{W}_{cauchy,+}(\cdot, 0) = \boldsymbol{W}_0^R & \text{in } \Omega_+ \end{cases} \tag{5.40}$$

and

$$\begin{cases} \mathcal{L}_- \boldsymbol{W}_{half,-} = 0, & \text{in } Q_- \\ \boldsymbol{W}_{half,-}(\cdot, 0) = 0 & \text{in } \Omega_+ \\ u_{half,-}(0, \cdot) = u_{cauchy,+}(0, \cdot) & \text{on }]0, T[\end{cases}, \tag{5.41}$$

This study will be conducted in Chapter 8 for the hybrid model, which will help obtain an integral representation of the solution and prove several properties such as the continuity of the model, that the coupling error is of order $O(\mu^2)$, and that the reflections can be larger depending on the directionality of the propagation.

5.4 Conclusions

In this chapter we have presented the problem of coupling two different phase resolving models through different types of interfaces on the $x - t$ plane, with attention to the case of vertical and horizontal interfaces. The discussion was made around the coupling of B and SV model, but the study can easily be generalized to other BT models.

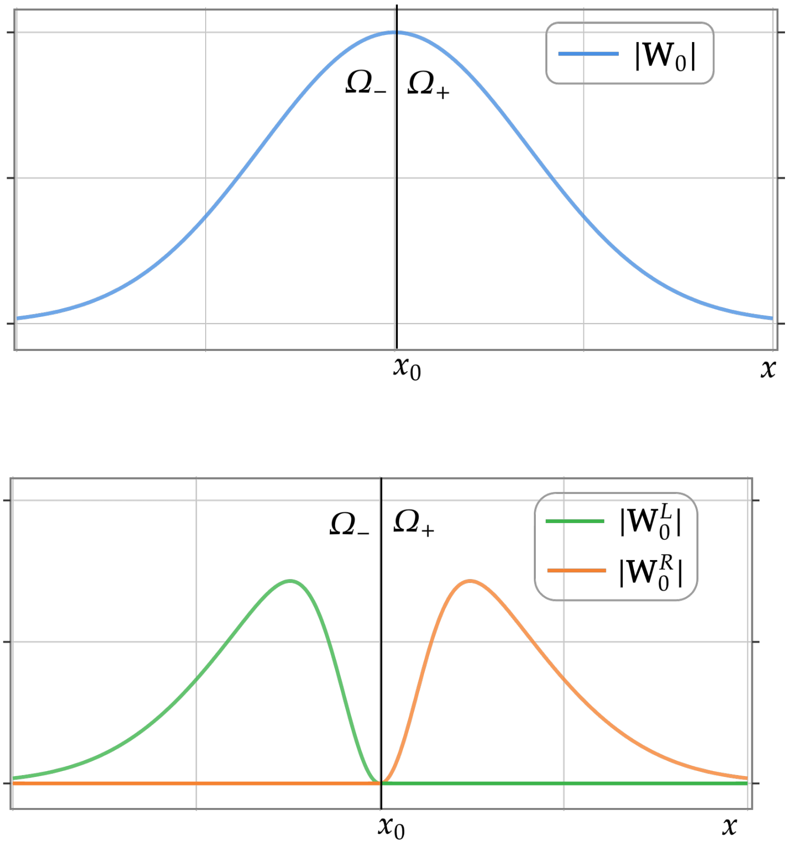

Figure 5.3: Sketch of the approximation used to handle the case of initial data with arbitrary support. The original initial condition $\boldsymbol{W}_0$ (top figure) is approximated as the superposition of two initial conditions $\boldsymbol{W}_0^L$, $\boldsymbol{W}_0^R$ that are supported on the left and on the right of the interface respectively.

The physical effects that these two types of interfaces can have on the flow were discussed. It was shown that, for a vertical interface, the main effect is a phase-change but that the magnitude and wavelengths are preserved; for a horizontal interface the main effect is a refraction due to the change in media, plus a smoothing effect in the SV to B case only. This last fact was only mentioned but will be demonstrated later in Chapter 6.

A discussion about how to measure the error w.r.t the 3D model was made. For a horizontal interface it was explained that the error only depends on the Cauchy problems of the BT equations involved, which are known result in the literature. For a horizontal interface the situation is different, and a definition of coupling error was proposed. This definition helps to isolate the artifacts introduced by a coupling technique from other effects. These other effects include those of the previous paragraph and also the errors due to the Cauchy and half-line problems involved in the coupling. The key element for this definition is the use of the one-way model as a reference. This will be crucial in the development of Chapter 8. Moreover, this definition will allow to characterize the coupling error as reflected waves coming from the interface.

To continue, in Chapter 6 we will study the Cauchy problems related to the B and SV models. This will reveal that the source of problem (III), Mesh dependence, is the weak-wellposedness of the Cauchy problem for the B equations. Then Chapter 7 will study the half-line problems, extending some results of the literature to non-classical solutions. This will also prove the smoothing effect of the dispersive boundary layer mentioned before. Finally, Chapter 8 will prove the well-posedness of the hybrid B-SV model using a domain decomposition method and the notion of coupling error presented before. This shows that problem (II) Instabilities does not come from the continuous level. Moreover, it will be shown that the coupling error is of order $O(\mu^2)$ if the right regularity of the data and solution are met, which is the source of problem (I) Oscillations that appears at the continuous level.

Chapter 6

Homogeneous Cauchy problems

In this chapter we study the Cauchy problems for the linearized Saint-Venant (SV) and Boussinesq (B) equations that will be used in the next chapters. The solution formula for the linear Saint-Venant model is classical and can be found in many books such as [82]. For the Boussinesq model the well-posedness was proved in [11], where the more general linear-*abcd* family of Boussinesq-type equations is studied. Using these results we will state that the Boussinesq model is *weakly well-posed*, according to the definition of Kreiss [76]. This fact contributes to explain problem (III):

(III) Mesh-dependence: What causes the large variations in the solution when changing the mesh size? Is it related to the instabilities?

The relation between well/ill-posedness with wave behavior has already been stated in [11] and references therein, for the *abcd* equations. The *abcd* equations are a system of weakly-dispersive weakly-nonlinear BT equations with four real-valued parameters a, b, c and d. In their linear form the *abcd* equations can be written as

$$\begin{aligned}(1 - b\partial_x^2)\partial_t \eta + (1 + a\partial_x^2)\partial_x u = 0\\(1 - d\partial_x^2)\partial_t u + (1 + c\partial_x^2)\partial_x \eta = 0\end{aligned} \tag{6.1}$$

so if $a = b = c = 0$ and $d = \mu^2$ one recovers the B equations, and if $a = b = c = d = 0$ the SV equations. For other values of a, b, c and d, Bonna, Chen & Saut [11] showed conditions for well-posedness and ill-posedness on different Sobolev spaces. In [11, Sec. 4.] and references therein, they discussed that the ill-posedness in L^p spaces, for some $p \in [1, \infty]$, $p \neq 2$, the problem was linked to the short-wave behavior of the phase velocity, which could easily be observed as spurious waves, instabilities or singularities in a numerical approximation. In the present work we complement their observations by showing that, despite the result that the linear Boussinesq model is well-posed according to Bonna, Chen & Saut [11], it is indeed weakly-wellposed according to [76]. This will explain why, as observed in Chapter 4, some artifacts introduced by the discretization are harmless while propagating on the SV subdomain but, when transmitted to the BT domain, become even larger than the wave itself. Such a problem is related to the issues of discretizing weakly-well-posed problems according to [76], which is also in line with the need for high resolution numerical methods for dispersive equations mentioned in [123].

6.1 Saint-Venant equations

Recalling from Chapter 5 that

$$\mathcal{L}_{SV} = \partial_t + B\partial_x, \quad B = \begin{pmatrix} 0 & 1 \\ 1 & 0 \end{pmatrix} \tag{6.2}$$

as is well-known, the problem

$$\begin{cases} \mathcal{L}_{SV}\boldsymbol{W} = 0 & \text{in } Q \\ \boldsymbol{W} = \boldsymbol{W}_0 & \text{in } \Omega \end{cases} \tag{6.3}$$

has a unique solution. It can be obtained from the diagonalization

$$\partial_t(\eta \pm u) \pm \partial_x(\eta \pm u) = 0 \tag{6.4}$$

that describes the Riemann invariants $\eta \pm u$ that are propagated along the characteristics $\frac{d}{dt}x(t) = \pm 1$. From here, the solution can be obtained as

$$\begin{aligned} \eta(x,t) &= \frac{1}{2}\left(\eta_0(x-t) + \eta_0(x+t)\right) + \frac{1}{2}(u_0(x-t) - u_0(x+t)) \\ u(x,t) &= \frac{1}{2}(\eta_0(x-t) - \eta_0(x+t)) + \frac{1}{2}(u_0(x-t) + u_0(x+t)) \end{aligned} \tag{6.5}$$

and moreover, the solution preserves the energy

$$|\eta(\cdot,t)|^2_{L^2(\Omega)} + |u(\cdot,t)|^2_{L^2(\Omega)} = |\eta_0|^2_{L^2(\Omega)} + |u_0|^2_{L^2(\Omega)}, \quad \forall t \geq 0 \tag{6.6}$$

which means that the solution has the same regularity as the initial data. For later reference, we write this fact as

Proposition 6.1. *If η_0 and u_0 are in $H^r(\Omega)$, with $r \geq 0$, then problem (6.3) has a unique solution (η, u) in $(H^{r,r}(\Omega\times]0,T[))^2 \cap (L^2(0,\infty; H^r(\Omega)))^2$ and the traces $u(x,\cdot)$ are in $H^r(0,T)$ for any $x \in \Omega$.*

6.2 Boussinesq equations

Recalling from Chapter 5 that

$$\mathcal{L}_B = (I - \mu^2\partial_x^2)\partial_t + B\partial_x, \quad A = \begin{pmatrix} 0 & 0 \\ 0 & \mu^2 \end{pmatrix} \tag{6.7}$$

with I the 2×2 identity matrix, now we study the dispersive case $\mu > 0$

$$\begin{cases} \mathcal{L}_B\boldsymbol{W} = 0 & \text{in } Q \\ \boldsymbol{W}(0,\cdot) = \boldsymbol{W}_0 & \text{in } \Omega \end{cases} \tag{6.8}$$

Let the Fourier transform of a function $\phi \in L^2(\mathbb{R})$ be

$$\hat{\phi}(\kappa) = \frac{1}{2\pi} \int_{\mathbb{R}} \phi(x) e^{-j\kappa x} dx, \quad \kappa \in \mathbb{R} \tag{6.9}$$

Applied on (6.8) gives

$$\begin{cases} Q(j\kappa)\partial_t \widehat{\boldsymbol{W}}(\kappa, t) = P(j\kappa)\widehat{\boldsymbol{W}}(\kappa, t) & (\kappa, t) \in \mathbb{R} \times]0, T[\\ \widehat{\boldsymbol{W}}(\kappa, 0) = \widehat{\boldsymbol{W}}_0(\kappa) & \kappa \in \mathbb{R} \end{cases} \tag{6.10}$$

where $\widehat{\boldsymbol{W}} = (\hat{\eta}, \hat{u})$ and $P(j\kappa) = -j\kappa B$ and $Q(j\kappa) = I + \kappa^2 A$ are the Fourier symbols of the differential operators $P(\partial_x) = -B\partial_x$ and $Q = (I - A\partial_x^2)$. The solution of (6.10) can be written as

$$\widehat{\boldsymbol{W}} = e^{Q^{-1}(j\kappa)P(j\kappa)t} \widehat{\boldsymbol{W}_0} \tag{6.11}$$

and taking the inverse Fourier transform one obtains

$$\boldsymbol{W}(x, t) = \int_{\mathbb{R}} e^{j\kappa x} e^{Q^{-1}(j\kappa)P(j\kappa)t} \widehat{\boldsymbol{W}}_0(\kappa) d\kappa \quad (x, t) \in Q \tag{6.12}$$

Following [76], this expression motivates a definition of well-posedness for problem (6.8), recalling that the norm of a matrix A is given by $|A| = \max\{|Au|, |u| = 1\}$, with $|\cdot|$ the Euclidean norm.

Definition 6.1 (Well-posedness)**.** *The Cauchy problem* (6.8) *is called well-posed if there exists two constants K and α such that*

$$|e^{Q^{-1}(j\kappa t)P(j\kappa)t}| \leq K e^{\alpha t}, \quad \kappa \in \mathbb{R} \tag{6.13}$$

As will be shown later, such constants do not exist for the Boussinesq equations. Instead the following definition will be used:

Definition 6.2 (Weak well-posedness)**.** *The Cauchy problem* (6.8) *is called weakly well-posed if there exists constants $q > 0$, K and α such that*

$$|e^{Q^{-1}(j\kappa t)P(j\kappa)t}| \leq K e^{\alpha t}(1 + |\kappa|^2)^q, \quad \kappa \in \mathbb{R}, t \geq 0 \tag{6.14}$$

As a consequence, if the problem is well-posed, then it is possible to estimate the L^2 norm of the solution with the L^2 norm of the initial data as

$$|\boldsymbol{W}(\cdot, t)|_{(L^2(\Omega))^2} \leq K e^{\alpha t} |\boldsymbol{W}_0|_{(L^2(\Omega))^2}, \quad t \geq 0 \tag{6.15}$$

while if the problem is weakly well-posed, then also the derivatives of the initial data must be accounted for

$$|\boldsymbol{W}(\cdot, t)|_{(L^2(\Omega))^2} \leq K e^{\alpha t} |\boldsymbol{W}_0|_{(H^q(\Omega))^2}, \quad t \geq 0 \tag{6.16}$$

In our case, we have that $Q^{-1}(j\kappa)P(j\kappa) = SJS^{-1}$ with S and J the matrices of eigenvectors and eigenvalues, respectively given by

$$S = \begin{pmatrix} -\sqrt{1 + \mu^2\kappa^2} & \sqrt{1 + \mu^2\kappa^2} \\ 1 & 1 \end{pmatrix}, \quad J = \begin{pmatrix} \dfrac{j\kappa}{\sqrt{1 + \mu^2\kappa^2}} & 0 \\ 0 & -\dfrac{j\kappa}{\sqrt{1 + \mu^2\kappa^2}} \end{pmatrix} \tag{6.17}$$

where $det(S) = -2\sqrt{1+\mu^2\kappa^2} \neq 0$ for any real κ, so it is well-defined. Recalling that $e^J = \sum_{k=0}^{\infty} \frac{J^k}{k!}$, the solution is

$$\widehat{\boldsymbol{W}} = Se^{Jt}S^{-1}\widehat{\boldsymbol{W}}_0 \quad \text{in } \mathbb{R}\times]0,T[\tag{6.18}$$

and by taking the inverse Fourier transform

$$\phi(x) = \int_{\mathbb{R}} e^{j\kappa x}\hat{\phi}(\kappa)d\kappa, \quad x \in \Omega \tag{6.19}$$

any solution to (6.8) also satisfies

$$\boldsymbol{W}(x,t) = \int_{\mathbb{R}} e^{j\kappa x}S(\kappa)e^{J(\kappa)t}S^{-1}(\kappa)\widehat{\boldsymbol{W}}_0(\kappa)d\kappa \quad \text{in } Q \tag{6.20}$$

since the Fourier representation is unique[1] we have that (6.8) has a unique solution given by (6.20).

We can now prove an energy estimate. Let

$$D(\kappa) = \begin{pmatrix} 1 & 0 \\ 0 & 1+\mu^2\kappa^2 \end{pmatrix} \tag{6.21}$$

so, dropping the $j\kappa$ arguments and defining the complex vector product $\langle a,b\rangle = \overline{a}^T b$, one has

$$\begin{aligned} \frac{d}{dt}\langle\widehat{\boldsymbol{W}}, D\widehat{\boldsymbol{W}}\rangle &= \langle\frac{d}{dt}\widehat{\boldsymbol{W}}, D\widehat{\boldsymbol{W}}\rangle + \langle\widehat{\boldsymbol{W}}, D\frac{d}{dt}\widehat{\boldsymbol{W}}\rangle \\ &= \langle Q^{-1}P\widehat{\boldsymbol{W}}, D\widehat{\boldsymbol{W}}\rangle + \langle\widehat{\boldsymbol{W}}, DQ^{-1}P\widehat{\boldsymbol{W}}\rangle \\ &= \langle\widehat{\boldsymbol{W}}, \left(Q^{-1}\overline{P}D + DQ^{-1}P\right)\widehat{\boldsymbol{W}}\rangle \end{aligned} \tag{6.22}$$

and

$$\left(Q^{-1}P\right)^* D = \begin{pmatrix} 0 & j\kappa \\ j\kappa & 0 \end{pmatrix} = -DQ^{-1}P \tag{6.23}$$

which means that

$$\langle\widehat{\boldsymbol{W}}, D\widehat{\boldsymbol{W}}\rangle = \langle\widehat{\boldsymbol{W}}_0, D\widehat{\boldsymbol{W}}_0\rangle \quad \text{in } \mathbb{R}\times\mathbb{R}^+ \tag{6.24}$$

thus integrating for $\kappa \in \mathbb{R}$ and applying Parseval's relation we obtain the following result

Theorem 6.1. *Let n be a non-negative integer. If $\boldsymbol{W}_0 = (\eta_0, u_0) \in H^n(\Omega) \times H^{n+1}(\Omega)$ then the Cauchy problem (6.8) has a unique solution $\boldsymbol{W} = (\eta, u) \in L^\infty(0,\infty; H^n(\Omega)\times H^{n+1}(\Omega))$. Moreover,the following energy estimate applies*

$$\int_{\mathbb{R}} |\partial_x^n\eta|^2 + |\partial_x^n u|^2 + \mu^2|\partial_x^{n+1}u|^2 dx = \int_{\mathbb{R}} |\partial_x^n\eta_0|^2 + |\partial_x^n u_0|^2 + \mu^2|\partial_x^{n+1}u_0|^2 dx, \quad \forall t \geq 0 \tag{6.25}$$

---

[1] Strictly speaking, this is due to Theorem C.2, the uniqueness of the Fourier representation for initial data in $C_0^\infty(\mathbb{R})$, and the density of $C_0^\infty(\mathbb{R})$ on Sobolev spaces [76].

The diagonal matrix J can also be written as

$$J(\kappa) = j\omega(\kappa)\begin{pmatrix} 1 & 0 \\ 0 & -1 \end{pmatrix}, \quad \omega(\kappa) = \frac{\kappa}{\sqrt{1+\mu^2\kappa^2}} \tag{6.26}$$

and ω is known as the dispersion relation of the Boussinesq equation. The dispersion relation links the frequency of the oscillations with the wave number of the initial condition. In particular, for the Boussinesq equations

$$|\omega(\kappa)| = \frac{1}{\mu}\frac{\mu|\kappa|}{\sqrt{1+\mu^2\kappa^2}} \leq \frac{1}{\mu}, \quad \forall\kappa \in \mathbb{R} \tag{6.27}$$

thus the time-spectrum of the solution has compact support, i.e., the solution is infinitely smooth in time. The following Proposition 6.2 expresses this fact in terms of the regularity of the solution.

Proposition 6.2. *Let* $r \geq 1$, $\boldsymbol{W}_0 \in H^r(Q) \times H^{r+1}(Q)$. *If* $\boldsymbol{W} = (\eta, u)$ *is the solution of* (6.8) *then*

$$\boldsymbol{W} \in \bigcup_{s\in\mathbb{N}_0} H^{r,s}(Q) \times H^{r+1,s}(Q)$$

and $|\boldsymbol{W}|_{H^{r,s}\times H^{r,s}} \leq C|\boldsymbol{W}_0|_{H^{r+1}\times H^{r+1}}$

Proof. Taking the time derivative of (6.11) and using the decomposition (6.17) one obtains

$$\partial_t^k\widehat{\boldsymbol{W}} = j\omega SRe^{Jt}S^{-1}\widehat{\boldsymbol{W}}_0, \quad R = \begin{pmatrix} 1 & 0 \\ 0 & -1 \end{pmatrix} \tag{6.28}$$

which means that

$$|\partial_t^k\widehat{\boldsymbol{W}}| \leq |\omega||S||S^{-1}||\widehat{\boldsymbol{W}}_0| \tag{6.29}$$

letting $\psi(\kappa) = 1 + \mu^2\kappa^2$ then

$$SS^* = \begin{pmatrix} 2\psi^2 & 0 \\ 0 & 2 \end{pmatrix}, \quad S^{-1}(S^{-1})^* = \frac{1}{4}\begin{pmatrix} 1+\psi^{-2} & 1-\psi^{-2} \\ 1-\psi^{-2} & 1+\psi^{-2} \end{pmatrix} \tag{6.30}$$

so $|S| = \sqrt{2}\psi$ and $|S^{-1}| = 1/\sqrt{2}$, and since $|Re^{Jt}| = 1$ we obtain

$$|\partial_t^k\widehat{\boldsymbol{W}}(\kappa,t)| \leq |\omega(\kappa)|(1+\mu^2\kappa^2)^{1/2}|\widehat{\boldsymbol{W}}_0(\kappa)| \tag{6.31}$$

and finally, we can compute

$$\begin{aligned}
\int_0^T\int_{\mathbb{R}}|\partial_t^k\boldsymbol{W}(x,t)|^2dxdt &= \int_0^T\int_{\mathbb{R}}|\partial_t^k\widehat{\boldsymbol{W}}(\kappa,t)|^2d\kappa dt \\
&\leq T\int_{\mathbb{R}}|\omega(\kappa)|^2|(1+\mu^2\kappa^2)|\widehat{\boldsymbol{W}}_0(\kappa)|^2d\kappa, \quad \text{(Eq. (6.31))} \\
&\leq T\int_{\mathbb{R}}\frac{1}{\mu^2}(1+\mu^2\kappa^2)|\widehat{\boldsymbol{W}}_0(\kappa)|^2d\kappa, \quad \text{(Eq. (6.27))} \\
&= \frac{T}{\mu^2}(|\boldsymbol{W}_0|^2 + \mu^2|\partial_x\boldsymbol{W}_0|^2), \quad \text{(Parseval)}
\end{aligned} \tag{6.32}$$

Because $r \geq 1$ implies $\boldsymbol{W}_0 \in H^1(\Omega)\times H^1(\Omega)$ we conclude that $\partial_t^k\boldsymbol{W} \in (L^2(0,T;L^2(\Omega)))^2$ for every $k \geq 1$.

□

One can wonder whether the $|\partial_x u_0|_{L^2(\Omega)}$ term can be removed in the previous bounds to make the system (6.8) well-posed. The answer is no, some solutions are such that η depends solely on $\mu\partial_x u$. For example, let us expand

$$\sqrt{1+\mu^2\kappa^2} = \mu\kappa\sqrt{1+\frac{1}{\mu^2\kappa^2}} = \mu\kappa + O\left(|\mu\kappa|^{-1}\right) \tag{6.33}$$

$$\omega(\kappa) = \frac{j}{\mu}\left(1+\frac{1}{\mu^2\kappa^2}\right)^{1/2} = \frac{j}{\mu} + O\left(|\mu\kappa|^{-2}\right) \tag{6.34}$$

so for $|\mu\kappa| > 1$, the matrices (6.17) can be written as

$$S = \begin{pmatrix} -\mu\kappa & \mu\kappa \\ 1 & 1 \end{pmatrix} + O\left(|\mu\kappa|^{-1}\right) \tag{6.35}$$

$$e^{Jt} = \begin{pmatrix} e^{\frac{jt}{\mu}} & 0 \\ 0 & e^{-\frac{jt}{\mu}} \end{pmatrix} + O\left(|\mu\kappa|^{-2}t\right) \tag{6.36}$$

$$S^{-1} = \frac{1}{2}\begin{pmatrix} -\frac{1}{\mu\kappa} & \frac{1}{\mu\kappa} \\ 1 & 1 \end{pmatrix} + O\left(|\mu\kappa|^{-1}\right) \tag{6.37}$$

Replacing back into (6.20) one obtains that

$$\widehat{\boldsymbol{W}}(\kappa,t) = \begin{pmatrix} \cos(t/\mu) & -j\mu\kappa\sin(t/\mu) \\ -\frac{j}{\mu\kappa}\sin(t\mu) & \cos(t/\mu) \end{pmatrix} \widehat{\boldsymbol{W}}_0(\kappa) + O\left(|\widehat{\boldsymbol{W}}_0(\kappa)\mu\kappa t|^{-1}\right), \quad (\kappa,t) \in \mathbb{R}\times]0,T[\tag{6.38}$$

so, in particular, if $\eta_0 = 0$ then

$$\widehat{\boldsymbol{W}}(\kappa,t) = \begin{pmatrix} -\mu\sin(t/\mu)j\kappa\hat{u}_0(\kappa) \\ \cos(t/\mu)\hat{u}_0(\kappa) \end{pmatrix} + O\left(|\widehat{\boldsymbol{W}}_0(\kappa)\mu\kappa t|^{-1}\right), \quad (\kappa,t) \in \mathbb{R}\times]0,T[\tag{6.39}$$

and taking the inverse Fourier transform, assuming that there exists $\kappa_0 > 1$ such that $supp(\widehat{\boldsymbol{W}}(\cdot,t)) \subset]-\infty,-\kappa_0] \cup [\kappa_0,\infty[$

$$\boldsymbol{W}(x,t) = \begin{pmatrix} -\mu\sin(t/\mu)\partial_x u_0(x) \\ \cos(t/\mu)u_0(x) \end{pmatrix} + O\left(|\boldsymbol{W}_0|_{L^2(\Omega)}|\kappa_0\mu t|^{-1}\right), \quad (x,t) \in \Omega\times]0,T[\tag{6.40}$$

which means that $\eta(\cdot,t) \in L^2(\Omega)$ if and only if $\partial_x u_0 \in L^2(\Omega)$. Moreover, writing the previous equations with dimensional variables using (5.7), discarding small terms we obtain

$$\boldsymbol{W}(x,t) = \begin{pmatrix} -h\sqrt{\frac{h}{3g}}\sin\left(t\sqrt{\frac{3g}{h}}\right)\partial_x u_0 \\ \cos\left(t\sqrt{\frac{3g}{h}}\right)u_0(x) \end{pmatrix}, \quad (x,t) \in \Omega\times]0,T[\tag{6.41}$$

then for a fixed x, $\eta(x,\cdot)$ is a sinusoidal wave with amplitude proportional to $h^{3/2}\partial_x u_0$, which can be arbitrarily large regardless of the size of u_0 or η_0.

To confirm this consider the initial condition of a wavepacket

$$\eta_0(x) = 0, \quad u_0(x) = \sin(x/L)e^{-x^2/\sigma^2} \tag{6.42}$$

with $L = 0.01$m and $\sigma = 10L$. Figures 6.1, 6.2, 6.3 compare numerical results with equation (6.41) on depths $h = 0.01$m, $h = 1$m and $h = 100$m. The numerical results are computed by sampling the initial data on a uniform grid of 3001 points in the interval $[-20, 20]$, and applying formula (6.20) with a fast Fourier transform (FFT). For $h = 0.01m$ in Figure 6.1, being the most shallow case, Eq. (6.40) is expected to have largest error, however, the differences between numerical and theoretical curves are only perceptible after $t\sqrt{3g/h} = 0.94$; this is explained by the fact that the error term in (6.40) increases with t too. For the larger depths $h = 1m$ and $h = 100m$, Figure 6.2 and Figure 6.3, the numerical results are almost indistinguishable from the theoretical ones of (6.41), thus verifying the validity of (6.41). At the same time, these results also demonstrate how the total height (difference between two peaks) grows from 7cm to 35666m from the smallest to largest depth.

6.3 Weak well-posedness as an explanation to Problem (III)

We have just shown that the total energy of the solution of the Boussinesq equations must include the $\partial_x u$ term

$$E_B(t) = |\eta_0|^2_{L^2(\Omega)} + |u_0|^2_{L^2(\Omega)} + \mu^2|\partial_x u_0|^2_{L^2(\Omega)}, \quad t \geq 0 \tag{6.43}$$

which is not the case with the SV equations, that preserves the L^2 norm

$$E_{SV}(t) = |\eta_0|^2_{L^2(\Omega)} + |u_0|^2_{L^2(\Omega)}, \quad t \geq 0 \tag{6.44}$$

As a consequence, waves that are small for the SV model can be arbitrarily large for the Boussinesq model if $\partial_x u_0$ is sufficiently large. In this section we will give a concrete example of how the small mesh-dependent artifacts in the SV model can cause mesh-dependent solutions when transmitted on the B model, even if the SV model is able to converge.

Let us consider the case of the horizontal interface of Figure 6.4, when the model switches from the SV equations to B after some time $t = T_0$, with the initial condition consisting of a rectangular wave in the velocity profile

$$\eta_0(x) = 0, \quad u_0(x) = H(L/2 - |x|) \tag{6.45}$$

where H is the Heaviside or step function, $L = 2/3$, $\Omega = (-100, 100)$ and $h_0 = 4$. The initial velocity profile u_0 is plotted in Figure 6.5. The SV model is discretized with a fourth-order finite difference scheme [2] from $t = 0$ to $T_0 = 1$. Since it is a fourth order linear scheme, oscillations are expected in the SV nature, because of Godunov's theorem, however, the scheme is still convergent when the mesh size is reduced. The B model is then solved with the FFT, by extending the result of the SV model at $t = T_0$ by zero on the interval $(-1100, 1100)$.

---

[2] This scheme will be presented later in Section 8.4.1

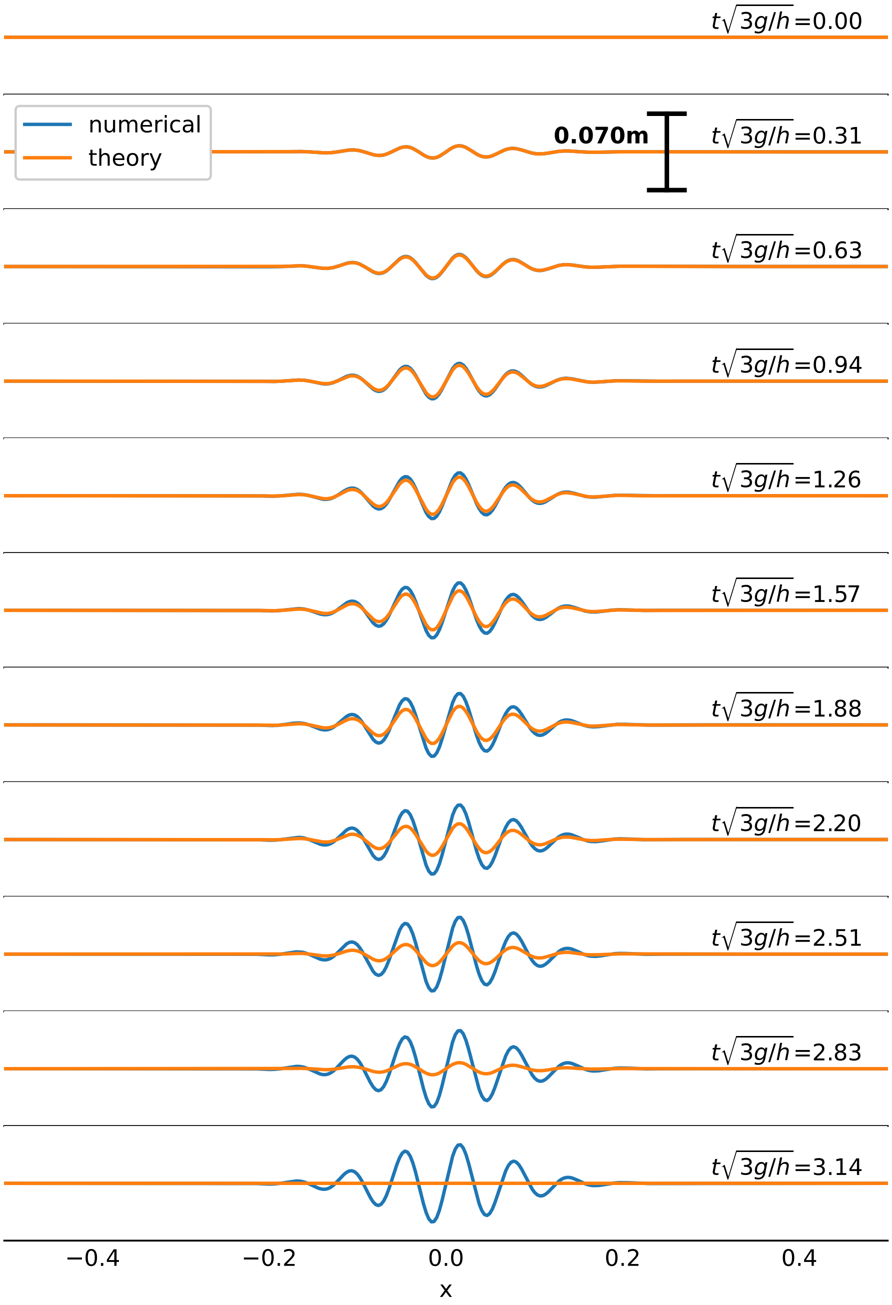

Figure 6.1: Free surface from wave packet data $h = 0.01$, $L = 0.01$

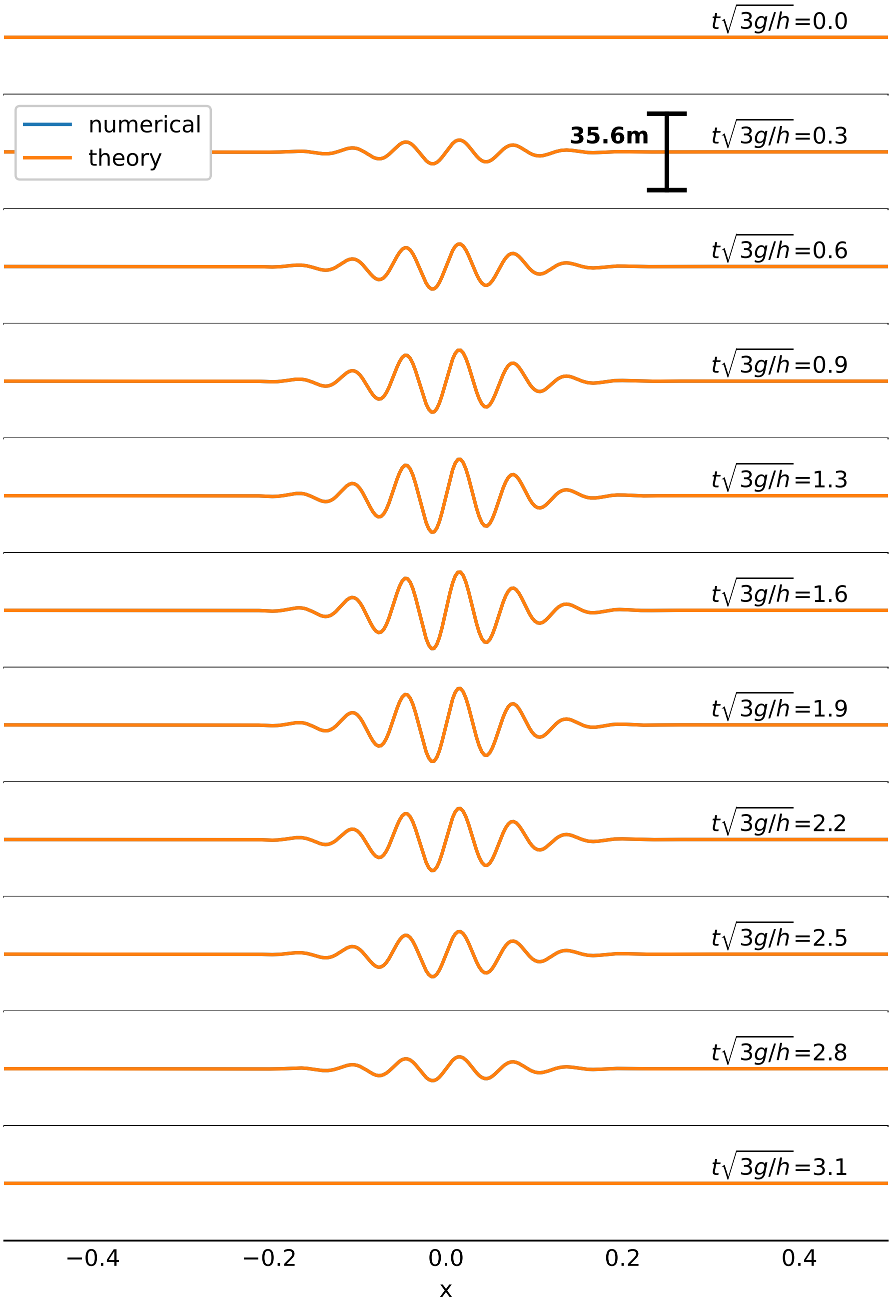

Figure 6.2: Free surface from wave packet data $h = 1.0$, $L = 0.01$

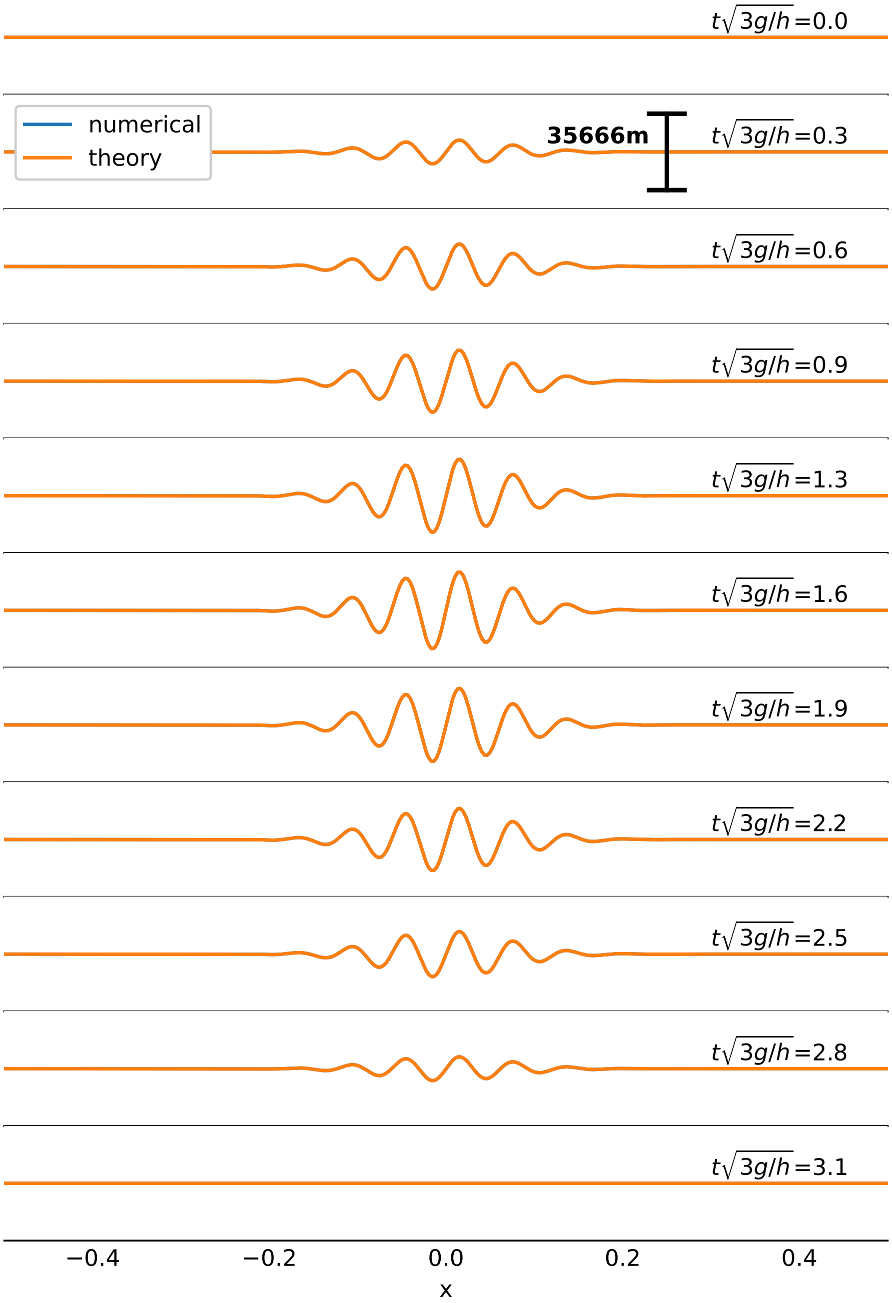

Figure 6.3: Free surface from wave packet data $h = 100.0$, $L = 0.01$

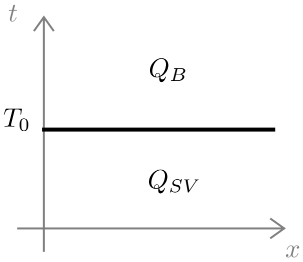

Figure 6.4: Case of a horizontal interface, transmitting data from the SV model to the Boussinesq model.

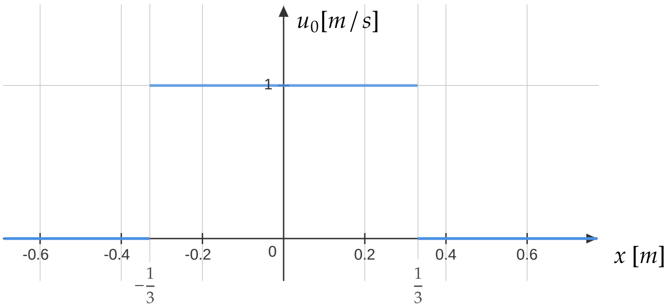

Figure 6.5: Initial velocity profile u_0 of Eq. (6.45).

Figure 6.6 shows the result of the SV model at $t = T_0$ that is used to initialize the BT model. The results of the B model at $t = T$ are shown in 6.7. The results confirm that, as the resolution is increased, the size of η (free surface) increases too. However, as shown in Fig. 6.8, if instead of the B model one continues with the SV model until $t = T$, the simulation is still oscillatory but the limit is approached as the resolution is improved. An empirical convergence rate is computed from the data in Fig. 6.9, obtaining a value close to 0.4. The low convergence rate is also expected because the solution being approximated is not smooth. The important observation is that the SV model is able to approach a mesh-independent solution, whereas the B model is not, due to the amplification of the mesh-dependent artifacts at the PDE level.

6.4 Conclusions

In this chapter we have recalled some properties of the homogeneous Cauchy problems of the SV and B equations. These are known results, but they were reformulated using the anisotropic Sobolev spaces of the Appendix D, to facilitate their use in the coming chapters.

Additionally, from this study, we were able to demonstrate the observations of the conclusions of Chapter 4, regarding question

(III) Mesh-dependance: What causes the large variations in the solution when changing the mesh size? Is it related to the instabilities?

It was demonstrated that to quantify the size or energy of a wave in the

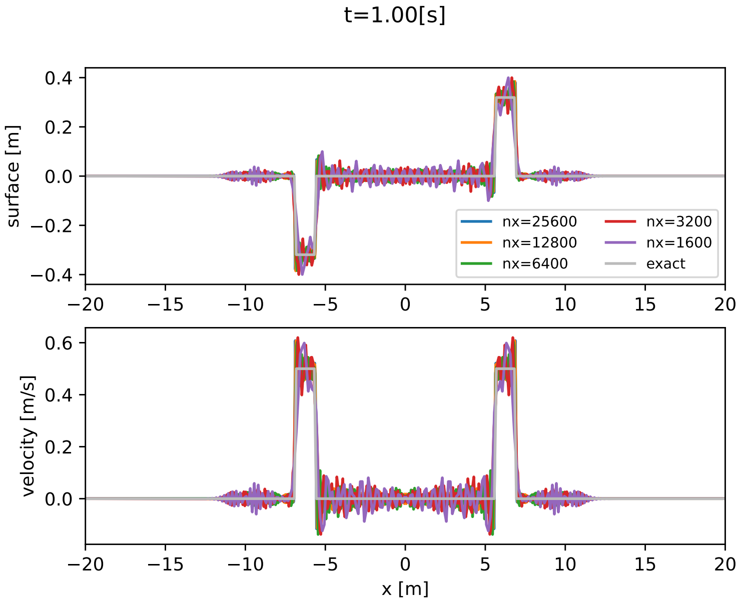

Figure 6.6: Solution obtained at $T = 1s$ with the SV model using the square wave of eq. (6.42) as initial condition (shown in fig. 6.5). This result is used as initial condition for the B model, whose results are shown in Figure 6.7.

.

SV model it suffices to use the L^2 norm of the initial data, however, in the B model, it is necessary to quantify the L^2 norm of $\partial_x u_0$ too. This is the issue of **weak-wellposedness** presented in [76]. As a consequence, mesh-dependent perturbations that have low energy in the SV model are not necessarily neglectable in the B model. Indeed, they can have huge amounts of energy, and lead to a completely different solution on each mesh size. This explains why some artifacts introduced by the discretization are harmless while propagating on the SV subdomain but, when transmitted to the BT domain, they become even larger than the wave itself.

Additionally, because these oscillations can be as large as $\partial_x u_0$, they could lead to negative water depths in nonlinear solvers, spoiling the stability of the numerical scheme too (problem (II) Instabilities).

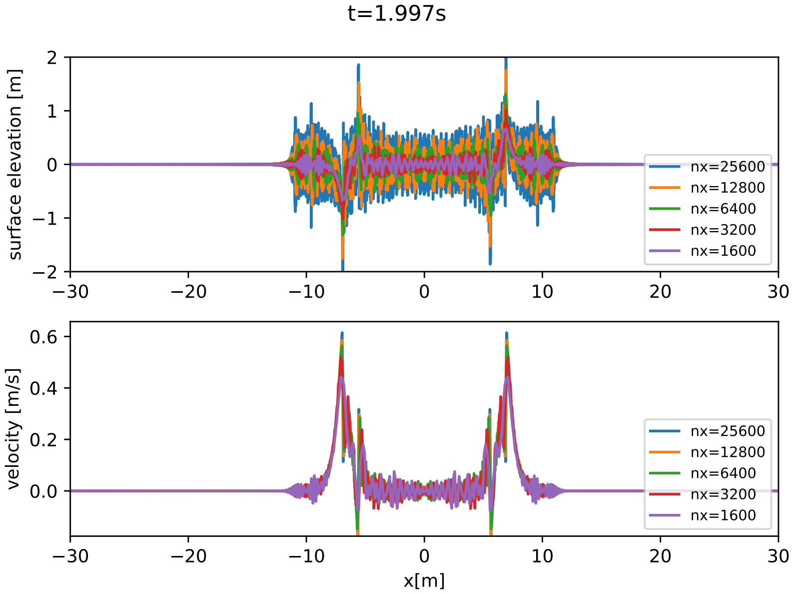

Figure 6.7: Solution obtained with the B model at $T = 2s$, computed using as initial condition the output of the SV model at $T = 1s$ from Figure 6.6. Lines of different colors represent different mesh resolutions. It is clear that as the mesh is refined the amplitude of the oscillations is larger, although the scheme remains stable.

.

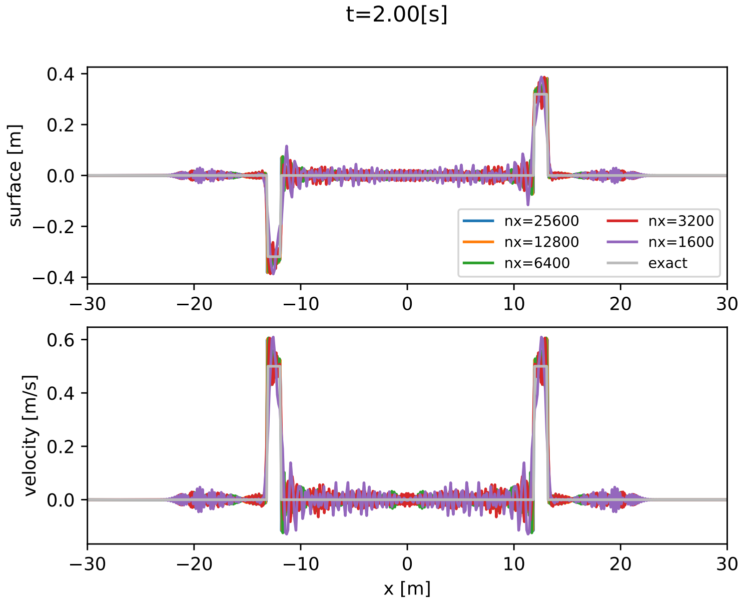

Figure 6.8: Square wave at $T = 2s$ computed with only the SV model. Despite being an oscillatory scheme the SV model is still able to approach a mesh-independent solution. This was not possible with the B model (Cf. Figure 6.7)

.

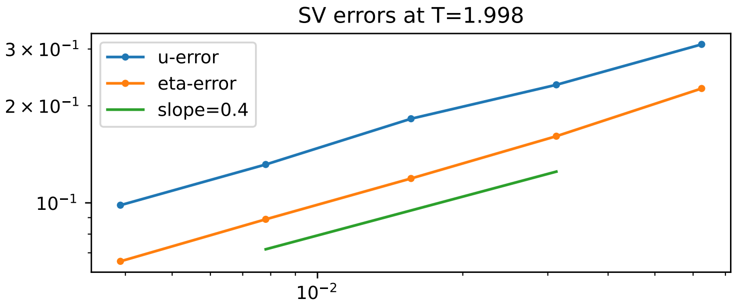

Figure 6.9: Convergence rate of the SV model using the oscillatory 4th order FD scheme on the case of the square wave at $T = 1$. Despite being oscillatory mesh-convergence is still possible with the SV model. This was not possible with the B model (Cf. Figure 6.7)

Chapter 7

Homogeneous problems on the half-line

In this chapter we are interested in the problems on the half lines $\Omega_- =]-\infty, 0[$ and $\Omega_+ =]0, \infty[$, $Q_\pm = \Omega_\pm \times]0,T[$, of functions $\boldsymbol{W}_- : [0,T] \times \overline{\Omega}_-$, $\boldsymbol{W}_+ : [0,T] \times \overline{\Omega}_+$ such that

$$\begin{cases} \mathcal{L}_\pm \boldsymbol{W}_\pm = 0 & \text{in } Q_\pm \\ \boldsymbol{W}_\pm(0,\cdot) = 0 & \text{in } \Omega_\pm \\ \boldsymbol{W}_\pm = \boldsymbol{W}_\Gamma & \text{in } \Gamma \end{cases} \tag{7.1}$$

where $\Gamma = \{(x,t) = (0,t)\}$ and $\boldsymbol{W}_{\Gamma_\pm} = (\eta_{\Gamma_\pm}, u_{\Gamma_\pm})$ is some given data.

Without loss of generality the results are shown only for the problems on Q_-, leaving only the two cases:

$$\mathcal{L}_- = \mathcal{L}_{SV}, \qquad \text{or} \qquad \mathcal{L}_- = \mathcal{L}_B \tag{7.2}$$

where, recalling from Chapter 5

$$\mathcal{L}_{SV} = \partial_t + B\partial_x, \quad B = \begin{pmatrix} 0 & 1 \\ 1 & 0 \end{pmatrix} \tag{7.3}$$

and

$$\mathcal{L}_B = (I - A\partial_x^2)\partial_t + B\partial_x, \quad A = \begin{pmatrix} 0 & 0 \\ 0 & \mu^2 \end{pmatrix} \tag{7.4}$$

notice that $\mathcal{L}_B = \mathcal{L}_{SV}$ when $\mu = 0$.

In the first case, $\mathcal{L}_- = \mathcal{L}_{SV}$, the solution is a classical result and can be obtained thanks to the method of the characteristics, as was done for the Cauchy problems of section 6.1. In the second case, $\mathcal{L}_- = \mathcal{L}_B$, the analysis is different and has already been studied in the linear case and smooth data, first in [39] and then in [64] and more recently for extended BT equations in [89]. In those references the Unified Transform Method (UTM) was used to show that, for smooth initial data, there exists a unique solution if some compatibility conditions are satisfied and if only one equation is imposed at the boundary. The main advantage of the UTM being that it provides an integral representation that converges uniformly.

In this chapter, we generalize the existing results to Dirichlet boundary data in $H^k(]0,T[), k \geq 0$ with no compatibility conditions required. This is done using the Laplace transform, so as mentioned in [64], the verification of the initial and boundary data is not straight, which motivates us to apply a density argument, similar to the one used for Cauchy problems in [76]. This analysis allows us to show that the problem is well-posed, in the sense that the model defines a linear bounded operator $\mathcal{T}$

$$\left\{\begin{array}{rl} H^k(0,T) \mapsto & H^{r,k+1}(Q_-) \times H^{r,k}(Q_-) \\ \mathcal{T} u_\Gamma = & \boldsymbol{W}_- \end{array}\right. \tag{7.5}$$

for every $r \geq 0$. This analysis also confirming the findings of [64], that one and only one boundary condition must be specified.

This result implies that the boundary data is regularized as it propagates into the domain. As a mechanism to transmit data between the two models, this is in high contrast with the case of the horizontal interface of Section 6.3. This regularizing effect was already observed in the nonlinear Boussinesq equations [18] as one of the effects of a dispersive boundary layer that appears in the IBVP of the weakly nonlinear Boussinesq model. This was also mentioned in [81]. Some details on how this boundary layer translates to the linear case are also examined in this chapter.

7.1 Laplace transform of the system

Let $\phi : \mathbb{R}^+ \cup \{0\} \to \mathbb{R}$ be a function such that there exists $\alpha > 0$ such that $t \to e^{-\sigma t}\phi(t)$ belongs to $L^2(0,T)$ for $\sigma > \alpha$. We will denote here by $\hat{\phi}$ the Laplace transform of this function

$$\hat{\phi}(s) = \frac{1}{2\pi}\int_0^\infty \phi(x,t) e^{-st} dt \tag{7.6}$$

where $s = \sigma + j\omega$, $\sigma > \alpha$, is the Laplace variable with frequency ω and decay σ. The inverse Laplace transform is then given by

$$\phi(t) = e^{\sigma t}\int_{\mathbb{R}} \hat{\phi}(\sigma + j\omega) e^{j\omega t} d\omega \tag{7.7}$$

Denoting $\widehat{\boldsymbol{W}}_- = (\hat{\eta}_-, \hat{u}_-)$ and taking the Laplace transform of $\mathcal{L}_B \boldsymbol{W}_- = 0$ one obtains

$$\left\{\begin{array}{rl} s\hat{\eta}_- + \partial_x \hat{u}_- & = 0 \\ s\hat{u}_- - s\mu^2\partial_x^2\hat{u}_- + \partial_x\hat{\eta}_- & = 0 \end{array}\right. \tag{7.8}$$

and taking the derivative on the first equation and substituting $\partial_x^2 \hat{u}_-$ on the second we obtain that $\widehat{\boldsymbol{W}}_-$ satisfies

$$\partial_x \widehat{\boldsymbol{W}}_- = R\widehat{\boldsymbol{W}}_-, \quad R = \begin{pmatrix} 0 & -s \\ -\frac{s}{1+\mu^2 s^2} & 0 \end{pmatrix} \tag{7.9}$$

and

$$\boldsymbol{W}_-(0,\cdot) = \boldsymbol{W}_\Gamma \tag{7.10}$$

Let

$$\lambda(s) = \sqrt{\frac{s^2}{1+\mu^2 s^2}} \tag{7.11}$$

with the square root taken on the branch with positive real part. This is a well-defined operation because $s \mapsto s^2/(1+\mu^2 s^2)$ maps $\mathbb{C}^+$ into $\mathbb{C} \setminus \mathbb{R}^-$. Then R satisfies

$$R = V\Lambda V^{-1}, \quad V = \begin{pmatrix} \frac{\lambda(s)}{s} & -\frac{\lambda(s)}{s} \\ 1 & 1 \end{pmatrix}, \quad \Lambda(s) = \begin{pmatrix} -\lambda(s) & 0 \\ 0 & \lambda(s) \end{pmatrix} \tag{7.12}$$

where $\det(V) = 2\lambda(s)/s = 2h/\sqrt{1+\mu^2 s^2} \neq 0$ for $s = \sigma + j\omega$ because $\sigma > 0$. So, any solution of equation (7.9) can be written as

$$\widehat{\boldsymbol{W}}_{-} = V e^{\Lambda x} V^{-1} \widehat{\boldsymbol{W}}_{\Gamma} \quad \text{in } \Omega_- \tag{7.13}$$

and denoting $V = (\boldsymbol{v}_1, \boldsymbol{v}_2)$ and $V^{-1} = (\boldsymbol{w}_1, \boldsymbol{w}_2)^T$, this is equivalent to

$$\widehat{\boldsymbol{W}}_- = (\boldsymbol{w}_1^T \widehat{\boldsymbol{W}}_{\Gamma_-}) e^{-\lambda(s)x} \boldsymbol{v}_1 + (\boldsymbol{w}_2^T \widehat{\boldsymbol{W}}_{\Gamma_-}) e^{\lambda(s)x} \boldsymbol{v}_2 \quad \text{in } \Omega_- \times \mathbb{C}^+ \tag{7.14}$$

Now, because $Re(\lambda(s)) > 0$ for $\mu \geq 0$ and $\sigma > 0$, we have that $x \mapsto e^{\lambda(s)x}$ and $x \mapsto e^{-\lambda(s)x}$ are unbounded in Ω_+ and Ω_- respectively. On the other side, from (7.7), the initial condition must satisfy

$$\boldsymbol{W}_-(\cdot, 0) = \int_{\mathbb{R}} \widehat{\boldsymbol{W}}(\cdot, \sigma + j\omega) d\omega = 0 \quad \text{in } \Omega_\pm \tag{7.15}$$

so a necessary condition to satisfy the initial condition is that the exponentials do not blowup, *i.e.*,

$$\boldsymbol{\omega}_1^T \widehat{\boldsymbol{W}}_{\Gamma-} = 0 \Leftrightarrow V^{-1} \boldsymbol{W}_{\Gamma-} = \begin{pmatrix} 0 \\ \alpha(s) \end{pmatrix} \quad \text{on } \mathbb{C}^+ \tag{7.16}$$

for some $\alpha(s)$, assuming that $\boldsymbol{W}_{\Gamma_-} \neq 0$, and recalling that $V^{-1} = (\boldsymbol{w}_1, \boldsymbol{w}_2)^T$. Left-multiplying this equation by V this means that the boundary data has to be colinear with $\boldsymbol{v}_2$, *i.e.*, $\widehat{\boldsymbol{W}}_{\Gamma_-} = \alpha_-(s)\boldsymbol{v}_2$. A similar reasoning on Q_+ leads to conclude that there must exists $\alpha_+(s)$ such that $\widehat{\boldsymbol{W}}_{\Gamma_+} = \alpha_+(s)\boldsymbol{v}_1$. Substituting on (7.14) one finds that any solution to (7.1) satisfies

$$\begin{array}{lll} \widehat{\boldsymbol{W}}_-(x,s) & = \alpha_-(s)\boldsymbol{v}_2 e^{\lambda(s)x} & (s,x) \in \mathbb{C}^+ \times \Omega_- \\ \widehat{\boldsymbol{W}}_+(x,s) & = \alpha_+(s)\boldsymbol{v}_1 e^{-\lambda(s)x} & (s,x) \in \mathbb{C}^+ \times \Omega_+ \end{array} \tag{7.17}$$

7.2 Saint-Venant equations

Equation (7.17) is also valid for the Saint-Venant equations, since it is the case when $\mu = 0$, so, either applying the inverse Laplace transform of (7.17) or using the Riemann invariants (6.4) one obtains that the solutions satisfy

$$\begin{array}{ll} \eta_-(x,t) = u_-(x,t) = u_{\Gamma_-}(t+x)H(t+x) & \text{in } \Omega_- \\ \eta_+(x,t) = u_+(x,t) = u_{\Gamma_+}(t-x)H(t+x) & \text{in } \Omega_+ \end{array} \tag{7.18}$$

Here $H(t)$ is the Heaviside function, the indicator function of the set $\{t > 0\}$. Notice we can choose the strict inequality to define H because, from (7.17) we have in Ω_-, for example, that

$$|s\hat{u}(x,s)| = |se^{-sx}\alpha(s)| \to 0 \quad \text{if } |s| \to \infty \tag{7.19}$$

because $\alpha(s)$ is in $L^2(\mathbb{R})$, so its limit for large s must be 0, and because the exponential decays faster than any polynomial. By the initial-value theorem, we conclude that $u(x,0) = 0$, despite the value of $u_{\Gamma_-}(0)$.

Proposition 7.1. *Let* $\boldsymbol{W}_{\Gamma_\pm} = (\eta_{\Gamma_\pm}, u_{\Gamma_\pm})$ *and* $r \geq 0$. *If* $u_{\Gamma_\pm} \in H^r(0,T)$ *and* $\eta_{\Gamma_\pm} = \pm u_{\Gamma_\pm}$ *then there exists a unique solution* $\boldsymbol{W}_\pm = (\eta_\pm, u_\pm) \in H^{r,r}(\Omega_\pm \times]0,T[)$ *given by* (7.18), *and for every* $x \in \Omega_\pm$ *one has* $u_\pm(x,\cdot) \in H^r(0,T)$. *Moreover, there exists* $C(T) > 0$ *such that*

$$|\boldsymbol{W}|_{H^{r,r}(\Omega_\pm \times]0,T[)} \leq C(T)|u_{\Gamma_\pm}|_{H^r(0,T)} \tag{7.20}$$

7.3 Boussinesq equations

In the case of the Boussinesq equations, $\mu > 0$, a density argument allows us to prove a similar result without recurring to compatibility conditions.

Theorem 7.1. *Let* $u_\Gamma \in H^k(0,T)$, $k \geq 0$, *there exists a unique solution to problem* (7.1) *given by* (7.17) *and*

$$\boldsymbol{W} \in \bigcup_{r \in \mathbb{N}_0} H^{r,k+3}(Q_-) \times H^{r,k+2}(Q_-)$$

Moreover, there exists $C(T,\mu,r) > 0$ *such that*

$$|\boldsymbol{W}|_{E^r} \leq C(T,\mu,r)|u_\Gamma|_{H^k(0,T)}$$

with $E^r = H^{r,k+1}(Q_-) \times H^{r,k}(Q_-)$

To prove this theorem we need to study the asymptotic behavior of the eigenvalues.

Lemma 7.1. *Let* $\mu > 0$ *and* $0 < r < 1$, *there exists* $C > 0$ *and* $R(s)$ *such that for every* $s \in \mathbb{C}^+$ *and* $|s|^2 > \dfrac{1}{\mu^2 r}$:

$$\lambda(s) = \frac{1}{\mu} + R(s), \quad |R(s)| \leq C\frac{1}{\mu^2|s|^2}$$

and C *only depends on* r.

Proof. Since we can write

$$\lambda(s) = \frac{1}{\mu}\left(1 + \frac{1}{\mu^2 s^2}\right)^{-1/2}$$

then because of the assumption $|1/(\mu s)| < r < 1$ we can apply Lemma B.2 and obtain such C and $R(s)$. ☐

As a consequence of Lemma 7.1 one can find the following estimations for large s, which will be useful in the next sections.

Lemma 7.2. *Let* $\mu > 0$, *there exists* $\sigma_0 > 0$ *such that if* $|s| > \sigma_0$ *then*

$$\frac{1}{2\mu} < |\lambda(s)| < \frac{3}{2\mu}$$

and

$$\frac{1}{2\mu} < Re(\lambda(s)) < \frac{3}{2\mu}$$

Proof. Let C and $R(s)$ be as in Lemma 7.1, then if $|s| > \sigma_0 = 2C/\mu$ and $|R(s)| \leq \frac{1}{2\mu}$, the conclusion is obtained from

$$\frac{1}{\mu} - |R(s)| \leq |\lambda(s)| \leq \frac{1}{\mu} + |R(s)|$$

and

$$\frac{1}{\mu} - |R(s)| \leq Re(\lambda(s)) \leq \frac{1}{\mu} + |R(s)|$$

. □

Proof of Theorem (7.1). The proof is done by a density argument. Let

$$M = \{f \in C_0^\infty(]0,T[) : \int_{\mathbb{R}} f(\omega)d\omega = 0\}$$

and M_0 the space of functions $f : [0,T] \to \mathbb{R}$ that can be written as

$$f(t) = e^{\sigma t} \int_{\mathbb{R}} \alpha_\sigma(\omega) e^{j\omega t} d\omega, \quad \alpha_\sigma \in M \tag{7.21}$$

with $\sigma > 0$. One can see that because of the assumptions on α_σ one has $f \in C^\infty(]0,T[)$, $f(0) = 0$ and $\alpha_\sigma(\omega)$ is the Laplace transform of f at $s = \sigma + j\omega$. We will prove that for any $n \geq 0$, $\boldsymbol{W}_-$ given by (7.17) defines a linear bounded operator

$$\left\{ \begin{array}{rl} M_0 \mapsto & H^{n,k+1}(Q_-) \times H^{n,k}(Q_-) \\ \mathcal{T}_0 u_\Gamma = & \boldsymbol{W}_- \end{array} \right. \tag{7.22}$$

and then use Theorem C.2 to show that there is a unique extension to

$$\left\{ \begin{array}{rl} H^k(0,T) \mapsto & H^{n,k+1}(Q_-) \times H^{n,k}(Q_-) \\ \mathcal{T} u_\Gamma = & \boldsymbol{W}_- \end{array} \right. \tag{7.23}$$

Let $\sigma > 0$ fixed and f, α as in (7.21). Letting $u_{\Gamma-} = f$ in (7.17)

$$\widehat{\boldsymbol{W}_-}(x, \sigma + j\omega) = \alpha_\sigma(\omega) \boldsymbol{v}_2(\sigma + j\omega) e^{\lambda(\sigma + j\omega)} x \tag{7.24}$$

so taking the inverse Laplace transform

$$\boldsymbol{W}_-(x,t) = e^{\sigma t} \int_{\mathbb{R}} \alpha_\sigma(\omega) \boldsymbol{v}_2(\sigma + j\omega) e^{\lambda(\sigma + j\omega)x} d\omega \tag{7.25}$$

we will verify that $\boldsymbol{W}_-$ verifies the initial and boundary conditions, proving that there exists a classical solution to (7.1).

A direct evaluation at $x = 0$ confirms the boundary condition $\boldsymbol{W}_-(0, \cdot) = f$. For the initial condition, because $\alpha_\sigma \in C_0^\infty$ and $\sigma > 0$ we have $\boldsymbol{W}_-(x, \cdot) \in C^\infty(]0,T[)$ so the integral can be evaluated pointwise in t. Evaluating at $t = 0$ we have

$$\boldsymbol{W}_-(x,0) = \int_{\mathbb{R}} \alpha_\sigma(\omega) \boldsymbol{v}_2(\sigma + j\omega) e^{\lambda(\sigma + j\omega)x} d\omega \tag{7.26}$$

so using Lemma 7.1

$$\begin{aligned} \boldsymbol{W}_-(x,0) &= e^{x/\mu} \int_{\mathbb{R}} \alpha_\sigma(\omega) \boldsymbol{v}_2 e^{R(s)x} d\omega \\ &\approx e^{x/\mu} \int_{\mathbb{R}} \alpha_\sigma(\omega) \boldsymbol{v}_2 (1 + R(s)x) d\omega \\ &= e^{x/\mu} \int_{\mathbb{R}} \alpha_\sigma(\omega) \boldsymbol{v}_2 R(s) x dx \end{aligned} \tag{7.27}$$

where we used the approximation of the exponential in the second line, and the assumption of the integral of α_σ in the third one. Now, using Lemma 7.2 again we can compute

$$|\boldsymbol{W}_-(x,0)| \leq e^{x/\mu} \int_{\mathbb{R}} |R(s)x||\boldsymbol{v}_2| d\omega \leq e^{x/\mu} \frac{2C|x|}{\mu^2\sigma^2} \tag{7.28}$$

because $|\boldsymbol{v}_2| \leq 2$, which means that for fixed $x \in \Omega_-$, since $\sigma > 0$ can be arbitrarily large, then necessarily $\boldsymbol{W}_-(x,0) = 0$. This proves that indeed $\boldsymbol{W}_-$ is a solution of (7.1) in Q_-. Moreover, because the Laplace-transform representation (7.17) is unique, it is the unique solution.

Now, to prove the smoothness, let $s = \sigma + j\omega$, because of (7.2) we have that if $\sigma > \sigma_0$ then $|s| > \sigma_0$ and

$$\frac{1}{2\mu} < |Re(\lambda(s))| < \frac{3}{2\mu} \tag{7.29}$$

for every $\omega \in \mathbb{R}$. Now because of (7.17) we have that

$$|\eta_-(s)| \leq \frac{|\alpha_\sigma(s)|}{|\mu s||\sqrt{1+(\mu s)^{-2}}|} e^{Re(\lambda(s))x}, \quad |u_-(s)| \leq |\alpha_\sigma(s)| e^{Re(\lambda(s))x} \tag{7.30}$$

but there exists a lower bound $0 < l(\mu,\sigma) \leq |\sqrt{1+(\mu s)^{-2}}|$ so also

$$|\eta_-(s)| \leq \frac{|\alpha_\sigma(s)|}{l(\mu,\sigma)\mu|s|} e^{Re(\lambda(s))x} \tag{7.31}$$

We will first show a continuity estimate for u, but because of the previous inequalities the same steps also apply for η_- and $\partial_t \eta_-$. From Lemma 7.2 we know there is $\sigma_0 > 0$ such that $\sigma > \sigma_0$ implies

$$Re(\lambda(s)) \geq \frac{1}{2\mu} \tag{7.32}$$

so there is C_1 such that

$$|\widehat{u}_-(s,x)| \leq C_1 |\alpha_-(s)| e^{\frac{1}{2\mu}x}, \quad x \in \Omega_- \tag{7.33}$$

so for $k \geq 0$, integrating we obtain

$$\begin{aligned} \int_0^T \int_{\Omega^-} |\partial_t^k u_-|^2 dx dt &\leq C(T) \int_{\Omega_-} \int_{\mathbb{R}} |s^k \hat{u}_-(\sigma + j\omega, x)|^2 d\omega dx \\ &\leq C(T) C_1 \int_{\mathbb{R}} |s^k \alpha_-(\sigma + j\omega)|^2 \int_{-\infty}^0 e^{x/\mu} dx d\omega \\ &= C(T) C_1 \mu \int_{\mathbb{R}} |s^k \alpha_-(\sigma + j\omega)|^2 d\omega \\ &= C(T) C_1 \mu \int_0^T |f^{(k)}(t)|^2 dt \end{aligned} \tag{7.34}$$

where the last line comes from the causality principle. This shows that η_-, u_- and $\partial_t \eta_-$ are in $H^{0,k}(Q_-)$ and

$$|\boldsymbol{W}_-|_{H^{0,k+1}(Q_-) \times H^{0,k}(Q_-)} \leq C(T) C_1 \mu |f|_{H^k(0,T)} \tag{7.35}$$

Also, for n positive and integer

$$\partial_x^n \widehat{\boldsymbol{W}}_- = \lambda(s)^n \widehat{\boldsymbol{W}}_-$$

so, using Theorem (7.2)

$$|\partial_x^n \widehat{\boldsymbol{W}}_-| = |\lambda(s)|^n |\widehat{\boldsymbol{W}}_-| \leq \left(\frac{3}{2\mu}\right)^n |\widehat{\boldsymbol{W}}_-|$$

so by Parseval's theorem $\partial_x^n \boldsymbol{W}_- \in H^{0,k+1} \times H^{0,k}$, *i.e.*, $\boldsymbol{W}_- \in H^{n,k}$, and

$$|\partial_x^n \boldsymbol{W}_-|_{L^2(0,T;L^2(\Omega_-))} \leq C(T) C_1 \mu \left(\frac{3}{2\mu}\right)^n |f|_{L^2(0,T)} \tag{7.36}$$

from where we obtain $C_2(n,\mu) > 0$ such that

$$|\boldsymbol{W}_-|_{H^{n,k+1}(Q_-)\times H^{n,k}(Q_-)} \leq C(T) C_1 \mu C_2(n,\mu) |f|_{H^k(0,T)} \tag{7.37}$$

So far, we have proved that the operator

$$\begin{cases} M_0 \subset H^k(0,T) & \to H^{n,k+1}(Q_-) \times H^{n,k}(Q_-) \\ \mathcal{T}_0 f & = \boldsymbol{W}_- \end{cases} \tag{7.38}$$

is well-defined, linear and bounded. Because of Theorem C.3 we know that M_0 is a dense subspace of $H^k(]0,T[)$ so by Theorem C.2 this means that there exists a unique bounded operator $\mathcal{T} : H^k(0,T) \to H^{n,k+1}(Q_-) \times H^{n,k}(Q_-)$ such that $\mathcal{T} f = \mathcal{T}_0 f$ for any $f \in M_0$.

Now, writing $\tilde{\boldsymbol{W}}_- = (\tilde{\eta}, \tilde{u}) = (\partial_t^k \eta, \partial_t^k u)$, then from (7.1)

$$\begin{aligned} \partial_t \tilde{\eta} + \partial_x \tilde{u} &= 0 \\ (1 - \mu^2 \partial_x^2) \partial_t \tilde{u} + \partial_x \tilde{\eta} &= 0 \end{aligned} \tag{7.39}$$

which can be rewritten as

$$\begin{aligned} (1 - \mu^2 \partial_x^2) \partial_t^2 \tilde{u} - \partial_x^2 \tilde{u} &= 0 \\ (1 - \mu^2 \partial_x^2) \partial_t^2 \tilde{\eta} - \partial_x^2 \tilde{\eta} &= 0 \end{aligned} \tag{7.40}$$

by taking ∂_x of the first one, ∂_t of the second and adding them; and by taking $(1-\mu^2\partial_x^2)\partial_t$ of the first one and $(1-\mu^2\partial_x^2)\partial_x$ of the second one and adding them. So by Theorem E.1 we obtain that $\partial_t^2 \tilde{u} \in H^{n,k}(Q_-)$ and $\partial_t^2 \tilde{\eta} \in H^{n,k+1}(Q_-)$ and, since $T < \infty$, we deduce that $\tilde{W} \in H^{k,2}$, hence $\boldsymbol{W} \in H^{n,k+3}(Q_-) \times H^{n,k+1}(Q_-)$ for any nonnegative integer k. ☐

7.4 The regularizing dispersive boundary layer

A dispersive boundary layer of size $O(\mu)$ with regularizing effects was already mentioned in [18] and [78]. This layer gives a more specific notion as to why the half-line problem (7.1) of the Boussinesq equations is well-posed for $L^2(]0,T[)$ data, whereas the Cauchy problem of section 6.2 was only weakly well-posed. This indicates a sort of greater robustness in the transmission of data through the boundary, compared to the initial condition. Moreover, unlike in [18], no compatibility conditions are required in the linear case either.

Looking at the dispersion relation

$$\omega(\kappa) = \frac{\kappa}{\sqrt{1+\mu^2\kappa^2}} \tag{7.41}$$

the regularizing effect can be understood as the truncation of the spectrum of the incoming data to the range of allowed frequencies: $\omega(\mathbb{R}) =]\frac{1}{\mu}, \frac{1}{\mu}[$. To see this, let us write the solution $\boldsymbol{W}_+$ using (7.17) as

$$\boldsymbol{W}_+(x,t) = e^{\sigma t} \int_{\mathbb{R}} \alpha_+(\sigma + j\omega) e^{-\lambda(\sigma+j\omega)x} e^{j\omega t} d\omega \tag{7.42}$$

where we assume $0 < \sigma \ll 1$. We can split the integral

$$\begin{aligned} \boldsymbol{W}_+(x,t) = e^{\sigma t} & \int_{|\omega|<1/\mu} \alpha_+(\sigma + j\omega) e^{-\lambda(\sigma+j\omega)x} e^{j\omega t} d\omega \\ + e^{\sigma t} & \int_{|\omega|>1/\mu} \alpha_+(\sigma + j\omega) e^{-\lambda(\sigma+j\omega)x} e^{j\omega t} d\omega \end{aligned} \tag{7.43}$$

and use Lemma 7.2 on the second term as

$$\begin{aligned} I &= \int_{|\omega|>1/\mu} \alpha_+(\sigma + j\omega) e^{-\lambda(\sigma+j\omega)x} e^{j\omega t} d\omega \\ &= \int_{|\omega|>1/\mu} \alpha_+(\sigma + j\omega) e^{-\frac{x}{\mu}+R(s)x} e^{j\omega t} d\omega \end{aligned} \tag{7.44}$$

from where we can compute that

$$|I| \leq e^{-x/\mu} \int_{|\omega|>1/\mu} |\alpha(\sigma + j\omega)| d\omega \tag{7.45}$$

where we have used that $Re(R(s)) > 0$ and assumed that $\alpha(\sigma + j\cdot) \in C_0^\infty(\mathbb{R})$ to estimate that α is integrable, which by density can be extended to $L^2(]0,T[)$. This shows that the contributions of frequencies outside the dispersion relation (*i.e.,* not in the image of $\omega(\kappa)$) are attenuated exponentially with a half-life $L = \mu \log(2)$, confirming the $O(\mu)$ width of the layer.

To illustrate and confirm these findings we consider the propagation of a wave-packet, a rectangular wave and a gaussian wave

$$f(t) = wp(t-5) + r(t-15) + g(t-35), \quad t \geq 0 \tag{7.46}$$

where

$$wp(t) = \cos(4\pi t) e^{-t^2}, \quad r(t) = H(2.5 - |t|), \quad g(t) = e^{-t^2} \tag{7.47}$$

and the propagation of the filtered signal $\tilde{f}(t)$ given by $\hat{\tilde{f}}(\sigma + j\omega) = H(\omega_0 - |\omega|)\hat{f}(\sigma + j\omega)$. In adimensional coordinates $\omega_0 = 1/\mu$, but substituting (5.7) one obtains $\omega_0 = \sqrt{3g/h}$. We will refer to f and $\tilde{f}$ as the full and filtered signals. To compute the solution $\boldsymbol{W}_+$ with this data the Fast-Fourier-Transform is used to discretize (7.17), taking $\sigma = 0.01$, $h = \sqrt{3}$ so $\mu = 1$ and $\omega_0 \approx 4.12Hz$, and sampling the boundary data until $T = 1000s$ with a $0.01s$ spacing.

Figure 7.1 shows the time-series of the computations for $x < 7L$. One can confirm that the wave-packet, having a central frequency $4\pi > 3\omega_0$, is already neglectable at $x = 4m$. This is in agreement with the theory, because for $h = \sqrt{3}$ the half-life is $L \approx 0.69$, so after $7L \approx 4.85$ there is a greater than 99% attenuation of the contributions of the high frequency harmonics. It is interesting though that the values of the wave packet are propagated and attenuated instantly in x, without further deformations in t.

For the rectangular wave, one can see that as it propagates further from the boundary, the wave gets smoothed and the agreement between the propagated full and filtered signals improves. Both observations happen over the same distance that the wave-packet was attenuated.

For the gaussian wave one can see that the full and filtered waves are identical from the beginning. This observation could have been anticipated by calculating the Fourier transform of the Gaussian wave

$$\hat{g}(0 + j\omega) = \sqrt{\pi} e^{-\frac{1}{2}\frac{\omega^2}{2}} \tag{7.48}$$

which has a standard deviation of $\sigma = \sqrt{2}$, and computing $\omega_0 \approx 2.94\sigma$, which indicates that the frequencies that contain 96% of its L^1 norm are allowed by the dispersion relation of the model, so the integral I is very small.

Finally, Figure 7.2 shows the wave profiles at different times. One can verify that the solution remains smooth, none of the high-frequency harmonics are visible for $x \geq 5$ and the full and filtered results match.

7.5 Conclusions

In this chapter we have studied the problems on the half-line of the SV and B equations. The results for the SV equations are known but were reformulated using the anisotropic Sobolev spaces of Appendix D. For the B case instead, two main contributions were developed:

1. **Extension to non-classical solutions:** We have generalized existing results to Dirichlet boundary data in $H^k(]0,T[), k \geq 0$, using the Laplace transform. This approach allows us to establish that the problem is well-posed, defining a linear bounded operator $\mathcal{T}$ mapping $H^k(0,T)$ to $H^{r,k+1}(Q_-) \times H^{r,k}(Q_-)$ for any $r \geq 0$ without compatibility conditions. We confirm that specifying a single boundary condition is sufficient, aligning with the findings in [64].
2. **Regularization of boundary data:** The boundary data experiences regularization as it propagates into the domain, contrasting with the horizontal interface problem discussed in Section 6.3. This regularizing effect, first noted in the dispersive boundary layer of the nonlinear Boussinesq model ([18]), is also evident in our linear case analysis.

Moreover, regarding problems (I), (II) and (III) of Chapter 4 and Chapter 5:

3. **Relation with problems (I), (II) and (III)**: From the previous result we conclude that in the half line problem of the B equations at the continuous level there is no additional oscillations (problem (I) oscillations), the model is stable (problem (II) Instabilities) and the continuity

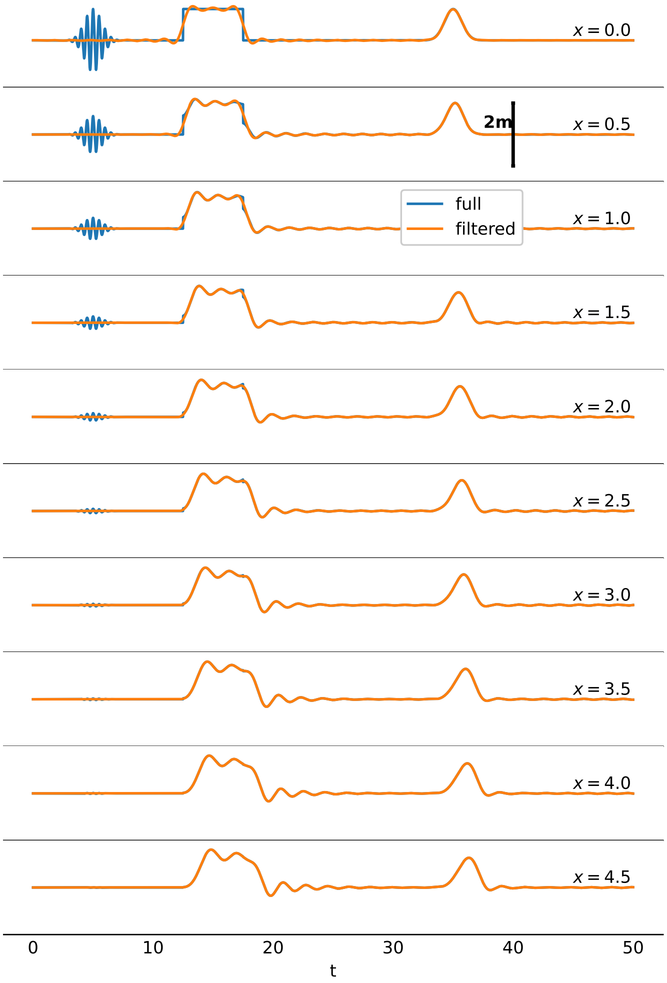

Figure 7.1: Dispersive layer: Time series at points close to the boundary.

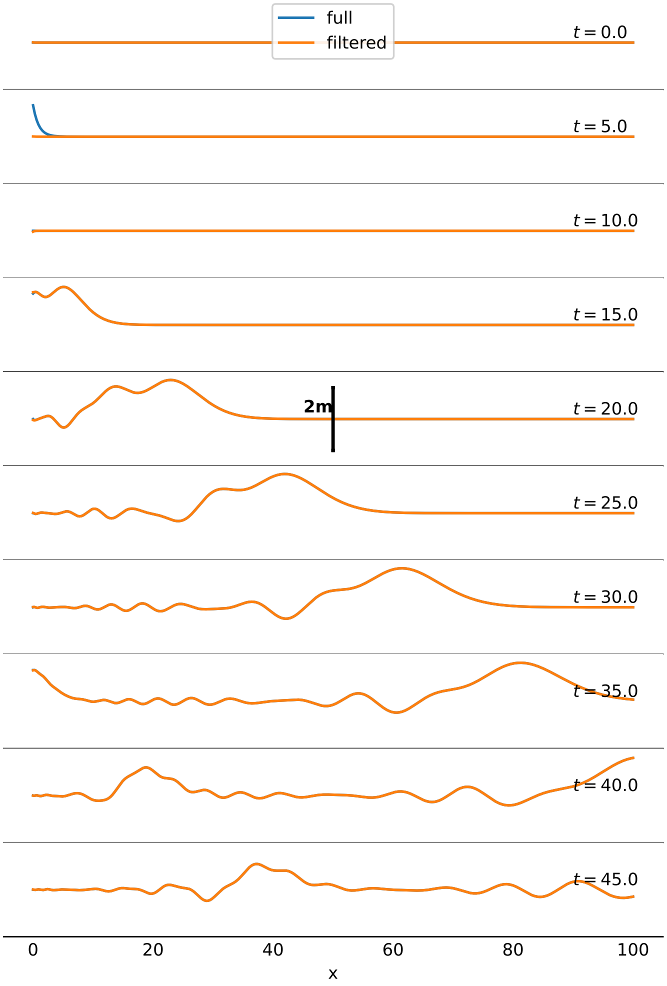

Figure 7.2: Dispersive layer: Wave profiles at different times. The wave on the $x = 0$ boundary at $t = 5.0s$ corresponds to the exponential profile of the wavepacket in the dispersive boundary layer. Contrast this result with Figure 7.1.

> on $H^k(0,T)$ to $H^{r,k+1}(Q_-) \times H^{r,k}(Q_-)$ ensures that small oscillations will remain small over time (problem (III)). In other words, none of the three problems come from the properties of the half-line problems on the B equations. For the SV equations it is known that the same conclusion applies.

Next chapter will also provide an explanation to problems (I) Oscillations, and (II) Instabilities. In fact, it will be shown that the oscillations are reflections emanating from the interface and that the hybrid model is well-posed, which implies it is stable. It is possible that the analysis of the discrete problems on the half-line could reveal more insights regarding problem (II), but this will be discussed in the final conclusions of Chapter 9. In any case, the following chapter will provide a method that can be extended to the discrete case too. This will also be discussed in the final conclusions of Chapter 9.

Chapter 8

The hybrid non-overlapping model

In this chapter we focus on the study of the hybrid model in the linear regime. To conduct the analysis, we begin by introducing the model and characterizing the coupling conditions that reformulate the problem as two coupled half-line problems (7.1). Then the existence, uniqueness and regularity is obtained by an iterative argument based on the Waveform Relaxation Method (WRM), borrowing many of the notations and techniques that were used for the domain decomposition of the advection-diffusion equation in the thesis of V. Martin [90]. Finally, the continuity with respect to the initial data, and the analysis of the coupling error is studied by means of the characterization of wave reflections that appear when waves cross the interface. In particular, this result contributes to the mathematical justification of the coupled model. This analysis will illustrate that this coupling acts as an absorbing boundary layer and elucidate why the reflections on the Saint-Venant (SV) domain can be more important than in the Boussinesq (B) domain.

8.1 Characterization of the coupling conditions

The hybrid Boussinesq Saint-Venant model (B-SV) is given by the following system of equations

$$\left\{\begin{aligned} \partial_t\eta + h\partial_x u &= 0 \quad \text{in } Q \\ \left(1-\chi\frac{h_0^2}{3}\partial_x^2\right)\partial_t u + g\partial_x\eta &= 0 \quad \text{in } Q \\ \eta(\cdot,0)=\eta_0, \quad u(\cdot,0) &= u_0 \text{ in } \Omega \end{aligned}\right. \tag{8.1}$$

where $\chi(x,t,\boldsymbol{W},...)$ is the indicator function of the dispersive domain, *i.e.*,

$$\chi(x,t,..) = \left\{\begin{array}{ll} 1 & (x,t)\in Q_B \\ & \\ 0 & (x,t)\in Q_{SV} \end{array}\right. \tag{8.2}$$

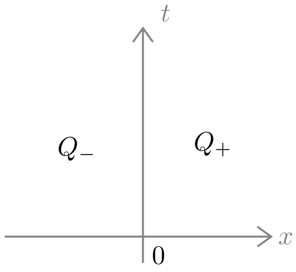

Figure 8.1: Vertical interface in the $x-t$ plane.

We will make the assumption of a vertical interface in the $x-t$ plane, as shown in Figure 8.1. This means that either

$$Q_B = Q_- \quad \text{and } Q_{SV} = Q_+ \tag{8.3}$$

or

$$Q_{SV} = Q_- \quad \text{and } Q_B = Q_+ \tag{8.4}$$

Using the adimensionalization

$$\begin{aligned} x' &= \frac{x}{L} \qquad t' = t\frac{\sqrt{gh}}{L} \\ \eta' &= \frac{\eta}{a} \qquad u' = \frac{u}{\frac{a}{h}\sqrt{gh}} \end{aligned} \tag{8.5}$$

the hybrid model becomes

$$\begin{cases} \partial_t \eta + \partial_x u &= 0 \quad \text{in } Q \\ \left(1-\chi\mu^2\partial_x^2\right)\partial_t u + g\partial_x\eta &= 0 \quad \text{in } Q \\ \eta(\cdot,0)=\eta_0, \quad u(\cdot,0) &= u_0 \text{ in } \Omega \end{cases} \tag{8.6}$$

with $\mu = h_0/\sqrt{3}$. Defining

$$\mathcal{L}_{hyb} = (I-\chi A)\partial_t + B\partial_x, \quad A = \begin{pmatrix} 0 & 0 \\ 0 & \mu^2 \end{pmatrix}, B = \begin{pmatrix} 0 & 1 \\ 1 & 0 \end{pmatrix}, \tag{8.7}$$

the hybrid model can be written more compactly as

$$\begin{cases} \mathcal{L}_{hyb}\boldsymbol{W} = 0 & \text{in } Q \\ \boldsymbol{W}(\cdot,0) = \boldsymbol{W}_0 & \text{in } \Omega \end{cases} \tag{8.8}$$

with $\boldsymbol{W} = (\eta, u)$ and $\boldsymbol{W}_0 = (\eta_0, u_0)$.

The operator $\mathcal{L}_{hyb}$ has a heterogeneous character thanks to the variable coefficient $\chi(x)$. To proceed with the analysis let us recall first that

$$\mathcal{L}_{SV} = \partial_t + B\partial_x, \quad \mathcal{L}_B = (I-A)\partial_t + B\partial_x, \tag{8.9}$$

Letting $\mathcal{L}_-$ and $\mathcal{L}_+$ be either $\mathcal{L}_{SV}$ or $\mathcal{L}_B$ according to Q_- and Q_+, the strategy for the analysis of the heterogeneous Cauchy problem (8.8) is to reformulate it as two coupled homogeneous problems in the half-line:

$$\begin{cases} \mathcal{L}_-\boldsymbol{W}_- = 0, & \text{in } Q_- \\ \boldsymbol{W}_-(\cdot,0) = \boldsymbol{W}_0, & \text{in } \Omega_- \end{cases} \quad \begin{cases} \mathcal{L}_+\boldsymbol{W}_+ = 0, & \text{in } Q_+ \\ \boldsymbol{W}_+(\cdot,0) = \boldsymbol{W}_0, & \text{in } \Omega_+ \end{cases} \tag{8.10}$$

by finding coupling conditions such that their solutions are the same, that is to say:

$$\begin{aligned} \boldsymbol{W} &= \boldsymbol{W}_-, \quad \text{in } Q_- \\ \boldsymbol{W} &= \boldsymbol{W}_+, \quad \text{in } Q_+ \end{aligned} \tag{8.11}$$

with $\boldsymbol{W}$ solution to (8.8) and $(\boldsymbol{W}_-, \boldsymbol{W}_+)$ solution of (8.10). The next theorem reveals the coupling conditions that reformulate problem (8.8) as an equivalent coupling of the two half-line problems (8.10).

Theorem 8.1 (Coupling conditions of the hybrid model)**.** *Suppose* $\boldsymbol{W} = (\eta, u)$ *is solution of* (8.8)*,* $\boldsymbol{W}_- = (\eta_-, u_-)$*,* $\boldsymbol{W}_+ = (\eta_+, u_+)$ *solve problems* (8.10)*, and the Laplace transforms of* $u_-(,\cdot), u_+(0,\cdot), \partial_x u_-(0,\cdot), \partial_x u_+(0,\cdot)$ *exist. Then* $\boldsymbol{W}_- = \boldsymbol{W}_{|\overline{Q}_-}$ *and* $\boldsymbol{W}_+ = \boldsymbol{W}_{|\overline{Q}_+}$ *if and only if*

$$\left.\begin{aligned} u_-(0,\cdot) &= u_+(0,\cdot) \\ \partial_x u_-(0,\cdot) &= \partial_x u_+(0,\cdot) \end{aligned}\right. \quad \text{in }]0,T[\tag{8.12}$$

Proof. Let

$$\begin{aligned} \boldsymbol{V}_- = (\zeta_-, v_-) &= \boldsymbol{W}_- - \boldsymbol{W} \quad \text{in } \overline{Q}_- \\ \boldsymbol{V}_+ = (\zeta_+, v_+) &= \boldsymbol{W}_+ - \boldsymbol{W} \quad \text{in} \overline{Q}_+ \end{aligned}$$

then $\boldsymbol{V}_-$ and $\boldsymbol{V}_+$ satisfy (8.10) with

$$\boldsymbol{V}_\pm(\cdot, 0) = 0, \quad \text{in } \Omega_\pm \tag{8.13}$$

($\Rightarrow$): Assuming that $\boldsymbol{W}_- = \boldsymbol{W}_{|\overline{Q}_-}$ and $\boldsymbol{W}_+ = \boldsymbol{W}_{|\overline{Q}_+}$, then v_- and v_+ are constant and equal to zero in $\overline{Q}_\pm$ as also are $\partial_x v_\pm$. Since both $\overline{Q}_\pm$ contain $\{x = 0, t \in [0,T]\}$, we have that $v_-(0,t) = v_+(0,t) = 0$ and $\partial_x v_-(0,t) = \partial_x v_+(0,t) = 0$. From the assumption that the Laplace transforms of $u_-(,\cdot), u_+(0,\cdot), \partial_x u_-(0,\cdot), \partial_x u_+(0,\cdot)$ exist, we deduce $\partial_x v_\pm(0,\cdot) = \partial_x u_\pm(0,\cdot) - \partial_x u(0,\cdot) = 0$, hence eq. (8.12) holds.

($\Leftarrow$): On the other side, let us denote by $\hat{()}$ the Laplace transform. Let us also assume that the equations (8.12) hold and let $\lambda_\pm(s)$ be such that

$$\begin{aligned} v_-(x,s) &= \hat{u}_-(0,s)e^{\lambda_-(s)x}, \quad (x,s) \in \Omega_- \times \mathbb{C}^+ \\ v_+(x,s) &= \hat{u}_+(0,s)e^{-\lambda_+(s)x}, \quad (x,s) \in \Omega_+ \times \mathbb{C}^+ \end{aligned} \tag{8.14}$$

as in Section 7.1. Because at $t = 0$ v_- and v_+ are null, from (8.14) we know that

$$\begin{aligned} \partial_x \hat{v}_-(0,s) &= \lambda_-(s)\hat{v}_-(0,s) \\ \partial_x \hat{v}_+(0,s) &= -\lambda_+(s)\hat{v}_+(0,s) \end{aligned}$$

Substracting both equations in (8.1)

$$\partial_x \hat{v}_-(0,s) - \partial_x \hat{v}_+(0,s) = (\lambda_-(s)\hat{v}_-(0,s) + \lambda_+(s)\hat{v}_+(0,s))$$

and, by definition of $v_\pm$, if the first equation of (8.12) holds then

$$\partial_x \hat{u}_-(0,s) - \partial_x \hat{u}_+(0,s) = (\lambda_-(s) + \lambda_+(s))2\hat{v}_i(0,s) \tag{8.15}$$

is true for both $\hat{v}_i = \hat{v}_-$ and $\hat{v}_i = \hat{v}_+$. Then, if the second equation of (8.12) also holds, the left hand side of (8.15) is zero. Since $Re(\lambda_-) > 0$ and $Re(\lambda_+) > 0$, necessarily v_+ and v_- are null. Then using the definition of $v_\pm$ we obtain the conclusion. □

At the same time, the coupling conditions (8.12) can be reformulated in multiple equivalent ways. In particular, if instead one defines transmission conditions using linear operators B_-, B_+ as

$$\begin{aligned} B_-(u_-(0,\cdot)) &= B_-(u_+(0,\cdot)) \\ B_+(u_-(0,\cdot)) &= B_+(u_+(0,\cdot)) \end{aligned} \quad \text{in }]0,T[\tag{8.16}$$

instead of (8.12), to preserve the solution of the hybrid model it is enough to choose B_- and B_+ such that their Laplace transforms satisfy

$$\begin{aligned} \widehat{Bu_-(0,\cdot)} &= \partial_x \widehat{u}_- + m_- \hat{u}_- + c_- \\ \widehat{Bu_+(0,\cdot)} &= \partial_x \widehat{u}_+ + m_+ \hat{u}_+ + c_+ \end{aligned} \quad \text{in } \mathbb{C}^+ \tag{8.17}$$

with $m_\pm(s), c_\pm(s) : \mathbb{C}^+ \to \mathbb{C}$ such that $m_- - m_+ \neq 0$, which is the condition for equations (8.16) to be linearly independent in the frequency domain of the Laplace transform. This "trick" was noted by [84] in the context of domain decomposition methods and nowadays is commonly used to define optimized Schwarz methods [42].

8.2 Existence, uniqueness and regularity

Without loss of generality we will assume that $\mathcal{L}_- = \mathcal{L}_B$ and $\mathcal{L}_+ = \mathcal{L}_{SV}$. This will be convenient for the analysis of this section and study the coupled half-lines problems

$$\begin{cases} \mathcal{L}_B \boldsymbol{W}_- & = 0 & \text{in } Q_- \\ \boldsymbol{W}_-(\cdot,0) & = \boldsymbol{W}_0 & \text{in } \Omega_- \\ (\partial_t + \partial_x) u_-(0,\cdot) & = (\partial_t + \partial_x) u_+(0,\cdot) & \text{in }]0,T[\end{cases}$$
$$\begin{cases} \mathcal{L}_{SV} \boldsymbol{W}_+ & = 0 & \text{in } Q_+ \\ \boldsymbol{W}_+(\cdot,0) & = \boldsymbol{W}_0 & \text{in } \Omega_+ \\ u_+(0,\cdot) & = u_-(0,\cdot) & \text{in }]0,T[\end{cases} \tag{8.18}$$

Since $B_- = \partial_t + \partial_x$ and B_+ satisfy (8.17), any solution to (8.18) will be a solution to the hybrid model. We will proceed with the analysis by applying the WRM to this problem, *i.e.*, by studying the algorithm

$$\begin{cases} \mathcal{L}_B \boldsymbol{W}_-^{k+1} & = 0 & \text{in } Q_- \\ \boldsymbol{W}_-^{k+1}(\cdot,0) & = \boldsymbol{W}_0 & \text{in } \Omega_- \\ (\partial_t + \partial_x) u_-^{k+1}(0,\cdot) & = (\partial_t + \partial_x) u_-^{k}(0,\cdot) & \text{in }]0,T[\end{cases}$$
$$\begin{cases} \mathcal{L}_{SV} \boldsymbol{W}_+^{k+1} & = 0 & \text{in } Q_+ \\ \boldsymbol{W}_+^{k+1}(\cdot,0) & = \boldsymbol{W}_0 & \text{in } \Omega_+ \\ u_+^{k+1}(\cdot,0) & = u_+^{k}(0,\cdot) & \text{in }]0,T[\end{cases} \tag{8.19}$$

and proving that it defines a sequence $(\boldsymbol{W}_-^k, \boldsymbol{W}_+^k)_{k=0}^{\infty}$ such that:

- The sequence is well defined: there exists a unique element for each k
- The sequence converges, and the limit does not depend on $(\boldsymbol{W}_-^0, \boldsymbol{W}_+^0)$

which implies that (8.8) is well-posed. As we will see, the choice of transmission conditions not only ensures that the algorithm converges but also that the limit is reached at $k = 2$, so the continuous dependance on the data easily holds.

Remark 8.1. *The reader may notice that the WRM is not employed for parallel computing, as for example was done in the PhD thesis of V. Martin [90]. In our case, this method is used as a mathematical tool, similar to how it was applied in the seminal work of Schwarz [105, 43].*

Remark 8.2. *One could also attempt to prove that for every k, $(\boldsymbol{W}_-^k, \boldsymbol{W}_+^k)$ depends continuously on the initial data. Such an attempt is reported in Appendix F for $k = 3$. The problem with this proof is that the assumptions of the trace theorems by Lions & Magenes [83] are too strict to match the required topologies obtained in Chapters 6 and 7 over the 3 steps of the algorithm. To deal with this issue an assumption of smoothness was applied on the solution of the half line problem of the B equations, which is in any case too strong to be valid. This calls for either a better characterization of the smoothing properties of the dispersive boundary layer or to use a more flexible estimate for the continuity of the traces.*

8.2.1 Initial boundary value problems involved

In this section we study the initial boundary value problems involved in algorithm (8.19). The overall idea is to write the solutions as the superposition of the solution to the Cauchy problem, $\boldsymbol{W}_{cauchy}$ with the same initial conditions, and the solution to the related homogeneous half-line problem $\boldsymbol{W}_c$ such that $\boldsymbol{W}_{cauchy} + \boldsymbol{W}_c$ proves the well-posedness of the problem. The analysis is performed only on Q_- since the proof on Q_+ is similar.

Saint-Venant equations

$$\begin{cases} \mathcal{L}_{SV}\boldsymbol{W} & = 0 \quad \text{in } Q_+ \\ \boldsymbol{W}(\cdot,0) & = \boldsymbol{W}_0 \quad \text{in } \Omega_+ \\ u_c(0,\cdot) & = g \quad \text{in }]0,T[\end{cases} \tag{8.20}$$

Proposition 8.1. *Let $r \geq 0$, $g \in H^r(0,T)$ and $(\eta_0, u_0) \in H^r(\Omega_+) \times H^r(\Omega_+)$. There exists a unique solution $\boldsymbol{W} = (\eta, u) \in H^{r,r}(Q_+)$ to problem (8.20) and*

$$(\partial_t + \partial_x)u(0,\cdot) \in H^{r-1}(0,T) \tag{8.21}$$

Proof. Let $\boldsymbol{W}_c = (\eta_c, u_c) = \boldsymbol{W} - \boldsymbol{W}_{cauchy}$ where $\boldsymbol{W}_{cauchy} = (\eta_{cauchy}, u_{cauchy}) \in H^{n,n}(Q_-)$ is solution to the Cauchy problem (6.3). Then, from Proposition 6.1, $u_{cauchy}(0,\cdot) \in H^r(0,T)$, which means that $g_c = u_{cauchy}(0,\cdot) - g \in H^r(0,T)$ also. Since $\boldsymbol{W}_c$ satisfies

$$\begin{cases} \mathcal{L}_{SV}\boldsymbol{W}_c & = 0 \quad \text{in } Q_+ \\ \boldsymbol{W}(\cdot,0) & = 0 \quad \text{in } \Omega_+ \\ u_c(0,\cdot) & = g_c \quad \text{in }]0,T[\end{cases} \tag{8.22}$$

because of Theorem 7.1 there exists a unique solution $\boldsymbol{W}_c$, it belongs to $H^{r,r}(Q_+)$ and $u_c(x,\cdot) \in H^r(0,T)$ for every $x \in \Omega_+$. Since $\boldsymbol{W} = \boldsymbol{W}_{cauchy} + \boldsymbol{W}_c$ we conclude the existence, uniqueness and regularity. Now for the trace, $\partial_t u(0,\cdot) \in$

$H^{r-1}(0,T)$ because $g \in H^r(0,T)$. And $\partial_x u(0,\cdot) \in H^{r-1}(0,T)$ too because $\partial_x u(0,\cdot) = \partial_x u_{cauchy}(0,\cdot) + \partial_x u_c(0,\cdot)$, and both are the transport of g_c and $\boldsymbol{W}_0$, so the regularity decreases by 1.

□

Boussinesq equations

Now for the Boussinesq equations

$$\begin{cases} \mathcal{L}_B \boldsymbol{W} & = 0 & \text{in } Q_- \\ \boldsymbol{W}(\cdot,0) & = \boldsymbol{W}_0 & \text{in } \Omega_- \\ (\partial_t + \partial_x)u(0,\cdot) & = g & \text{in }]0,T[\end{cases} \tag{8.23}$$

Theorem 8.2. *Let $\boldsymbol{W}_0 \in H^r(\Omega) \times H^{r+1}(\Omega)$ and $g \in H^s(0,T)$ with $r > 1/2$, then there exists a unique solution $\boldsymbol{W}$ to problem (8.23) and $\boldsymbol{W} \in H^{r,s+1}(Q_-) \times H^{r+1,s+1}(Q_-)$.*

Proof. Let $\boldsymbol{W}_c = (\eta_c, u_c) = \boldsymbol{W} - \boldsymbol{W}_{cauchy}$ where $\boldsymbol{W}_{cauchy} = (\eta_{cauchy}, u_{cauchy})$ is the solution of the Cauchy problem (6.8). Then, from Theorem 7.1,

$$\boldsymbol{W}_{cauchy} \in E_{cauchy} = \bigcup_{s_1 \geq 0} H^{r,s_1}(Q_-) \times H^{r+1,s_1}(Q_-) \tag{8.24}$$

and if we assume $s_1 > 0$ and $r > 1/2$, from Theorem D.2 one can compute that

$$g_{cauchy} = (\partial_t + \partial_x) u_{cauchy}(0,\cdot) \in H^{\nu_1}(0,T), \quad \nu_1(s_1) = s_1 \left(1 - \frac{3}{2(r+1)}\right), \forall s_1 > 0 \tag{8.25}$$

Since $\nu_1(s)$ can take any positive real value let s_1' such that $\nu_1(s_1) \geq s$ for every $s_1 \geq s_1'$, then $g_c = g_{cauchy} - g \in H^s(0,T)$. Since $\boldsymbol{W}_c$ satisfies

$$\begin{cases} \mathcal{L}_B \boldsymbol{W}_c & = 0 & \text{in } Q_- \\ \boldsymbol{W}(\cdot,0) & = 0 & \text{in } \Omega_- \\ (\partial_x + \partial_t)u(0,\cdot) & = g_c & \text{in }]0,T[\end{cases} \tag{8.26}$$

let $\alpha_-(s) = \hat{u}_-(0,s)$, taking the Laplace transform of (8.26)

$$\alpha_-(s) = \frac{\hat{g}_c(s)}{s + \lambda(s)} \tag{8.27}$$

for $s = \sigma + j\omega$, $\sigma > 0$, so it is well-defined as a pseudo-differential operator. Because $Re(\lambda(s)) > 0$, $|s + \lambda(s)| = |s||1 + \lambda(s)/s| \geq |s|$ due to $Re(\lambda(s)/s) > 0$ too

$$|\alpha_-(s)| \leq \frac{|g_c(s)|}{|s|} \tag{8.28}$$

and so

$$u_-(0,\cdot) = \mathcal{L}^{-1}(\alpha_-) \in H^{s+1} \tag{8.29}$$

Using Theorem 7.1 there exists a unique solution $\boldsymbol{W}_c$ and

$$\boldsymbol{W}_c \in E_c = \bigcup_{n \in \mathbb{N}_0} H^{n,s+4}(Q_-) \times H^{n,s+3}(Q_-) \tag{8.30}$$

which implies that the unique solution to problem (8.23) is $\boldsymbol{W} = \boldsymbol{W}_{cauchy} + \boldsymbol{W}_c$ and

$$\boldsymbol{W} \in E_{cauchy} \cap E_c = H^{r,s+4}(Q_-) \times H^{r,s+3}(Q_-) \tag{8.31}$$

□

8.2.2 Boussinesq-Saint-Venant algorithm

The algorithm (8.19) can be initialized as follows

$$
\begin{array}{l}
\left\{\begin{array}{lll}
\mathcal{L}_B \boldsymbol{W}^{\mathbf{0}}_- & = 0 & \text{in } Q_- \\
\boldsymbol{W}^0_-(\cdot,0) & = \boldsymbol{W}_0 & \text{in } \Omega_- \\
\partial_t u_-^{k+1}(0,\cdot) + \partial_x u_-^{k+1}(0,\cdot) & = g_-^0 & \text{in }]0,T[
\end{array}\right. \\
\\
\left\{\begin{array}{lll}
\mathcal{L}_{SV} \boldsymbol{W}^{\mathbf{0}}_+ & = 0 & \text{in }]0,T[\times\Omega_+ \\
\boldsymbol{W}^0_+(\cdot,0) & = \boldsymbol{W}_0 & \text{in } \Omega_+ \\
u_+^{k+1}(0,\cdot) & = g_+ & \text{in }]0,T[
\end{array}\right.
\end{array}
\tag{8.32}
$$

Proposition 8.2. *Let $r \geq 1$, $0 \leq s \leq r-1$, $g^0_- \in H^s(0,T)$, g^0_+ in $H^{s+1}(0,T)$, and $\boldsymbol{W}_0 \in H^r(\Omega) \times H^{r+1}(\Omega)$, the algorithm (8.19) initialized by (8.32) defines unique sequences $(\boldsymbol{W}^k_-)_k$ and $(\boldsymbol{W}^k_+)_k$ for $k \geq 0$ integer, and $\boldsymbol{W}^k_- \in H^{r,s+3}(Q_-) \times H^{r+1,s+4}(Q_-)$ and $\boldsymbol{W}^k_+ \in H^{r,r}(Q_+) \times H^{r,r}(Q_+)$.*

Proof. Let $g^0_- \in H^{s_-}(0,T)$ and $g^0_+ \in H^{s_+}(0,T)$ with $s_-, s_+ \geq 0$ to be defined. From Proposition 8.1 and equation (8.29) of Theorem 8.2 for Q_-, and from Proposition 8.1 for Q_+, we have the following mapping

$$
\begin{array}{llll}
H^{s_-}(0,T) & \to H^{r,s_-+3}(Q_-) \times H^{r+1,s_-+4}(Q_-) & \to H^{s_-+1} \\
g^0_- & \to \boldsymbol{W}^k_- & \to g^1_+ \\
\\
H^{s_+}(0,T) & \to H^{n,n}(Q_+) \times H^{n,n}(Q_+) & \to H^{n-1}(0,T) \\
g^0_+ & \to \boldsymbol{W}^k_+ & \to g^1_-
\end{array}
\tag{8.33}
$$

with $n = min(s_+, r)$, so to be able to use g^1_+ and g^1_- in the next iteration without degrading the regularity, s_- and s_+ must satisfy the inequalities

$$
\begin{array}{r}
s_- + 1 \geq s_+ \\
min(s_+, r) - 1 \geq s_-
\end{array}
\tag{8.34}
$$

which defining $s_- = s$, $s_+ = s+1$ are satisfied if $s \leq r-1$. Because the same argument can be applied inductively, the proof is complete. ☐

Theorem 8.3. *Let $r \geq 0$, and $\boldsymbol{W}_0 \in H^r(\Omega) \times H^{r+1}(\Omega)$, the following two statements are true*

(i) The algorithm (8.19), initialized with (8.32), converges in 2 additional iterations and the limit does not depend on g^0_- nor g^0_+

(ii) There exists a unique solution $\boldsymbol{W}$ to problem (8.8) and

$$
\begin{array}{l}
\boldsymbol{W}_{|Q_-} \in H^{r,r+2}(Q_-) \times H^{r+1,r+3}(Q_-) \\
\boldsymbol{W}_{|Q_+} \in H^{r,r}(Q_+) \times H^{r,r}(Q_+)
\end{array}
\tag{8.35}
$$

Proof. Let $\boldsymbol{W}^k_\pm$ be the difference between iterations $k-1$ and k in algorithm (8.19) for integer $k \geq 1$. By linearity this difference satisfies

$$\left\{\begin{array}{rll} \mathcal{L}_-\boldsymbol{W}^k_- & = 0 & \text{in } Q_- \\ \boldsymbol{W}^k_-(\cdot,0) & = 0 & \text{in } \Omega_- \\ \partial_t u^k_-(0,\cdot)+\partial_x u^k_-(0,\cdot) & = \partial_t u^{k-1}_+(0,\cdot)+\partial_x u^{k-1}_+(0,\cdot) & \text{in }]0,T[\end{array}\right. \tag{8.36}$$

$$\left\{\begin{array}{lll} \mathcal{L}_+\boldsymbol{W}^k_+ & = 0 & \text{in } Q_+ \\ \boldsymbol{W}^k_+(\cdot,0) & = 0 & \text{in } \Omega_+ \\ u^k_+(0,\cdot) & = u^{k-1}_-(0,\cdot) & \text{in }]0,T[\end{array}\right. \tag{8.37}$$

taking the Laplace transform and using (7.17), one has for $k \geq 0$ that there exists $\alpha^k_\pm(s)$, $s \in \mathbb{C}^+$, such that

$$\begin{aligned} \hat{u}^k_-(s,x) &= \alpha^k_-(s)e^{\lambda(s)x} \quad x \in \Omega_- \\ \hat{u}^k_+(s,x) &= \alpha^k_+(s)e^{-sx} \quad x \in \Omega_+ \end{aligned} \tag{8.38}$$

which means that $\partial_x \hat{u}^k_-(s) = \lambda(s)\alpha^k_-(s)$ and $\partial_x \hat{u}^k_+(s) = -s\alpha^k_+(s)$ and the boundary condition in (8.36) can be developed as

$$\begin{aligned} & s\hat{u}^k_-(0,s) + \partial_x \hat{u}^k_-(0,s) = s\hat{u}^k_+(s,0) + \partial_x \hat{u}^k_+(s,0) \\ \Leftrightarrow\ & (s+\lambda(s))\alpha^k_-(s,0) = 0 \end{aligned} \tag{8.39}$$

and because $Re(s+\lambda(s)) > 0$ we deduce that $\alpha^k_-(s) = 0$ for every integer $k \geq 1$.

Replacing equation (8.38) in the boundary condition in (8.37) we obtain $\alpha^{k+1}_+(s) = \alpha^k_-(s) = 0$ for $k \geq 1$, so $\alpha^k_+(s) = 0$ for every $k \geq 2$. Replacing in (8.38) this means that $\boldsymbol{W}^k_\pm = 0$ for $k \geq 2$ so the sequence has converged on $k = 2$ already. Moreover, if one chooses a different initialization (g^0_-, g^0_+), then taking $\boldsymbol{W}^k_\pm$ as the difference between the solution at iteration k and the limit already found, by the same argument one has that $\boldsymbol{W}^k_\pm = 0$ on $k \geq 2$, proving that the same limit is reached.

Let now $\boldsymbol{W}^2_\pm$ be the limit of algorithm (8.19). From Theorem 8.3 we know that $\boldsymbol{W}^2_\pm$ is unique, solves problem (8.18), and because the transmission conditions of (8.18) satisfy (8.17), from Theorem 8.1 we deduce that the reconstruction

$$\boldsymbol{W} = \left\{\begin{array}{ll} \boldsymbol{W}_- & \text{in } \overline{Q}_- \\ \boldsymbol{W}_+ & \text{in } Q_+ \end{array}\right. \tag{8.40}$$

is also a solution to the hybrid's model of problem (8.8) too. Moreover, the solution is unique, otherwise if $\boldsymbol{W}' = (\eta', u')$ is another solution of (8.8) then from Theorem 8.1 and (8.17) it would solve problem (8.18), and the algorithm (8.19) initialized with

$$\begin{aligned} g^0_- &= (\partial_t + \partial_x)u'(0,\cdot) \\ g^0_+ &= u'(0,\cdot) \end{aligned} \tag{8.41}$$

would converge at $k = 0$ already, so by uniqueness of the limit necessarily $\boldsymbol{W}' = \boldsymbol{W}$. Finally, because we can pick $g^0_- = g^0_+ = 0$, then one can choose the maximum s that satisfies Proposition 8.2, *i.e.*, $s = r - 1$, which gives the regularity of the solution. □

8.3 Coupling error (reflections) and continuity

In this section we focus on the derivation of an explicit solution of (8.8) in the case where $\boldsymbol{W}_0$ is supported in one of the subdomains. For simplicity we will assume that $supp(\boldsymbol{W}_0) \subset \Omega_-$ and that either $\mathcal{L}_- = \mathcal{L}_B$ and $\mathcal{L}_+ = \mathcal{L}_{SV}$, the BSV case, or $\mathcal{L}_- = \mathcal{L}_{SV}$ and $\mathcal{L}_+ = \mathcal{L}_B$, the SVB case. We will denote by $(\lambda_-(s), \boldsymbol{v}_1^-, \boldsymbol{v}_2^-)$ and $(\lambda_+(s), \boldsymbol{v}_1^+, \boldsymbol{v}_2^+)$ the positive eigenvalue and pair of eigenvectors of the diagonalization (7.12), for $\mathcal{L}_-$ and $\mathcal{L}_+$ respectively, which is valid for both $\mu = 0$ and $\mu > 0$.

The idea is to use these assumptions to write the solution $\boldsymbol{W}$ as

$$\boldsymbol{W} = \boldsymbol{W}^\star + \boldsymbol{W}' \quad \text{in } Q \tag{8.42}$$

where $\boldsymbol{W}'$ is an unknown perturbation of $\boldsymbol{W}^\star$, the solution to the one-way coupling, given by

$$\boldsymbol{W}^\star = \begin{cases} \boldsymbol{W}_{cauchy,-} & \text{in } Q_- \\ \boldsymbol{W}_{half,+} & \text{in } Q_+ \end{cases} \tag{8.43}$$

with $\boldsymbol{W}_{cauchy,-}$ and $\boldsymbol{W}_{half,+}$ the solutions to the Cauchy and half-line problems

$$\begin{cases} \mathcal{L}_-\boldsymbol{W}_{cauchy,-} = 0, & \text{in } Q \\ \boldsymbol{W}_{cauchy,-}(\cdot,0) = \boldsymbol{W}_0 & \text{in } \Omega \end{cases} \tag{8.44}$$

and

$$\begin{cases} \mathcal{L}_+\boldsymbol{W}_{half,+} = 0, & \text{in } Q_+ \\ \boldsymbol{W}_{half,+}(\cdot,0) = 0 & \text{in } \Omega_+ \\ u_{half,+}(0,\cdot) = u_{cauchy,-}(0,\cdot) & \text{on }]0,T[\end{cases}, \tag{8.45}$$

By definition $\boldsymbol{W}'$ is unknown and will be obtained using Laplace-transform formulas and a reflection method. This method is similar to the one used in the study of one-dimensional IBVPs of the 1D wave equation [35], except that in this case the amplitude of the reflection, the reflection coefficient, depends on the frequency, *i.e.*, it is a filter. Such a reflection coefficient has also been derived in the study of absorbing boundary conditions [34, 33, 49, 58] . But so far, to the author's knowledge, this is the first time it is used to study the coupling of wave equations with different dispersion relations.

In the following we start by deriving the reflection coefficient using another choice of transmission conditions equivalent to (8.12). Then, we use the reflection method to analyze $\boldsymbol{W}'$, distinguishing the cases $\mathcal{L}_- = \mathcal{L}_B$ and $\mathcal{L}_- = \mathcal{L}_{SV}$.

8.3.1 Reflection coefficient

To derive the solution for the perturbation $\boldsymbol{W}'$ we will use the transmission conditions

$$\begin{cases} (\partial_x + \lambda_+)\hat{u}_-(0,\cdot) &= (\partial_x + \lambda_+)\hat{u}_+(0,\cdot) & \text{in } \mathbb{C}^+ \\ u_+(0,\cdot) &= u_-(0,\cdot) & \text{in }]0,T[\end{cases} \tag{8.46}$$

which satisfy (8.17), so they are equivalent to (8.12) and by Theorem (8.1) the solution of (8.10) will be the same as the solution of the hybrid model. Moreover, because $supp(\boldsymbol{W}_0) \subset \Omega_-$, using the results and notations of the half line problems of Chapter 7, $\boldsymbol{W}_+$ satisfies

$$\widehat{\boldsymbol{W}}_+(x,s) = \hat{u}(0,s)\boldsymbol{v}_1^+ e^{-\lambda_+(s)x}, \quad (x,s) \in \Omega_+ \times \mathbb{C}^+ \tag{8.47}$$

and the right hand side of the first line of equation (8.46) is

$$(\partial_x + \lambda_+)\hat{u}_+(0,\cdot) = 0 \tag{8.48}$$

which is the exact absorbing boundary condition of the operator $\mathcal{L}_+$. In the BSV the operator is local and corresponds to the transport operator

$$(\partial_t + \partial_x)u_-(0,\cdot) = 0 \tag{8.49}$$

while in the SVB case it is a pseudo-differential operator and was described in [65].

Because of (8.46), denoting $\boldsymbol{W}'_- = (\eta'_-, u'_-) = \boldsymbol{W}_- - \boldsymbol{W}^\star_{cauchy,-}$:

$$(\partial_x + \lambda_+)\hat{u}'_-(0,\cdot) = -(\partial_x + \lambda_+)\hat{u}^\star_{cauchy,-}(0,\cdot) \quad \text{, in } \mathbb{C}^+ \tag{8.50}$$

and because $\hat{u}^\star_{cauchy,-}$ also satisfies the half-line problem (7.17) in Q_+ with trace $u^\star_{cauchy,-}(\cdot,)$, we have that

$$\begin{array}{rll} \partial_x \widehat{u}^\star_{cauchy,-} & = -\lambda_- \widehat{u}^\star_{cauchy,-} & \text{in } \overline{\Omega_+} \times \mathbb{C}^+ \\ \partial_x \widehat{u}'_- & = \lambda_- \widehat{u}'_- & \text{in } \overline{\Omega_-} \times \mathbb{C}^+ \end{array} \tag{8.51}$$

substituting into (8.50) we obtain that

$$\hat{u}'_-(0,s) = r(s)\widehat{u}^\star_{cauchy,-}(0,s) \quad s \in \mathbb{C}^+ \quad \text{with} \quad r(s) = \frac{\lambda_-(s) - \lambda_+(s)}{\lambda_-(s) + \lambda_+(s)} \tag{8.52}$$

from (8.52) we can obtain $\boldsymbol{W}'_-$ and $\boldsymbol{W}'_+$ from the propagation of the signal

$$u_\Gamma = \mathcal{L}^{-1}(r\hat{u}^\star_{cauchy,-}(0,\cdot)) \quad \text{in }]-,T[\tag{8.53}$$

on each half-line problem (7.1), however, a more expressive formula can be obtained. Using (7.17) for $\boldsymbol{W}'_-$ and $\boldsymbol{W}^\star_{cauchy,-}$, we know that

$$\begin{array}{rll} \widehat{\boldsymbol{W}'_-}(x,s) & = r(s)\widehat{u}^\star_{cauchy,-}(0,s)\boldsymbol{v}_2^- e^{\lambda_-(s)x} & \text{in } \Omega_- \times \mathbb{C}^+ \\ \widehat{\boldsymbol{W}}^\star_{cauchy,-}(x,s) & = \widehat{u}^\star_{cauchy,-}(0,s)\boldsymbol{v}_1^- e^{-\lambda_-(s)x} & \text{in } \Omega_+ \times \mathbb{C}^+ \end{array} \tag{8.54}$$

and since

$$\boldsymbol{v}_2^- = G\boldsymbol{v}_1^- \quad \text{with } G = \begin{pmatrix} -1 & 0 \\ 0 & 1 \end{pmatrix} \tag{8.55}$$

we obtain

$$\widehat{\boldsymbol{W}'_-}(x,s) = r(s)G\widehat{\boldsymbol{W}}^\star_{cauchy,-}(-x,s) \quad \text{in } \overline{\Omega}_- \times \mathbb{C}^+ \tag{8.56}$$

This expression shows already that the perturbation of the one-way coupling solution can be described by reflecting $\boldsymbol{W}^\star_{cauchy,-}$ through the x axis and by filtering the solution in time by $r(s)$. This is why we refer to $\boldsymbol{W}'_\pm$ as reflections, even though $\boldsymbol{W}'_+$ is in the opposite direction. The formulation (8.56) of the reflections may seem (anti) symmetric because $r(s)$ in (8.52) only changes sign when $\mathcal{L}_-$ is $\mathcal{L}_B$ or $\mathcal{L}_{SV}$. By using a reflection technique similar to the one sometimes used for the 1D wave equation [35], the following sections show a more explicit representation that reveals the differences between these two cases.

Remark 8.3. *The reflection coefficient could be derived in the BSV case by noticing that* (8.46) *can be written as*

$$(\partial_t + \partial_x)u_-(0,\cdot) = 0 \tag{8.57}$$

so, following a classical procedure on absorbing boundary conditions [33, 34, 58] one can replace $u_-(x,t) = e^{j(\kappa x - \omega(\kappa)t)} + r(\kappa)e^{j(-\kappa x - \omega(\kappa)t)}$*, with* $\omega(\kappa)$ *the dispersion relation of the Boussinesq model, evaluate at* $x = 0$ *and obtain*

$$r(\kappa) = \frac{\sqrt{1+\mu^2\kappa^2} - 1}{\sqrt{1+\mu^2\kappa^2} + 1} \tag{8.58}$$

which coincides with one of the formulas of Section 8.4. However, in the SVB case, the transparent boundary condition (8.46) *is a nonlocal pseudo-differential operator [65], and the application of this simple method is not clear. With the current derivation, not only this case can be handled, but also a precise analysis of the model can be derived for arbitrary initial data, which is not possible with the more classical approach.*

8.3.2 Boussinesq to Saint-Venant case

We start with the case $\mathcal{L}_- = \mathcal{L}_B$ and $\mathcal{L}_+ = \mathcal{L}_{SV}$ (BSV) using the dispersion relation in (6.26) that will denoted by $\omega_-(\kappa)$. In the next Theorem 8.4 the Taylor expansion of $r(s)$ with convergence region $|\mu s| < 1$

$$r_N(s) = \sum_{n=1}^{N} a_n(\mu s)^{2n} \tag{8.59}$$

will simplify the inversion of (8.56) and reformulate $\boldsymbol{W}'_-$ as the solution of a Cauchy problem.

Theorem 8.4. *Let* $\mathcal{L}_- = \mathcal{L}_B$*. If* $\boldsymbol{W}_0$ *is supported on* Ω_- *then* $\widehat{\boldsymbol{W}'_-}$ *is the restriction to* Ω_- *of the solution of the Cauchy problem*

$$\begin{cases} \mathcal{L}_B \boldsymbol{W} = 0 & \text{in } Q \\ \boldsymbol{W}(0,\cdot) = \mathcal{F}^{-1}\left(r(j\omega_-)\right) * GR\boldsymbol{W}_0 & \text{in } \Omega \end{cases} \tag{8.60}$$

where R *is such that* $Rf(x) = f(-x)$ *and* $\mathcal{F}^{-1}$ *is the inverse Fourier transform.*

Proof. Let $\widehat{\boldsymbol{W}}^N$ be such that

$$\widehat{\boldsymbol{W}}^N(x,s) = r_N(s)G\widehat{\boldsymbol{W}}^\star_-(-x,s) \quad x \in \Omega_- \tag{8.61}$$

taking the inverse Laplace transform this means that

$$\boldsymbol{W}^N_-(x,t) = \mathcal{L}^{-1}(r_N(s)) * G\boldsymbol{W}^\star_-(-x,\cdot) \tag{8.62}$$

since it is a finite sum, we can write

$$\mathcal{L}^{-1}(r_N(s)) * f = \sum_{n=1}^{N} a_n \mu^{2n} \partial_t^{2n} f \tag{8.63}$$

also, from (6.20)

$$\boldsymbol{W}(-x,t)=\int_{\mathbb{R}} e^{j\kappa x}S^{-1}e^{Jt}S\widehat{\boldsymbol{W}}_0(-\kappa)d\kappa \tag{8.64}$$

which means that

$$\begin{aligned}\boldsymbol{W}_-^N(x,t)&=\mathcal{L}^{-1}(r_N(s))*G\boldsymbol{W}_-^\star(-x,\cdot)\\&=\sum_{n=1}^N a_n\mu^{2n}\partial_t^{2n}G\boldsymbol{W}_-^\star(-x,\cdot)\\&=\int_{\mathbb{R}}\sum_{n=1}^N a_n\mu^{2n}e^{j\kappa x}S^{-1}\partial_t^{2n}\left(e^{Jt}\right)SG\widehat{\boldsymbol{W}}_0(-\kappa)d\kappa\end{aligned} \tag{8.65}$$

and since

$$\partial_t^{2n}e^{Jt}=(j\omega_-(\kappa))^{2n}e^{Jt} \tag{8.66}$$

after rearranging one can substitute the definition of r_N as

$$\begin{aligned}\boldsymbol{W}_-^N(x,t)&=\int_{\mathbb{R}} e^{j\kappa x}S^{-1}e^{Jt}S\left(\sum_{n=1}^N a_n(\mu j\omega)^{2n}G\widehat{\boldsymbol{W}}_0(-\kappa)\right)d\kappa\\&=\int_{\mathbb{R}} e^{j\kappa x}S^{-1}e^{Jt}S\left(r_N(j\omega)G\widehat{\boldsymbol{W}}_0(-\kappa)\right)d\kappa\end{aligned} \tag{8.67}$$

since $\mu|\omega(\kappa)|<1$ we can take the limit $N\to\infty$ to obtain

$$\boldsymbol{W}_-'(x,t)=\int_{\mathbb{R}} e^{j\kappa x}S^{-1}e^{Jt}S\left(r(j\omega)G\widehat{\boldsymbol{W}}_0(-\kappa)\right)d\kappa \tag{8.68}$$

and comparing with (6.20) we conclude that $\boldsymbol{W}_-'$ is the solution of (6.8) with initial condition $\mathcal{F}^{-1}(r(j\omega))*GR\boldsymbol{W}_0$. ☐

8.3.3 Saint-Venant to Boussinesq case

The key argument for the convergence of the integrals involved in the proof of Theorem 8.4 is that the dispersion relation satisfies $\mu|\omega|<1$, so the Taylor series converges. Under this assumption one can repeat the same argument (8.4) to obtain that

Proposition 8.3. *If $\mathcal{L}_-=\mathcal{L}_{SV}$, $\boldsymbol{W}_0$ is supported on Ω_- and $\mathcal{F}(\boldsymbol{W}_0)$ is supported on $]-\frac{1}{\mu},\frac{1}{\mu}[$, then $\boldsymbol{W}_-$ is the restriction to $\overline{\Omega}_-$ of the solution of he Cauchy problem*

$$\begin{cases}\mathcal{L}_{SV}\boldsymbol{W}=0 & \text{in } Q\\ \boldsymbol{W}(0,\cdot)=\mathcal{F}^{-1}(r(j\omega_-))*GR\boldsymbol{W}_0 & \text{in } \Omega\end{cases} \tag{8.69}$$

The assumption on the spectrum is too strong, however, using formula (6.5) and the assumption on the support of the initial data one obtains the following:

Theorem 8.5. *If $\mathcal{L}_-=\mathcal{L}_{SV}$, $\boldsymbol{W}_0$ is supported on Ω_- then $\boldsymbol{W}_-'=(\eta_-',u_-')$ is the restriction to $\overline{\Omega_-}$ of the solution $\boldsymbol{W}=(\eta,u)$ of the Cauchy problem*

$$\begin{cases}\mathcal{L}_{SV}\boldsymbol{W}=0 & \text{in } Q\\ \boldsymbol{W}(0,\cdot)=H(x)\mathcal{L}^{-1}(r)*GR\boldsymbol{W}_0 & \text{in } \Omega\end{cases} \tag{8.70}$$

Proof. From (6.5), because $\boldsymbol{W}_0 = 0$ in Q_+

$$u^\star_{cauchy,-}(0,t) = \frac{1}{2}(\eta_0 + u_0)(-t) \quad t \geq 0 \tag{8.71}$$

substituting on the first equation of (8.54) we obtain

$$\widehat{\boldsymbol{W}'_-}(x,s) = \frac{r(s)}{2}(\widehat{R\eta_0}(s) + \widehat{Ru_0}(s)) \begin{pmatrix} -1 \\ 1 \end{pmatrix} e^{sx} \tag{8.72}$$

so taking the inverse Laplace transform

$$\begin{aligned} \eta'_-(x,t) &= -\mathcal{L}^{-1}\left(\frac{r}{2}(\widehat{R\eta_0} + \widehat{Ru_0})\right)(t+x)H(t+x) \\ u'_-(x,t) &= \mathcal{L}^{-1}\left(\frac{r}{2}(\widehat{R\eta_0} + \widehat{Ru_0})\right)(t+x)H(t+x) \end{aligned}, \quad \text{in } \Omega_- \tag{8.73}$$

if we now denote $\tilde{\eta}_0(x) = -\mathcal{L}^{-1}(r\widehat{R\eta_0})$ and $\tilde{u}_0(x) = \mathcal{L}^{-1}(r\widehat{Ru_0})$ then

$$\begin{aligned} \eta'_-(x,t) &= \frac{1}{2}(\tilde{\eta}_0(x+t) - \tilde{u}_0(x+t)) \\ u'_-(x,t) &= -\frac{1}{2}(\tilde{\eta}_0(x+t) - \tilde{u}_0(x+t)) \end{aligned} \tag{8.74}$$

which contrasted with (6.5) proves the conclusion. □

8.3.4 Continuity on the initial data

Because $\boldsymbol{W}_- = \boldsymbol{W}^\star_{cauchy,-} + \boldsymbol{W}'_-$ we can leverage our knowledge that both $\boldsymbol{W}^\star_{cauchy,-}$ and $\boldsymbol{W}'_-$ solve a Cauchy problem that depends on $\boldsymbol{W}_0$ to prove that the hybrid model depends continuously on the initial data. This result can later be extended to data not necessarily contained on one side of the interface by means of a density argument. To simplify the notation, in the following we will denote

$$a \lesssim b \tag{8.75}$$

to say that there exists a constant $C > 0$ such that $a \leq Cb$.

Proposition 8.4. *Let $n \geq 0$, $\boldsymbol{W}_0 \in H^{n+1}(\Omega) \times H^{n+1}(\Omega)$ with supp($\boldsymbol{W}_0$) $\subset \mathbb{R}^-$ and $\boldsymbol{W}$ the solution of the hybrid model. There exists a constant $C > 0$ such that*

$$|\boldsymbol{W}|_{(H^{n,n}(Q))^2} \leq C|\boldsymbol{W}_0|_{H^{n+1}\times H^{n+1}(\Omega)} \tag{8.76}$$

Proof. B to SV case: Let $\mathcal{L}_- = \mathcal{L}_B$ and $\mathcal{L}_+ = \mathcal{L}_{SV}$ and $\boldsymbol{W}_- = \boldsymbol{W}_{|Q_-}$ and $\boldsymbol{W}_+ = \boldsymbol{W}_{|Q_+}$. From (8.42) we have $\boldsymbol{W}_- = \boldsymbol{W}^\star_{cauchy,-} + \boldsymbol{W}'_-$, so using Theorem 8.4 we deduce that $\boldsymbol{W}_-$ is solution of the Cauchy problem (6.8) with initial condition $\boldsymbol{W}_0^-$ given by

$$\mathcal{F}(\boldsymbol{W}_0^-) = (I + rGR)\mathcal{F}(\boldsymbol{W}_0), \tag{8.77}$$

hence, using that $|r| \leq 1$ and Theorem 6.1

$$\begin{aligned} |\boldsymbol{W}_-|_{H^{n,s}(Q_-)\times H^{n,s}(Q_-)} &\lesssim |\boldsymbol{W}_0^-|_{H^{n+1}(\Omega_-)\times H^{n+1}(\Omega_-)} \\ &\leq |\boldsymbol{W}_0|_{H^{n+1}(\Omega)\times H^{n+1}(\Omega)} \end{aligned}, \quad \forall s \geq 0 \tag{8.78}$$

and $u'_- \in H^{n+1,s}(Q_-)$ so from Theorem D.2 $u_-(0,\cdot) \in H^{\nu_0}$ with $\nu_0 = s\dfrac{n+1/2}{n+1}$. Choosing s such that $\nu_0 = n$ then from Proposition 7.1 and the continuity of the trace in Theorem D.2

$$\begin{aligned} |\boldsymbol{W}_+|_{(H^{n,n}(Q_+))^2} &\lesssim |u_-(0,\cdot)|_{H^n} \\ &\lesssim |\boldsymbol{W}_-|_{H^{n,n}(Q_-)\times H^{n,n}(Q_-)} \\ &\lesssim |\boldsymbol{W}_0|_{H^{n+1}(\Omega)\times H^{n+1}(\Omega)} \end{aligned} \tag{8.79}$$

hence reconstructing the solution we obtain

$$|\boldsymbol{W}|_{(H^{n,n}(Q))^2} \lesssim |\boldsymbol{W}_0|_{(H^{n+1}(\Omega))^2} \tag{8.80}$$

SV to B case: Let now $\mathcal{L}_- = \mathcal{L}_{SV}$ and $\mathcal{L}_+ = \mathcal{L}_B$. From Theorem 8.5, $\boldsymbol{W}_-$ is the solution of the Cauchy problem (6.3) with initial condition $\boldsymbol{W}_0^-$ given by

$$\mathcal{L}(\boldsymbol{W}_0^-) = (I + rGR)\mathcal{L}(\boldsymbol{W}_0) \tag{8.81}$$

hence, using the Proposition 6.1 and $|r| \leq 1$

$$\begin{aligned} |\boldsymbol{W}_-|_{(H^{m,m}(Q_-))^2} &\lesssim |\boldsymbol{W}_0^-|_{H^m(\Omega_-)\times H^m(\Omega_-)} \\ &\lesssim |\boldsymbol{W}_0|_{H^m(\Omega)\times H^m(\Omega)} \end{aligned} \tag{8.82}$$

also $u'_- \in H^{m,m}(Q_-)$ and $u_-(0,\cdot) \in H^m(0,T)$. Then, from Theorem 7.1 and the continuity of the trace w.r.t the initial data (which can be derived from (6.5))

$$\begin{aligned} |\boldsymbol{W}_+|_{H^{r,m+1}(Q_+)\times H^{r,m}(Q_+)} &\lesssim |u_-(0,\cdot)|_{H^m} \\ &\lesssim |\boldsymbol{W}_0^-|_{(H^m(\Omega_-))^2} \\ &\lesssim |\boldsymbol{W}_0|_{(H^m(\Omega))^2} \end{aligned} \tag{8.83}$$

Taking $r = m$ and reconstructing $\boldsymbol{W}|_{Q_-} = \boldsymbol{W}_-$ and $\boldsymbol{W}_{Q_+} = \boldsymbol{W}_+$

$$|\boldsymbol{W}|_{(H^{m,m}(\Omega))^2} \lesssim |\boldsymbol{W}_0|_{H^m(\Omega)\times H^m(\Omega)} \tag{8.84}$$

and taking $m = n+1$ this implies

$$|\boldsymbol{W}|_{(H^{n,n}(Q))^2} \lesssim |\boldsymbol{W}_0|_{(H^{n+1}(\Omega))^2} \tag{8.85}$$

□

Proposition 8.5. *Let $n \geq 0$, if $\boldsymbol{W}_0 \in H^{n+1}(\Omega) \times H^{n+1}(\Omega)$ and $\boldsymbol{W}$ is the solution of the hybrid model, then there exists a constant $C > 0$ such that*

$$|\boldsymbol{W}|_{(H^{n,n}(Q))^2} \leq C|\boldsymbol{W}_0|_{H^{n+1}\times H^{n+1}(\Omega)} \tag{8.86}$$

Proof. The proof will be done by a density argument. Let $\boldsymbol{W} \in M \times M$, with

$$M = \{f \in C^\infty(\mathbb{R}) : \quad f(0) = 0)\} \tag{8.87}$$

and let $\mathcal{T}_0$ such that

$$\boldsymbol{W} = \mathcal{T}_0\boldsymbol{W}_0 \tag{8.88}$$

is the solution of hybrid's problem (8.8). Define

$$\boldsymbol{W}_0^L = \left\{ \begin{array}{ll} \boldsymbol{W}_0 & \text{in } \Omega_- \\ 0 & \text{in } \Omega_+ \end{array} \right. , \quad \boldsymbol{W}_0^R = \left\{ \begin{array}{ll} 0 & \text{in } \Omega_- \\ \boldsymbol{W}_0 & \text{in } \Omega_+ \end{array} \right. , \tag{8.89}$$

then from Proposition 8.4

$$|\mathcal{T}_0 \boldsymbol{W}_0^L|_{(H^{n,n}(Q))^2} \lesssim |\boldsymbol{W}_0^L|_{(H^{n+1}(\Omega))^2} \tag{8.90}$$

$$|\mathcal{T}_0 \boldsymbol{W}_0^R|_{(H^{n,n}(Q))^2} \lesssim |\boldsymbol{W}_0^R|_{(H^{n+1}(\Omega))^2} \tag{8.91}$$

and by linearity

$$|\mathcal{T}_0 \boldsymbol{W}_0|_{(H^{n,n}(Q))^2} \lesssim |\boldsymbol{W}_0|_{(H^{n+1}(\Omega))^2} \tag{8.92}$$

which means that $\mathcal{T}_0$ is a linear bounded operator from $(C_0^\infty(\mathbb{R}))^2 \subset (H^{n+1}(\Omega))^2$ to $(H^{n,n}(Q))^2$. From Theorem C.4 we deduce that $(C_0^\infty(\mathbb{R}))^2$ is dense in $(H^{n+1}(\Omega))^2$ which, due to Theorem C.2, means that there exists a unique continuous operator

$$\begin{array}{lll} \mathcal{T}: & (H^{n+1}(\Omega))^2 & \rightarrow (H^{n,n}(Q))^2 \\ & \boldsymbol{W}_0 & \rightarrow \boldsymbol{W} = \mathcal{T}\boldsymbol{W}_0 \end{array} \tag{8.93}$$

such that $\mathcal{T}\boldsymbol{W}_0 = \mathcal{T}_0 \boldsymbol{W}_0$ for every $\boldsymbol{W}_0 \in M$. □

8.3.5 Estimation of the coupling error

As already stated, the size of the reflections $\boldsymbol{W}'_\pm$ is a measure of the error introduced by a particular coupling technique. In this section we study its asymptotic behavior as $\mu \to 0$. For this, the following Lemma 8.1 quantifies the asymptotic behavior of the trace of the reflections at $x = 0$, which will facilitate the estimation of $\boldsymbol{W}'_\pm$.

Lemma 8.1. *Let $f \in H^{n+2}(\mathbb{R}^+)$ with $n \geq 0$ integer, there exits $C > 0$ such that*

$$|\mathcal{L}^{-1}(r) * f|_{H^n(\mathbb{R}^+)} \leq C\mu^2 |f|_{H^{n+2}(\mathbb{R}^-)} \tag{8.94}$$

Proof. From Theorem C.1 there exists a family of functions $(\hat{f}_h)_{h>0} \subset C_0^\infty(\mathbb{R})$, and positive constants c_1, c_2, such that

$$\hat{f}_h = \hat{f} \text{ in } \left(-\frac{c_1}{h}, \frac{c_1}{h}\right) \subset supp(\hat{f}_h) = (-\frac{c_2}{h}, \frac{c_2}{h})$$

and

$$|\hat{f} - \hat{f}_h|_{H^n(\mathbb{R})} \leq C_1 h |\hat{f}|_{H^{n+1}(\mathbb{R})} \tag{8.95}$$

so we can compute

$$\begin{aligned} |r\hat{f}|^2_{H^n(\mathbb{R})} &\leq |r(\hat{f} - \hat{f}_h)|^2_{H^n(\mathbb{R})} + |r\hat{f}_h|^2_{H^n(\mathbb{R})} \\ &= \int_{\mathbb{R}} (1+\omega^2)^n |r|^2 |\hat{f} - \hat{f}_h|^2 d\omega + \int_{\mathbb{R}} (1+\omega^2)^n |r|^2 |\hat{f}_h|^2 d\omega \\ &= \int_{|\omega| \geq \frac{c_1}{h}} (1+\omega^2)^n |r|^2 |\hat{f} - \hat{f}_h|^2 d\omega + \int_{|\omega| \leq \frac{c_2}{h}} (1+\omega^2)^n |r|^2 |\hat{f}_h|^2 d\omega \end{aligned} \tag{8.96}$$

where the limit of the first integral is obtained from the region where $\hat{f} = \hat{f}_h$, and the limit of the second integral from the support of $\hat{f}_h$. Since $|r| \leq 1$, we can proceed to use (8.95) to obtain

$$|r\hat{f}|^2_{H^n(\mathbb{R})} \leq C_1^2 h^2 |\hat{f}|^2_{H^{n+1}(\mathbb{R})} + \int_{|\omega| \leq \frac{c}{h}} |r|^2 |\hat{f}_h|^2 d\omega \tag{8.97}$$

Since we have

$$r(s) = -\frac{1}{4}\mu^2 s^2 + O(|\mu s|^4) \quad \text{if } |\mu s| \leq c' < 1 \tag{8.98}$$

then choosing $h = \dfrac{c}{c'}\mu^2$ and σ very small, developing the integral one obtains that there exists $C_2 > 0$ such that

$$\int_{|\omega| \leq \frac{c}{h}} |r|^2 |\hat{f}_h|^2 d\omega \leq C_2 \mu^4 |f_h|_{H^{n+2}} \tag{8.99}$$

from where we deduce that there exists C_3 such that

$$|\mathcal{L}^{-1}(r) * f|^2_{H^n(\mathbb{R}^+)} \leq \mu^4 C_3 |f_h|^2_{H^{n+2}(\mathbb{R}^+)} \tag{8.100}$$

□

The next Proposition 8.6 shows that as $\mu \to 0$ the size of the coupling error $\boldsymbol{W}'_\pm$, *i.e.*, the reflections, is $O(\mu^2)$.

Proposition 8.6. *Let* $\boldsymbol{W}_0 \in (H^n(\Omega))^2$ *and supp*$(\boldsymbol{W}_0) \subset \Omega_-$*, for every* $r, k > 0$ *there exists* $C(r,k) > 0$ *and* $C > 0$ *such that if* $\mathcal{L}_- = \mathcal{L}_B$ *then*

$$\begin{aligned} |\boldsymbol{W}'_-|_{H^{r,k+1}(Q_-)\times H^{r,k}(Q_-)} &\leq C(r,k)\mu^2 |\boldsymbol{W}_0|_{(H^n(\Omega))^2} \\ |\boldsymbol{W}'_+|_{H^{k,k}(Q_+)\times H^{k,k}(Q_+)} &\leq C(r,k)\mu^2 |\boldsymbol{W}_0|_{(H^n(\Omega))^2} \end{aligned} \tag{8.101}$$

and if $\mathcal{L}_- = \mathcal{L}_{SV}$ *then there is* $C_1 > 0$ *and* $C_2(r) > 0$ *such that*

$$\begin{aligned} |\boldsymbol{W}'_-|_{H^{n,n}(Q_-)\times H^{n,n}(Q_-)} &\leq C_1 \mu^2 |\boldsymbol{W}_0|_{(H^{n+2}(\Omega))^2} \\ |\boldsymbol{W}'_+|_{H^{r,n+1}(Q_+)\times H^{r,n}(Q_+)} &\leq C_2(r) \mu^2 |\boldsymbol{W}_0|_{(H^{n+2}(\Omega))^2} \end{aligned} \tag{8.102}$$

Proof. Suppose $\mathcal{L}_- = \mathcal{L}_B$ then for all $r \geq 0$ and $k \geq 0$

$$\begin{aligned} |\boldsymbol{W}'_-|_{H^{r,k+1}(Q_-)\times H^{r,k}(Q_-)} &\lesssim |u'_-(0,\cdot)|_{H^k}(0,T) \quad \text{(Theorem 7.1)} \\ &\lesssim C\mu^2 |u^\star_{cauchy,-}(0,\cdot)|_{H^{k+2}(0,T)} \quad \text{(Lemma 8.1)} \\ &\lesssim C\mu^2 |\boldsymbol{W}^\star_{cauchy,-}|_{(H^{n,s_k}(Q))^2} \quad \text{(Theorem D.2)} \\ &\lesssim \mu^2 |\boldsymbol{W}_0|_{(H^n(\Omega))^2} \quad \text{(Theorem 6.1)} \end{aligned} \tag{8.103}$$

with $s_k = (k+2)\frac{n+1}{n+1/2}$, thanks to the continuity of the trace in Theorem D.2. Similarly

$$\begin{aligned} |\boldsymbol{W}'_+|_{H^{k,k}(Q_+)\times H^{k,k}(Q_+)} &\lesssim |u'_-(0,\cdot)|_{H^k}(0,T) \quad \text{(Proposition 7.1)} \\ &\lesssim C\mu^2 |u^\star_{cauchy,-}(0,\cdot)|_{H^{k+2}((0,T))} \quad \text{(Lemma 8.1)} \\ &\lesssim C\mu^2 |\boldsymbol{W}^\star_{cauchy,-}|_{(H^{n,s_k}(Q))} \quad \text{(Theorem D.2)} \\ &\lesssim \mu^2 |\boldsymbol{W}_0|_{(H^n(\Omega))^2} \quad \text{(Theorem 6.1)} \end{aligned} \tag{8.104}$$

Suppose now that $\mathcal{L}_- = \mathcal{L}_B$, then

$$\begin{aligned}
|\boldsymbol{W}'_-|_{H^{n,n}(Q_-)\times H^{n,n}(Q_-)} &\lesssim |u'_-(0,\cdot)|_{H^n}(0,T) \quad \text{(Proposition 7.1)}\\
&\lesssim C\mu^2|u^\star_{cauchy,-}(0,\cdot)|_{H^{n+2}(0,T)} \quad \text{(Lemma 8.1)}\\
&\lesssim C\mu^2|\boldsymbol{W}^\star_{cauchy,-}|_{(H^{n+2,n+2}(Q))^2} \quad \text{(Proposition 6.1)}\\
&\lesssim \mu^2|\boldsymbol{W}_0|_{(H^{n+2}(\Omega))^2} \quad \text{(Theorem 6.1)}
\end{aligned} \tag{8.105}$$

and for every $r \geq 0$

$$\begin{aligned}
|\boldsymbol{W}'_+|_{H^{r,n+1}(Q_+)\times H^{r,n}(Q_+)} &\lesssim |u'_-(0,\cdot)|_{H^n(0,T)} \quad \text{(Theorem 7.1)}\\
&\lesssim C\mu^2|u^\star_{cauchy,-}(0,\cdot)|_{H^{n+2}(0,T)} \quad \text{(Lemma 8.1)}\\
&\lesssim C\mu^2|\boldsymbol{W}^\star_{cauchy,-}|_{(H^{n+2,n+2}(Q))^2} \quad \text{(Theorem D.2)}\\
&\lesssim \mu^2|\boldsymbol{W}_0|_{(H^{n+2}(\Omega))^2} \quad \text{(Theorem 6.1)}
\end{aligned} \tag{8.106}$$

□

To generalize this result to the case of initial data with arbitrary support, let us define

$$\boldsymbol{W}^{\star\star\star} = \boldsymbol{W}^\star_L + \boldsymbol{W}^\star_R \tag{8.107}$$

where $\boldsymbol{W}^\star_L$ is the solution of the one-way coupling (5.16) initialized with $\boldsymbol{W}^L_0$ as in (8.89); and $\boldsymbol{W}^\star_R$ is the solution of the one-way coupling initialized with $\boldsymbol{W}^R_0$, but solved in the opposite direction, *i.e.*,

$$\boldsymbol{W}^\star_R = \left\{ \begin{array}{ll} \boldsymbol{W}_{half,-} & \text{in } Q_- \\ \boldsymbol{W}_{cauchy,+} & \text{in } Q_+ \end{array} \right. \tag{8.108}$$

where

$$\left\{ \begin{array}{ll} \mathcal{L}_+\boldsymbol{W}_{cauchy,+} = 0, & \text{in } Q_+ \\ \boldsymbol{W}_{cauchy,+}(\cdot,0) = \boldsymbol{W}^R_0 & \text{in } \Omega_+ \end{array} \right. \tag{8.109}$$

and

$$\left\{ \begin{array}{cl} \mathcal{L}_-\boldsymbol{W}_{half,-} = 0, & \text{in } Q_- \\ \boldsymbol{W}_{half,-}(\cdot,0) = 0 & \text{in } \Omega_+ \\ u_{half,-}(0,\cdot) = u_{cauchy,+}(0,\cdot) & \text{on }]0,T[\end{array} \right. , \tag{8.110}$$

so defining $\boldsymbol{W}' = \boldsymbol{W} - \boldsymbol{W}^{\star\star\star}$ one has the following result:

Theorem 8.6. *Let $\boldsymbol{W}_0 \in H^{n+2}(\Omega)\times H^{n+2}(\Omega)$, there exists $C > 0$ such that as μ goes to 0*

$$|\boldsymbol{W}'|_{(H^{n,n}(\Omega))^2} \leq C\mu^2|\boldsymbol{W}_0|_{H^{n+2}(\Omega)\times H^{n+2}(\Omega)} \tag{8.111}$$

Proof. Let

$$M = \{f \in C^\infty(\mathbb{R}) : \quad f(0) = 0)\} \tag{8.112}$$

and suppose $\boldsymbol{W}_0 \in M$. Also notice that

$$\begin{aligned}
\boldsymbol{W}' &= \boldsymbol{W} - \boldsymbol{W}^{\star\star\star}\\
&= (\boldsymbol{W}_L - \boldsymbol{W}^\star_L) + (\boldsymbol{W}_R - \boldsymbol{W}^\star_R)
\end{aligned} \tag{8.113}$$

and from Proposition 8.6 one can deduce that

$$|\boldsymbol{W}'_L|_{(H^{n,n}(Q))^2} \leq C\mu^2 |\boldsymbol{W}_0|_{H^{n+2}(\Omega)\times H^{n+2}(\Omega)} \tag{8.114}$$

$$|\boldsymbol{W}'_R|_{(H^{n,n}(Q))^2} \leq C\mu^2 |\boldsymbol{W}_0|_{H^{n+2}(\Omega)\times H^{n+2}(\Omega)} \tag{8.115}$$

which means that

$$|\boldsymbol{W}'|_{(H^{n,n}(Q))^2} \leq C\mu^2 |\boldsymbol{W}_0|_{H^{n+2}(\Omega)\times H^{n+2}(\Omega)} \tag{8.116}$$

which means that the mapping

$$\begin{array}{ll} \mathcal{T}'_0 : M^2 & \rightarrow (H^{n,n}(Q))^2 \\ \boldsymbol{W}_0 & \rightarrow \boldsymbol{W}' \end{array} \tag{8.117}$$

is continuous, and because M is dense in $H^{n+2}(\Omega)$ (Theorem C.4) it has a unique extension (Theorem C.2)

$$\begin{array}{ll} \mathcal{T}' : (H^{n+2}(\Omega))^2 & \rightarrow (H^{n,n}(Q))^2 \\ \boldsymbol{W}_0 & \rightarrow \boldsymbol{W}' \end{array} \tag{8.118}$$

and (8.116) holds. □

8.4 Numerical verification of the size of the reflections

As we just saw, the reflections decrease as $O(\mu^2)$ in both cases (SVB and BSV), however, one can readily notice in (8.6) that when the wave propagates in the BSV case the regularity estimate of $\boldsymbol{W}'$ is much better than in the SVB case.

However, a more explicit explanation can be found by studying the filter $r(j\omega)$ that appears in both (8.4) and (8.5). For BSV and, in the limit $\sigma \rightarrow 0$ for SVB, these filters take the form

$$r_{BSV}(j\omega_1(\kappa)) = \frac{\sqrt{1+(\mu\kappa)^2}-1}{\sqrt{1+(\mu\kappa)^2}+1} \tag{8.119}$$

and

$$r_{SVB}(j\omega_1(\kappa)) = \frac{1-\sqrt{1-(\mu\kappa)^2}}{1+\sqrt{1-(\mu\kappa)^2}} \tag{8.120}$$

or changing to dimensional variables using (5.7)

$$r_{BSV}(j\omega_1(\kappa)) = \frac{\sqrt{1+\frac{h_0^2}{3}\kappa^2}-1}{\sqrt{1+\frac{h_0^2}{3}\kappa^2}+1} \tag{8.121}$$

and

$$r_{SVB}(j\omega_1(\kappa)) = \frac{1-\sqrt{1-\frac{h_0^2}{3}\kappa^2}}{1+\sqrt{1-\frac{h_0^2}{3}\kappa^2}} \tag{8.122}$$

One can already notice that $|r_{SVB}(\kappa)|$ and $|r_{BSV}(\kappa)|$ are increasing functions of $h_0|\kappa|$ and also that $|r_{SVB}(\kappa)| > |r_{BSV}(\kappa)|$. Morover, in the limit $h_0|\kappa| \rightarrow \infty$ $|r_{SVB}| = |r_{BSV}| = 1$ but $|r_{BSV}| < 1$ for every κ, while $|r_{SVB}| = 1$ for every $\frac{h_0^2}{3}\kappa^2 > 1$. This means that one should expect larger reflections in deeper waters and on SVB. These effects will be discussed with numerical examples in the next section, along with the study of the behavior when $\mu \rightarrow 0$.

8.4.1 Discretization

For the purpose of the discrete hybrid model it is more convenient to write the equations as

$$\begin{aligned}\partial_t\eta + h\partial_x u &= 0\\ \partial_t q + g\partial_x\eta &= 0\\ u - \frac{h_0^2}{3}\chi(x)\partial_x^2 u &= q\end{aligned}\tag{8.123}$$

where we introduced the auxiliar variable q. Denoting by H be the Heaviside function, χ will be either $H(x)$ or $1 - H(x)$, depending on the case, and $g = 9.81m/s^2$. The discretization consists of a regular grid of sizes $(\Delta x, \Delta t)$ in space and time with nodes $(x_i)_{i=-2}^{n_x+3}$ and $(t_n)_{n=0}^{N}$, including 2 ghost cells on each side in x. Space derivatives are approximated with the fourth-order centered finite differences:

$$\begin{aligned}(\partial_x u)_i^n &= \frac{1}{\Delta x}\left(\frac{1}{12}u_{i-2}^n - \frac{2}{3}u_{i-1}^n + \frac{2}{3}u_{i+1}^n - \frac{1}{12}u_{i+2}^n\right)\\ (\partial_x^2 u)_i^n &= \frac{1}{\Delta x}\left(-\frac{1}{12}u_{i-2}^n - \frac{4}{3}u_{i-1}^n - \frac{5}{2}u_i^n + \frac{4}{3}u_{i+1}^n - \frac{1}{12}u_{i+2}^n\right)\end{aligned}\tag{8.124}$$

where we denote $f(x_i, t_n) \approx f_i^n$. A third-order Runge-Kutta scheme is used in time, such that if we write the hybrid model as

$$\partial_t \boldsymbol{U} = F(\eta, u, q)\tag{8.125}$$

with $\boldsymbol{U} = (\eta, q)^T$ and $F(\eta, u, q) = (-h_0\partial_x u, -g\partial_x\eta)^T$ then

$$\begin{aligned}\boldsymbol{U}^{(1)} &= \boldsymbol{U}^n + \Delta t F(\eta^n, u^n, q^n)\\ \boldsymbol{U}^{(2)} &= \frac{3}{4}\boldsymbol{U}^n + \frac{1}{4}\boldsymbol{U}^{(1)} + \frac{1}{4}\Delta t F(\eta^{(1)}, u^{(1)}, q^{(1)})\\ \boldsymbol{U}^{n+1} &= \frac{1}{3}\boldsymbol{U}^n + \frac{2}{3}\boldsymbol{U}^{(2)} + \frac{2}{3}\Delta t F(\eta^{(2)}, u^{(2)}, q^{(2)})\end{aligned}\tag{8.126}$$

Regarding the one-way model, $\boldsymbol{W}_-^\star$ is obtained using the previous scheme by setting $\chi(x) = 1$ for $x \in \mathbb{R}$ or 0 depending on the case (BSV or SVB resp.). For $\boldsymbol{W}_+^\star$, in the SVB case, the second line of equation (7.17) is discretized by approximating $\alpha_+(\sigma + j\omega)$ with the Fast Fourier Transform (FFT) of $e^{-\sigma t_n}u_{i\star}^n$, where $i\star$ is such that $\chi(x_{i\star}) \neq \chi(x_{i\star+1})$. Also, $u_{i\star}^n$ is extended by 0 until $n = 20N$ in order to improve the resolution in the frequency domain. The same strategy is used with $\mu = 0$ to obtain $\boldsymbol{W}_+^\star$ in the SVB case, although the solution could be obtained from (7.18) as well.

8.4.2 Initial conditions

Two types of wave profiles are examined. The first is a smooth Gaussian wave

$$\begin{aligned}\eta_0(x) &= 0\\ u_0(x) &= \frac{1}{\sqrt{2\pi\sigma^2}}e^{-\frac{1}{2}\frac{(x-x_0)^2}{\sigma^2}} \qquad x \in \mathbb{R}\end{aligned}\tag{8.127}$$

with $\sigma = 2/\sqrt{3}$. The second type of wave profile is the rectangular wave

$$\begin{aligned} \eta_0(x) &= 0 \\ u_0(x) &= H(L - |x - x_0|) \end{aligned} \quad x \in \mathbb{R} \tag{8.128}$$

which is interesting as a proxy for the propagation of shock waves formed with the SV model in the nonlinear regime. These waves are compared in the deep water and shallow water cases with $h = 4m$ and $h = 1m$ respectively. In all cases the domain is truncated to $\Omega = (-200m, 200m)$ which is large enough to avoid any influence from the boundaries. The mesh and timestep sizes are $\Delta x = 0.025m$ and $\Delta t = 0.15\Delta x/\sqrt{gh}$.

8.4.3 Results and discussion

For the Gaussian wave, Figures 8.2 and 8.3 show the results at different times in the BSV case and Figures 8.4 and 8.5 in the SVB case. In each figure the results of the hybrid and one-way coupled model, u and $u^\star$, are shown first, followed by the numerical solution of the problems describing the reflections Theorem 8.4 and Theorem 8.5, shown in the graph as "filtered reflected Cauchy", along with the difference of the hybrid and the one-way coupling $u' = u - u^\star$. The discussion is only around the values of the velocity u, since for the surface elevation η it is similar.

Furthermore, one can see that u' and $u^\star_-$ coincide for every $x < 0$, verifying the theory. Similarly, one can see that indeed the reflected wave decreases with the depth h_0 and that reflections are larger on SVB than on BSV, which is explained by the range of frequencies that are attenuated by the reflection coefficient ($|r| < 1$), which is only a compact interval in SVB, whereas it is the whole real line in BSV. Both facts, the decrease in size of the reflections with the depth and with BSV, can be verified by comparing the initial spectrum with the modulus of the reflection coefficients in 8.7 with 8.6. Besides the magnitude of the reflections alone, one can see that even in the case with the smallest reflections (shallow water and BSV, Fig. 8.2) the domain solving SV equations propagates the reflections more visibly. This can be explained by the fact that the phase speed of the SV equations is constant for all wave numbers, while it is close to 0 for large wave numbers in the Boussinesq equations. Figures 8.8 and 8.9 show similar results with the rectangular initial wave profile. A similar conclusion can be obtained in this case, that is, the verification of the reflection's formula and the decrease in size with the depth. However, in this case the reflections are much larger even in the shallow-water case. As can be seen in Figures 8.11 this can be explained by the fact that the spectrum of the initial condition decays as slow as $1/\kappa$, hence it is not compact, decreases slowly, so more harmonics are reflected. Notice also that high-frequency harmonics, both from reflections and from the square wave, are smoothed by the Boussinesq model. This can be explained by the dispersive boundary layer explained in Section 7.4, that filters out frequencies not allowed in the dispersion relation, *i.e.*, whose temporal variations have frequencies $|\omega| > \sqrt{gh}/\mu$, with $\mu = h_0/\sqrt{3}$. Current results have lots of numerical dispersion, but even those spurious waves are filtered out by the Boussinesq model.

Table 8.1 shows the empirical convergence order p obtained from computing the L^2 difference $u - u^\star$ at $x = 0$, and fitting the curve $c\mu^p$ with a linear regression

Initial condition	**Case**	**Order** $O(\mu^p)$
Gaussian	BSV	1.996
	SVB	2.000
Rectangular	BSV	1.992
	SVB	1.989

Table 8.1: Empirical convergence rates obtained when decreasing μ.

in the log-log plane. The results are computed for the Gaussian and rectangular initial conditions varying h_0 between 10^{-6} and $10^{-}2$ such that $\log(h_0)$ has a uniform spacing of 0.5. This is done for both SVB and BSV cases. The results show a good agreement with the theoretical result $O(\mu^2)$ of Theorem 8.6.

8.5 Conclusions

In this chapter, we have analyzed the hybrid model on the case of a vertical interface in the $x - t$ plane. This was done using the results of Chapter 6 and Chapter 7. Adopting a domain decomposition approach, the chapter began by defining a unique class of transmission conditions that enabled the reformulation of the hybrid model as a transmission problem between two half-line problems of different equations. We first proved the existence, uniqueness, and regularity of the problem using a Waveform Relaxation Method with an optimized version of the previous transmission conditions (transport-Dirichlet). This was done in the spirit of the original proof by Schwarz [105], and its application to parallel computing is also plausible, as both operators are local and convergence was achieved in just three iterations.

We then proceeded to study the **coupling error**, as defined in Chapter 5. It was demonstrated that the coupling error can indeed be described as **wave reflections** generated at the interface; this notion was carefully explained. A reflection coefficient was obtained, and the effect of the directionality of the propagation was studied, finding that reflections are larger when waves propagate from the SV domain onto the B domain, because the reflection coefficient is larger in magnitude than in the other direction. It was also shown that the coupling error is of order $O(\mu^2)$ but control over the $n + 2 - th$ derivative of the initial data is required, which is due to the quadratic asymptotic behavior of the reflection coefficient. This reveals also that the hybrid model acts as an **absorbing boundary layer for weakly dispersive models**, because reflections are as small as $O(\mu^2)$.

This analysis allowed us to prove the **continuity** for arbitrary initial data in a specific topology, which also implies that the model is **stable**. Like the B equation, it was found that the model is **weakly well-posed** as well, meaning that to control the norm of the $n-th$ space derivative of the solution, one needs to ensure square integrability of the $n+1-th$ derivative of the initial data, *i.e.,* the model is weakly well-posed as well.

Regardings the questions proposed on Chapter 4 and Chapter 5, these facts demonstrate that:

- **(I) Oscillations: Are the short oscillations that have been reported a part of the solution or a problem of the discretization?:**

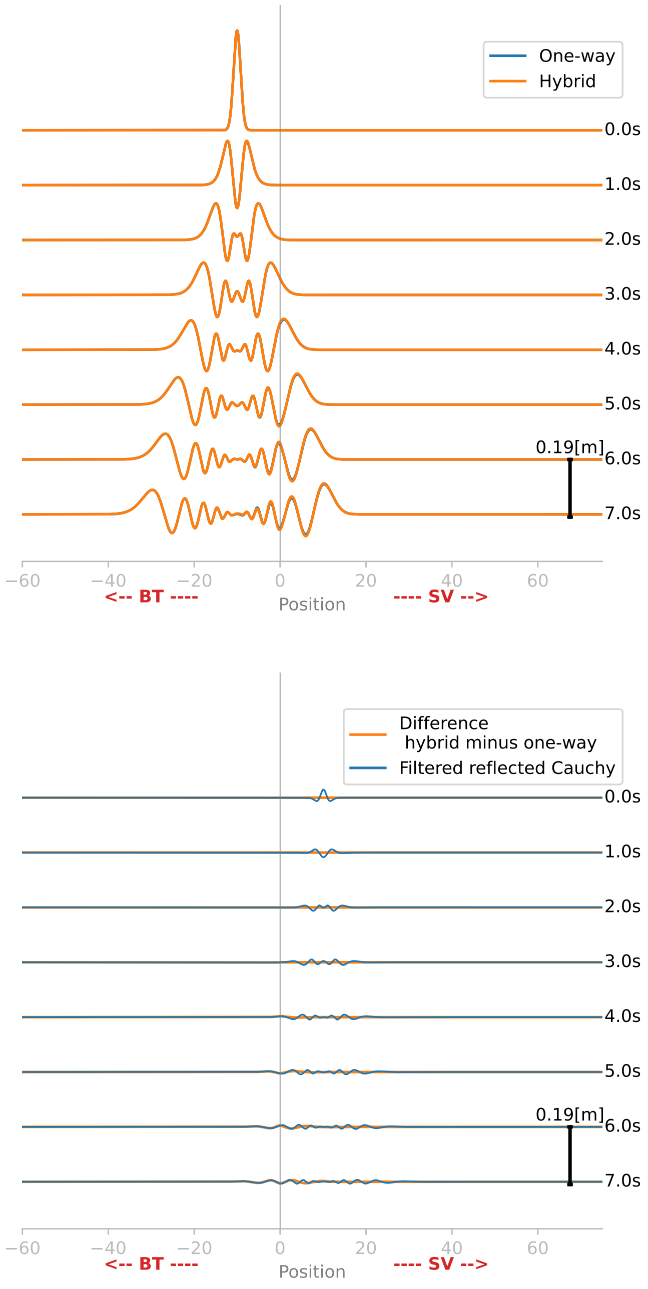

Figure 8.2: BTSV $\sigma = 2/\sqrt{3}$, $h = 1$

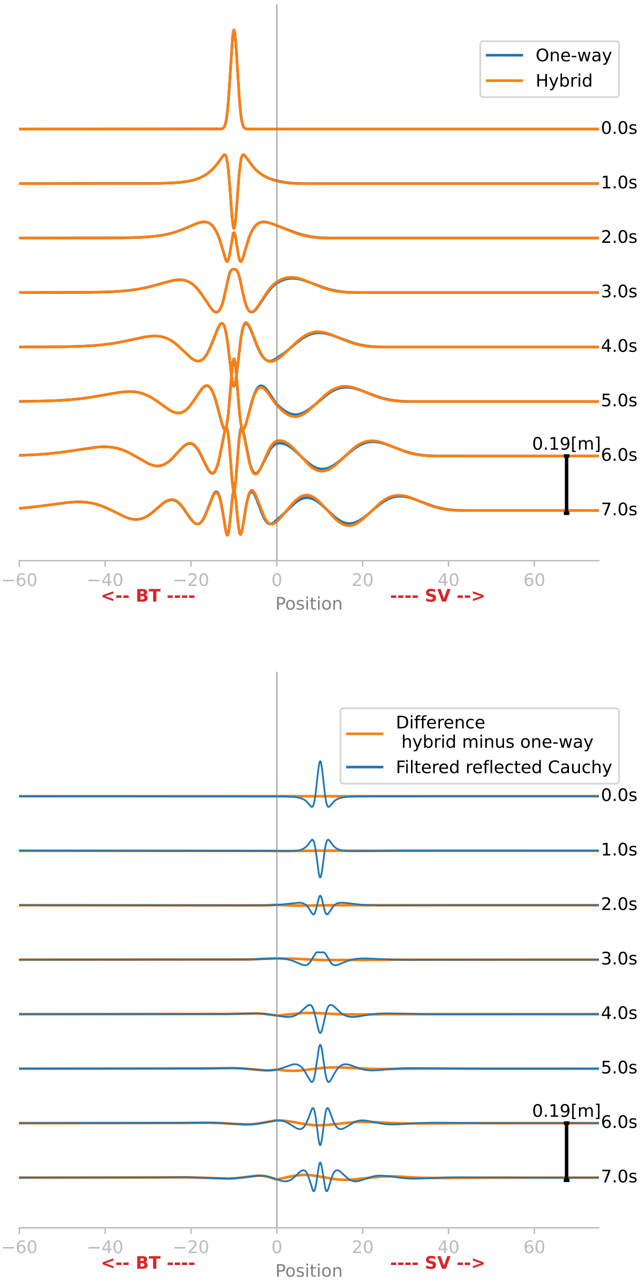

Figure 8.3: BTSV $\sigma = 2/\sqrt{3}$, $h = 4$

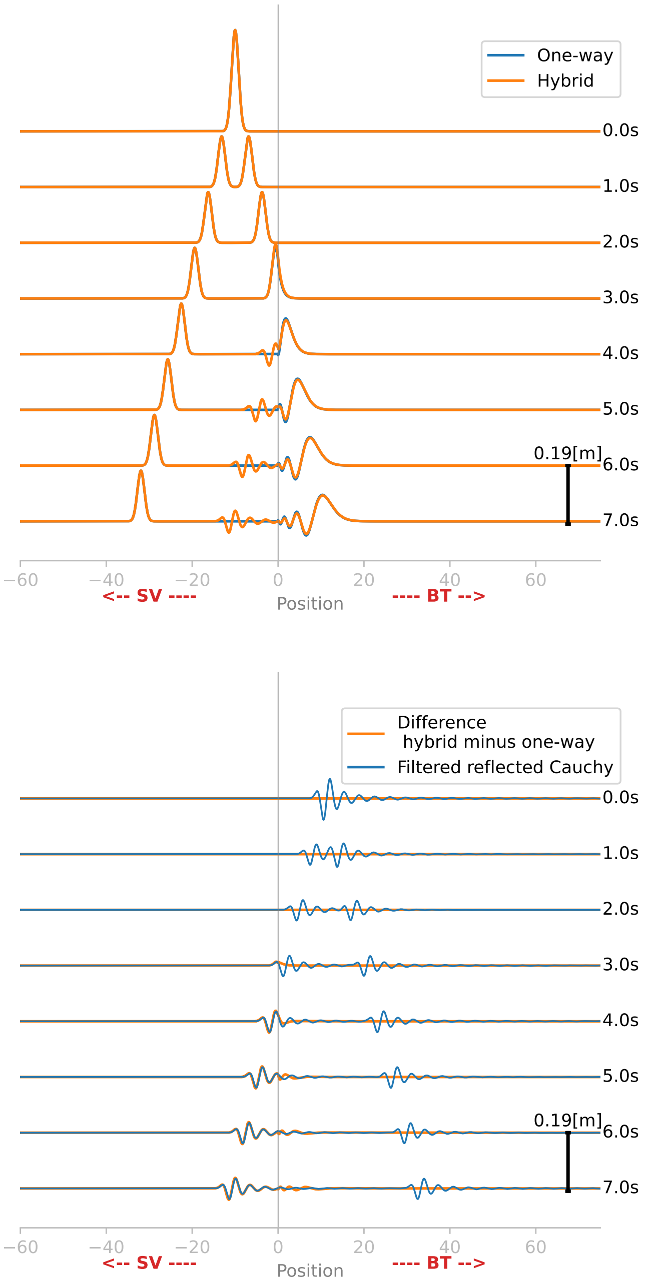

Figure 8.4: SVBT $\sigma = 2/\sqrt{3}$, $h = 1$

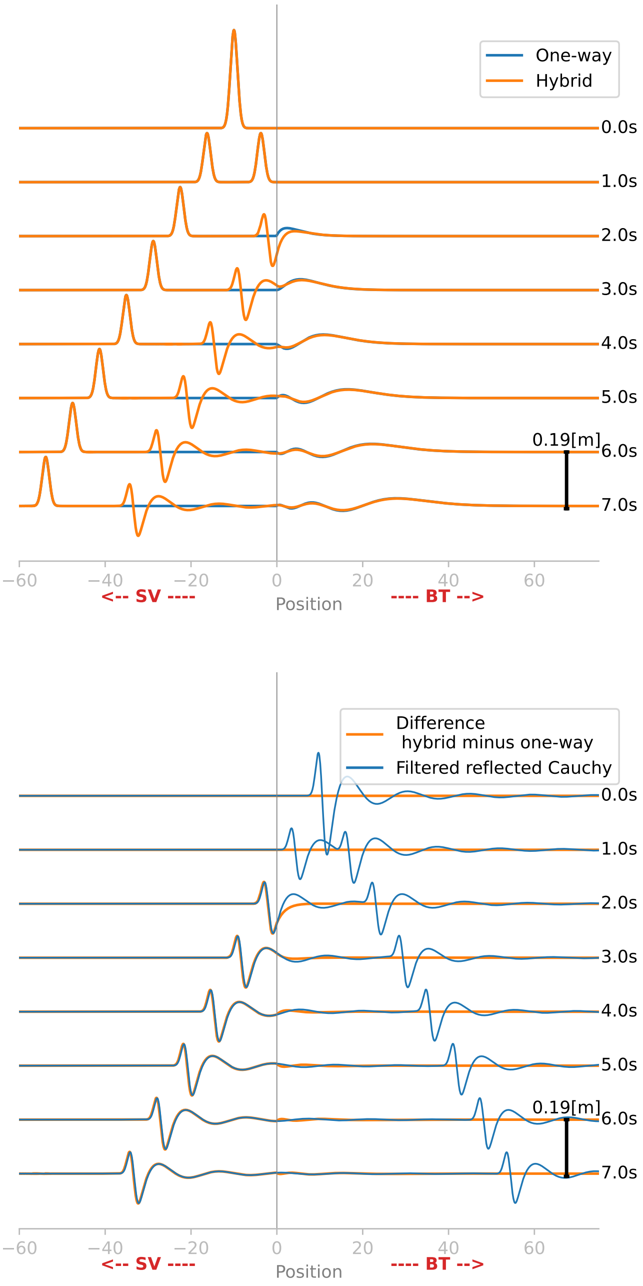

Figure 8.5: SVBT $\sigma = 2/\sqrt{3}$, $h = 4$

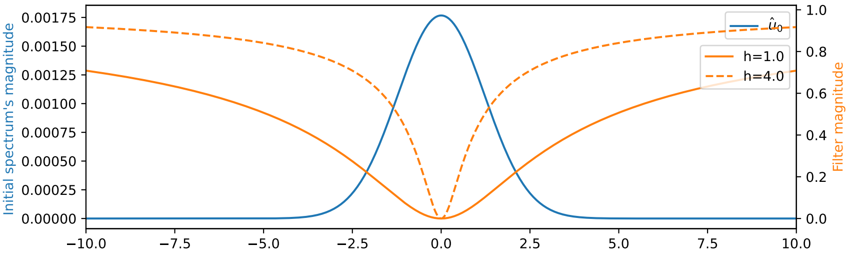

Figure 8.6: Spectrum vs reflection coefficient BSV

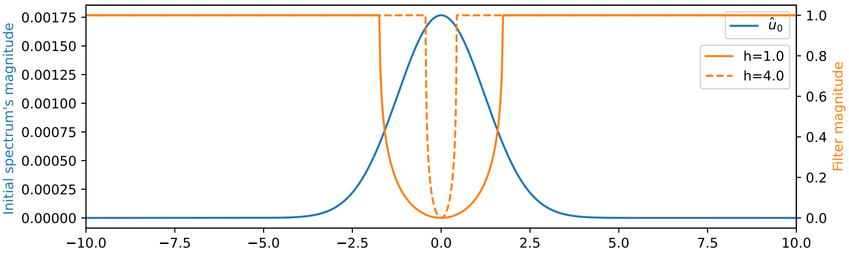

Figure 8.7: Spectrum vs reflection coefficient BSV

Indeed these oscillations are reflections generated by the vertical interface, and they are mostly short waves because of the high-pass character of the reflection coefficient.

- **(II) Instabilities: What is causing the instabilities? Are they coming from the PDE or from the discrete equation? How to fix them?** The hybrid model is continuous, hence it is stable. Further analysis is required at the discrete level.

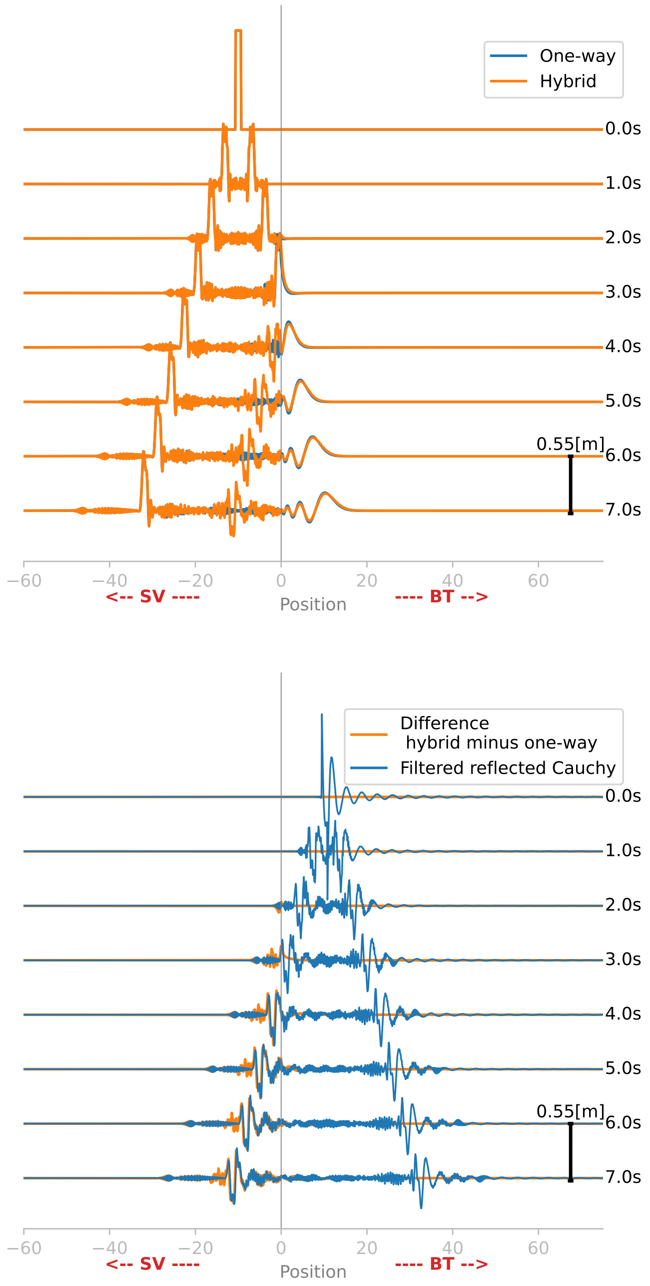

Figure 8.8: SVBT $L = 2/\sqrt{3}$, $h = 1$

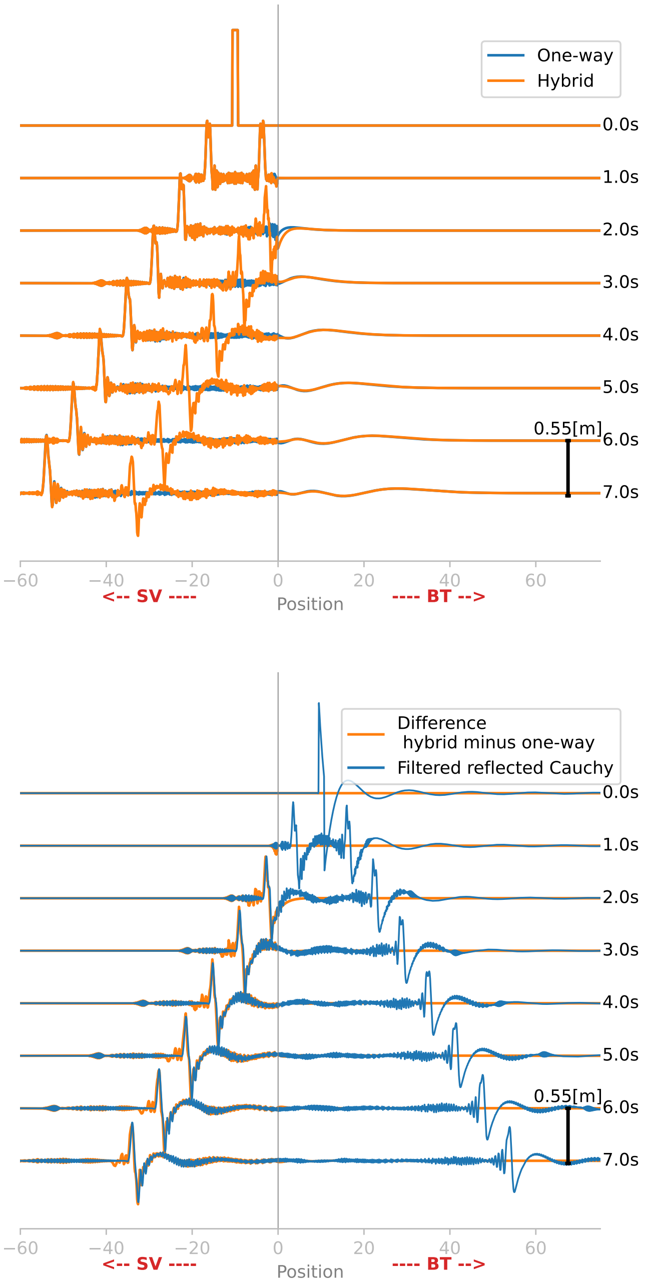

Figure 8.9: SVBT $L = 2/\sqrt{3}$, $h = 4$

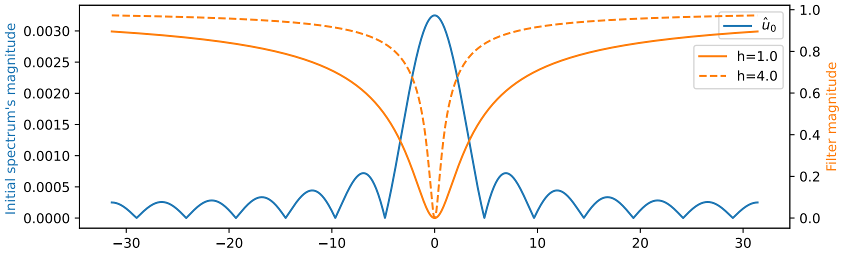

Figure 8.10: Spectrum vs reflection coefficient BSV

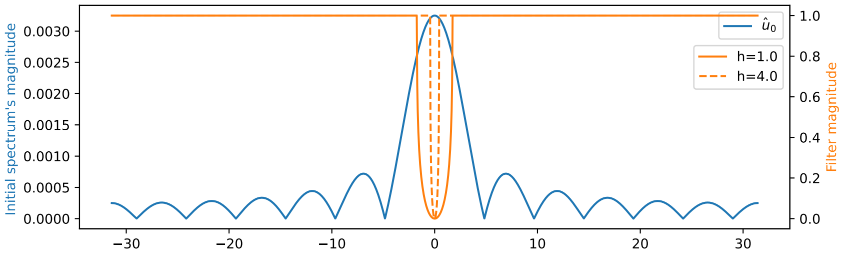

Figure 8.11: Spectrum vs reflection coefficient SVB

Chapter 9

Conclusions and perspectives

In this thesis we have studied how to couple different phase-resolving water wave models that have been developed since the mid 19th century, namely Boussinesq-type and Saint-Venant equations. Despite the existence of such a variety of models with different performances, as well as different proposals on how to couple them for different applications, so far there is a remarkable lack of consensus on the artifacts to expect from such a strategy, as well as a vague understanding of how to analyze and compare them. In particular, for one of the most popular coupling methods used for modeling wave breaking, the hybrid model, it was noted that different authors had reported different types of such artifacts, such as: (I) Oscillations, (II) Instabilities, and (III) Mesh dependent solutions.

Given this context, the objectives of this PhD thesis were:

Objective 1. To develop new coupled phase-resolving coastal wave models

Objective 2. To study and explain the source of any artifacts observed

Objective 3. To contribute to their mathematical justification (as approximations of the 3D model)

With these goals in mind, we proposed the following principle to drive the discussion throughout the whole thesis:

The ideal coupled model is the one closest to the 3D model

with the 3D model taken, for example, as the free-surface Euler or Navier Stokes equations. This principle was deduced from the fact that, as with regular BT or SV models, in most situations, the main reason not to use the 3D most accurate model, is its huge complexity and computational cost. This notion is already used in the literature to justify linear and non-linear BT models, as was discussed in Chapter 1.

9.1 Conclusions

One conclusion of transversal character from Part II is that the **one-way model is the optimal coupled model** in the case of the vertical interface (static switch) and initial conditions supported on one side of the interface. This is regardless of the nonlinearity regime and is consistent with the observation by Dubach [31], that absorbing conditions are the optimal choice too. In addition to Dubach's statement, this model adds a notion of what happens *on the other side of the interface* too in this reference solution. Of course this model has many limitations for practical computations, but it is very useful for quantifying the **coupling error** and measure the performance of a given coupled model.

The conclusions drawn from this study regarding the main objectives just proposed are:

Objective 1: New coupled models were proposed on Chapter 2 and Chapter 4. In both cases they displayed some or all of the artifacts that the hybrid model had too, that is to say: (I) Oscillations, (II) Instabilities, and/or (III) Mesh-dependent solutions. The results and analysis from this thesis suggest it is important to pay attention to these three aspects when designing coupled models, so a great deal of attention was dedicated to objectives 2 and 3. Some specific conclusions for each of the new proposed models are:

- **Derivation of depth-averaged coupling conditions** (Chapter 2): Thanks to the framework developed in Part (II) we can more confidently say that the oscillations observed at the interface are wave reflections. However, since now we know that the one-way model is the best coupled model, then a direct application of this idea would be to derive absorbing conditions for the BT models starting from the Euler model. This would prove a consistency property between the operators. However, recalling that the motivation of that chapter was to start from "the other end", the 3D model, and learn how to improve the coupling of BT models, another useful path would be to study the **half-line model error**, *i.e.,* to find the best transmission conditions for the one-way coupling of 3D-BT models. This could also be considered an extension of the analysis in Chapter 3, about the improved 1D/2D coupling. This is more clear now, due to the framework presented in Chapter 5.
- **Viscous and direct/SWRM overlapping methods**: In Chapter 2 we saw 3 new coupling methods that improved the stability of the hybrid model. Conducting an analysis like the one of Part II Chapter 8 at the continuous and discrete levels would allow to quantify their reflection coefficients and to prove their well-posedness and stability condition at the discrete level. This will be discussed in the next Section 9.2 Perspectives.

Objective 2 It was demonstrated that **issue (II), Instabilities**, is a problem at the discrete level, not the continuous one. This was done first numerically in the nonlinear case (Chapter 4) and then theoretically in the linear case (Chapter 8). Both studies revealed that there does exist a mesh-independent solution in the hybrid model and, from Chapter 8, that this solution depends continuously on the initial data (linear case), and hence, the model is stable. Additionally, it was shown that the source of **problem (III), Mesh-dependent solutions**, appears at the continuous level, regardless of the discrete scheme chosen. This was done numerically in Chapter 4 and then theoretically in Chapter 6. The problem arises from the weak well-posedness of the BT models: because it is not possible to remove the $\partial_x u_0$ term in the continuity estimate of the BT model, mesh-dependent waves that are neglectable for the SV model are significant in the BT model, leading to completely different solutions and possible negative depths and instabilities on different mesh sizes. These oscillations could be triggered by any small perturbation regardless of their source (discretization, source terms, etc), but the unphysical amplification happens at the continuous level. This is assuming a transmission from the SV to the B model through a horizontal interface, *i.e.,* through the initial condition of the Cauchy problem. It was also demonstrated that the source of **problem (I), Oscillations**, is at the continuous level too, but it was proved that the oscillations are reflected waves emanating from the interface, that are asymptotically small at order $O(\mu^2)$. This was discovered numerically in Chapter 4 and then theoretically demonstrated in Chapter 8; it also confirms a conjecture of Shi et et al., [106] observed from numerical results. It was also proved that the size of these reflections is larger when waves are initially supported in the SV subdomain than in the B subdomain.

In addition to problems (I) to (III), for Objective 2, other effects that are expected from the coupling of linear equations were discussed. We present them as expected effects of the models, as opposed to the unexpected artifacts of the previous three problems. In particular, we discussed in Chapter 5 that, in the case of a horizontal interface (transmisison through initial conditions), because of the causality principle, the transmission can only be done in one way, forward in time, and in this case the length of the waves does not change because of switching equations. The vertical interface (static switch) was studied from the behavior of the one-way model. Unlike with the horizontal interface, the main effect of the interface is an artificial refraction that changes the wavelengths inversely to the change in phase speed. In addition, for the propagation from SV to B subdomains, short waves that do not respect the dispersion relation of the B model are filtered out through a distance of $O(\mu^2)$. This is a property of the half-line problem of the Boussinesq equations, described by a dispersive boundary layer of length $O(\mu)$. **The analysis of the half line linear BT problems is a new result that did not exist in the literature before**, although the dispersive boundary layer had been identified in the nonlinear case [18, 81]. Moreover, these observations are very likely applicable to the coupling of other linear BT models.

Objective 3: The justification of the coupling with a horizontal interface (initial conditions) depends only on the justification of the Cauchy problems, which already exists in the literature [77]. We recall that, by justification, we mean to prove the well-posedness of the model and to show that their solution is an approximation of the 3D model. To justify the coupled models in the case of a vertical interface (static switch), in Chapter 5 we proposed to quantify three types of errors:

1. Cauchy model error
2. Half-line model error

3. Coupling error

The sum of these three errors provides an upper bound for the total error with respect to the 3D model, but only the third type of error, the coupling error, is directly related to the coupling technique; the other two refer to the error estimates for the Cauchy problems and half-line problems of each equation with respect to the 3D model, and not so directly to the coupling itself. The computation of the coupling error is very pragmatical and can be easily applied to any phase-resolving model, regardless of the nonlinearity: it is simply the difference with the one-way model. One of the main limitations of this metric is the assumption that the support has to be on one side of the vertical interface. However, under the assumption of linearity it was discussed in Chapter 5 and proved in Chapter 8 that, one can split the initial support in two functions supported on each side of the interface respectively, and then use the superposition of two one-way models as a reference. Whether this is a good idea or not with nonlinear models is an open question. The analysis of Chapter 8 revealed that this coupling error is completely described by the reflections that originate at the interface. These reflections are the source of the mesh-independent small oscillations (problem (I) Oscillations) that were also found in the literature. Moreover, using Fourier analysis, we were able to obtain an explicit integral representation of the solution in Chapter 8 from where the continuity, the asymptotic size $O(\mu^2)$ of the coupling error/reflections, and the effect of directionality were quantified.

9.2 Perspectives

Besides these conclusions, there are several extensions and open questions that, more or less directly, can follow from this research. We list them below. We first start adressing an important limitation of the present work: the analysis of the discrete case; and then continue with other ideas. We sorted them in a way that, in our opinion, the first ones could be applied with the lesser number of modifications of the present work.

Analysis of discrete equations: As the reader may have noticed, of the three problems (I), (II) and (III) that were reported in the literature, the one that has a somewhat less satisfactory answer in the present work is (II), Instabilities. In fact, we were able to prove that the instabilities must come from the discrete level, because the continuous-level problem is well-posed, and we also proposed some numerical evidence of how to improve the stability (viscous, overlapping SWRM and direct overlapping methods of Chapter 4), but no analysis was shown that proved mathematically that indeed some discrete hybrid models were unstable.

A possible way to conduct this analysis is to replicate all chapters of Part II at the discrete level. That is, one must start from a discrete equation whose initial-value problem is well-posed. Then study the half-line problems with homogeneous initial conditions and show that they are well-posed too. At this point one must surely have derived a stability condition for the mesh size and timestep. Then, one can proceed to prove the well-posedness and to compute the reflection coefficient as in Chapter 8. The main difference, in terms of analytical tools, is that one must use the Zeta transform instead of the Laplace

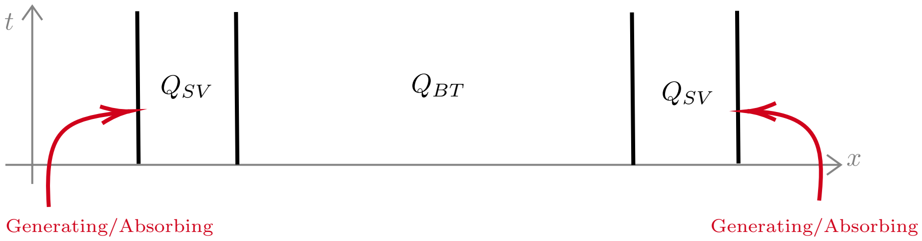

Figure 9.1: Sketch of how couplig with BT with SV equations can be used to absorb/generate waves from/to the BT subdomain.

transform, for which examples for the analysis of the exact absorbing boundary conditions already exist [65, 22]. We conjecture from the observations of Chapter 8, that if the discrete hybrid model is unstable, then it is so because the reflection coefficient is not uniformly bounded in the frequency part of the Zeta-transform variable. One could also extend this result to the nonlinear case with the methodologies for coupling nonlinear hyperbolic problems [53, 52, 17], which has been done very recently in the (not yet peer-reviewed) report of M. Parisot [97], but we do not know of precedents or clues of whether these techniques can be used to estimate the coupling error not.

Coupling, as an absorbing boundary layer for BT models The idea is to take advantage of two features: (1) the absorbing ability of the BT-SV interface demonstrated in Chapter 8; and (2) the existing absorbing techniques for truncating the SV domain, as in Figure 9.1. More concretely, the idea is to solve a BT model in the numerical domain, and switch to the SV model close to the boundaries. Then, in this boundary one can apply absorbing techniques. In the continuous level the exact absorbing boundary conditions of the SV equations are local, thanks to the hyperbolic structure of the problem [77], so their implementation is much simpler. Sponge layers or perfectly-matched layers could also be applied. Applying it directly to the SV domain could be simpler, at least for decreasing the size of the matrices involved in the implicit dispersive terms of the solver. Moreover, if the SV model is shrinked to the limit of 0 width, then this approach could serve as a justification to use the absorbing conditions of the SV model with the BT model, though the numerical stability must be demonstrated, as also the equivalence in the nonlinear case. The only price to pay for this simplification (in the linear case) is the reflection of order $O(\mu^2)$, however, as it was demonstrated in Chapter 8, the propagation from the B domain onto the SV model generates the smallest reflections.

Coupling, as a generating boundary layer for BT models: Similarly to the previous case, now we propose to take advantage of existing wave-generation techniques for the SV model to introduce waves inside the domain, as in Figure 9.1, for the price of an $O(\mu^2)$ error (coupling error) propagating inside the domain. This sure works in the linear setting, because the SV model (wave equation) does not deform the boundary data as it propagates. As was discussed in Chapter 7, the half-line problem for the SV model is local and described by the method of characteristics, while for the B equations it leads to a nonlocal operator, so this would be a much more convenient way to handle it. Moreover, one can think of decreasing the size of the SV domain until the generating boundary and the interface are at an arbitrarily small distance. In this case, the analyis we provided on the hybrid model would justify the use of the Riemann invariants explained in [81] as a generating boundary condition. Such generating boundary conditions have already been used for the fully nonlinear Green-Naghdi equations in references [**bonneton2011589**, 26, 92, 23]. In those references, the authors justified their choice with a physical argument, by stating that the timescales on which weakly dispersive effects are important is much longer than the hyperbolic propagation of the wave. From our present study, we now know more precisely that, for the linear model, such an approximation is $O(\mu^2)$ accurate (coupling error) with respect to the exact generating conditions of the BT model. Two precautions must be takn into consideration though. The first one is that the analysis must be adapted to the nonlinear equations, especially the characterization of the coupling conditions in the hybrid model. The second one is that the coupling in the SV-to-B direction had the largest reflection coefficient, so it may be convenient to filter high-frequencies from the spectrum of the input signal to control them.

2D hybrid models: Different extensions of this analysis are possible. The first one could be the extension to truly 2D models (instead of 1D used here) with the same BT and SV equations. In this case one should proceed as in the thesis of V. Martin [90] and use a Fourier-Laplace transform to deal with the added dimension. An interesting question is: How much does the directionality of the wave affect the reflection coefficient? This would be useful to compare this approach with reflections generated by other absorbing/generating boundary conditions as in the applications mentioned in the previous two paragraphs.

New coupling conditions For the analysis of new coupling conditions, different than the hybrid's, the key step is the reformulation of the original coupling conditions to arrive to the expression

$$\hat{u}'(0,s) = r(s)u^\star(0,s), s \in \mathbb{C}^+ \tag{9.1}$$

with $\hat{()}$ denoting the Laplace transform, $s = \sigma + j\omega$ the Laplace-transform variable; u' the coupling error of the velocity; u^{star} the solution of the one way model; and $r(s)$ the reflection coefficient. We conjecture that the coupled model will be well-posed in the same Sobolev spaces of Chapter 8 as long as $|r(s)|^2$ is uniformly bounded in ω. Proceeding as in Chapter 8, we deduce that the asymptotic accuracy of the model will be completely determined by the behavior or $r(s)$ for the limit $\omega \ll 1$. This strategy could be applied on overlapping models such as those of Chapter 4, to the study of smooth transitions between the two models, or other operators such as Ventcell conditions, among others.

New hybrid models: In the linear case, the idea is to study the hybrid model of more general BT models such as the *abcd* equations

$$\begin{aligned}(1 - b\partial_x^2)\partial_t\eta + (1 + a\partial_x^2)\partial_x u = 0\\ (1 - d\partial_x^2)\partial_t u + (1 + c\partial_x^2)\partial_x\eta = 0\end{aligned} \tag{9.2}$$

or others proposed in [11], by changing the values of the constants a, b, c, d on different parts of the domain. In this case, whenever $a = c = 0$ and either $b > 0$ or $d > 0$, the space derivatives in the equations are at most of second order, so taking the Laplace transform, the characteristic equation will have two roots $\lambda_\pm(s)$, hence the reflection coefficient will be

$$r(s) = \frac{\lambda_-(s) - \lambda_+(s)}{\lambda_-(s) + \lambda_+(s)} \tag{9.3}$$

with $s = \sigma + j\omega \in \mathbb{C}^+$, just like in Chapter 8. Following the conjecture of the previous paragraph, if one can prove that $|r(s)|$ is uniformly bounded in ω then the problem will be well-posed in the same Sobolev spaces of Chapter 8. The asymptotic behavior will also be characterized by the limit $\omega \ll 1$. However, if $a \neq 0$ and $b \neq 0$ or if BT models with higher-order x derivatives are used, then the characteristic polynomials will have more roots so the analysis must be made more carefully, as for example was done for the absorbing boundary conditions in [21, 129, 22].

Optimized Schwarz methods for domain decomposition of BT models: Here the interest is to solve problems of huge computational size that would either not fit in memory or have unfeasible computational times in regular computers, and use massively parallel computing architectures instead. The idea is that instead of solving the problem once on the whole domain, one can distribute each subdomain on different processors and iterate using the Waveform Relaxation Method (WRM). This was done in the thesis of V. Martin [90] for the Advection-Diffussion equation. From the present work we already have the basic ingredients for the B equations: the properties of the Cauchy and half-line problems of chapters Chapter 6 and Chapter 7, so the additional work consists on reformulating the coupling conditions so that the number of iterations is minimized. Notice that, even though in Chapter 8 this was obtained easily (convergence in 3 iterations), this was because the optimal transmission conditions are local for the SV model. This is not the case for general BT or other models, or in 2D, so some trade-offs have to be made in terms of the spectrum of the data and number of iterations. This is the framework known as Optimized Schwarz Methods [42].

Full justification and/of the half-line problem: In Chapter 7 we have proved the well-posedness, regularity and dispersive boundary layer of the half-line problem. The next step is to prove that the **half-line model error** introduced in Chapter 5 also converges to zero when $0 < \mu \ll 1$, recalling that the half-line model error consists in the difference between the 3D solution $\boldsymbol{W}_{3D}$ on the half-line Q_+, and the half-line solution $\boldsymbol{W}_{half,+}$. As pointed out in Chapter 5 this is a problem with interesting questions all by itself. For example: Is it better (or does it matter) to specify η or u on the boundary? Or maybe another boundary condition? In the case of wave generation this is important, because η is easier to measure in the laboratory or the field than u, as mentioned in the derivation of generating conditions for the nonlinear Boussinesq equation [81]. For the case of model coupling we do not have such a constraint, hence η or u or another quantity could be specified. Moreover, as we saw in Chapter 7, the half-line error can be used in conjuction with the **Cauchy model error** and the **coupling error** to provide an upper bound for estimating the accuracy of a coupled model. In this case the half-line model error appears twice, (1) to account for the propagated error of the neighbor model, and (2) to account for the error on its own domain. Of course, this would only be useful for building this particular upper bound of the total error (difference with the 3D model), and maybe there exists a better method to measure it.

Using the Waveform Relaxation Method to prove continuity on the initial data: The last idea is of more interest to learn about the theoretical tools. In this case we wonder if the proof of Appendix F can be improved. This proof looks to demonstrate the continuity of the hybrid model w.r.t. the initial data using the Waveform Relaxation Method (WRM) with Transport and Dirichlet transmission conditions. This proof takes advantage that the WRM converged in 3 iterations to roll back to the initialization of the algorithm, estimating the traces with the solution of a given iteration, and then estimating the solution with the trace of a previous iteration, recursively until the initialization of the algorithm. The problem with this proof is that the assumptions of the theorems by Lions & Magenes were too strict to match the required topologies obtained in Chapters 6 and 7 over the 3 steps of the algorithm. To deal with this issue an assumption of smoothness was applied on the solution of the half line problem of the B equations, which is in any case too strong to be valid in its current form. This calls for either a better characterization of the smoothing properties of the dispersive boundary layer described on Chapter 7, or to use a more flexible estimate for the continuity of the traces.

Appendix A

Fourier and Laplace transforms

Here we recall some definitions and properties of the Fourier transforms, that can be found also in [76].

The Fourier transform of a function $f \in L^1(\mathbb{R})$ is given by

$$\mathcal{F}(f)(\kappa) = \hat{f}(\kappa) = \frac{1}{2\pi} \int_{\mathbb{R}} f(x) e^{j\kappa x} dx, \quad \kappa \in \mathbb{R} \tag{A.1}$$

and its inverse

$$(\mathcal{F}^{-1}\hat{f}) d\kappa = \int_{\mathbb{R}} \hat{f}(\kappa) e^{-\kappa x} d\kappa \tag{A.2}$$

One important property of this transform is Parseval's theorem that states that if $f \in L^1(\mathbb{R}) \cap L^2(\mathbb{R})$ then

$$|f|_{L^2(\mathbb{R})} = |\mathcal{F}(f)|_{L^2(\mathbb{R})} \tag{A.3}$$

And from this theorem, using that $C_0^\infty(\mathbb{R})$ functions are dense in $L^1(\mathbb{R})$ and also $L^2(\mathbb{R})$ one deduces that

Theorem A.1. *The Fourier transform* (A.1) *is a well-defined isometric operator from* $L^2(\mathbb{R})$ *to* $L^2(\mathbb{R})$. *In other words, for every* $f \in L^2(\mathbb{R})$ *there exists a unique function* $\mathcal{F}(f) \in L^2(\mathbb{R})$ *and*

$$|f|_{L^2(\mathbb{R})} = |\mathcal{F}(f)|_{L^2(\mathbb{R})} \tag{A.4}$$

The Laplace transform can be introduced by the fact that many functions are not regular enough to have a Fourier transform, but their irregularity is only due to fast, exponential growth. To study these functions one defines the **exponential class of functions** by all functions $f \in [0, \infty[\to \mathbb{C}$ such that there exists $\alpha \in \mathbb{R}$ such that for every $\sigma > \alpha$, $(t \mapsto f(t)e^{-\sigma t}) \in L^2(\mathbb{R})$. Then, for any function of the exponential class, the Laplace transform is defined as

$$\mathcal{L}(f)(\sigma + j\omega) = \mathcal{F}(fe^{-\sigma t})(\omega) = \frac{1}{2\pi} \int f(t) e^{-(\sigma + j\omega)t} d\omega \tag{A.5}$$

Now, by applying Parseval's theorem to $t \mapsto f(t)e^{-\sigma t}$ one can show that, for every $T > 0$, the Laplace transform satisfies:

$$\int_0^T |f(t)|^2 dt \leq \frac{e^{2\sigma T}}{2\pi} \int_{\mathbb{R}} |(\mathcal{L}(f)(\omega))|^2 |\sigma + j\omega|^2 d\omega \tag{A.6}$$

The following theorem, known as the Causality principle, states that changes in the future do not alter the past:

Theorem A.2. *Let $f(t)$ and $g(t)$, $t \in [0, \infty[$, two functions of the exponential class. If their Laplace transform satisfy*

$$|(\mathcal{L}f)(s)|^2 \leq c_1 |(\mathcal{L}g)|^2, \qquad \textit{with } Re(s) > \alpha \tag{A.7}$$

Then,

$$g(t) = 0, t \in [0, T] \Rightarrow f(t) = 0, \quad t \in [0, T] \tag{A.8}$$

Appendix B

Complex analysis

As can be found in [2], the following Theorem helps to estimate the residual of a Taylor expansion of an analytic function:

Lemma B.1. *If $f(z)$ is analytic in a region $\Omega \subset \mathbb{C}$, then for $z_0 \in \Omega$*

$$f(z) = f(z_0) + f'(z_0)(z - z_0) + \dots f^(n)(z_0) + f_{n+1}(z)(z - z_0)^{n+1}$$

with

$$f_{n+1}(z) = \frac{1}{2\pi} \int_C \frac{f(\zeta) d\zeta}{(\zeta - z_0)^{n+1}(\zeta - z)}$$

with C any circle $|z - z_0| = \rho$ such that the closed disk $|z - z_0| \leq \rho$ is contained in Ω. Moreover, if M denotes the maximum of $|f(z)$ on C, we obtain the estimate

$$|f_{n+1}(z)(z - z_0)^{n+1}| \leq \frac{M|z - z_0|^{n+1}}{\rho^n(\rho - |z - z_0|)}$$

and so, the remainder term tends uniformly to zero in every disk $|z - z_0| \leq r < \rho$.

The following lemma is result of the previous one

Lemma B.2. *Let $f(z) = (1 + z)^{-1/2}$ and $|z| \leq r < 1$. Then $f(z) = 1 + R(z)$ with $|R(z)| \leq C|z|$ for some $C > 0$.*

Proof. First, let $z = \rho e^{i\theta}$, $\rho > 0$ and $\theta \in [0, 2\pi)$, then $|f(z)|^2 \leq \dfrac{1}{1 - \rho} = f(-\rho)$, so by theorem B.1, letting $M = f(-\rho)$, for every $|z| < r < 1$

$$|R(z)| \leq \frac{M|z|}{\rho(\rho - |z|)} \leq \frac{M|z|}{\rho(\rho - r)} = C|z|$$

□

Appendix C

Approximation theory

Theorem C.1. *Let $r \geq 0$ integer, if $f \in H^r(\mathbb{R}^+)$ then there exists a family of functions $(f_h)_{h>0} \subset C^\infty$ and positive constants c, C such that $\hat{f}_h \in C_0^\infty(\mathbb{R})$ and*

$$|f^{(n)} - f_h^{(n)}|_{L^2(\mathbb{R})} \leq Ch^{r-n}|f^{(r)}|_{L^2(\mathbb{R})}, \quad \hat{f} = \hat{f}_h \ \textit{in} \ ]\frac{c}{h}, \frac{c}{h}[\tag{C.1}$$

for n integer between 0 and r

Proof. Let $\hat{\cdot}$ denote the Fourier transform; $\varphi \in C^\infty(\mathbb{R})$ such that $|\hat{\varphi}| \leq 1$, $\hat{\varphi} = 1$ in $(-c, c)$ and denote

$$\varphi_h(x) = \frac{1}{h}\varphi\left(\frac{x}{h}\right) \quad , x \in \mathbb{R} \tag{C.2}$$

then $\hat{\varphi}_h = \hat{\varphi}(h\cdot)$, so $\varphi_h = 1$ in $(-\frac{c}{h}, \frac{c}{h})$, then

$$\begin{aligned} |f^{(n)} - (f * \varphi_h)^{(n)}|^2_{L^2(\mathbb{R})} &= |\omega^n(\hat{f} - \hat{f}\hat{\varphi}_h)|^2_{L^2(\mathbb{R})} \\ &= \int_{|\omega| \geq \frac{c}{h}} |\omega|^{2n}|\hat{f}(\omega) - \hat{f}(\omega)\hat{\varphi}_h(\omega)d\omega \\ &\leq \left(\frac{h|\omega|}{c}\right)^{2r-2n} \int |\omega|^{2n}|\hat{f}(\omega) - \hat{f}(\omega)\hat{\varphi}_h(\omega)|^2 d\omega \\ &\leq 4\left(\frac{h^2}{c^2}\right)^{r-n} |f^{(r)}|^2_{L^2(\mathbb{R})} \end{aligned} \tag{C.3}$$

wheret the last inequality is obtained from $|\hat{\rho}_h| < 1$, a triangle inequality and the Fourier's identity for the derivative. □

The following theorem is quoted from [76]

Theorem C.2. *Let B_1 and B_2 denoted normed spaces, let M denote a dense subspace of B_1 and let B_2 be complete. If $S_0 : M \to B_2$ is a bounded linear operator, then there is a unique bounded linear operator $S : B_1 \to B_2$ with $Sf = S_0 f$ for all $f \in M$. The operator S is called the extension of S_0.*

The next theorem shows that smooth functions that integrate to 0 are dense in $L^2(\mathbb{R})$

Theorem C.3. *Let* $M = \{g \in C_0^\infty(\mathbb{R}) : \int g(x)dx = 0\}$ *and* $f \in H^r(\mathbb{R})$, $r \geq 0$. *Then, for every* $\varepsilon > 0$ *there exists a function* $g \in M$ *such that*

$$|f - g|_{H^r(\mathbb{R})} < \varepsilon \tag{C.4}$$

Proof. Because of the density of $C_0^\infty(\mathbb{R})$ in $H^r(\mathbb{R})$ there exists $h \in C_0^\infty$ such that

$$|f - h|_{H^r(\mathbb{R})} < \varepsilon \tag{C.5}$$

Let

$$C = \int h(x)dx \tag{C.6}$$

and for $L > 0$, let $\phi \in C_0^\infty(\mathbb{R})$ a bump function such that *supp*$(\phi) \subset (-1, 1)$ and $\int \phi dx = 1$, and define $\phi_L(x) = \frac{1}{L}\phi(\frac{x}{L})$, then

$$\phi_L^{(n)}(x) = \frac{1}{L^{n+1}}\phi^{(n)}(\frac{x}{L}), \quad \text{and} \int \phi_L(x)dx = 1 \tag{C.7}$$

and let $M = \max_n |\phi^{(n)|^2}$, then

$$\begin{aligned} |\phi_L^{(m)}|_{L^2}^2 &= \int_L^L |\phi_L^{(n)}(x)|^2 dx \\ &\leq \frac{1}{L^{2(n+1)}} \int_L^L |\phi^{(n)}(\frac{x}{L})|^2 dx \\ &\leq \frac{M2L}{L^{2(n+1)}} = \frac{2M}{L^{2n+1}} \end{aligned} \tag{C.8}$$

hence

$$|\phi_L|_{H^n} \leq \frac{2M(n+1)}{L} \tag{C.9}$$

Let $C = \int h dx$ and

$$g(x) = h(x) - C\phi_L(x) \tag{C.10}$$

then by construction $g \in M$ and

$$\begin{aligned} |f - g|_{H^r(\mathbb{R})} &\leq |f - h|_{H^r(\mathbb{R})} + C|\phi_L|_{H^n} \\ &\leq \varepsilon + \frac{2M(n+1)}{L} \end{aligned} \tag{C.11}$$

so choosing $L = 2M(n+1)/\varepsilon$, we conclude that $g \in M$ and

$$|f - g|_{H^r(\mathbb{R})} \leq 2\varepsilon \tag{C.12}$$

□

Theorem C.4. *Let* $M = \{g \in C^\infty(\mathbb{R}) : g(0) = 0\}$ *and* $f \in H^r(\mathbb{R})$, $r \geq 0$. *Then, for every* $\varepsilon > 0$ *there exists a function* $g \in M$ *such that*

$$|f - g|_{H^r(\mathbb{R})} < \varepsilon \tag{C.13}$$

Proof. Let $\hat{f}$ denote the Fourier transform of f and $M_0 = \{g \in C_0^\infty(\mathbb{R}) : \int g(\kappa)d\kappa = 0\}$, then by Theorem C.3 there exists $g \in M_0$ such that

$$|\hat{f} - g|_{H^n} \leq \varepsilon \tag{C.14}$$

so denoting $\mathcal{F}^{-1}(g)$ the inverse Fourier transform of g one has $g \in C^\infty$ and

$$g(0) = \int \hat{g}(\kappa)d\kappa = 0 \tag{C.15}$$

so $g \in M$ and from Parseval's theorem

$$|f - \mathcal{F}^{-1}(g)|_{H^n} \leq \varepsilon \tag{C.16}$$

□

Appendix D

Anisotropic Sobolev spaces

Here we review the definitions of anisotropic Sobolev spaces and trace theorems found in [83].

Let Ω be an open set in $\mathbb{R}$. Let $T > 0$ and $Q = \Omega\times]0, T[$. Let r, s be two non-negative real numbers, then the anisotropic spaces of degrees r and s are defined as

$$H^{r,s}(Q) = L^2(0, T; H^r(\Omega)) \cap H^s(0, T; L^2(\Omega))$$

let $\Gamma = \{x = 0\}$, then, in general dimensions one has

$$H^{r,s}(\Gamma \times T) = L^2(0, T; H^r(\Gamma)) \cap H^s(0, T; L^2(\Gamma))$$

but since here Γ only contains one point, one has

$$H^{r,s}(\Gamma \times (0, T)) = H^s(0, T)$$

The following theorem characterizes the derivatives of a function on $H^{r,s}(Q)$

Theorem D.1. *If $u \in H^{r,s}(Q)$, with r and s two strictly positive real numbers, and j, k are two integeres such that $1 - \left(\frac{j}{r} + \frac{k}{s}\right) \geq 0$, then we have*

$$\partial_x^j \partial_t^k u \in H^{\mu,\nu}(Q)$$

with $\frac{\mu}{r} = \frac{\nu}{s} = 1 - \left(\frac{j}{r} + \frac{k}{s}\right)$

The following theorem helps characterize a function in $H^{r,s}(Q)$ in terms of its traces and initial condition. For this, let $\Omega = \mathbb{R}^-$, $T = +\infty$ so $Q = \mathbb{R}^- \times \mathbb{R}^+$, then let

$$F = \left\{ \begin{array}{l} (f_k, g_j) \in \prod_{k\leq s-1/2} H^{p_k}(\Omega) \times \prod_{j<r-1/2} H^{\nu_j}(0,\infty) \\ \\ p_k = \dfrac{r}{s}(s-k-1/2), \quad \dfrac{\nu_j}{s} = \dfrac{r-j-1/2}{r} \quad , k, j \text{ integers,} \end{array} \right.$$

such that

$$\left. \begin{array}{r} \int_0^\infty |\partial_x^j f_k(-\sigma^s) - \partial_t^k g_j(\sigma^r)|^2 \dfrac{d\sigma}{\sigma} < \infty \quad \text{if } \dfrac{j}{r} + \dfrac{k}{s} = 1 - \dfrac{1}{2}\left(\dfrac{1}{r} + \dfrac{1}{s}\right) \\ \\ \partial_t^k g(0) = \partial_x^j f_k(0) \quad \text{if } \dfrac{j}{r} + \dfrac{k}{s} < 1 - \dfrac{1}{2}\left(\dfrac{1}{r} + \dfrac{1}{s}\right) \end{array} \right\}$$

Theorem D.2. *Let r and s be be positive real numbers such that $1-\dfrac{1}{2}\left(\dfrac{1}{r}+\dfrac{1}{s}\right)>0$. Then the application*

$$u \to (f_k, g_j) = \begin{cases} (\partial_t^k u(x,0))_{k<s-1/2} \\ \\ (\partial_x^j u(0,t))_{j<r-1/2} \end{cases}$$

is linear, continuous and surjective from $H^{r,s}(\Omega\times]0,\infty[)$ to F.

Appendix E

The elliptic ODE

Theorem E.1. *Let n be a non-negative integer, $g \in H^n(\mathbb{R}^-)$ and $y_0 \in \mathbb{R}$, then there exists one and only one function $y_1 : \mathbb{R}^- \to \mathbb{R}$ such that*

$$y_1 - \mu^2 y_1'' = g \quad , y(0) = y_0 \tag{E.1}$$

Also, there is one and only one function $y_2 : \mathbb{R}^- \to \mathbb{R}$ such that

$$y_2 - \mu^2 y_2'' = g \quad , y'(0) = y_0 \tag{E.2}$$

also $y_i \in H^{n+2}(\mathbb{R}^-)$ and for integer k from 0 to n

$$|y_i^{(k)}|^2_{L^2(\Omega)} + \mu^2 |y_i^{(k+1)}|^2_{L^2(\Omega)} + y^{(k)}(0)y^{(k+1)}(0) \leq \frac{1}{2}|g^{(n)}|^2_{L^2(\Omega)} \tag{E.3}$$

Proof. The existence and uniqueness are given by the formula

$$y(x) = \frac{1}{\mu}\int_0^x \sinh((z-x)/\mu)g(z)dz + ce^{x/\mu} \tag{E.4}$$

where $c = y_0$ in the Dirichlet case, and $c = \mu y_0$ in the Neumann case. The smoothness can be obtained by multiplying by y and integrating by parts to obtain

$$\int_{-\infty}^0 y^2(x) + \mu^2(y'(x))^2 dx + y(0)y'(0) - y(-\infty)y'(-\infty) = \int_{-\infty}^0 g(x)y(x)dx \tag{E.5}$$

and using the inequality

$$ab \leq \frac{a^2}{2\alpha} + \alpha\frac{b^2}{2} \tag{E.6}$$

with $\alpha = 1$ to obtain

$$\int_{-\infty}^0 y^2 + \mu^2(y'(x))^2 dx + y(0)y'(0) + y(-\infty)y'(-\infty) \leq \frac{1}{2}\int_{-\infty}^0 g(x)^2 dx \tag{E.7}$$

which implies that $y \in H^1(\mathbb{R}^-)$, and $y(-\infty) = y'(-\infty) = 0$. For the regularity, because of the ODE, we have $y'' = (g-y)/\mu \in L^2(\mathbb{R}^-)$ so $y \in H^2(\mathbb{R}^+)$. Now, for integer k from 1 to n by linearity $\tilde{y} = y^{(k)}$ and $\tilde{g} = g^{(k)}$ also satisfy (E.1), from where one obtains the energy estimates and $y \in H^{n+2}(\mathbb{R})$. $\square$

Appendix F

Proving continuity with the SWRM

Here we attempt to prove the continuity of the hybrid model of Chapter 8 by using the convergence of the algorithm (8.19). The next lemma uses these

Lemma F.1. *Let* $n \geq 0$ *and* $m \geq 0$ *such that* $\boldsymbol{W}_{0|\Omega_-} \in E_0^-$ *and* $\boldsymbol{W}_{0|\Omega_+} \in E_0^+$ *with*

$$E_0^- = H^{n+1}(\Omega_-) \times H^{n+1}(\Omega_-), \quad E_0^+ = H^m(\Omega_+) \times H^m(\Omega_+) \tag{F.1}$$

then at each iteration k *of algorithm* (8.19) *the solution* $(\boldsymbol{W}_-^k, \boldsymbol{W}_+^k)$ *satisfies*

$$\begin{aligned} |\boldsymbol{W}_-^k|_{E^-} &\lesssim |\boldsymbol{W}_0|_{E_0^-} + |\boldsymbol{W}_+^{k-1}|_{(H^{m,m})^2} \\ |\boldsymbol{W}_+^k|_{E^+} &\lesssim |\boldsymbol{W}_0|_{E_0^+} + |\boldsymbol{W}_-^{k-1}|_{(H^{n,s^\star})^2} \end{aligned} \tag{F.2}$$

with $E_- = H^{n,s}(Q_-) \times H^{n,s}(Q_-)$ *and* $E_+ = H^{m,m}(Q_+) \times H^{m,m}(Q_+)$ *and*

$$s^\star \geq \frac{1+s}{1-\frac{1}{2n}}, \quad s = m-1 \tag{F.3}$$

Proof. Let $\boldsymbol{W}_-^{k+1}, \boldsymbol{W}_+^{k+1}$ from algorithm (8.19). We begin by studying $\boldsymbol{W}_-^{k+1}$ first.

Let $\boldsymbol{W}_-^{k+1} = \boldsymbol{W}_{cauchy} + \boldsymbol{W}_c$ as in Theorem 8.2, page 174. Then from Theorem 6.1, page 146, one obtains

$$|\boldsymbol{W}_{cauchy}|_{E_-} \leq |\boldsymbol{W}_0|_{E_0^-} \tag{F.4}$$

and from Theorem 7.1

$$|\boldsymbol{W}_c|_{E_-} \lesssim |g_c^{k+1}|_{H^s(0,T)}, \quad \forall s \geq 0 \tag{F.5}$$

$$|\boldsymbol{W}_-^{k+1}|_{E^-} \lesssim |\boldsymbol{W}_0^-|_{E_0^-} + |g_c^{k+1}|_{H^s(0,T)} \tag{F.6}$$

with $g_c^{k+1} = g_{cauchy} - g_-^{k+1}$, and $g_{cauchy} = (\partial_t + \partial x)u_{cauchy}(0,\cdot)$. Because of Theorem 6.1, fixing s, we know that for every $j \geq 0$ $u_{cauchy} \in H^{n,s+j}(Q_-)$ so from Theorem D.2

$$\begin{gathered} \partial_t u_{cauchy}(0,\cdot) \in H^{\nu_0-1}, \quad \partial_x u_{cauchy}(0,\cdot) \in H^{\nu_1} \\ \frac{\nu_0}{s+j} = 1 - \frac{1}{2n}\frac{\nu_1}{s+j} = 1 - \frac{3}{2n} \end{gathered} \tag{F.7}$$

so $g_{cauchy} \in H^{\nu_0-1}(Q_-) \cap H^{\nu_1}$ and the mapping is continuous, hence

$$\begin{aligned} |g_{cauchy}|_{H^{\nu_0-1}\cap H^{\nu_1}} &\lesssim |u_{cauchy}|_{H^{n,s+j}} \\ &\lesssim |\boldsymbol{W}_{cauchy}|_{H^{n,s+j}\times H^{n,s+j}} \\ &\lesssim |\boldsymbol{W}_0|_{E_0^-} \end{aligned} \tag{F.8}$$

and from eq. (F.7) it is possible to compute that there is j such that $s \leq min(\nu_0 - 1, \nu_1)$ if $n \neq 1/2$ and $n \neq 1$, hence we obtain

$$|g_{cauchy}|_{H^s(Q_-)} \lesssim |\boldsymbol{W}_0|_{E_-} \tag{F.9}$$

and

$$\begin{aligned} |\boldsymbol{W}_-^{k+1}|_{E^-} &\lesssim |\boldsymbol{W}_0^-|_{E_0^-} + |g_c^{k+1}|_{H^s(0,T)} \\ &\leq |\boldsymbol{W}_0^-|_{E_0^-} + |g_{cauchy}|_{H^s(0,T)} + |g_-^{k+1}|_{H^s(0,T)} \\ &\lesssim |\boldsymbol{W}_0^-|_{E_0^-} + |g_-^{k+1}|_{H^s(0,T)} \end{aligned} \tag{F.10}$$

On the otherside, writing now $\boldsymbol{W}_+^{k+1} = \boldsymbol{W}_{cauchy} + \boldsymbol{W}_c$ as in Equation (8.20), we have that

$$\begin{aligned} |\boldsymbol{W}_+^{k+1}|_{E_+} &\leq |\boldsymbol{W}_{cauchy}|_{E_+} \\ &\lesssim |\boldsymbol{W}_0|_{E_0^+} + |\boldsymbol{W}_c|_{E^+} \\ &\lesssim |\boldsymbol{W}_0|_{E_0^+} + |g_c|_{H^m(0,T)} \\ &\lesssim |\boldsymbol{W}_0|_{E_0^+} + |g_+^{k+1}|_{H^m(0,T)} \end{aligned} \tag{F.11}$$

Now for the SV trace $g_-^{k+1} = (\partial_t + \partial_x)u_+^k(0,\cdot)$ if we assume that $s \leq m - 1$, then by the method of characteristics one obtains that

$$|g_-^{k+1}|_{H^s(0,T)} \leq |g_-^{k+1}|_{H^{m-1}} \lesssim |\boldsymbol{W}_+^k|_{(H^{m,m})^2} \tag{F.12}$$

and on the Bousinesq trace we have that $g_+^{k+1} = u_-^k(0,\cdot)$, **we will make the assumption that**

$$u_-^k \in H^{n,s}, \quad \forall s \geq 0 \tag{F.13}$$

which is reasonable only if the smoothing effect of the dispersive boundary layer occurs on a very small length. Making this assumption we obtain from Theorem D.2 that

$$u_-^k(0,\cdot) \in H^{\nu_0}(0,T), \quad \nu_0 = s^\star\left(1 - \frac{1}{2n^\star}\right), \quad s^\star > 0 \tag{F.14}$$

and from the continuity of the trace operator

$$|g_+^{k+1}|_{H^{\nu_0}(0,T)} \lesssim |\boldsymbol{W}_-^k|_{H^{n,s^\star}} \tag{F.15}$$

so to arrive to the conclusion we need $m, \nu_0, n, s^\star$ to be such that

$$|g_+^{k+1}|_{H^m(0,T)} \lesssim |g_+^{k+1}|_{H^{\nu_0}(0,T)} \lesssim |\boldsymbol{W}_-^k|_{H^{n,s^\star}} \tag{F.16}$$

which is equivalent to requiring that $m \leq \nu_0$, or in another words

$$s^\star \geq \frac{1+s}{1-\frac{1}{2n}} \tag{F.17}$$

but from the constrain of the SV trace we know that $s \leq m-1$, so taking $s = m-1$ we obtain the conclusion. □

Theorem F.1. *Let* $n \geq 0$ *and* $\boldsymbol{W}_0 \in H^{n+1}(\Omega) \times H^{n+1}(\Omega)$*, the limit* $k \geq 2$ *of the algorithm in* (8.19)*, page 172, given by* $(\boldsymbol{W}_-^2, \boldsymbol{W}_+^2)$*, satisfies*

$$|\boldsymbol{W}_-^2|_{(H^{n,s})^2} \lesssim |\boldsymbol{W}_0|_{(H^{n+1})^2} \tag{F.18}$$

and

$$|\boldsymbol{W}_+^2|_{(H^{n,s})^2} \lesssim |\boldsymbol{W}_0|_{(H^{n+1})} \tag{F.19}$$

Proof. To prove the continuity we will roll back from the second iteration using Lemma F.1 as

$$\begin{aligned}
|\boldsymbol{W}_-^2|_{(H^{n,s})^2} &\lesssim |\boldsymbol{W}_0|_{(H^{n+1})^2} + |\boldsymbol{W}_+^1|_{H^{m,m}} \\
&\lesssim |\boldsymbol{W}_0|_{(H^{n+1})^2} + |\boldsymbol{W}_-^0|_{(H^{n,s_1})^2}, \quad s_1 = \frac{m}{1-\frac{1}{2n}} \\
&\lesssim |\boldsymbol{W}_0|_{(H^{n+1})^2} + |g_+^0|_{H^{s_1}}
\end{aligned} \tag{F.20}$$

and on the other side of the domain

$$\begin{aligned}
|\boldsymbol{W}_+^2|_{(H^{n,s})^2} &\lesssim |\boldsymbol{W}_0|_{(H^{n+1})^2} + |\boldsymbol{W}_+^1|_{H^{m,m}} \\
&\lesssim |\boldsymbol{W}_0|_{(H^{n+1})} + |\boldsymbol{W}_-^1|_{(H^{n,s_2})^2}, \quad s_2 = \frac{1+s}{1-\frac{1}{2n}} \\
&\lesssim |\boldsymbol{W}_0|_{(H^{n+1})} + |\boldsymbol{W}_+^0|_{(H^{m_2,m_2})^2}, \quad m_2 = s_2 + 1 \\
&\lesssim |\boldsymbol{W}_0|_{(H^{n+1})} + |g_-^0|_{H^{s_2}}
\end{aligned} \tag{F.21}$$

because the limit does not depend on $g_\pm^0$ we can conclude by taking $g_\pm^0 = 0$. □

Bibliography

[1] A. Abdolali and J. T. Kirby. “Role of Compressibility on Tsunami Propagation”. In: *Journal of Geophysical Research: Oceans* 122.12 (2017), pp. 9780–9794.

[2] L. V. Ahlfors. *Complex Analysis: An Introduction to The Theory of Analytic Functions of One Complex Variable.* 3rd ed. McGraw-Hill, 1979, p. 345.

[3] G. B. Airy. *Tides and waves.* B. Fellowes, 1845.

[4] B. Alvarez-Samaniego and D. Lannes. “Large time existence for 3 D water-waves and asymptotics”. In: *Inventiones mathematicae* 171.3 (2008), pp. 485–541.

[5] C. J. Amick. “Regularity and uniqueness of solutions to the Boussinesq system of equations”. In: *Journal of Differential Equations* 54.2 (1984), pp. 231–247.

[6] P. Bacigaluppi, R. Ricchiuto, and P. Bonneton. “Implementation and Evaluation of Breaking Detection Criteria for a Hybrid Boussinesq Model”. In: *Water Waves* 2.2 (Nov. 2020), pp. 207–241.

[7] J. A. Battjes. “Shallow water wave modelling”. In: *Proc. Int. Symp.: Wavesphysical and numerical modelling, Vancouver.* 1994, pp. 1–23.

[8] C. Besse, J. F. Coulombel, and P. Noble. “Discrete transparent boundary conditions for the two-dimensional leap-frog scheme: approximation and fast implementation”. In: *ESAIM: Mathematical Modelling and Numerical Analysis* 55 (2021), S535–S571.

[9] C. Besse, M. Ehrhardt, and I. Lacroix-Violet. “Discrete artificial boundary conditions for the linearized Korteweg–de Vries equation”. In: *Numerical Methods for Partial Differential Equations* 32.5 (2016), pp. 1455–1484.

[10] C. Besse, B. Mésognon-Gireau, and P. Noble. “Artificial boundary conditions for the linearized Benjamin–Bona–Mahony equation”. In: *Numerische Mathematik* 139.2 (2018), pp. 281–314.

[11] Bona, J. L., Chen, M., and Saut, J.-C. “Boussinesq Equations and Other Systems for Small-Amplitude Long Waves in Nonlinear Dispersive Media. I: Derivation and Linear Theory”. In: *Journal of Nonlinear Science* 12.4 (Aug. 2002), pp. 283–318.

[12] P. Bonneton. “Modelling of periodic wave transformation in the inner surf zone”. In: *Ocean Engineering* 34.10 (2007), pp. 1459–1471.

[13] P. Bonneton, E. Barthelemy, E. Chazel, R. Cienfuegos, D. Lannes, F. Marche, and M. Tissier. “Recent advances in Serre–Green Naghdi modelling for wave transformation, breaking and runup processes”. In: *European Journal of Mechanics - B/Fluids* 30.6 (2011). Special Issue: Nearshore Hydrodynamics, pp. 589–597.

[14] P. Bonneton, N. Bruneau, B. Castelle, and F. Marche. *Large-scale vorticity generation due to dissipating waves in the surf zone.* 2010.

[15] P. Bonneton, F. Chazel, D. Lannes, F. Marche, and M. Tissier. “A splitting approach for the fully nonlinear and weakly dispersive Green–Naghdi model”. In: *Journal of Computational Physics* 230.4 (Feb. 2011), pp. 1479–1498.

[16] J. Boussinesq. “Théorie des ondes et des remous qui se propagent le long d’un canal rectangulaire horizontal, en communiquant au liquide contenu dans ce canal des vitesses sensiblement pareilles de la surface au fond”. In: *Journal de Mathématiques Pures et Appliquées* 17 (1872), pp. 55–108.

[17] B. Boutin. “Mathematical and numerical study of nonlinear hyperbolic equations: model coupling and nonclassical shocks”. PhD thesis. France: MATHEMATICAL METHODS and COMPUTING, 2009.

[18] D. Bresch, D. Lannes, and G. Métivier. “Waves interacting with a partially immersed obstacle in the Boussinesq regime”. In: *Analysis and PDE* 14.4 (2021), pp. 1085–1124.

[19] F. Brezzi, C. Canuto, and A. Russo. “A self-adaptive formulation for the Euler/Navier-Stokes coupling”. In: *Computer Methods in Applied Mechanics and Engineering* 73.3 (1989), pp. 317–330.

[20] M. Brocchini. “A reasoned overview on Boussinesq-type models: the interplay between physics, mathematics and numerics”. In: *Proceedings of the Royal Society A: Mathematical, Physical and Engineering Sciences* 469.2160 (2013), p. 20130496.

[21] J. G. Caldas Steinstraesser, R. A. Cienfuegos Carrasco, J. D. Galaz Mora, and A. Rousseau. “A Schwarz-based domain decomposition method for the dispersion equation”. In: *Journal of Applied Analysis & Computations* 8.3 (2018), p. 859.

[22] J.G. Caldas Steinstraesser, G. Kemlin, and A. Rousseau. “A domain decomposition method for linearized Boussinesq-type equations”. In: *Journal of Mathematical Study* 52.3 (2019), pp. 320–340.

[23] B. Carrión Aretxabala and R. A. Cienfuegos Carrasco. “Implementación de un modelo híbrido boussinesq-saint venant de propagación de oleaje”. Tesis (Ingeniero Civil de Industrias, Diploma en Ingeniería Hidráulica). Santiago, Chile: Pontificia Universidad Católica de Chile, 2008.

[24] M. J. Castro, A.M. Ferreiro Ferreiro, J.A. García-Rodríguez, J.M. González-Vida, J. Macías, C. Parés, and M. E. Vázquez-Cendón. “The numerical treatment of wet/dry fronts in shallow flows: application to one-layer and two-layer systems”. In: *Mathematical and Computer Modelling* 42.3 (2005), pp. 419–439.

[25] Y. A Cengel. *Introduction to thermodynamics and heat transfer.* Vol. 846. McGraw-Hill New York, 1997.

[26] R. Cienfuegos, E. Barthélemy, and P. Bonneton. “A fourth-order compact finite volume scheme for fully nonlinear and weakly dispersive Boussinesq-type equations. Part II: boundary conditions and validation”. In: *International Journal for Numerical Methods in Fluids* 53.9 (2007), pp. 1423–1455.

[27] J-F Coulombel and F. Lagoutière. *The Neumann numerical boundary condition for transport equations.* 2020.

[28] W. Craig and C. Sulem. “Numerical Simulation of Gravity Waves”. In: *Journal of Computational Physics* 108.1 (1993), pp. 73–83.

[29] W. Craig, S. Sulem, and P. L. Sulem. “Nonlinear modulation of gravity waves: a rigorous approach”. In: *Nonlinearity* 5.2 (Mar. 1992), p. 497.

[30] M. W. Dingemans. *Water Wave Propagation Over Uneven Bottoms.* World Scientific Publishing Company, 1997.

[31] E. Dubach. “Contribution à la résolution des équations fluides en domaine non borné”. PhD thesis. Paris 13, 1993.

[32] D. Dutykh, T. Katsaounis, and D. Mitsotakis. “Finite volume schemes for dispersive wave propagation and runup”. In: *Journal of Computational Physics* 230.8 (2011), pp. 3035–3061.

[33] B. Engquist and A. Majda. “Absorbing Boundary Conditions for the Numerical Simulation of Waves”. In: *Mathematics of Computation* 31.139 (1977), pp. 629–651.

[34] B. Engquist and A. Majda. “Radiation boundary conditions for acoustic and elastic wave calculations”. In: *Communications on Pure and Applied Mathematics* 32.3 (1979), pp. 313–357.

[35] W. D. Evans. “Partial Differential Equations”. In: *Bulletin of the London Mathematical Society* 20.4 (1988), pp. 375–376.

[36] A. G. Filippini. “Free surface flow simulation in estuarine and coastal environments: numerical development and application on unstructured meshes”. PhD thesis. Bordeaux, 2016.

[37] A. G. Filippini, S. De Brye, V. Perrier, F. Marche, N Ricchiuto, D. Lannes, and P. Bonneton. “UHAINA: A parallel high performance unstructured near-shore wave model”. In: *Journées Nationales Génie Côtier-Génie Civil.* Vol. 15. Editions Paralia. 2018, pp. 47–56.

[38] A. G. Filippini, M. Kazolea, and M. Ricchiuto. “A flexible genuinely nonlinear approach for nonlinear wave propagation, breaking and runup”. In: *Journal of Computational Physics* 310 (2016), pp. 381–417.

[39] A. S. Fokas and B. Pelloni. “Boundary Value Problems for Boussinesq Type Systems”. In: *Mathematical Physics, Analysis and Geometry* 8.1 (Feb. 2005), pp. 59–96.

[40] D. Funaro, A. Quarteroni, and P. Zanolli. “An iterative procedure with interface relaxation for domain decomposition methods”. In: *SIAM Journal on Numerical Analysis* 25.6 (1988), pp. 1213–1236.

[41] J. Galaz, M. Kazolea, and A. Rousseau. “Coupling Dispersive Shallow Water Models by Deriving Asymptotic Interface Operators”. In: *Domain Decomposition Methods in Science and Engineering XXVII.* Lecture Notes in Computational Science and Engineering. In print. Springer-Verlag, 2023.

[42] M. J. Gander. “Optimized Schwarz Methods”. In: *SIAM Journal on Numerical Analysis* 44.2 (2006), pp. 699–731.

[43] M. J. Gander. “Schwarz methods over the course of time.” eng. In: *ETNA. Electronic Transactions on Numerical Analysis [electronic only]* 31 (2008), pp. 228–255.

[44] M. J. Gander, :. Halpern, and F. Nataf. “Optimal Schwarz waveform relaxation for the one dimensional wave equation”. In: *SIAM Journal on Numerical Analysis* 41.5 (2003), pp. 1643–1681.

[45] M. J. Gander, L. Halpern, and V Martin. “How Close to the Fully Viscous Solution Can One Get with Inviscid Approximations in Subregions ?” In: *Domain Decomposition Methods in Science and Engineering XIX.* Ed. by Yunqing Huang, Ralf Kornhuber, Olof Widlund, and Jinchao Xu. Berlin, Heidelberg: Springer Berlin Heidelberg, 2011, pp. 237–244.

[46] M. J. Gander, L. Halpern, and F. Nataf. “Optimal Schwarz Waveform Relaxation for the One Dimensional Wave Equation”. In: *SIAM Journal on Numerical Analysis* 41.5 (2003), pp. 1643–1681.

[47] M. J. Gander and V. Martin. “An Introduction to Heterogeneous Domain Decomposition Methods for Multi-Physics Problems”. In: *Domain Decomposition Methods in Science and Engineering XXVII.* Lecture Notes in Computational Science and Engineering. In print. Springer-Verlag, 2023.

[48] F. Gastaldi and A. Quarteroni. “On the Coupling of Hyperbolic and Parabolic Systems: Analitical and Numerical Approach”. In: *Proceedings of the Third German-Italian Symposium Applications of Mathematics in Industry and Technology: June 18–22, 1988 Siena (Under the auspices of the CNR—DFG agreement).* Springer. 1989, pp. 123–165.

[49] D. Givoli. “High-order local non-reflecting boundary conditions: a review”. In: *Wave Motion* 39.4 (2004). New computational methods for wave propagation, pp. 319–326.

[50] S. Glimsdal, G. K. Pedersen, C. B. Harbitz, and F. Løvholt. “Dispersion of tsunamis: does it really matter?” In: *Natural Hazards and Earth System Sciences* 13.6 (2013), pp. 1507–1526.

[51] Frangle Plazma Goat. *Tidal river bore on the river ribble Lancashire shown along the section of river between the entrance to the River Douglas and Preston.* CC BY-SA 3.0, no changes made. via Wikimedia Commons. 2008.

[52] E. Godlewski, K. C. Le Thanh, and P.A. Raviart. “The numerical interface coupling of nonlinear hyperbolic systems of conservation laws: II. The case of systems”. In: *ESAIM: Mathematical Modelling and Numerical Analysis* 39.4 (2005), pp. 649–692.

[53] E. Godlewski and P.A. Raviart. “The numerical interface coupling of nonlinear hyperbolic systems of conservation laws: I. The scalar case”. In: *Numerische Mathematik* 97.1 (2004), pp. 81–130.

[54] S. Gottlieb. “On high order strong stability preserving runge-kutta and multi step time discretizations”. In: *Journal of Scientific Computing* 25.1–2 (Nov. 2005), pp. 105–128.

[55] A. E. Green and P. M. Naghdi. “A derivation of equations for wave propagation in water of variable depth”. In: *Journal of Fluid Mechanics* 78.2 (1976), pp. 237–246.

[56] The Wamdi Group. “The WAM Model—A Third Generation Ocean Wave Prediction Model”. In: *Journal of Physical Oceanography* 18.12 (Dec. 1988), pp. 1775–1810.

[57] E. Guisado-Pintado. “Shallow water wave modelling in the nearshore (SWAN)”. In: *Sandy Beach Morphodynamics*. Ed. by Derek W.T. Jackson and Andrew D. Short. Elsevier, 2020, pp. 391–419.

[58] L. Halpern. “Absorbing boundary conditions for the discretization schemes of the one-dimensional wave equation”. In: *Mathematics of Computation* 38.158 (1982), pp. 415–429.

[59] F. Hecht. “New development in FreeFem++”. In: *J. Numer. Math.* 20.3-4 (2012), pp. 251–265.

[60] T. W. Hsu, J. M Liau, S. J Liang, S. H Ou, and Y. T. Li. “A note on the derivation of wave action balance equation in frequency space”. In: *China Ocean Engineering* 25.1 (Mar. 2011), pp. 133–138.

[61] M.E. Hubbard and P. Garcia-Navarro. “Flux Difference Splitting and the Balancing of Source Terms and Flux Gradients”. In: *Journal of Computational Physics* 165.1 (2000), pp. 89–125.

[62] F. Imamura, A. C. Yalciner, and G. Ozyurt. “Tsunami modelling manual”. In: *UNESCO IOC international training course on Tsunami Numerical Modelling* (2006), pp. 137–209.

[63] IUGG/IOC Time Project. *IOC Manuals and Guides No. 35.* UNESCO 1997 (English). Intergovernmental Oceanographic Commission (IOC) of UNESCO. 1997.

[64] C. M. Johnston, C. T. Gartman, and D. Mantzavinos. “The linearized classical Boussinesq system on the half-line”. In: *Studies in Applied Mathematics* 146.3 (2021), pp. 635–657.

[65] M. Kazakova and P. Noble. “Discrete Transparent Boundary Conditions for the Linearized Green–Naghdi System of Equations”. In: *SIAM Journal on Numerical Analysis* 58.1 (2020), pp. 657–683.

[66] M. Kazakova and G. L. Richard. “A new model of shoaling and breaking waves: one-dimensional solitary wave on a mild sloping beach”. In: *Journal of Fluid Mechanics* 862 (2019), pp. 552–591.

[67] M. Kazolea and A. I. Delis. “A well-balanced shock-capturing hybrid finite volume-finite difference numerical scheme for extended 1D Boussinesq models”. In: *Appl. Numer. Math.* 67 (May 2013), pp. 167–186.

[68] M. Kazolea and A.I. Delis. “A well-balanced shock-capturing hybrid finite volume–finite difference numerical scheme for extended 1D Boussinesq models”. In: *Applied Numerical Mathematics* 67 (2013). NUMAN 2010, pp. 167–186.

[69] M. Kazolea, A.I. Delis, and C.E. Synolakis. “Numerical treatment of wave breaking on unstructured finite volume approximations for extended Boussinesq-type equations”. In: *Journal of Computational Physics* 271 (2014). Frontiers in Computational Physics, pp. 281–305.

[70] M. Kazolea and M. Ricchiuto. “On wave breaking for Boussinesq-type models”. In: *Ocean Modelling* 123 (2018), pp. 16–39.

[71] M. Kazolea and M. Ricchiuto. “Full Nonlinearity in Weakly Dispersive Boussinesq Models: Luxury or Necessity”. In: *Journal of Hydraulic Engineering* 150.1 (2024), p. 04023061.

[72] G. Khakimzyanov, D. Dutykh, and Z. I. Fedotova. “Dispersive Shallow Water Wave Modelling. Part III: Model Derivation on a Globally Spherical Geometry”. In: *Communications in Computational Physics* 23.2 (2018), pp. 315–360.

[73] D-H Kim, P.J. Lynett, and S.A. Socolofsky. “A depth-integrated model for weakly dispersive, turbulent, and rotational fluid flows”. In: *Ocean Modelling* 27.3 (2009), pp. 198–214.

[74] J. Kim, G.K. Pedersen, F. Løvholt, and R. J. LeVeque. “A Boussinesq type extension of the GeoClaw model - a study of wave breaking phenomena applying dispersive long wave models”. In: *Coastal Engineering* 122 (2017), pp. 75–86.

[75] G. J. Komen, L. Cavaleri, M. Donelan, K. Hasselmann, S. Hasselmann, and P. A. E. M. Janssen. *Dynamics and Modelling of Ocean Waves.* 1996.

[76] H-O Kreiss and J Lorenz. *Initial-Boundary Value Problems and the Navier-Stokes Equations.* Society for Industrial and Applied Mathematics: Philadelphia, Pennsylvania, USA, 2004.

[77] D. Lannes. *The water waves problem: mathematical analysis and asymptotics.* Vol. 188. American Mathematical Soc., 2013.

[78] D. Lannes. “Modeling shallow water waves”. In: *Nonlinearity* 33.5 (Mar. 2020), R1.

[79] D. Lannes and P. Bonneton. “Derivation of asymptotic two-dimensional time-dependent equations for surface water wave propagation”. In: *Physics of fluids* 21.1 (2009), p. 016601.

[80] D. Lannes and F. Marche. “A new class of fully nonlinear and weakly dispersive Green–Naghdi models for efficient 2D simulations”. In: *Journal of Computational Physics* 282 (2015), pp. 238–268.

[81] D. Lannes and W. Weynans. “Generating boundary conditions for a Boussinesq system*”. In: *Nonlinearity* 33.12 (Oct. 2020), p. 6868.

[82] R. Leveque. *Finite Volume Methods for Hyperbolic Problems.* Vol. 39. 1. Feb. 2004, pp. 88–89.

[83] J-L Lions and E. Magenes. “Problèmes aux limites non homogènes. II”. fr. In: *Annales de l’Institut Fourier* 11 (1961), pp. 137–178.

[84] P-L Lions. “On the Schwarz alternating method. III: a variant for nonoverlapping subdomains”. In: *Third international symposium on domain decomposition methods for partial differential equations.* Vol. 6. SIAM Philadelphia. 1990, pp. 202–223.

[85] F. Lovholt, G. Pedersen, and S. Glimsdal. “Coupling of Dispersive Tsunami Propagation and Shallow Water Coastal Response”. In: *The Open Oceanography Journal* 4.1 (May 2010), pp. 71–82.

[86] P.A. Madsen, D.R. Fuhrman, and H.A. Schäffer. “On the solitary wave paradigm for tsunamis”. In: *Journal of Geophysical Research: Oceans* 113.C12 (2008).

[87] P.A. Madsen, O. R. Sørensen, and H. A. Schäffer. “Surf zone dynamics simulated by a Boussinesq type model. Part I. Model description and cross-shore motion of regular waves”. In: *Coastal Engineering* 32.4 (1997), pp. 255–287.

[88] F. Magoulés and R. Putanowicz. “Optimal convergence of non-overlapping Schwarz methods for the Helmholtz equation”. In: *Journal of Computational Acoustics* 13.03 (2005), pp. 525–545.

[89] D. Mantzavinos and D. Mitsotakis. “Extended water wave systems of Boussinesq equations on a finite interval: Theory and numerical analysis”. In: *Journal de Mathématiques Pures et Appliquées* 169 (2023), pp. 109–137.

[90] V. Martin. “Méthodes de décomposition de domaine de type relaxation d’ondes pour des équations de l’océanographie”. 2003PA132022. PhD thesis. 2003, 291 p.

[91] T.P.A. Mathew. “Heterogeneous Domain Decomposition Methods”. In: *Domain Decomposition Methods for the Numerical Solution of Partial Differential Equations.* Vol. 61. Lecture Notes in Computational Science and Engineering. Berlin, Heidelberg: Springer, 2008.

[92] E. Mignot and R. Cienfuegos. “On the application of a Boussinesq model to river flows including shocks”. In: *Coastal Engineering* 56.1 (2009), pp. 23–31.

[93] J. Monbaliu. “Chapter 5 Spectral wave models in coastal areas”. In: *Advances in Coastal Modeling.* Ed. by V.C. Lakhan. Vol. 67. Elsevier Oceanography Series. Elsevier, 2003, pp. 133–158.

[94] I.K. Nikolos and A.I. Delis. “An unstructured node-centered finite volume scheme for shallow water flows with wet/dry fronts over complex topography”. In: *Computer Methods in Applied Mechanics and Engineering* 198.47 (2009), pp. 3723–3750.

[95] O. Nwogu. “Alternative Form of Boussinesq Equations for Nearshore Wave Propagation”. In: *Journal of Waterway, Port, Coastal, and Ocean Engineering* 119.6 (1993), pp. 618–638.

[96] O. Nwogu. “Numerical Prediction of Breaking Waves and Currents with a Boussinesq Model”. In: *Coastal Engineering 1996*, pp. 4807–4820.

[97] M. Parisot. “Thick interfaces coupling technique for weakly dispersive models of waves”. In: (2024). (Submitted).

[98] G. Pedersen and F. Løvholt. *Documentation of a Global Boussinesq Solver.* Research report Preprint series. Mechanics and Applied Mathematics. University of Oslo, 2008.

[99] D. H. Peregrine. “Long waves on a beach”. In: *Journal of fluid mechanics* 27.4 (1967), pp. 815–827.

[100] A. Quarteroni, F. Pasquarelli, and A. Valli. “Heterogeneous domain decomposition: principles, algorithms, applications”. In: *Fifth International Symposium on Domain Decomposition Methods for Partial Differential Equations.* SIAM Philadelphia. 1992, pp. 129–150.

[101] P.L Roe. “Approximate Riemann solvers, parameter vectors, and difference schemes”. In: *Journal of Computational Physics* 43.2 (1981), pp. 357–372.

[102] V. Roeber and K.F. Cheung. “Boussinesq-type model for energetic breaking waves in fringing reef environments”. In: *Coastal Engineering* 70 (2012), pp. 1–20.

[103] A.B. de Saint Venant. “Théorie du mouvement non-permanent des eaux, avec application aux crues des rivières et á l’introduction des marées dans leur lit”. In: *C. R. Math. Acad. Sci. Paris* 73 (1871), pp. 147–154.

[104] M.E. Schonbek. “Existence of solutions for the boussinesq system of equations”. In: *Journal of Differential Equations* 42.3 (1981), pp. 325–352.

[105] H.A. Schwarz. *Ueber einen Grenzübergang durch alternirendes Verfahren.* Zürcher u. Furrer, 1870.

[106] F. Shi, J.T. Kirby, J.C. Harris, J.D. Geiman, and S.T. Grilli. “A high-order adaptive time-stepping TVD solver for Boussinesq modeling of breaking waves and coastal inundation”. In: *Ocean Modelling* 43-44 (2012), pp. 36–51.

[107] J. J. Stoker. *Water Waves: The Mathematical Theory with Applications.* Wiley, Jan. 1992.

[108] I.A. Svendsen. “Mass flux and undertow in a surf zone”. In: *Coastal Engineering* 8.4 (1984), pp. 347–365.

[109] C.E. Synolakis. “The runup of solitary waves”. In: *Journal of Fluid Mechanics* 185 (1987), pp. 523–545.

[110] S. Tavakkol and P. Lynett. “Celeris: A GPU-accelerated open source software with a Boussinesq-type wave solver for real-time interactive simulation and visualization”. In: *Computer Physics Communications* 217 (2017), pp. 117–127.

[111] S. Tavakkol and P. Lynett. “Celeris Base: An interactive and immersive Boussinesq-type nearshore wave simulation software”. In: *Computer Physics Communications* 248 (2020), p. 106966.

[112] M. Tayachi, A. Rousseau, E. Blayo, N. Goutal, and V. Martin. “Design and analysis of a Schwarz coupling method for a dimensionally heterogeneous problem”. In: *International Journal for Numerical Methods in Fluids* 75.6 (2014), pp. 446–465.

[113] M. Tissier, P. Bonneton, F. Marche, F. Chazel, and D. Lannes. "Serre Green-Naghdi modelling of wave transformation breaking and run-up using a high-order finite-volume finite-difference scheme". In: *Proceedings of the International Conference on Coastal Engineering; No 32 (2010): Proceedings of 32nd Conference on Coastal Engineering, Shanghai, China, 2010.; waves.13* 1 (Feb. 2011).

[114] M. Tissier, P. Bonneton, F. Marche, F. Chazel, and D. Lannes. "A new approach to handle wave breaking in fully non-linear Boussinesq models". In: *Coastal Engineering* 67 (2012), pp. 54–66.

[115] V.V. Titov and F.I. Gonzalez. *Implementation and testing of the Method of Splitting Tsunami (MOST) model.* Tech. rep. NOAA technical memorandum ERL PMEL; 112; Contribution (Pacific Marine Environmental Laboratory (U.S.)); no. 1927. Pacific Marine Environmental Laboratory (U.S.), 1997.

[116] H.L. Tolman. "A Third-Generation Model for Wind Waves on Slowly Varying, Unsteady, and Inhomogeneous Depths and Currents". In: *Journal of Physical Oceanography* 21.6 (1991), pp. 782–797.

[117] M. Tonelli and M. Petti. "Hybrid finite volume–finite difference scheme for 2DH improved Boussinesq equations". In: *Coastal Engineering* 56.5-6 (2009), pp. 609–620.

[118] M. Tonelli and M. Petti. "Finite volume scheme for the solution of 2D extended Boussinesq equations in the surf zone". In: *Ocean Engineering* 37.7 (2010), pp. 567–582.

[119] M. Tonelli and M. Petti. "Simulation of wave breaking over complex bathymetries by a Boussinesq model". In: *Journal of Hydraulic Research* 49.4 (2011), pp. 473–486.

[120] M. Tonelli and M. Petti. "Shock-capturing Boussinesq model for irregular wave propagation". In: *Coastal Engineering* 61 (2012), pp. 8–19.

[121] M. Tonelli and M. Petti. "Numerical simulation of wave overtopping at coastal dikes and low-crested structures by means of a shock-capturing Boussinesq model". In: *Coastal Engineering* 79 (2013), pp. 75–88.

[122] S. Watada, S. Kusumoto, and K. Satake. "Traveltime delay and initial phase reversal of distant tsunamis coupled with the self-gravitating elastic Earth". In: *Journal of Geophysical Research: Solid Earth* 119.5 (2014), pp. 4287–4310.

[123] G. Wei and J. T. Kirby. "Time-Dependent Numerical Code for Extended Boussinesq Equations". In: *Journal of Waterway, Port, Coastal, and Ocean Engineering* 121.5 (1995), pp. 251–261.

[124] G. Wei and J.T. Kirby. "Time-dependent numerical code for extended Boussinesq equations". In: *Journal of waterway, port, coastal, and ocean engineering* 121.5 (1995), pp. 251–261.

[125] G. B. Whitham. "Linear Dispersive Waves". In: *Linear and Nonlinear Waves.* John Wiley & Sons, Ltd, 1999. Chap. 11, pp. 361–402.

[126] S. Yamamoto, S. Kano, and H. Daiguji. "An efficient CFD approach for simulating unsteady hypersonic shock–shock interference flows". In: *Computers & Fluids* 27.5 (1998), pp. 571–580.

[127] V. E. Zakharov. “Stability of periodic waves of finite amplitude on the surface of a deep fluid”. In: *Journal of Applied Mechanics and Technical Physics* 9.2 (Mar. 1968), pp. 190–194.

[128] J.A. Zelt. “The run-up of nonbreaking and breaking solitary waves”. In: *Coastal Engineering* 15.3 (1991), pp. 205–246.

[129] C. Zheng, X. Wen, and H. Han. “Numerical solution to a linearized KdV equation on unbounded domain”. In: *Numerical Methods for Partial Differential Equations: An International Journal* 24.2 (2008), pp. 383–399.